Drift Wave Models for 3-Dimensional Plasmas

A thesis submitted for the degree
of Doctor of Philosophy of
the Australian National University

Jerome Laurent Vincent Lewandowski

November 12, 1997

The work contained in this thesis is my own original research, produced in collaboration with my supervisor — Dr. M. Persson. Any material taken from other references is explicitly acknowledged as such.

Jerome L.V. Lewandowski

November 12, 1997

Abstract

The work presented in this thesis is concerned with the properties of slow, drift-type instabilities, the so-called drift waves, in 3-Dimensional, magnetically-confined plasmas. Since the mode structure and the growth rate of numerous microinstabilities depend crucially on the topology of the confining magnetic field, the first part of this thesis is devoted to the study, derivation and visualization of key magnetic field attributes. In the second part of this thesis, possible physics models for studying drift-waves in 3-Dimensional magnetic topologies are discussed. The emphasis is put on retaining the details of the confining magnetic field. The simplest model to consider slow, drift-type modes is the so-called cold ion model. This model is solved numerically for a helically-symmetric configuration. A model for drift waves derived from standard fluid equations is also presented. The comparison between this model and the cold ion model is discussed. Drift waves calculations are then considered using the gyro-kinetic model. Applications and limitations of the gyro-kinetic formalism are presented and generalization to fully 3-Dimensional plasma geometry is discussed. A novel initial-value, linear ion gyro-kinetic code, in which the 3-Dimensional magnetic geometry is implemented using straight-field-line coordinates, is presented. The electron population is assumed to be in the collisional regime. We present numerical calculations of drift waves in the geometry of the toroidal heliac H1-NF.

In chapter 1, the motives, goals and possibilities of fusion energy research are briefly discussed. The main theoretical and experimental goals of magnetic confinement research are introduced. The topic of cross-field transport in stellarator and tokamak plasmas is discussed in some detail. In chapter 2, we introduce the energy principle and discuss the key attributes of the confining magnetic field and

their affects on the plasma stability. In particular, the local magnetic shear and the magnetic curvature are discussed. These quantities are derived for two linear configurations: the general screw pinch and the helically-symmetric configuration. Influence of toroidicity effects on the magnetic field key attributes are considered separately in chapter 3. The low-pressure tokamak configuration and the stellarator configuration are studied. Possible models to study drift waves in 3-Dimensional geometries are discussed in chapter 4. A simple fluid model is presented and the relevant effects arising from the magnetic field topology are specifically discussed. A drift wave model in the cold ion approximation is also presented and numerical results for a helically-symmetric configuration are given. In chapter 5, the linear gyro-kinetic formalism is presented and its applications and intrinsic limitations are discussed. A numerical code to solve the linear gyro-kinetic equation in stellarator geometry is presented in chapter 6. Numerical results for H1-NF are also reported. We conclude with some remarks and possible improvements in chapter 7.

Calculations of the local magnetic shear for low-β tokamak plasmas, described in chapter 3, has been published in Lewandowski and Persson [1, 2]. Drift wave calculations in a helically-symmetric configuration has been published in Persson *et al* [3].

Acknowledgements

I would like to thank my supervisor, Dr. Mikael Persson, for the assistance and encouragement that he has provided throughout the period of my research. His constant support has contributed a great deal in the completion of this thesis.

I would like to thank Dr. Henry Gardner for patiently providing crucial data for plasma equilibria. Thanks to Prof R.L. Dewar for fruitful discussions and for helping with academic (and related) matters.

Dr. R.E. Waltz is acknowledged for his help regarding the understanding of various aspects of anomalous transport.

Thank you to the members of my family in Canada, France and Poland for their unconditional support during my graduate studies. I owe them my tiniest achievements.

A warm thank you to my soulmate, Hema, for her constant support during my doctoral studies.

This thesis is dedicated to Joseph Lewandowski.

Contents

CHAPTER 1

Introduction

1.1 Fusion research

Modern civilizations are dependent on electrical energy. In the newly industrialized part of the world, the demand for electrical power is increasing steeply, with the consumption doubling approximately every ten years. This trend cannot continue indefinitely but there is still a strong need to develop an environmentally attractive, commercially viable, and sustainable energy source for the next century. To develop a system capable of providing such a source of energy is the mission of the fusion energy research community.

There is presently a great imbalance in the world energy consumption. As an example, in 1990, the per capita consumption of energy in India and China were 1/6 and 1/3 of the world average [4], respectively. Over the next decades, it is likely that these figures will increase considerably. A large part of this increase will no doubt be generated by conventional burning of fossil fuels. This will degrade the local environments greatly and the impact on the global environment will be staggering. Hence, there is a great need to develop viable renewable energy sources and increase the efforts on developing new technologies such as those of controlled thermo-nuclear fusion.

Fusion technologies hold a great promise for the future. Widespread introduction of fusion energy power plants could substantially reduce the environmental impacts of increasing worldwide demands for electricity.

For more than fifty years, researchers from around the world have worked towards achieving controlled thermo-nuclear fusion. Fusion is the process by which light elements are fused together, forming heavier elements and liberating energy in the process. There are two different paths to achieve this goal. In inertial fusion, a small pellet of solid fuel is bombarded by photons generated by high energy lasers, or by ions generated by particle accelerators. The second, and perhaps more promising, avenue is by means of magnetic confinement. In this scheme, a fully ionized gas (plasma), is confined in a strong magnetic field. The goal is to confine a plasma of sufficiently high temperature and density and for a sufficiently long period of time as to allow the particles to fuse. Current research efforts are mainly focused on two different concepts, the tokamak and the stellarator. Both these confinement devices are closed systems of toroidal shape. The tokamak plasma has one continuous symmetry property (toroidal or axi-symmetry) and can, to a very good approximation, be described by 2-dimensional equations. The stellarator is however fully 3-dimensional. Unless sufficient non-inductive current drive can be achieved, the tokamak is an inherently pulsed device whereas the stellarator is in principle a steady-state device.

Physics problems in magnetic fusion can be divided into four basic areas: equilibrium, stability, transport and heating. This division is somewhat artificial since the plasma experiments simultaneously involve the above-mentioned four areas and interaction between them. Nevertheless, one can use the above division as a convenient framework for theoretical studies since the fully self-consistent problem is too big to be treated.

The equilibrium and stability are only briefly considered in this thesis, while special attention is paid to the transport issue. Our main interest is the so-called 'anomalous transport', with specific emphasis on the underlying instabilities of drift type. Heating is not addressed.

1.2 Transport

In an homogeneous, straight, magnetic field **B**, the particles can diffuse across the magnetic field by means of collisions; this is the classical transport. In a toroidal configuration, the magnetic field is necessarily inhomogeneous and toroidicity effects affect the particle trajectories. The toroidicity-induced transport is called 'neoclassical transport'. However, experimental measurements indicate that, both in tokamaks and stellarators, the *actual* cross-field transport is much larger than the neoclassical transport and it is called anomalous for this reason [6, 67]. For example, the electron perpendicular transport is almost always anomalous in character. The ion perpendicular transport, however, is sometimes in good agreement with neoclassical predictions. Short-range forces (collisions) and long-range forces (collective phenomena or 'waves') can affect the particle and energy transports across the magnetic surfaces. Slow, short-scale instabilities (microinstabilities) are major contenders to explain the anomalous transport in tokamaks and stellarators [5, 6, 7, 8, 9]. Microinstabilities can be driven unstable by tapping the free energy contained in the density and ion and electron temperatures gradients. Another source of free energy is available when the particle distribution functions depart from Maxwellian distributions. Non-maxwellian effects can be generated by the interaction of the heating mechanism with the plasma or by the presence of particles with high kinetic energy.

Drift waves form a special class of microinstabilities. These instabilities can be driven unstable when potential, $\widetilde{\Phi}$, and density, $\widetilde{n}$, perturbations are driven out of phase [9]. Collisional effects, particle trapping, inverse electron-Landau damping, magnetic drift resonances are possible causes which can trigger locally the departure from an adiabatic response. The nonadiabatic plasma response, if present, leads to the formation of fluctuating electric field, $\widetilde{\mathbf{E}}_{||}$, and current, $\widetilde{\mathbf{J}}_{||}$, along **B**; in turn, a fluctuating cross-field current, $\widetilde{\mathbf{J}}_{\perp}$, is generated in order to maintain the plasma quasineutrality. The $\widetilde{\mathbf{J}}_{\perp} \times \mathbf{B}$ force can then enhance the initial perturbation. At large β (plasma pressure/kinetic pressure), magnetic perturbations have to be taken into account. However, experimental measurements suggest that in both tokamaks and stellarators the observed anomalous transport can often be explained by *electrostatic* fluctuations.

Drift wave dynamics in tokamak geometry is now fairly well understood. The nonlinear behavior of drift waves has been studied using extensive, large-scale numerical codes. However, the overall picture indicates that there is a great deal of work that remains to be done. The best signature of this state of affairs is that the design of the next generation of large-scale experiments rely on the use of empirical or semi-empirical scaling laws. Tokamaks and stellarators appear to have different scaling laws for the energy confinement time, τ_{E}. Tokamaks in the low confinement mode (L-mode) appear to show a Bohm scaling for τ_{E} [10, 11]. In the Bohm regime, the correlation length of the fluctuations scales like the minor radius of the machine. Experimental data for stellarators is far less extensive than that for tokamaks. However, as far as data is available, stellarators appear to have a gyro-Bohm scaling for the confinement time [12]. For the gyro-Bohm scaling the fluctuation correlation length scales like the ion gyro-radius. The difference in τ_{E} is not understood.

The *local* properties of the confining magnetic field for the stellarator and tokamak configurations are quite different. The details of the magnetic field are worth studying for two reasons. First almost all microinstabilities are sensitive to the details of the equilibrium magnetic field $\mathbf{B}$. For example, the local magnetic shear, the normal magnetic curvature, the geodesic magnetic curvature and the variation of $\mathbf{B}$ along the field line are important quantities that can affect the drift-wave-driven transport. In some cases, the *global* (surface-averaged) properties of $\mathbf{B}$ can give an approximately correct physical picture. However, in order to assess the difference between stellarator and tokamaks one has to carefully retain the details of $\mathbf{B}$ before any definite conclusion can be reached. The second reason is related to the design of large-scale fusion experiments. If the τ_{E} scaling can be explained on theoretical grounds, it might be possible to design a confinement devices with optimum stability *and* transport properties. However, a formidable amount of computational work would be required to reach robust conclusions.

Before considering physical models for drift waves in stellarator geometry, a better understanding of the magnetic field properties of such a configuration seems to be

the first logical step. In chapters 2 and 3, some key attributes of the magnetic field topology of the general screw pinch, helically-symmetric configuration, tokamak configuration and stellarator configuration are calculated and discussed. In particular the importance of toroidicity-induced effects is considered. Visualization techniques are used to display quantities of interest. In chapter 3, analytical calculations are carried out for the low-β tokamak configuration. In particular it is shown how the shear-reversed configuration enhances the stabilizing effect of the local magnetic shear [1, 2]. The magnetic field attributes of stellarator plasmas are computed numerically and visualization techniques are used to display the relevant physical quantities. The calculations for four different stellarators are presented.

The second part of this thesis is devoted to drift wave calculations. The 3-dimensional character of the confining magnetic field of stellarators leads to complications in the study of drift waves. Therefore we first consider simple physical models, such as the cold ion model, but retain the full three-dimensional details of $\mathbf{B}$.

Two fluid models are presented in chapter 4. One model is obtained using Braginskii equations [13], while the second model, the cold ion model (CIM), is derived by making simplifications in a refined *kinetic* treatment, followed by an appropriate average over velocity space. The simple fluid model and the CIM both retain essential features of the drift wave, such as curvature effects, ion sound wave coupling and finite gyro-radius effects (inertial correction). These two models lead to two different eigenmode equations. The eigenmode equation of the CIM is solved numerically for a helically-symmetric equilibrium; the drift wave spectrum in such a configuration is presented [3].

In the above-mentioned fluid models, the nonadiabatic part of the electron response, which is the destabilizing mechanism, is introduced as an *ad hoc* parameter. The linear growth rate is directly related to this parameter, which is not satisfactory. Furthermore, these models leave out important driving mechanisms such as particle trapping and un-trapping and collisional effects. A more realistic model can be obtained with a kinetic approach. One possible kinetic model, the linear gyro-kinetic

model, is presented in chapters 5 and 6.

In chapter 5, the linear gyro-kinetic model is presented. The assumptions, orderings and limitations of the gyro-kinetic model are discussed in some detail. We also discuss the difficulties in solving the gyro-kinetic equation for realistic plasma configurations.

Based on the discussion of chapter 5, we present a novel fluid/gyro-kinetic model for fully 3-dimensional plasmas. In this model, particle trapping and ion collisional effects are neglected. An eikonal representation for fluctuating quantities reduces the problem to a time-dependent, along-the-field-line problem. Numerical results for the toroidal heliac H1-NF are presented.

We summarize our results in chapter 7. Concluding remarks and possible improvements of the present work are discussed.

CHAPTER 2

Magnetic Field Structure of Magnetically Confined Plasmas (Part I)

2.1 Introduction

In this chapter, we present a detailed study of the magnetic field structure of confined plasmas. In order to get physical insight, we identify the magnetic field attributes that enter the ideal MHD energy principle and that can also affect the drift wave dynamics. These magnetic field attributes are calculated for two toroidicity-free configurations: the general screw pinch and the helically-symmetric configuration. We develop numerical techniques to visualize the properties of the magnetic field for 3-Dimensional plasmas. Specific examples for the helically-symmetric configuration are presented.

In general, drift waves and other microinstabilities depend sensitively on the local properties of the confining magnetic field. For example, the component of the magnetic field curvature which is normal to the magnetic surface can cause modes with long parallel wavelength to 'balloon' on the outside of the torus. The local magnetic shear, however, usually has a stabilizing influence on such modes. The full problem of microinstability-driven cross-field transport over the entire plasma volume is a formidable task. A more tractable problem is to study the *linear* problem one magnetic surface at a time. In this context, it is worth considering the details of the magnetic field properties of a given surface. It is then convenient to separate the local magnetic shear into two parts: one part is constant on a given magnetic surface

and is called the 'global shear'; the second part varies in the magnetic surface and is called the 'residual local shear'. The surface average of the residual local shear identically vanishes. The same procedure can be adopted for the normal curvature.

A simple starting point is to consider the energy principle and to identify the magnetic field attributes that can affect the stability. The energy principle is derived from the ideal magnetohydrodynamic (MHD) one-fluid equations [14, 15]. It is worth mentioning that the equations from which the energy principle is derived do not segregate the ion and electron populations – the plasma is seen as *one* perfectly-conducting fluid. Resistive and viscous effects, which are not retained in the ideal MHD equations, can be important for drift waves. Indeed, it is precisely *nonideal* effects that can destabilize the drift waves. Nevertheless, some key features of the magnetic field in the ideal MHD energy can be important for drift wave dynamics.

The magnetic field key attributes in stability and transport problems enter in conjunction with other quantities. For example, the local magnetic shear and the magnetic curvature that enter the energy principle are coupled to the fluid displacement. In turn, the specific form of the fluid displacement indicates which magnetic field properties are important in the problem.

The remainder of this chapter is divided into four sections. In section 2.2 we introduce the energy principle and identify the magnetic field properties than can affect the plasma (ideal MHD) stability. Among these properties, the local magnetic shear and the magnetic curvature are discussed in section 2.3. Finally, we determine explicit expressions for the magnetic field key attributes for the general screw pinch in section 2.4 and for the helically-symmetric configuration (straight stellarator) in section 2.5. Specific examples of visualization for the helically-symmetric configuration are given in section 2.6. The effects of toroidicity on the magnetic field strength, the local magnetic shear and the magnetic curvature are reported in chapter 3.

2.2 The energy principle

The key attributes of a magnetic configuration can be introduced in the context of the MHD energy principle. The energy principle [14, 15], valid for arbitrary magnetic geometry, gives exact information about instability thresholds and estimates of the mode eigenfrequencies (growth rates). Because of its inherent mathematical simplicity, the energy principle offers an attractive method to consider plasma stability of fully 3-Dimensional plasma geometries, such as stellarators and tokamaks with coil ripple effects.

Ideal MHD instabilities can be driven by the parallel current density (current-driven modes) or by the perpendicular pressure gradient (pressure-driven modes). The least stable pressure-driven modes, such as interchange modes [16] and ballooning modes [17], are characterized by long parallel wavelengths and short perpendicular wavelengths and occur when (1) the *average* normal curvature is unfavorable (interchange modes) or (2) the *local* normal curvature is convex to the plasma (ballooning modes). Waltz and Boozer [18] have recently pointed out that the *local* magnetic shear [19, 20] rather than the *global* shear determines the radial localization of ballooning modes in low-shear stellarators. Three-dimensional ballooning modes calculations for the low-shear stellarator H1-NF [21] suggest that the *local* variation of the magnetic curvature and the local magnetic shear dominate over surface-averaged quantities [22].

In the context of ideal MHD theory, viscosity effects, heat flow, ohmic dissipation and resistivity effects are neglected. The plasma is seen as a highly conducting medium and the displacement current is neglected [23, 24]. Plasma fluid elements move with the magnetic field [25] (frozen-in condition). Furthermore, steady-state plasma flows are neglected [23]. The macroscopic plasma stability can be studied by introducing small perturbations in the equilibrium configuration [26]. If $\boldsymbol{\xi}$ measures the displacement of a fluid element from its equilibrium position, a variational principle can be constructed [26, 23]. The plasma potential energy variation due to

the perturbation $\boldsymbol{\xi}$ is conveniently written as follows [14, 15]

$$\delta W = \delta W_1 + \delta W_2 + \delta W_3 + \delta W_4 \,, \tag{2.1}$$

where

$$\delta W_1 \equiv \frac{1}{2\mu_0}\int_\Omega d^3x \left[\tilde{\mathbf{B}}_\perp^2 + \left(\tilde{\mathbf{B}}_{||} - \mu_0 \frac{\boldsymbol{\xi}\cdot\boldsymbol{\nabla} p}{B^2}\right)^2\right] , \tag{2.2}$$

$$\delta W_2 \equiv -\frac{1}{2}\int_\Omega d^3x \, \frac{J_{||}}{B} \, (\boldsymbol{\xi}\times\mathbf{B})\cdot\boldsymbol{\nabla}\times(\boldsymbol{\xi}\times\mathbf{B}) \,, \tag{2.3}$$

$$\delta W_3 \equiv \frac{1}{2}\int_\Omega d^3x \, \Gamma \, p \, (\boldsymbol{\nabla}\cdot\boldsymbol{\xi})^2 \,, \tag{2.4}$$

$$\delta W_4 \equiv -\int_\Omega d^3x \, (\boldsymbol{\xi}\cdot\boldsymbol{\kappa})(\boldsymbol{\xi}\cdot\boldsymbol{\nabla} p) \,. \tag{2.5}$$

Terms of order ξ^3 and higher have been neglected and linear terms vanish because we perturb around an equilibrium. d^3x is a plasma volume element and integration is carried out over the entire plasma volume Ω. The plasma is assumed to be surrounded by a conducting wall at which the normal component of the fluid displacement vanishes. $\mathbf{B}$ and $\tilde{\mathbf{B}} \equiv \boldsymbol{\nabla}\times(\boldsymbol{\xi}\times\mathbf{B})$ are the equilibrium and perturbed magnetic fields, respectively. Subscripts '$||$' and '$\perp$' refer to the directions parallel and perpendicular to the equilibrium magnetic field, respectively. Γ is the adiabatic index and $\Gamma = 5/3$ for a system with 3 degrees of freedom. p and $J_{||}$ are the equilibrium plasma pressure and parallel current density, respectively. Finally $\boldsymbol{\kappa} \equiv B^{-1}\mathbf{B}\cdot\boldsymbol{\nabla}(\mathbf{B}/B)$ is the magnetic curvature.

For short-perpendicular-wavelength perturbations, the terms of δW can be interpreted as follows. The first term in δW_1 represents the energy required to bend the magnetic field line while the second term is called the field compression term. The second term, δW_2, is the free energy arising from the parallel current density and is responsible for kink instabilities [27, 28]. The third term, δW_3, represents the energy required to compress the plasma. The remaining contribution to the potential energy variation, δW_4, proportional to the perpendicular current density, is responsible for interchange [16] and ballooning [17] instabilities. The positive-definite contributions δW_1 and δW_3 are always stabilizing but the current-driven terms, δW_2 and δW_4, can be positive or negative and can lead to instabilities.

For fully 3-Dimensional configurations, such as the stellarator and the tokamak with coil ripple effects, it is convenient to defined a set of 'local' vectors attached to the magnetic field line. When deriving (2.1) the existence of nested magnetic surfaces has been assumed. The radial label used here is ψ, where $2\pi\psi$ is the enclosed poloidal (magnetic) flux.

In order to get physical insight, it is convenient to introduce a set of natural coordinates. By 'natural coordinates', we mean coordinates which reflect the *local* form of the confining magnetic field. In this system, magnetic field lines can be chosen to be coordinates curves [29]. One coordinate, denoted ρ, is chosen to be constant along the field line, $\mathbf{B}\cdot\nabla\rho \equiv 0$. For the remainder of this thesis, we shall assume that, even for non-axisymmetric configurations, a suitable set of nested toroidal magnetic surfaces exists. The poloidal cross-section of these magnetic surfaces forms a set of smooth closed curves. In other words, we *assume* that it is always possible to find a ρ which satisfies the above-mentioned conditions. The coordinate ρ is called a surface label and can be chosen to be the enclosed poloidal flux, the enclosed toroidal flux, the rotational transform, the enclosed plasma volume or any combination of theses quantities. The two remaining coordinates are used to label a point on a given magnetic surface (a magnetic surface is defined as $\rho = \text{const}$).

A set of 3 'natural' vectors can also be defined. One vector is chosen to be along $\mathbf{B}$ and the 2 remaining vectors are chosen to be orthogonal to $\mathbf{B}$. A natural choice is to define the following vector set:

$$\begin{aligned} \hat{\mathbf{e}}_{||} &\equiv \frac{\mathbf{B}}{B} \ , \\ \hat{\mathbf{n}} &\equiv \frac{\nabla\psi}{\sqrt{\nabla\psi\cdot\nabla\psi}} \ , \\ \hat{\mathbf{b}} &\equiv \hat{\mathbf{e}}_{||}\times\hat{\mathbf{n}} \ . \end{aligned} \tag{2.6}$$

Here $\hat{\mathbf{e}}_{||}$ is a unit vector along $\mathbf{B}$ (unit parallel vector); $\hat{\mathbf{n}}$ is a unit vector normal to the magnetic surface $\psi = \text{const}$ and pointing outwards (unit normal vector); and, by construction, $\hat{\mathbf{b}}$ is perpendicular both to $\mathbf{B}$ and to the normal to the magnetic surface (unit binormal vector). Here we have used $\rho = \psi$ as the flux label. It is worth noting that each vector defined in equation (2.6) depends, in general, on the

3 coordinates of space. By construction, the vector set $\left\{\hat{\mathbf{e}}_{||}, \hat{\mathbf{n}}, \hat{\mathbf{b}}\right\}$ is orthonormal. Any vector $\mathbf{A}$ can be written as

$$\mathbf{A} = \left(\mathbf{A}\cdot\hat{\mathbf{e}}_{||}\right)\hat{\mathbf{e}}_{||} + \mathbf{A}_{\perp} \,, \tag{2.7}$$

where $\mathbf{A}_{\perp} \equiv \hat{\mathbf{e}}_{||}\times\left(\mathbf{A}\times\hat{\mathbf{e}}_{||}\right)$ is the perpendicular component of $\mathbf{A}$. Alternatively, one can project $\mathbf{A}$ onto the orthonormal vector set (2.6) yielding

$$\mathbf{A} = A_{||}\hat{\mathbf{e}}_{||} + A_{\mathrm{N}}\hat{\mathbf{n}} + A_{\mathrm{G}}\hat{\mathbf{b}} \,, \tag{2.8}$$

where $A_{||} \equiv \mathbf{A}\cdot\hat{\mathbf{e}}_{||}$, $A_{\mathrm{N}} \equiv \mathbf{A}\cdot\hat{\mathbf{n}}$ and $A_{\mathrm{G}} \equiv \mathbf{A}\cdot\hat{\mathbf{b}}$ are the parallel, normal and geodesic components of $\mathbf{A}$, respectively. We shall retain the above notation throughout this thesis.

We now discuss each contribution in δW.

The field line bending term in δW_1 is proportional to $\tilde{B}_{\perp}^2$. Following Greene and Johnson [30], the geodesic component of the perturbed magnetic field can be written as

$$\frac{\tilde{B}_{\mathrm{G}}}{B} = \frac{\nabla_{||}\left(H\xi_{\mathrm{G}}\right)}{H} + \frac{\mathcal{S}}{H^2}\,\xi_{\mathrm{N}} \,, \tag{2.9}$$

whereas the normal component of $\tilde{\mathbf{B}}$ is

$$\frac{\tilde{B}_{\mathrm{N}}}{B} = \frac{\nabla_{||}\left(|\boldsymbol{\nabla}\psi|\xi_{\mathrm{N}}\right)}{|\boldsymbol{\nabla}\psi|} \,. \tag{2.10}$$

In equations (2.9,2.10), we have defined $H \equiv B/|\boldsymbol{\nabla}\psi|$ and $\nabla_{||} \equiv \hat{\mathbf{e}}_{||}\cdot\boldsymbol{\nabla}$ is the gradient operator along $\mathbf{B}$. Finally, $\mathcal{S}$ is the local magnetic shear [19, 20]

$$\mathcal{S} \equiv -\mathbf{s}\cdot\left(\boldsymbol{\nabla}\times\mathbf{s}\right) \,, \tag{2.11}$$

where $\mathbf{s} \equiv -H\hat{\mathbf{b}}$ is a vector lying in the magnetic surface and orthogonal to $\mathbf{B}$. As noted by Ware [31], the last term in equation (2.9) is 'the amount a field line must be stretched if it is to exactly replace a neighboring field line in the course of the perturbation' [31]. Since the geodesic component of the perturbed magnetic field enters as a squared quantity in the energy principle, it is always stabilizing. Clearly from equation (2.9), a nonvanishing shear (irrespective of the sign) is stabilizing. The $\tilde{B}_{\mathrm{G}}^2$ contribution in δW_1 involves a term proportional to $\mathcal{S}^2$. As we shall see in section 3.1.3, the $\mathcal{S}^2$ term in δW can be very useful in explaining the favorable

properties of the reversed-shear tokamak configuration.

We now proceed with the kinking contribution to δW. After straightforward algebra, one gets

$$\delta W_2 = \int_\Omega d^3x \rho_B \mu_0 J_{||} \left\{ \frac{\xi_N}{B} \left[\frac{\nabla_{||}(H\xi_G)}{H} + \frac{\mathcal{S}}{H^2}\,\xi_N \right] - \frac{\xi_G}{B|\boldsymbol{\nabla}\psi|}\,\nabla_{||}(|\boldsymbol{\nabla}\psi|\xi_N) \right\}, \quad (2.12)$$

where $\rho_B \equiv B^2/2\mu_0$ is the magnetic energy density. The contribution involving the LMS is stabilizing or destabilizing depending on the sign of $J_{||}\mathcal{S}$. For tokamaks with strong positive global shear, the interaction of the current density with the LMS is stabilizing if $\mathbf{J}\cdot\mathbf{B}$ is positive, and destabilizing otherwise. At low β, stellarators have (usually) small or negligible parallel current except, perhaps, when the heating system induces such a current. Thus, for low-pressure stellarator plasmas, the kinking contribution in δW should be small.

The term arising from the compression of the fluid displacement, δW_3, is always positive or zero, and it is not discussed further.

The remaining term, δW_4, represents the interaction between the fluid displacement and the magnetic curvature; it can be cast in the form

$$\delta W_4 = -\int_\Omega d^3x\, |\boldsymbol{\nabla}\psi|\, \frac{dp}{d\psi}\, \xi_N \left(\xi_N \kappa_N + \xi_G \kappa_G\right) , \quad (2.13)$$

where, following our notation, κ_N and κ_G are the normal and geodesic curvatures, respectively. Under normal conditions of operation, the pressure gradient $dp/d\psi$ is negative. The importance of δW_4 in the total potential energy variation is evident in equation (2.13); a large pressure gradient can locally couple with the components of the magnetic curvature to generate a negative (destabilizing) contribution to δW. The factor multiplying the normal component of the fluid displacement scales like $-\dot{p}\kappa_N$, where a dot denoted a derivative with respect to ψ. Therefore, assuming a negative pressure gradient, a negative κ_N decreases δW_4. In this case, the normal curvature is said to be unfavorable. The region of the plasma where κ_N is positive is stabilizing; the normal curvature is said to be favorable there. It is worth noting that the geodesic curvature also enters δW_4. However, one has to know the sign of

the quantity $\xi_N \xi_G$ before deciding of the impact (even in a purely qualitative way) of the geodesic curvature on δW_4. The normal curvature, however, multiplies the *square* of ξ_N which is always positive or zero.

In summary, in a configuration with not too large parallel current, a nonvanishing LMS is beneficial for the MHD stability of the plasma. The region of the plasma where the normal component of the magnetic curvature is negative is detrimental for the MHD stability. Therefore, the region of the plasma with small LMS and unfavorable magnetic curvature is expected to be the region where localized MHD-type modes can be driven unstable. For modes which extend over a large fraction of the plasma volume (global modes), the surface-averaged value of κ_N and $\mathcal{S}$ are figures of merit of a magnetic configuration. In the next section, the magnetic curvature and the LMS are discussed in further detail.

2.3 Local field-line geometry

In this section, the magnetic curvature and the local magnetic shear are presented and their respective influence on plasma stability are discussed in more detail.

2.3.1 The magnetic curvature

The magnetic field line curvature is the variation of the unit parallel vector along the tangent to a magnetic field line

$$\boldsymbol{\kappa} \equiv \left(\hat{\mathbf{e}}_{||} \cdot \boldsymbol{\nabla}\right) \hat{\mathbf{e}}_{||} \,. \tag{2.14}$$

The magnetic curvature can be written in an alternative meaningful form. Combining the MHD radial force balance equation, $\mathbf{J} \times \mathbf{B} = c\boldsymbol{\nabla} p$, and Ampere's law, $4\pi \mathbf{J} = c\boldsymbol{\nabla} \times \mathbf{B}$, the magnetic curvature can written as

$$\begin{aligned} \boldsymbol{\kappa} &= -\hat{\mathbf{e}}_{||} \times \left(\boldsymbol{\nabla} \times \hat{\mathbf{e}}_{||}\right) \\ &= \frac{4\pi}{cB}\, \mathbf{J} \times \hat{\mathbf{e}}_{||} + \hat{\mathbf{e}}_{||} \times \left(\frac{\boldsymbol{\nabla} B}{B} \times \hat{\mathbf{e}}_{||}\right) \end{aligned}$$

$$= \frac{4\pi}{B^2}\,\boldsymbol{\nabla}_\perp p + \frac{\boldsymbol{\nabla}_\perp B}{B}$$
$$= \frac{4\pi}{B^2}\,\boldsymbol{\nabla}_\perp \rho_{\mathrm{E}}\ . \tag{2.15}$$

Here $\rho_{\mathrm{E}} \equiv p + B^2/8\pi$ is the total energy density, that it is the sum of the plasma energy density (p) and the magnetic energy density ($B^2/8\pi$). The perpendicular gradient operator in the above equation is defined as $\boldsymbol{\nabla}_\perp = \left(\hat{\mathbf{n}}\hat{\mathbf{n}} + \hat{\mathbf{b}}\hat{\mathbf{b}}\right)\cdot\boldsymbol{\nabla}$. The representation (2.15) for the magnetic curvature provides a simple physical interpretation. The part of the gradient of the total energy density which is orthogonal to $\mathbf{B}$ is supported by the field line tension through the curvature [31, 14]. The magnetic curvature scales like $\bar{R}^{-1}$, where $\bar{R}$ is the average major radius of the machine. It is sometimes useful to estimate the radius of curvature defined as

$$R_{\mathrm{c}} \equiv \frac{1}{\sqrt{\boldsymbol{\kappa}\cdot\boldsymbol{\kappa}}}\ . \tag{2.16}$$

Therefore, the magnitude of the magnetic curvature is smaller on the outside of the machine (large R_{c}) and larger on the inside of the machine (smaller R_{c}). When the plasma pressure is small, the total energy density ρ_{E} is approximately equal to the magnetic energy density and the magnetic curvature then reduces to [32, 29]

$$\boldsymbol{\kappa} = \frac{\boldsymbol{\nabla}_\perp B}{B} + \mathcal{O}\left(\beta/\bar{R}\right)\ , \tag{2.17}$$

showing that, neglecting finite-β effects, the curvature depends solely on the vacuum magnetic field and it is effectively the reciprocal of the scalelength for perpendicular variation of B [29].

As discussed in the previous section, the surface average of the normal curvature and of the LMS are figures of merit of a confinement scheme. The surface average of any arbitrary function F is defined as [29]

$$\langle F\rangle(\psi) \equiv \frac{1}{A}\int_0^{2\pi} d\theta \int_0^{2\pi} d\zeta\ \mathcal{J}\ F(\psi,\theta,\zeta)\ , \tag{2.18}$$

where $\mathcal{J} \equiv [\boldsymbol{\nabla}\psi\cdot(\boldsymbol{\nabla}\theta\times\boldsymbol{\nabla}\zeta)]^{-1}$ is the Jacobian of the transformation from the coordinate system (ψ,θ,ζ) to Cartesian coordinates. Here, θ and ζ are the magnetic poloidal and toroidal angles, respectively. In general, the Jacobian depends on all 3 coordinates of space. In equation (2.18), we have defined the following flux surface

quantity

$$\begin{aligned} A(\psi) &\equiv \int_0^{2\pi} d\theta \int_0^{2\pi} d\zeta \mathcal{J}(\psi,\theta,\zeta) \ , \\ &= \frac{dV}{d\psi} \ , \end{aligned} \tag{2.19}$$

where $V(\psi)$ is the volume enclosed within ψ. By definition the surface average $\langle F \rangle$ has the same dimensionality as F itself. Configurations with a negative $\langle \kappa_N \rangle$, such as the general screw pinch (section 2.5), are expected to be strongly MHD unstable. As we shall see in the next chapter, toroidicity effects are often beneficial, at least for the surface-averaged curvature. The design of magnetic confinement devices are often numerically optimized to enhance the (positive) average curvature. The geodesic curvature is closely related to the current flowing parallel to the magnetic field direction. It can be shown [30] that the surface average of the geodesic curvature identically vanishes. However, $\langle \kappa_G \rangle$ is finite for a vacuum field.

2.3.2 The local magnetic shear

As we discussed previously, the local magnetic shear (LMS) is an important magnetic field attribute of a configuration. For example, a small LMS in the region of unfavorable curvature can contribute towards driving the MHD ballooning modes unstable [20]. Ballooning modes are driven by curvature and stabilized by shear. Furthermore, it can be shown that the existence of global shear eliminates the possibility of a plasma perturbation for which all stabilizing terms vanish [14]. It was recently pointed out [18] that the *local* magnetic shear rather than the *global* shear determines radial localization of ballooning modes in stellarators. The importance of LMS with respect to the maximum achievable β and to the cross-field transport has become evident in recent experiments. Experiments in TFTR [33, 34, 35], JET [36] and DIII-D [37, 38] with reversed-safety-factor profiles have shown that a negative global shear reduces the turbulence level in the plasma edge with the direct consequence of increasing the maximum and volume-averaged β. This point is discussed in more detail in chapter 3.

We now consider the LMS as defined by equation (2.11). The definition of the

local magnetic shear is [19]

$$\mathcal{S} = -\mathbf{s}\cdot(\boldsymbol{\nabla}\times\mathbf{s}) \ , \tag{2.20}$$

where $\mathbf{s} \equiv \boldsymbol{\nabla}\psi\times\mathbf{B}/\left|\boldsymbol{\nabla}\psi\right|^2$ is a vector lying in the magnetic surface and orthogonal to $\mathbf{B}$. For convenience the magnetic field is written in straight-field-line coordinates [39, 40]

$$\mathbf{B} = \boldsymbol{\nabla}\alpha\times\boldsymbol{\nabla}\psi \ , \tag{2.21}$$

where $\alpha \equiv \zeta - q\left(\psi\right)\theta$ is the field label and q is the safety factor. The vector $\mathbf{s}$ now reads $\mathbf{s} = \boldsymbol{\nabla}\alpha - \Lambda\boldsymbol{\nabla}\psi$ where

$$\begin{aligned}\Lambda &\equiv \frac{\boldsymbol{\nabla}\alpha\cdot\boldsymbol{\nabla}\psi}{\boldsymbol{\nabla}\psi\cdot\boldsymbol{\nabla}\psi} \ , \\ &= -\left(\bar{\mathcal{R}} + \frac{dq}{d\psi}\,\theta\right) \ ,\end{aligned} \tag{2.22}$$

is related to the part of $\boldsymbol{\nabla}\alpha$ which is normal to the magnetic surface, and where we have introduced the integrated residual shear [19],

$$\bar{\mathcal{R}} \equiv \frac{q\boldsymbol{\nabla}\psi\cdot\boldsymbol{\nabla}\theta - \boldsymbol{\nabla}\psi\cdot\boldsymbol{\nabla}\zeta}{\boldsymbol{\nabla}\psi\cdot\boldsymbol{\nabla}\psi} \ . \tag{2.23}$$

Using the vector identity $\boldsymbol{\nabla}\times\boldsymbol{\nabla}W \equiv 0$, for any scalar W, the LMS can be written as follows

$$\begin{aligned}\mathcal{S} &= (\boldsymbol{\nabla}\alpha - \Lambda\boldsymbol{\nabla}\psi)\cdot(\boldsymbol{\nabla}\Lambda\times\boldsymbol{\nabla}\psi) \ , \\ &= \boldsymbol{\nabla}\alpha\cdot(\boldsymbol{\nabla}\Lambda\times\boldsymbol{\nabla}\psi) \ , \\ &= -\mathbf{B}\cdot\boldsymbol{\nabla}\Lambda \ , \\ &= \frac{1}{\mathcal{J}}\,\frac{dq}{d\psi} + (\mathbf{B}\cdot\boldsymbol{\nabla})\,\bar{\mathcal{R}} \ .\end{aligned} \tag{2.24}$$

The surface average of the last term vanishes because $\langle\mathbf{B}\cdot\boldsymbol{\nabla}F\rangle$ identically vanishes for any function F. The surface-averaged LMS is called the global shear. The global shear is denoted $\widehat{\mathcal{S}}$ and can obtained immediately from equation (2.24)

$$\widehat{\mathcal{S}} \equiv \langle\mathcal{S}\rangle = \frac{4\pi^2}{A\left(\psi\right)}\,\frac{dq}{d\psi} \ . \tag{2.25}$$

The flux surface quantity A is given by equation (2.19). Collecting our results, the LMS can now be written as

$$\mathcal{S} = \widehat{\mathcal{S}} + \mathcal{R} \ , \tag{2.26}$$

where $\mathcal{R}$ is the residual shear [20] and its average over a magnetic surface vanishes. A dimensional analysis of the LMS shows that this quantity scales like $\bar{R}^{-3}$, where as before, $\bar{R}$ is the average major radius of the configuration. The magnetic shear length

$$L_{\mathrm{s}} \equiv \left(\frac{1}{\hat{\mathcal{S}}}\right)^{1/3} \tag{2.27}$$

is relevant for the study of microinstabilities. In tokamak geometry, the magnetic shear length is sometimes defined as $L_{\mathrm{s}} \equiv qR/\hat{s}$ where $\hat{s} \equiv r(dq/dr)/q$ is the lowest-order global magnetic shear. In the tokamak case, the magnetic shear length is a flux surface quantity. The global shear is a figure of merit of confinement devices. Tokamaks under standard conditions of operation are characterized by a strong, positive global shear which increases monotonically from the magnetic axis to the plasma edge. Some tokamaks with reversed-safety-factor profile [36, 37, 42, 35, 34, 43], display a negative global shear in the bulk of the plasma and a positive $\hat{\mathcal{S}}$ as one moves towards the plasma edge. Finally, some stellarators such as H1-NF [21, 44], TJ-II [45] and WII-AS [46], have negligible global shear over the entire plasma volume. In the next sections, we determine the magnetic curvature and the LMS for the general screw pinch and the helically-symmetric configuration. Both these configurations are straight, that is without toroidicity. Toroidicity effects are discussed in chapter 3.

2.4 The general screw pinch

In this section, we consider a 1-Dimensional configuration: the general screw pinch. We begin our discussion by determining the form of the equilibrium magnetic field. The question of toroidal force balance does not enter since, by definition, the geometry is linear [47]. In view of the symmetry of the problem, it is convenient to perform calculations in cylindrical coordinates (r, ϕ, z). Azimuthal symmetry indicates that $\partial F/\partial\phi \equiv 0$ for any scalar F. The radial component of the magnetic field vanishes. The divergence-free condition for the magnetic field shows that the remaining components of $\mathbf{B}$ depend only on r. Combining the radial force balance

equation with Ampere's law yields

$$\frac{d}{dr}\left(B^2 + 8\pi p\right) = -\frac{2B_\phi^2}{r} \quad , \tag{2.28}$$

where $p = p(r)$ is the plasma pressure. For a θ pinch ($B_\phi = 0$), the energy density $\rho_{\rm E}$ is independent of the radial coordinate: the plasma is entirely confined by the applied magnetic field. For a Z pinch ($B_z = 0$), it is the tension force arising from the magnetic curvature which confines the plasma. In the general case, there are two free functions in the equilibrium (say B_ϕ and p). The third function (B_z) is determined by solving equation (2.28) with appropriate boundary conditions. When B_ϕ and B_z are both nonzero, the magnetic lines wraps around the column along helical paths; the rotational transform is therefore nonzero. The safety factor is

$$q(r) = \frac{rB_z}{R_0 B_\phi} \quad , \tag{2.29}$$

where $2\pi R_0$ is the periodicity length. Comparing equation (2.15) with the equilibrium relation (2.28) we immediately get the magnetic curvature

$$\boldsymbol{\kappa} = -\frac{1}{r}\left(\frac{B_\phi}{B}\right)^2 \hat{\mathbf{r}} \, , \tag{2.30}$$

where $\hat{\mathbf{r}}$ is a unit vector along r. Clearly from the above equation, the geodesic curvature vanishes and the magnetic curvature only has a normal component. The normal curvature is unfavorable everywhere. When the general screw pinch is bent into a torus, toroidicity effects make the *surface-averaged* normal curvature favorable, provided q is larger than unity (chapter 3).

We now determine the LMS. The LMS has been formally defined for a plasma configuration with closed, nested magnetic surfaces. For the general screw pinch, the magnetic surfaces are opened. The magnetic field is written as

$$\mathbf{B} = \boldsymbol{\nabla}\alpha \times \boldsymbol{\nabla}\Psi \, , \tag{2.31}$$

where, in analogy with the toroidal configuration, we define the field line label as

$$\alpha \equiv \frac{z}{R_0} - q\phi \, . \tag{2.32}$$

The magnetic surface label Ψ is determined by substituting (2.32) in (2.31) which yields

$$B_\phi = \frac{1}{R_0}\frac{d\Psi}{dr} \quad , \tag{2.33}$$

and

$$B_z = \frac{q}{r}\,\frac{d\Psi}{dr} \quad . \tag{2.34}$$

Using the definition for the safety factor (2.29) we note that these equations are identical. Integrating equation (2.33) with respect to r gives $\Psi = \Psi_\phi/2\pi$ where

$$\Psi_\phi \equiv 2\pi R_0 \int_0^r B_\phi\,(r')\,dr' \ , \tag{2.35}$$

is the azimuthal magnetic flux.

The vector $\mathbf{s}$ in the expression for the LMS becomes

$$\begin{aligned} \mathbf{s} &= \frac{\boldsymbol{\nabla}\Psi\times\mathbf{B}}{\boldsymbol{\nabla}\Psi\cdot\boldsymbol{\nabla}\Psi} \\ &= \frac{1}{R_0}\left(\widehat{\mathbf{z}} - \frac{B_z}{B_\phi}\,\widehat{\boldsymbol{\phi}}\right) \ . \end{aligned} \tag{2.36}$$

After straightforward algebra, one gets the LMS for the general screw pinch

$$\mathcal{S} = \frac{1}{rR_0}\,\frac{dq}{dr} \ , \tag{2.37}$$

which is a flux surface quantity; therefore the residual shear of the general screw pinch configuration always vanishes. This result is not surprising since the components of the magnetic field are flux surface quantities. The LMS for the general screw pinch is singular at the magnetic axis. It is worth pointing out that the LMS does *not* enter the energy potential variation (2.1) as an isolated quantity. In fact, it can be shown that the LMS is always multiplied by the positive-definite quantity $|\boldsymbol{\nabla}\psi|^2$. The LMS is singular at the origin but the relevant quantity in the energy principle is $|\boldsymbol{\nabla}\psi|^2\,\mathcal{S}$, which is *well behaved* at the magnetic axis.

2.5 The helically-symmetric configuration

In this section, we consider the helically-symmetric configuration, also referred below as the straight stellarator configuration. It can be seen as the lowest-order stellarator model and contains no toroidicity effects. Calculations in helically-symmetric geometry are somewhat less involved than those for the fully 3-Dimensional stellarator geometry; for this reason, it is often used to get physical insight about stellarators [48, 18, 3].

We here assume that the plasma pressure is small enough so that the equilibrium magnetic field can be approximated by the vacuum solution [49]. The straight stellarator has one ignorable coordinate, the helical coordinate, and the configuration is essentially 2-Dimensional. When the current density is neglected, reduced Maxwell's equations show that the (vacuum) magnetic field can be described by the magnetic scalar potential χ, which satisfies Laplace's equation [49]

$$\nabla^2\chi = 0\,. \tag{2.38}$$

The above equation can be used to represent a magnetic field with helical symmetry. The magnetic scalar potential can be expressed in a series of cylindrical harmonics involving modified Bessel functions that satisfies Laplace's equation (2.38). The components of the magnetic field are then easily determined from $\mathbf{B} = \boldsymbol{\nabla}\chi$. In cylindrical coordinates, the components of the magnetic field are

$$\begin{aligned} B_r &= MB_{\rm h}I'_M(M\rho)\sin(Mu)\ , \\ B_\phi &= M\frac{B_{\rm h}}{\rho}\,I_M(M\rho)\cos(Mu)\ , \qquad (2.39)\\ B_z &= B_0 - MB_{\rm h}I_M(M\rho)\cos(Mu)\ . \qquad (2.40) \end{aligned}$$

Here M is the number of poloidal field periods of the external helical coils, I_M is the modified Bessel function of order M, B_0 is the strength of a uniform, axial magnetic field and $B_{\rm h}$ is the modulating helical field strength. Existence of closed magnetic surfaces [49] requires that the helical modulation $B_{\rm h}$ must be smaller than the axial part B_0. With one ignorable coordinate, the magnetic field depends only on $\rho \equiv Qr$ and $u \equiv \theta - Qz$, where $Q \equiv N/MR$ is the pitch of the field lines, N is the number of toroidal field coils and $2\pi R$ is the periodicity length of the configuration. A prime denotes a derivative with respect to the argument. It is convenient to write the magnetic field in Clebsch form

$$\mathbf{B} = \boldsymbol{\nabla}\alpha\times\boldsymbol{\nabla}\Psi\ , \tag{2.41}$$

where

$$\Psi = \frac{B_0R^2}{2N/M}\left[\rho^2 - 2\frac{B_{\rm h}}{B_0}\,\rho I'_M\cos(Mu)\right]\ , \tag{2.42}$$

is the helical magnetic flux. The magnetic helical flux depends on all 3 cylindrical coordinates. A magnetic surface is determined by solving the implicit equation

$\Psi(r,\phi,z) = \text{const}$ or, alternatively, one has to determine $\rho = \rho(\theta, z)$ such that the helical flux (2.42) remains constant. The problem reduces to a root finding problem for ρ of the form $C(\rho) = 0$ where

$$C(\rho) \equiv \rho^2 - 2\frac{B_\mathrm{h}}{B_0}\,\rho I'_M \cos(Mu) - 2\frac{N}{M}\,\bar{\Psi}\,. \tag{2.43}$$

Here $\bar{\Psi} \equiv \Psi/(B_0 R^2)$ is a parameter. The function C displays a parabolic behavior for small ρ. As ρ increases, the negative contribution from I'_M increases in magnitude. Clearly the existence of closed magnetic surfaces depends on the ratio B_h/B_0. The root equation $C(\rho) = 0$ has been solved numerically using the bissectrix method [50], for each azimuthal angle ϕ and height z. Modified Bessel functions of arbitrary order M (and their derivatives) can be written in terms of I_0 and I_1 via recurrence relations. In turn I_0 and I_1 are approximated in terms of a polynomial expansion [51]. Drift wave models, such as the cold ion model (chapter 4), usually make use of the 1-Dimensional WKB representation (in the linear approximation). In these models, the lowest-order perpendicular wavevector is related to the vector $\boldsymbol{\nabla}\alpha$. The vector $\boldsymbol{\nabla}\alpha$ is a multiple-valued function and can be written as

$$\boldsymbol{\nabla}\alpha = \Lambda\boldsymbol{\nabla}\Psi + \mathbf{s}\,, \tag{2.44}$$

where $\mathbf{s} \equiv \boldsymbol{\nabla}\Psi\times\mathbf{B}/\boldsymbol{\nabla}\Psi\cdot\boldsymbol{\nabla}\Psi$ and $\Lambda \equiv \boldsymbol{\nabla}\alpha\cdot\boldsymbol{\nabla}\Psi/\boldsymbol{\nabla}\Psi\cdot\boldsymbol{\nabla}\Psi$ is related to the part of $\boldsymbol{\nabla}\alpha$ along the normal to the magnetic surface. The function Λ satisfies (appendix A)

$$\nabla_{||}\Lambda = -\frac{\mathcal{S}}{B}\,, \tag{2.45}$$

where $\mathcal{S}$ is the local magnetic shear and $\nabla_{||} \equiv B^{-1}\mathbf{B}\cdot\boldsymbol{\nabla}$ is the parallel gradient operator. The parallel gradient operator is written in cylindrical coordinates in which the radial coordinate ρ is constrained to $C(\rho) = 0$, that is to a given magnetic surface. Equation (2.45) has been integrated numerically using the fifth-order Runge-Kutta method [50]. The degree of freedom in specifying $\boldsymbol{\nabla}\alpha$ is evident when one formally integrates equation (2.45) yielding

$$\Lambda(L) = \Lambda(0) - \int_0^L \frac{\mathcal{S}(L')}{B(L')}\,dL'\,, \tag{2.46}$$

where L is the length along the field line. $\Lambda(0)$ is a free parameter and represents the value of Λ at the position the along-the-field-line integration is started.

The magnetic curvature can be determined in cylindrical coordinates

$$\boldsymbol{\kappa} = \kappa_r \, \widehat{\mathbf{r}} + \kappa_z \, \widehat{\mathbf{z}} + \kappa_\phi \, \widehat{\boldsymbol{\phi}} \, , \tag{2.47}$$

where $\left(\widehat{\mathbf{r}}, \widehat{\boldsymbol{\phi}}, \widehat{\mathbf{z}}\right)$ are the unit vectors in cylindrical coordinates and $\kappa_r \equiv \boldsymbol{\kappa}\cdot\widehat{\mathbf{r}}$, $\kappa_z \equiv \boldsymbol{\kappa}\cdot\widehat{\mathbf{z}}$ and $\kappa_\phi \equiv \boldsymbol{\kappa}\cdot\widehat{\boldsymbol{\phi}}$ are the cylindrical components of the magnetic curvature. Similarly the normal and binormal unit vectors are written in terms of their cylindrical components. For instance, the normal curvature reads

$$\kappa_{\mathrm{N}} = (\boldsymbol{\kappa}\cdot\widehat{\mathbf{r}})\,(\widehat{\mathbf{n}}\cdot\widehat{\mathbf{r}}) + (\boldsymbol{\kappa}\cdot\widehat{\mathbf{z}})\,(\widehat{\mathbf{n}}\cdot\widehat{\mathbf{z}}) + (\boldsymbol{\kappa}\cdot\widehat{\boldsymbol{\phi}})(\widehat{\mathbf{n}}\cdot\widehat{\boldsymbol{\phi}}) \, . \tag{2.48}$$

No additional physical insight can be gained by writting down the explicit form for κ_{N} and κ_{G}. Details of the derivations are therefore reported in appendix A. The local magnetic shear can be obtained in a similar way. The vector $\mathbf{s}$ can be written in terms of its cylindrical components. The gradient operator is also written in cylindrical coordinates and the LMS is readily obtained. Mathematical details can be found in Appendix A.

2.6 Visualization

In order to get physical insight, we have developed numerical techniques to visualize 3-Dimensional plasmas. The graphic package used here is the Advanced Visualization Systems (AVS) [52]. Our visualization techniques are suitable for open-ended configurations (such as the straight stellarator) and for closed configurations (tokamak and stellarators). Generalization of these techniques to other geometries, such as the spheromak and the reversed-field pinch, is straightforward.

We first briefly describe the visualization techniques used in this thesis and then display the physical quantities of interest (B, normal and geodesic curvatures, LMS). For sake of generality, we consider the 3-Dimensional case with closed magnetic surfaces since it is the most difficult geometry as far as visualization techniques are concerned. We assume that the shape of each magnetic surface is known and that it can be described as a continuous function of the poloidal angle, θ, and of the toroidal angle, ζ. A magnetic surface can be seen as a square of side 2π in the (θ, ζ)

space. We setup two regular grids as follows

$$\theta_i = (i - 1/2)\,\Delta\theta\ ,$$
$$\zeta_j = (j - 1/2)\,\Delta\zeta\ , \tag{2.49}$$

where $i = 1, ..., N_\theta$ and $j = 1, ..., N_\zeta$. Here $\Delta\theta = 2\pi/N_\theta$ and $\Delta\zeta = 2\pi/N_\zeta$ are the mesh sizes in the poloidal and toroidal directions, respectively. The position vector, written in Cartesian coordinates, $\mathbf{r}_{ij} = x_{ij}\hat{\mathbf{x}} + y_{ij}\hat{\mathbf{y}} + z_{ij}\hat{\mathbf{z}}$ is known at each grid point. In practice, the Cartesian components of the position vector are obtained analytically in the low-β tokamak case and in the helically-symmetric configuration but are computed numerically in the stellarator case.
Then each grid point is appropriately labeled. Such a labeled grid point is called a node. A set a 4 closest nodes defines a cell. The ensemble of cells defines the magnetic surface. We have encountered a number of difficulties in displaying 3-Dimensional plasma geometries. In particular, the order in the grid point numbering has to be chosen so that the normal to the magnetic surface for *each* cell points outward. Also a special treatment of the grid points at the boundaries $\theta = 0, 2\pi$ and $\zeta = 0, 2\pi$ is needed in order to satisfy the periodicity requirements in the poloidal and toroidal directions. Once this is done, the AVS package can be used to display, manipulate and modify the plots.

As an example, we display the magnetic field attributes of a straight stellarator with $M = 2$, $N = 5$ and $B_h/B_0 = 0.58$, which is a toroidicity-free approximation of Wendelstein VIIA [46]. All the figures are for the same magnetic surface $\Psi/\Psi_{max} = 0.1$, which corresponds to a point halfway between the magnetic axis and the separatrix. Here Ψ_{max} is the enclosed helical flux at the separatrix.

The magnetic field strength is shown in Figure 2.1. The region of high (low) $|\mathbf{B}|$ is shown in red (blue). The helical symmetry of the configuration is clearly visible. We note that the region of high $|\mathbf{B}|$ is where the 'torsion' of the surface is the strongest.

The normal curvature, for the same magnetic surface as in Figure 2.1, is shown in Figure 2.2. The region of unfavorable (favorable) normal curvature is colored in blue (red). The similitude between B and κ_{N} is evident, as one would expect in a

low-β configuration.

The geodesic curvature, κ_G, is shown in Figure 2.3. κ_G is positive where κ_N is negative, and vice-versa. The surface average has been computed numerically and it vanishes.

The LMS is shown in Figure 2.4. Unlike previous figures, the LMS does not vary much over a large fraction of the magnetic surface. However, a strong local variation can be seen across the outer edges of the configuration. The surface average of the LMS is small. The shear length is accordingly very large, corresponding to a nearly shearless configuration.

In this Chapter, we have identified a set of magnetic field key attributes that enter the energy principle. Some specific properties of the confining magnetic field, such as the LMS and the normal curvature, can also affect the drift wave dynamics. Specific examples for the general screw pinch and the helically-symmetric configuration were presented. Visualization techniques were developed and the magnetic field key attributes of the helically-symmetric configuration were displayed.

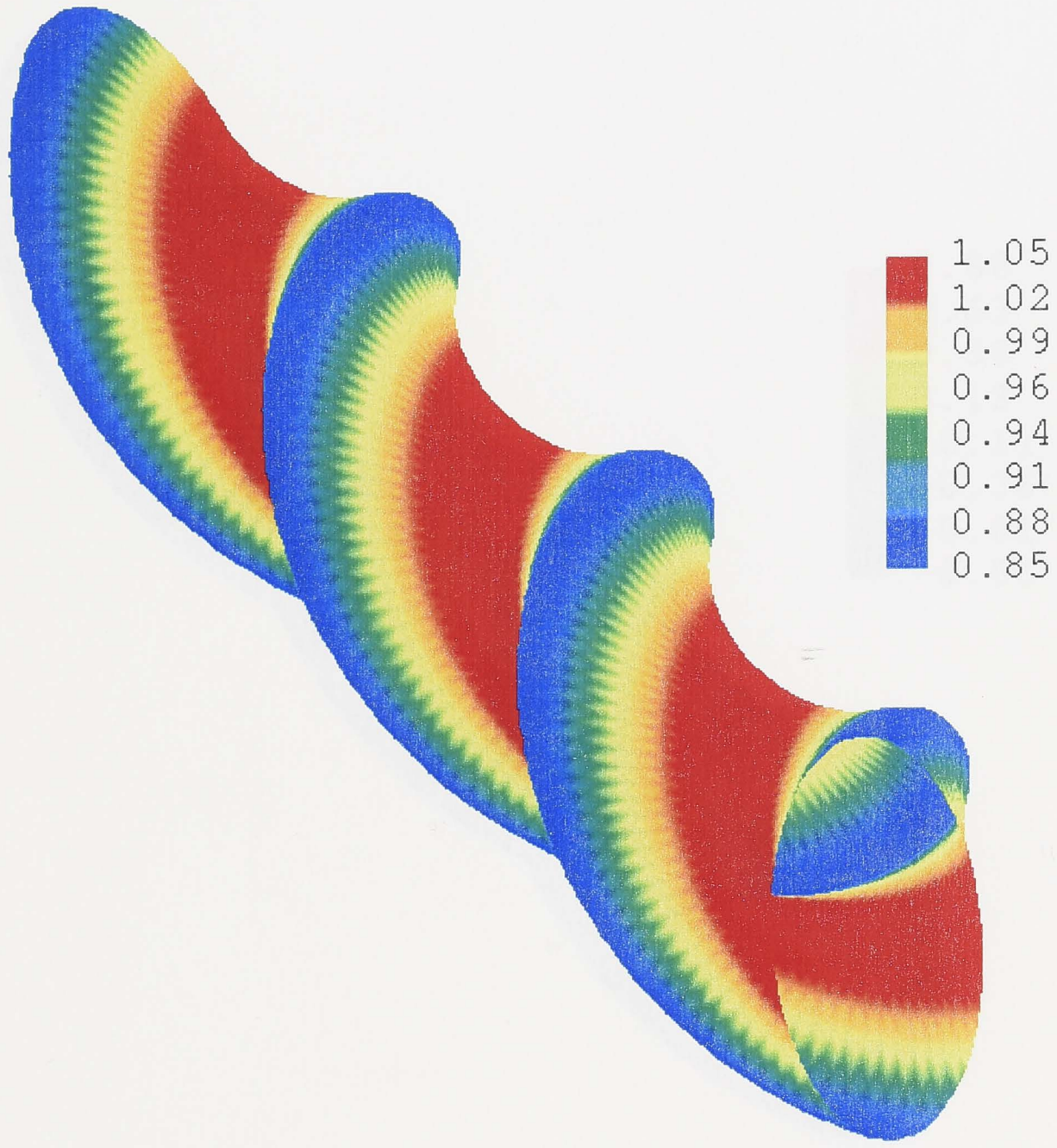

Figure 2.1: The magnetic field strength of a helically symmetric configuration with $M = 2$, $N = 5$, $B_h/B_0 = 0.58$. The magnetic surface shown is defined as $\Psi/\Psi_{max} = 0.1$, nearly halfway between the magnetic axis and the separatrix. The magnetic field strength is normalized to B_0 (magnetic axis).

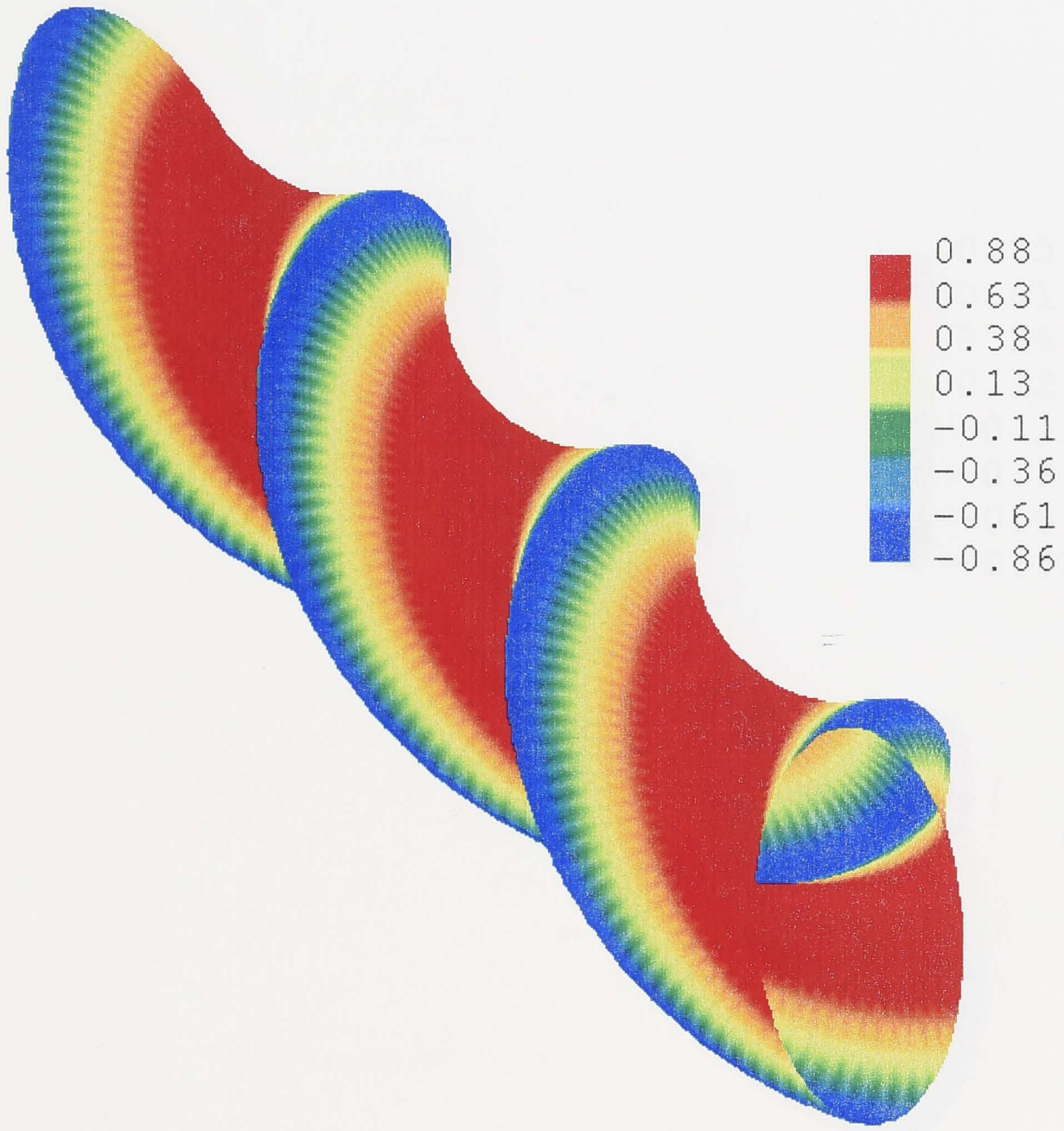

Figure 2.2: The normal component of the magnetic curvature for the same magnetic surface as in Figure 2.1. The normal curvature is normalized to $1/R$, where $2\pi R$ is the periodicity length.

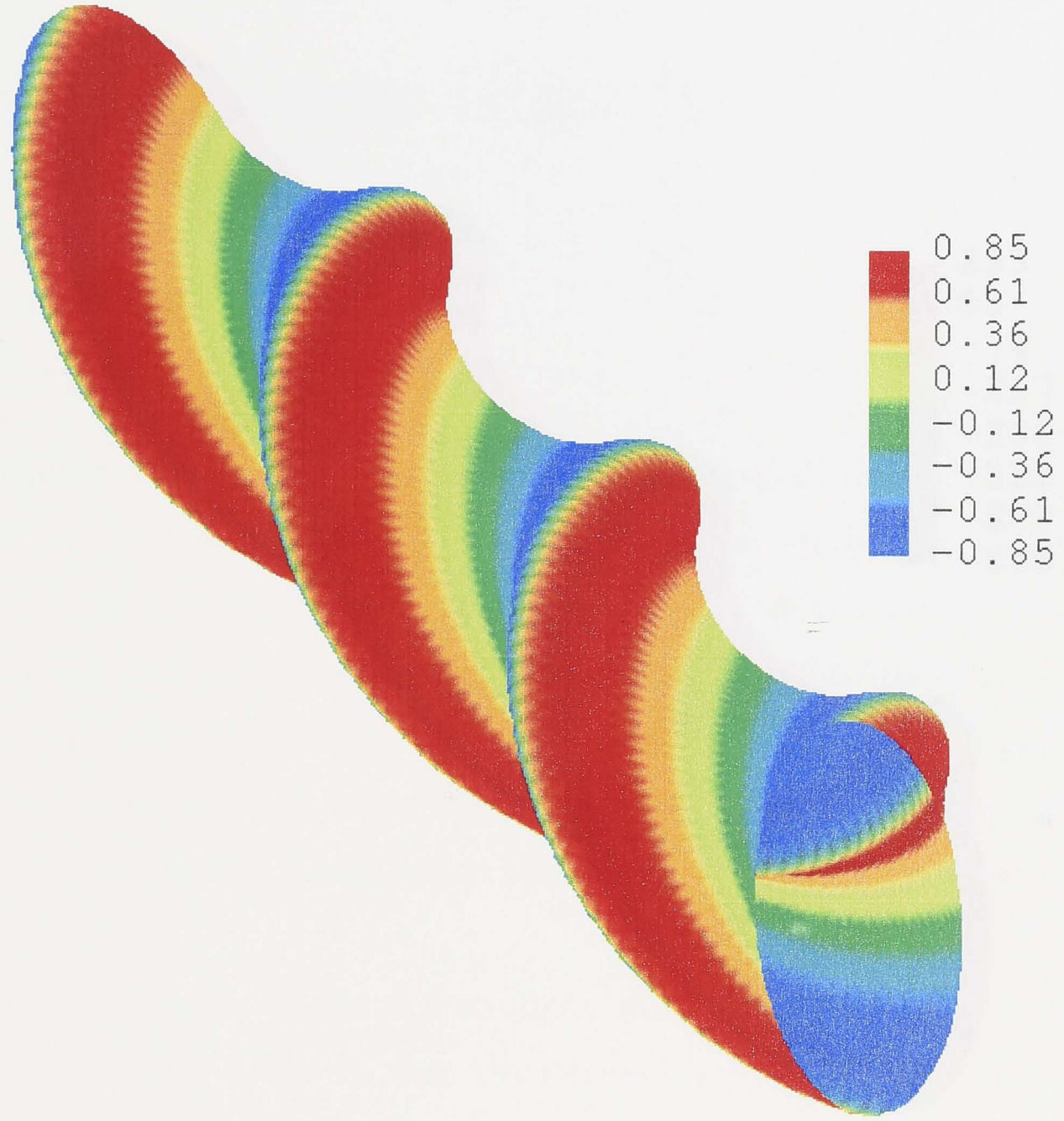

Figure 2.3: The geodesic component of the magnetic curvature for the same magnetic surface as in Figure 2.1. The geodesic curvature is normalized to $1/R$, where $2\pi R$ is the periodicity length.

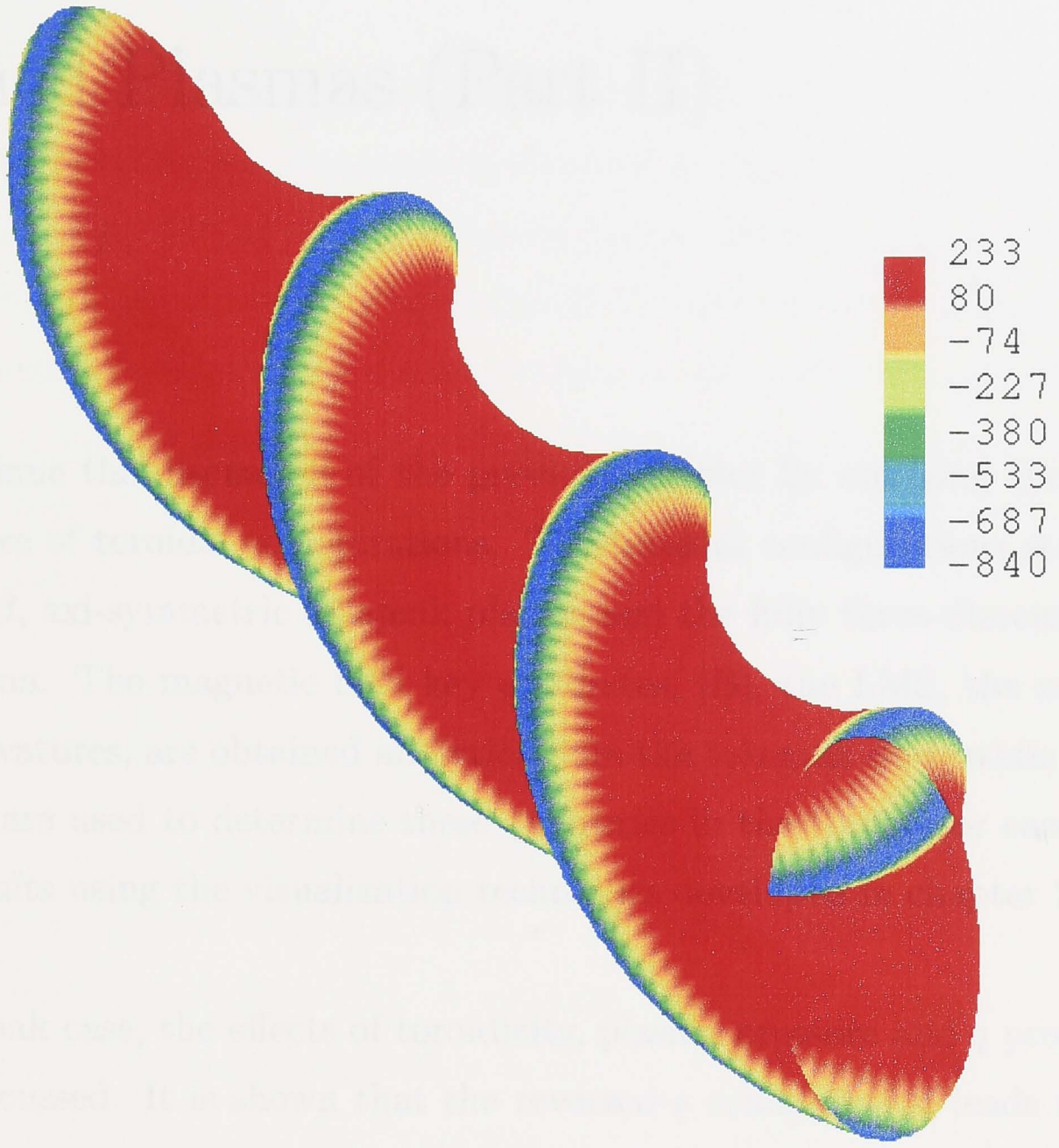

Figure 2.4: The local magnetic shear (LMS) for the same magnetic surface as in Figure 2.1. The LMS is normalized to $1/R^3$, where $2\pi R$ is the periodicity length.

CHAPTER 3

Magnetic Field Structure of Magnetically Confined Plasmas (Part II)

We continue the discussion of the previous chapter by studying the magnetic field structure of toroidal configurations. The toroidal configurations studied here are the low-β, axi-symmetric tokamak plasma and the fully three-dimensional stellarator plasma. The magnetic field key attributes, $|\mathbf{B}|$, the LMS, the normal and geodesic curvatures, are obtained analytically in the tokamak case, while numerical calculations are used to determine these quantities in the stellarator case. We display our results using the visualization techniques developed in chapter 2.

In the tokamak case, the effects of toroidicity, plasma pressure and q profile on the LMS are discussed. It is shown that the reversed-q configuration leads to the formation of a region of negative LMS where the normal curvature is unfavorable [1, 2].

The magnetic field key attributes are computed numerically for four stellarators: H1-NF [21], TJ-II [45], Wendelstein-7AS (W-7AS) [46] and the Large Helical Device (LHD) [41]. It is shown that the magnetic field properties of these configurations differ substantially.

In the second part of chapter 2, it has been shown that the general screw pinch has unfavorable, surface-averaged magnetic curvature [equation (2.30)] and a vanishing residual shear [equation (2.37)]. When the magnetic surfaces are not circular, as in the helically-symmetric configuration, the surface-averaged magnetic

curvature can be (not always) less unfavorable. The noncircularity of the magnetic surfaces implies that the magnetic field cannot be constant on these surfaces. As a consequence, the residual shear does not vanish everywhere on the magnetic surface. As we shall see in this chapter, toroidicity effects alter substantially the key attributes such as the magnetic field strength, the magnetic curvature and the LMS.

We restrict our attention to the low-β tokamak, which is a 2-Dimensional configuration, and to the fully 3-Dimensional stellarator configuration. An inverse aspect ratio expansion is used for the tokamak configuration. We use numerical calculations for the stellarator configuration. The derivation for the stellarator geometry is made in general magnetic coordinates: no assumption is made about the coordinate system. However, we still assume that nested magnetic surfaces do exist. Our results are valid for any other magnetic geometries, provided that a numerically-computed equilibrium is given.

3.1 The low-β tokamak configuration

In this section, we consider an axi-symmetric, low-pressure tokamak configuration with nested, shifted magnetic surfaces. An inverse-aspect-ratio expansion is used to determine the equilibrium. A suitable system of curvilinear coordinates, closely related to Shafranov coordinates, is introduced. Calculations are performed in this coordinate system and final expressions are expanded in terms of the inverse aspect ratio parameter. We first study the equilibrium and then proceed with the magnetic curvature, the LMS and their respective surface-averaged expressions.

3.1.1 The equilibrium

The equilibrium is determined through an expansion analysis in term of a smallness parameter. The expansion parameter used here is the inverse aspect ratio $\epsilon \equiv a/R_0$, where a is the minor radius of the magnetic surfaces and R_0 is the radius of the magnetic axis. The expansion parameter ϵ is not optimal and typically lies in the range from 1/3 to 1/4 for existing tokamaks.

Plasma equilibria in axi-symmetric confinement devices are governed by the

Grad-Shafranov equation [53, 54]. The Grad-Shafranov equation (GSE) is a non-linear, elliptic equation and, in general, has to be solved numerically. When the plasma pressure is not too high, or for special pressure and safety factor profiles, analytical solutions to the GSE can be found [55, 32]. In a low-β plasma, $\beta \sim \epsilon^2$, the magnetic surfaces are circular but are shifted towards the outboard side of the plasma. For a high-β plasma, $\beta \geq \epsilon$, triangularity and ellipticity effects become important and, in general, the equilibrium has to be solved numerically.

In an axi-symmetric configuration, the azimuthal angle in cylindrical coordinates, ϕ, is an ignorable coordinate. Here the origin of the cylindrical coordinates is taken to be at the intersection of the axis of revolution with the mid-plane of the machine. The equilibrium magnetic field can be written as [56]

$$\mathbf{B} = F_1\left(\psi,\bar{\theta}\right)\boldsymbol{\nabla}\psi\times\boldsymbol{\nabla}\bar{\theta} + F_2\left(\psi,\bar{\theta}\right)\left(\boldsymbol{\nabla}\psi\times\boldsymbol{\nabla}\bar{\theta}\right)\times\boldsymbol{\nabla}\psi\ , \tag{3.1}$$

where $2\pi\psi$ is the enclosed poloidal flux and $\bar{\theta}$ is a general poloidal angle. Here F_1 and F_2 are two arbitrary functions that reflect the two degrees of freedom in the representation (3.1). One degree of freedom is eliminated by demanding that the quantity $\mathcal{J}B^2$ to be a flux surface quantity [54, 39]. Without loss of generality, one can introduce a general toroidal angle

$$\zeta = \phi - \lambda\left(\psi,\bar{\theta}\right)\ , \tag{3.2}$$

which is also an ignorable coordinate. Here λ is the stream function [32]. The second degree of freedom in the representation of $\mathbf{B}$ is eliminated by demanding that the field lines appear to be straight in the $\left(\bar{\theta},\zeta\right)$ plane so that

$$\frac{\mathbf{B}\cdot\boldsymbol{\nabla}\zeta}{\mathbf{B}\cdot\boldsymbol{\nabla}\bar{\theta}} \equiv q\left(\psi\right)\ , \tag{3.3}$$

is a flux surface quantity. $q\left(\psi\right)$ is the safety factor. Introducing the field line label $\alpha \equiv \zeta - q\left(\psi\right)\bar{\theta}$, the magnetic field can now be written in Clebsch form [29]

$$\mathbf{B} = \boldsymbol{\nabla}\alpha\times\boldsymbol{\nabla}\psi\ . \tag{3.4}$$

We consider a low-β, axi-symmetric plasma surrounded by a conducting circular vessel and assume the following orderings

$$\beta = \mathcal{O}\left(\epsilon^2\right)\ ,\ \ q = \mathcal{O}\left(1\right)\ . \tag{3.5}$$

A safety factor of the order of unity implies that the poloidal component of the magnetic field is one order smaller in ϵ than its toroidal component. When requirements (3.5) are fulfilled, the Grad-Shafranov equation can be solved analytically. It is convenient to seek a solution in cylindrical coordinates (R, Z, ϕ), right-handed in that order. Then a point on a given magnetic surface can be specified as follows [32]

$$\begin{aligned} R(r,\theta) &= R_0 + r\cos\theta - \Delta(r) \ , \\ Z(r,\theta) &= r\sin\theta \ , \\ \phi &= \phi \ . \end{aligned} \tag{3.6}$$

Here R_0 is the radius of the magnetic axis, r is the local minor radius measured from the magnetic axis and Δ is the Shafranov shift [53]. The local poloidal angle θ increases as one moves anti-clockwise in the $X - Z$ Cartesian plane. The plasma outboard is defined as $\theta = 0$, whereas the plasma inboard is defined as $\theta = \pi$. For a tokamak equilibrium satisfying orderings (3.5), the flux label ψ depends only on r

$$\psi(r) = B_0 \int_0^r \frac{r'}{q(r')}\, dr' \ . \tag{3.7}$$

Substituting equation (3.6) in the Grad-Shafranov equation [54, 53]

$$\boldsymbol{\nabla}\cdot\left(\frac{\boldsymbol{\nabla}\psi}{R^2 q}\right) + q\frac{dp}{d\psi} + \frac{qG}{R^2}\frac{dG}{d\psi} = 0 \ , \tag{3.8}$$

where $2\pi G(\psi)$ is the poloidal current flowing outside the flux surface, and expanding up to second order in ϵ yields two *decoupled* equations. One equation provides a relation for the Shafranov shift [53]

$$\Delta(r) = \frac{1}{R_0}\int_0^r dr' \left[\frac{q^2}{r'^3}\int_0^{r'} dr'' \frac{r''^3}{q^2}\left(1 - 2\frac{R_0^2 q^2}{B_0^2 r''}\frac{dp}{dr''}\right)\right] . \tag{3.9}$$

For given pressure and safety factor profiles, the Shafranov shift is uniquely determined. The θ-dependent part of the Grad-Shafranov equation yields an equation for the stream function

$$\frac{\partial\lambda}{\partial\theta} = Q\left(1 - \frac{R}{\bar{\eta}}\right) \ , \tag{3.10}$$

where $\bar{\eta}(r,\theta) \equiv R_0\left(1 - \dot{\Delta}\cos\theta\right)$ and a dot denotes a derivative with respect to r. Here $Q \equiv q\bar{\eta}/R$ is the field line pitch. Integrating equation (3.10) with respect to θ and substituting the result in equation (3.2), we get the field line label

$$\alpha = \phi - q\theta + q\left[\frac{r}{R_0} + \dot{\Delta}(\sin\theta - \sin\theta_0)\right] + \mathcal{O}\left(\epsilon^2\right) \ , \tag{3.11}$$

Using the above equation in the Clebsch form (3.4) for $\mathbf{B}$ yields

$$\mathbf{B} = \boldsymbol{\nabla}\phi \times \boldsymbol{\nabla}\psi + Q\boldsymbol{\nabla}\psi \times \boldsymbol{\nabla}\theta \ , \tag{3.12}$$

where the first term on the right-hand side is the poloidal component of $\mathbf{B}$ whereas the second term is the toroidal component. The poloidal component reads

$$B_\theta = \frac{B_0 r}{q R_0} \left(1 - \frac{r}{R_0} \cos\theta + \dot{\Delta}\cos\theta\right) + \mathcal{O}\left(\epsilon^3\right) \ , \tag{3.13}$$

and the toroidal component is

$$B_\phi = B_0 \left(1 - \frac{r}{R_0} \cos\theta + \frac{\Delta}{R_0}\right) + \mathcal{O}\left(\epsilon^3\right) \ . \tag{3.14}$$

The first term on the right-hand side of equation (3.13) is the cylindrical contribution, the second term is due to toroidal bending and the third term, a finite-β effect, arises because of the compression of the magnetic surface. Finite β effects in B_θ and B_ϕ are second-order corrections.

3.1.2 The magnetic curvature

It is convenient to perform calculations in the local coordinate system (r, θ, ϕ) rather than in magnetic coordinates. Noting that the enclosed poloidal flux is a function of r only we see that the gradient operator takes the form

$$\boldsymbol{\nabla} = \boldsymbol{\nabla} r \frac{\partial}{\partial r} + \boldsymbol{\nabla}\theta \frac{\partial}{\partial \theta} + \left(\boldsymbol{\nabla}\phi - \frac{\partial \lambda}{\partial \theta}\boldsymbol{\nabla}\theta - \frac{\partial \lambda}{\partial r}\boldsymbol{\nabla} r\right)\frac{\partial}{\partial \phi} \ . \tag{3.15}$$

The last term does not contribute when $\boldsymbol{\nabla}$ operates on a *scalar* quantity because the equilibrium is axi-symmetric. Final expressions are then expanded in ascending powers of ϵ. The algebra is tedious but straightforward and the details of the calculations are given in appendix B. The normal curvature is written as

$$\kappa_{\mathrm{N}} = \kappa_{\mathrm{N}}^{(0)} + \kappa_{\mathrm{N}}^{(1)} + \kappa_{\mathrm{N}}^{(2)} + \mathcal{O}\left(\epsilon^3\right) \ , \tag{3.16}$$

where the superscripts indicate the corresponding order in ϵ, we get

$$\kappa_{\mathrm{N}}^{(0)} = -\frac{\cos\theta}{R_0} \ , \tag{3.17}$$

$$\kappa_{\mathrm{N}}^{(1)} = \frac{r}{{R_0}^2}\left(\cos\theta - \frac{1}{q^2}\right) \ , \tag{3.18}$$

and

$$\kappa_{\mathrm{N}}^{(2)} = -\frac{r^2}{{R_0}^3}\,\cos\theta\left[\cos^2\theta + \frac{1}{q^2}\left(2\frac{R_0\dot{\Delta}}{r} - 1\right) + \frac{R_0\Delta}{r^2}\right] . \tag{3.19}$$

The cylindrical contribution in the normal curvature is given by the term $-r/\left(qR_0\right)^2$ in $\kappa_{\mathrm{N}}^{(1)}$. This contribution is independent of the poloidal angle. Therefore a large safety factor is beneficial since it reduces the surface-averaged magnetic curvature. The first term on the right-hand side of equation (3.18) is a toroidal bending contribution and it is *stabilizing*. It is worth noting that the finite-β corrections enter κ_{N} to second order in ϵ. As we shall see below this is also true for the geodesic component of the magnetic curvature.

Similarly, the geodesic component of the magnetic curvature can be written as

$$\kappa_{\mathrm{G}} = \kappa_{\mathrm{G}}^{(0)} + \kappa_{\mathrm{G}}^{(1)} + \kappa_{\mathrm{G}}^{(2)} + \mathcal{O}\left(\epsilon^3\right) , \tag{3.20}$$

where

$$\kappa_{\mathrm{G}}^{(0)} = \frac{\sin\theta}{R_0} , \tag{3.21}$$

$$\kappa_{\mathrm{G}}^{(1)} = -\frac{r}{R_0}\,\sin\theta\cos\theta , \tag{3.22}$$

and

$$\kappa_{\mathrm{G}}^{(2)} = \frac{r^2}{R_0^3}\,\sin\theta\left[\cos^2\theta + \frac{R_0\Delta}{r^2} - \frac{1}{2q^2}\left(1 + 2\frac{R_0\dot{\Delta}}{r}\right)\right] . \tag{3.23}$$

It can be shown that the surface-averaged geodesic curvature vanishes to all order in ϵ. The corrections arising from the Shafranov shift enter to second order in ϵ.

3.1.3 The local magnetic shear

The method for deriving the LMS is identical to the one presented in the previous section. Detailed calculations are reported in appendix B. The final expression for the LMS in a low-β tokamak plasma reads [1, 2]

$$\mathcal{S} = \mathcal{S}^{(0)} + \mathcal{S}^{(1)} + \mathcal{S}^{(2)} + \mathcal{O}\left(\epsilon^3\right) , \tag{3.24}$$

where

$$\mathcal{S}^{(0)} = \frac{\hat{s}}{{R_0}^3} , \tag{3.25}$$

$$\mathcal{S}^{(1)} = -\frac{r}{{R_0}^4}\,\cos\theta\left[1 + R_0\ddot{\Delta} + \frac{R_0\dot{\Delta}}{r}\,(1-2\hat{s})\right]\,, \tag{3.26}$$

and

$$\begin{aligned}\mathcal{S}^{(2)} &= -\frac{r}{{R_0}^4}\cos^2\theta\left[2\dot{\Delta} - \frac{r}{R_0} + R_0\ddot{\Delta}\left(3\dot{\Delta} - \frac{r}{R_0}\right) + R_0\hat{s}\frac{\dot{\Delta}^2}{r}\right] \\ &- \dot{\Delta}^2\left[1 + \cos^2\theta\left(1 - \frac{r}{R_0\ddot{\Delta}}\right)\right]\,. \end{aligned} \tag{3.27}$$

In equations (3.25-3.27), we have introduced the shear parameter $\hat{s} \equiv r\dot{q}/q$. We note that the finite-β corrections enter to *first* order in ϵ. The global magnetic shear is $\widehat{\mathcal{S}} = \hat{s}/{R_0}^3$. Therefore the residual shear is given by the sum of $\mathcal{S}^{(1)}$ and $\mathcal{S}^{(2)}$.

In section 2.2, we pointed out that one of the terms in the field line bending contribution scales like

$$\mathcal{S}^2 = \widehat{\mathcal{S}}^2 + 2\,\mathcal{R}\,\widehat{\mathcal{S}} + \mathcal{R}^2\,. \tag{3.28}$$

If, for simplicity, we neglect the second order corrections, the residual shear reduces to $\mathcal{S}^{(1)}$. Then, for a peaked q profile ($\hat{s} \sim 1$), the first term on the right-hand side of equation (3.28) is $\mathcal{O}(1)$, the second term is $\mathcal{O}(\epsilon)$ and the last term is $\mathcal{O}(\epsilon^2)$.

We first consider the case of a positive global shear. For a positive global shear of order unity, the last term in the square brackets of equation (3.26) is negative. The residual shear is negative. As $\hat{s}$ increases, the residual shear decreases; as a consequence, the first term on the right-hand side of equation (3.28) increases but the second term decreases. In equation (3.28), the first term (stabilizing contribution) on the right-hand side scales like $\hat{s}^2$ but the second term (destabilizing contribution) scales linearly with $\hat{s}$ so that the left-hand side increases as $\hat{s}$ increases. In summary, for a positive global shear, the first and third terms on the right-hand side of equation (3.28) are *stabilizing* while the second term is *destabilizing*.

To see what might happen in a reversed-shear experiment, we make the transformation $\hat{s} \mapsto -\hat{s}$ in the above equations. The first term on the right-hand side of equation (3.28) remains unchanged. The residual shear, however, becomes more negative. Furthermore, the product $\mathcal{R}\,\widehat{\mathcal{S}}$ is now *positive*. We conclude that, for a configuration with negative global shear, *all* the terms on the right-hand side of equation (3.28) are *stabilizing*. This is a simple explanation for the favorable conditions of the reversed-shear configuration.

However, we also have to consider how the transformation $\hat{s} \mapsto -\hat{s}$ can affect the normal curvature. Returning to equation (3.16), we see that the lowest and first order terms of the normal curvature remain unchanged in the reversed-shear case. Therefore, we conclude that the reversed-shear configuration leads mainly to an increase of the stabilizing contribution of the field line bending term, while the destabilizing normal curvature changes only slightly.

We can also investigate the effect of a steepening of the pressure gradient. For a standard pressure profile, we have $R_0 B_0^{-2} dp/dr \sim \epsilon$ and

$$\frac{d\Delta}{dr} \sim \epsilon \ , \quad R_0 \frac{d^2\Delta}{dr^2} \sim 1 \ . \tag{3.29}$$

Following Connor *et al* [57], we now assume that the pressure gradient is large, $R_0 B_0^{-2} dp/dr \sim 1$, in a small layer $\delta r/R_0 \sim \epsilon^2$. It can be shown that the ordering (3.29) is now replaced by

$$\frac{d\Delta}{dr} \sim \epsilon \ , \quad R_0 \frac{d^2\Delta}{dr^2} \sim \frac{1}{\epsilon} \gg 1 \ . \tag{3.30}$$

Ordering (3.30) leads to some simplifications in the expression for the LMS. Taking into account (3.30), and neglecting corrections of $\mathcal{O}(\epsilon^2)$ and higher, the LMS becomes

$$\mathcal{S} = \frac{1}{{R_0}^3} \left[\hat{s} - \frac{r}{R_0} \cos\theta \, (1 + \bar{\alpha}) \right] \ , \tag{3.31}$$

where $\bar{\alpha} \equiv -2q^2 R_0 \dot{p}/B_0^2$ is the ballooning parameter [57]. The second term on the right-hand side of equation (3.31) is sometimes referred to as the local shear [32]. For simplicity, we consider the case of a positive global shear and study the case $\theta = 0$, where the normal curvature is unfavorable. As the pressure gradient increases then $\bar{\alpha}$ also increases and, according to equation (3.31), the LMS decreases. As $\bar{\alpha}$ is increased further, the LMS ultimately vanishes and the *destabilizing* normal curvature is not balanced by any *stabilizing* contribution. In this case, ballooning modes can be driven unstable [20]. If the pressure gradient further increases then the local magnetic shear becomes negative. For a large pressure gradient, the poloidal field on the outside of the torus strengthens and the Shafranov shift increases. This shortens the connection length and diminishes the drive of the instability. For such a pressure gradient, the mode enters the second stability region [20].

We now illustrate our qualitative discussion with specific cases.

3.1.4 Visualization

The visualization techniques used in this section are very similar to the ones described in chapter 2 for the helically-symmetric configuration. Unlike the straight stellarator configuration, however, the tokamak configuration closes upon itself. Therefore, when building the AVS structure, we must ensure that the poloidal and toroidal periodicity requirements are satisfied simultaneously. The rest of the visualization techniques is the same as before.

For the following specific cases, the pressure profile is parabolic

$$p(r) = p(0)\left[1 - \left(\frac{r}{a}\right)^2\right], \tag{3.32}$$

where a is the minor radius of the last closed magnetic surface. In view of the ordering used in this chapter, the central plasma pressure cannot be too large. Specifically we demand $p(0)/B_0^2 \leq (a/R_0)^2$. The safety factor profile is chosen of the form

$$q(r) = q(0)\left(1 + \left(\frac{r}{a}\right)^{2\lambda}\left[\left(\frac{q(a)}{q(0)}\right)^{\lambda} - 1\right]\right)^{1/\lambda}. \tag{3.33}$$

Here again the safety factor must be of the order of unity. Since our ordering parameter is ϵ, one must choose the parameters in equation (3.33) in such a way that $q(a) \leq R_0/a$, which is typically 3 for realistic tokamaks.

In the following, we will display the magnetic field strength, the normal and geodesic curvatures and the LMS for different equilibria, all of which have $q(0) = 1.1$ and $q(a) = 2.4$.

In Figures 3.1 to 3.5, the following parameters are used: $\epsilon = 0.3$ and $\lambda = 1.0$ (peaked profile). The magnetic field strength, normalized to B_0 (axis), is shown in Figure 3.1 for a central $\beta = 1\%$. The Shafranov shift is small, and the magnetic surfaces are nearly concentric with their center almost coincide with the geometrical radius of the machine. The lines $\theta = \text{const}$ and $r = \text{const}$ intersect almost at right angle. The $1/R$ dependence of the magnetic field strength is visible.
The magnetic field strength for a central $\beta = 2\%$ is shown in Figure 3.2. The shift

of the magnetic surfaces, although small, is visible.

Figure 3.3 shows $|\mathbf{B}|$ for a central $\beta = 4\%$. The compression of the magnetic surfaces towards the outside of the plasma is important. Due to the Shafranov shift, the lines $\theta = \text{const}$ and $r = \text{const}$ are clearly not orthogonal.

The normal component of the magnetic curvature, for the same parameters as in Figure 3.3, is shown in Figure 3.4. The region of unfavorable curvature is colored in blue, while the region of favorable curvature is colored in yellow, orange and red.

The geodesic component of the magnetic curvature, for the same parameters as in Figure 3.3, is shown in Figure 3.5. κ_G is small in the inside and in the outside of the plasma. The geodesic curvature is maximum (minimum) at the top (bottom) of the plasma cross-section, where the normal curvature approximately vanishes.

The LMS for a case with $R_0 = 3$ m, $a = 0.3$ m ($\epsilon = 0.1$), central $\beta = 0.5\%$ and a flat q profile with $\lambda = 4$, is shown in Figure 3.6. In physical units, the maximum shear is 2.70×10^{-2} m^{-3} and the minimum shear is -3.88×10^{-3} m^{-3}. The region of negative LMS is shown in dark blue. The region where the LMS is the largest is colored in red. In the low-β, large-aspect-ratio case shown in Figure 3.6, the LMS is approximately a flux surface quantity, except near the magnetic axis where the residual part of $\mathcal{S}$ can be comparable to the global part of $\mathcal{S}$.

Figure 3.7 shows a case with $R_0 = 3$ m, $a = 0.9$ m ($\epsilon = 0.3$), central $\beta = 2.0\%$ and $\lambda = 1.2$. The LMS is no longer a flux surface quantity because the residual part of $\mathcal{S}$, proportional to ϵ, is now important. This effect is amplified due to the large central β, and the region of negative LMS is clearly off-axis. Comparing with Figure 3.6, the region of strong LMS is now located in the inside of the plasma, $\pi/2 \leq \theta \leq 3\pi/2$. The minimum shear is now -1.19×10^{-2} m^{-3} and the maximum value of $\mathcal{S}$ is 5.93×10^{-2} m^{-3}. With λ close to unity, the current profile is centrally peaked and the global shear remains quite large in most parts of the plasma.

Figure 3.8 shows the LMS for the same parameters as in Figure 3.7 except that $\lambda = 4.0$. The corresponding current profile is rather flat and the central global shear is weak. As a result, the contribution of the residual shear is important over a large fraction of the plasma; the region of negative LMS, shown in blue, is larger than in the previous cases.

Finally, Figure 3.9 shows the LMS for a reversed-shear configuration. The safety

factor is chosen as a third-order polynomial with a local minimum of $q = 1.01$ at $r/a = 0.5$ and, as before, $q(0) = 1.1$ and $q(a) = 2.4$. The region of negative LMS now extends out to the plasma edge essentially filling the whole region of unfavorable curvature (see Figure 3.3). In this case, the negative contribution of the residual shear in the outbard side of the plasma combines with the global shear to increase the region of negative LMS. We note that the LMS is positive on the inside of the machine.

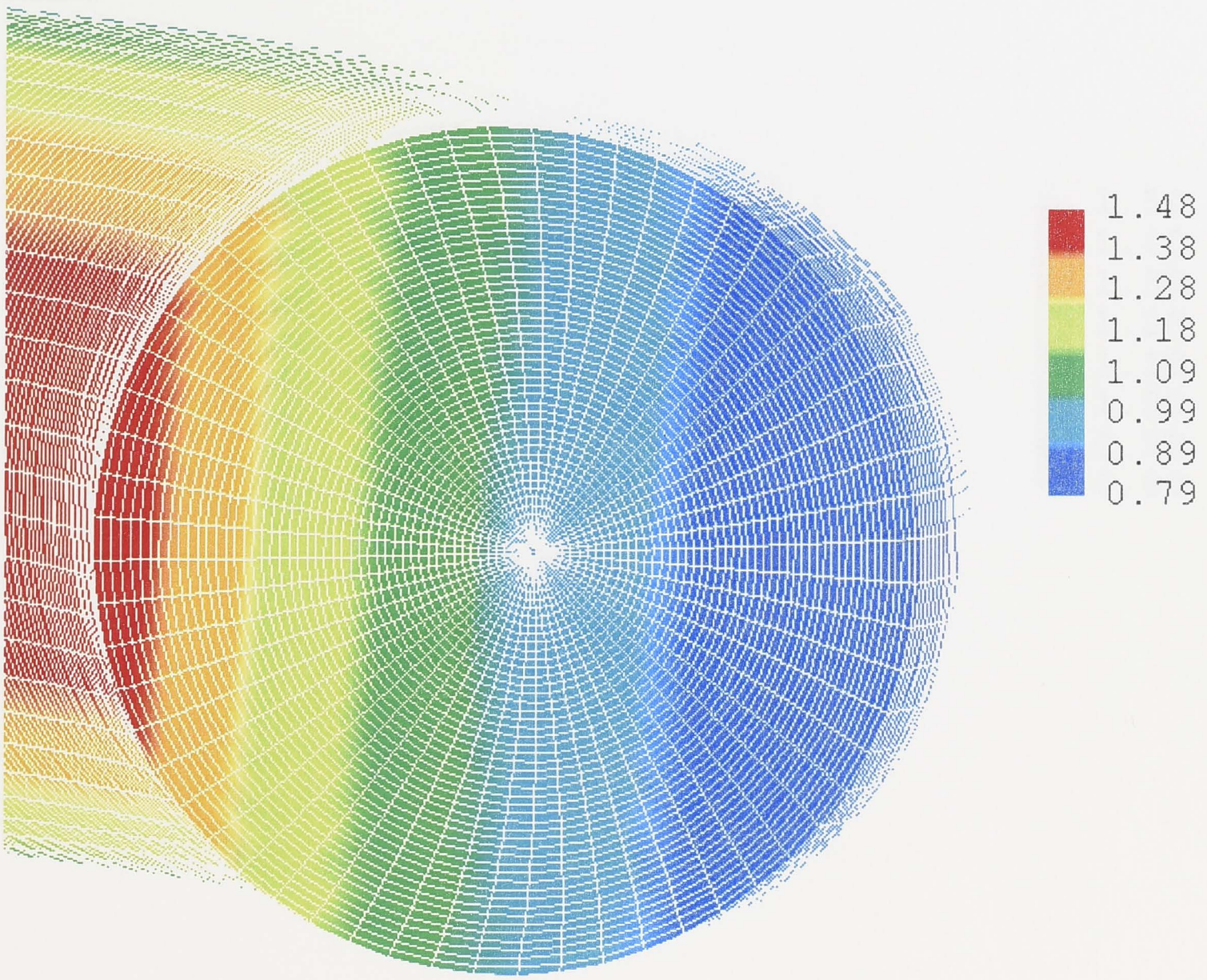

Figure 3.1: The magnetic field strength for a second-order equilibrium, with central $\beta = 1\%$, $q(0) = 1.1$, $q(a) = 2.4$, $\epsilon = 0.3$ and $\lambda = 1.0$. The magnetic field strength is normalized to B_0 (axis). The $1/R$ dependence of B is visible.

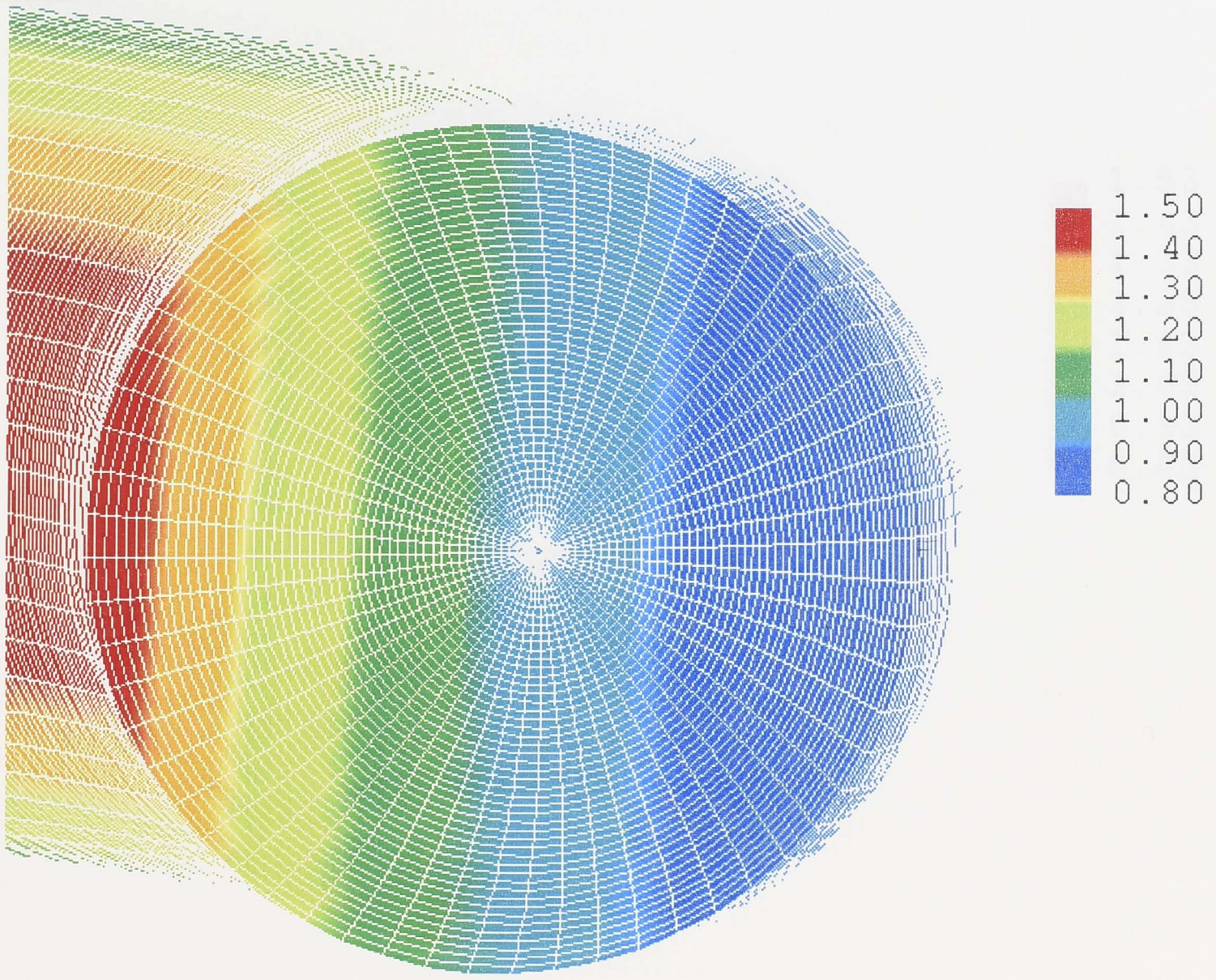

Figure 3.2: The magnetic field strength for a second-order equilibrium, with central $\beta = 2\%$, $q(0) = 1.1$, $q(a) = 2.4$, $\epsilon = 0.3$ and $\lambda = 1.0$. The magnetic field strength is normalized to B_0 (axis).

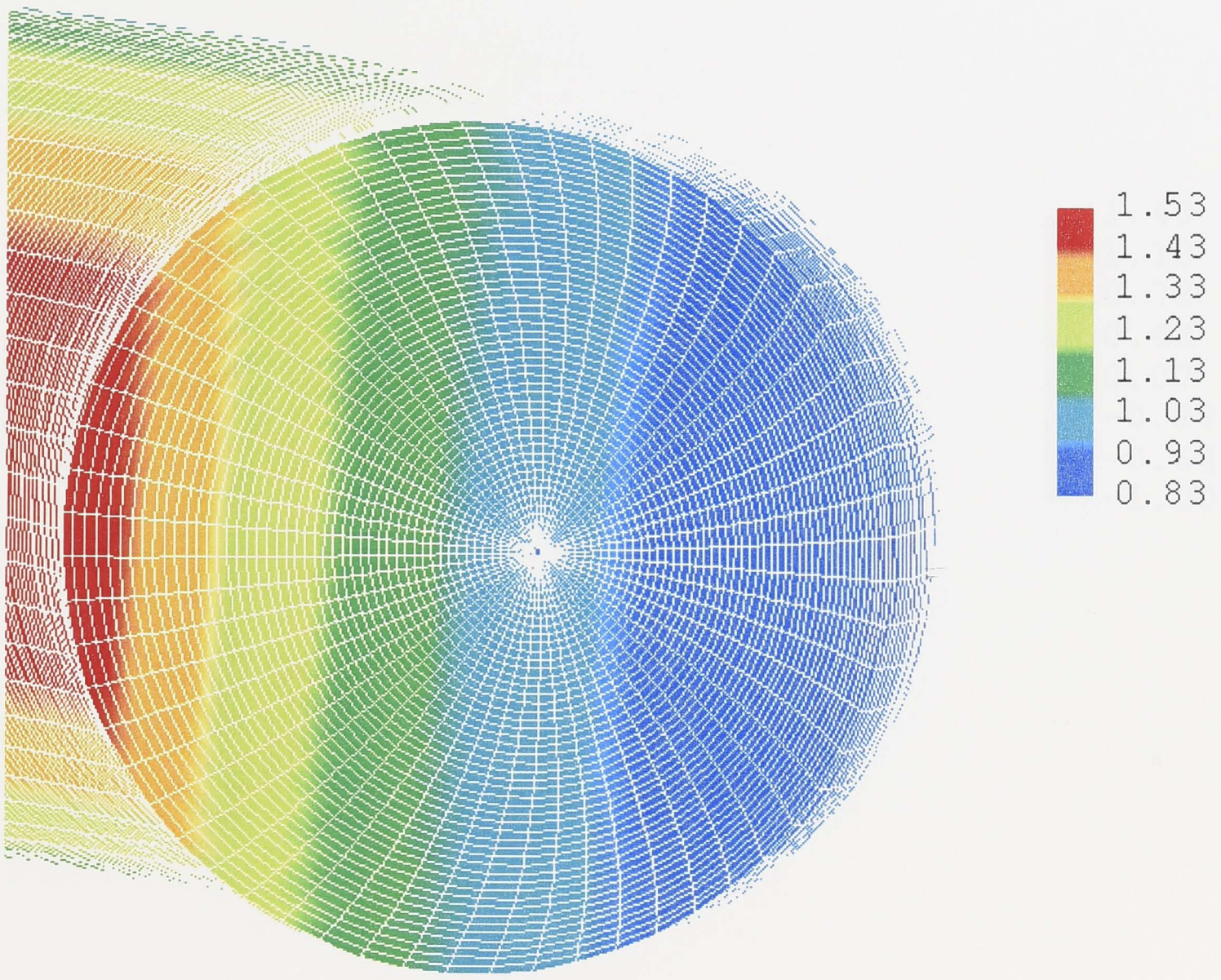

Figure 3.3: The magnetic field strength for a second-order equilibrium, with central $\beta = 4\%$, $q(0) = 1.1$, $q(a) = 2.4$, $\epsilon = 0.3$ and $\lambda = 1.0$. The magnetic field strength is normalized to B_0 (axis). The Shafranov shift of the magnetic surfaces is visible.

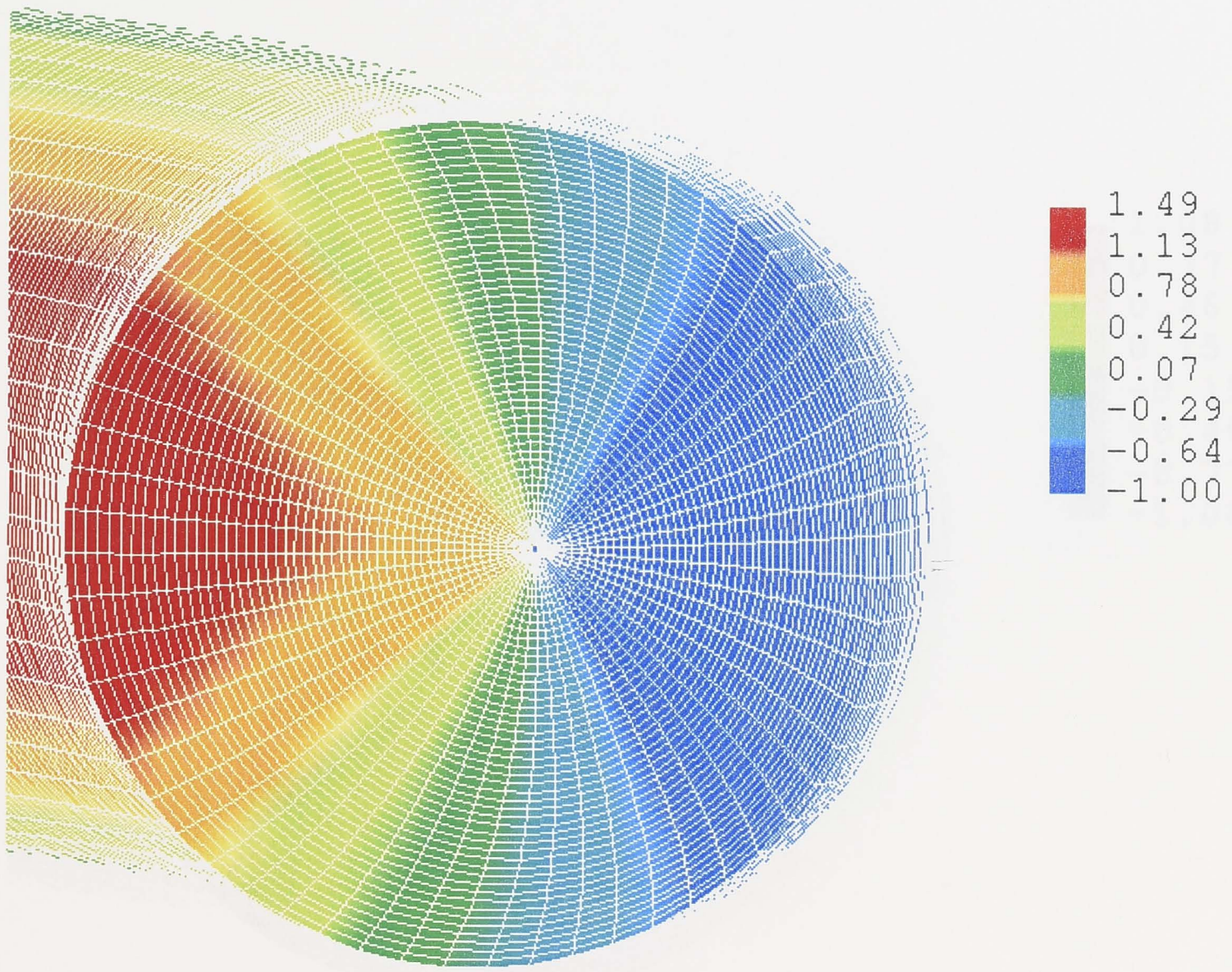

Figure 3.4: The normal component of the magnetic curvature for a second-order equilibrium, with central $\beta = 4\%$, $q(0) = 1.1$, $q(a) = 2.4$, $\epsilon = 0.3$ and $\lambda = 1.0$. The normal curvature is normalized to $1/R$. The region of favorable (unfavorable) curvature is shown in red (blue).

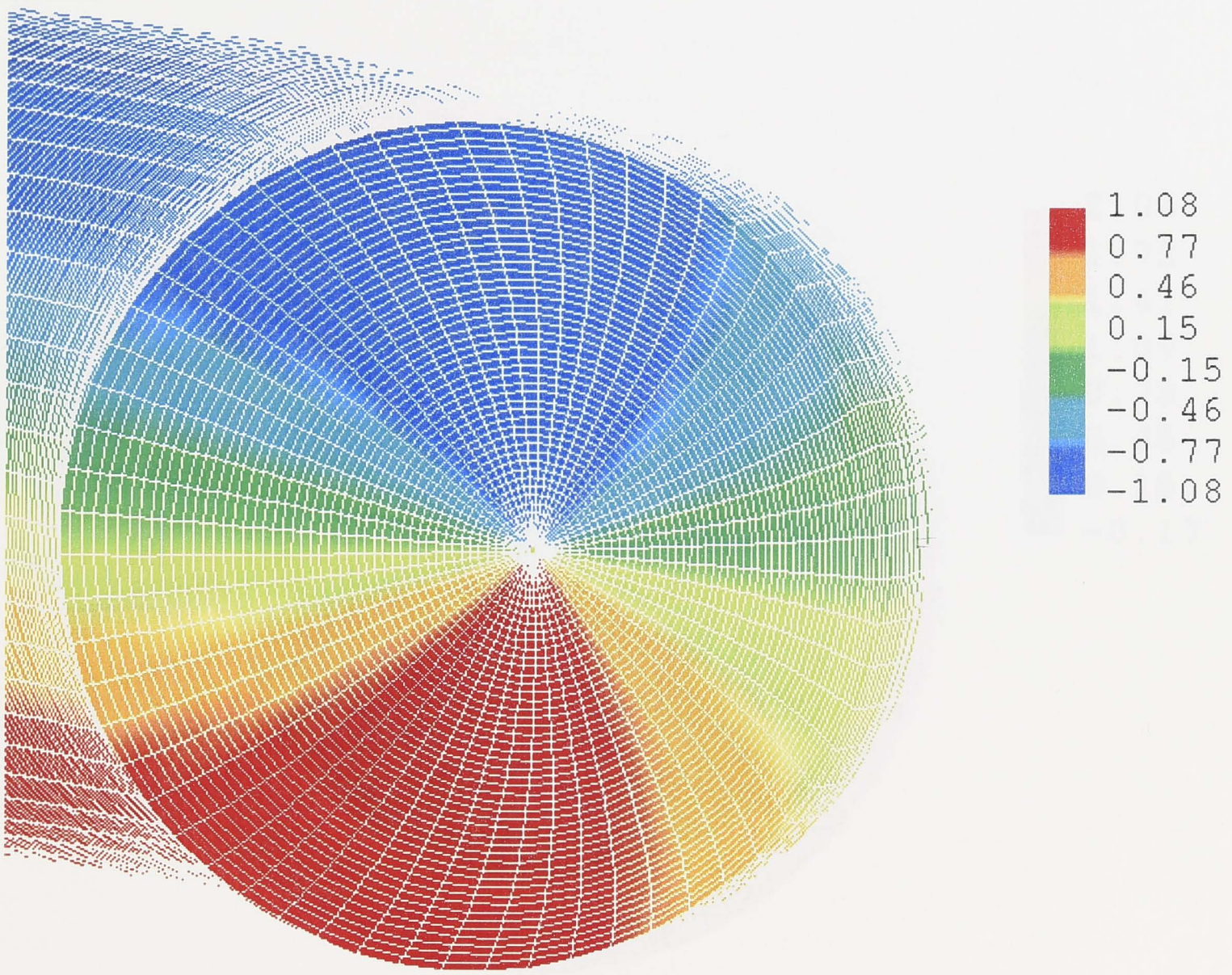

Figure 3.5: The geodesic component of the magnetic curvature for a second-order equilibrium, with central $\beta = 4\%$, $q(0) = 1.1$, $q(a) = 2.4$, $\epsilon = 0.3$ and $\lambda = 1.0$. The geodesic curvature is normalized to $1/R$.

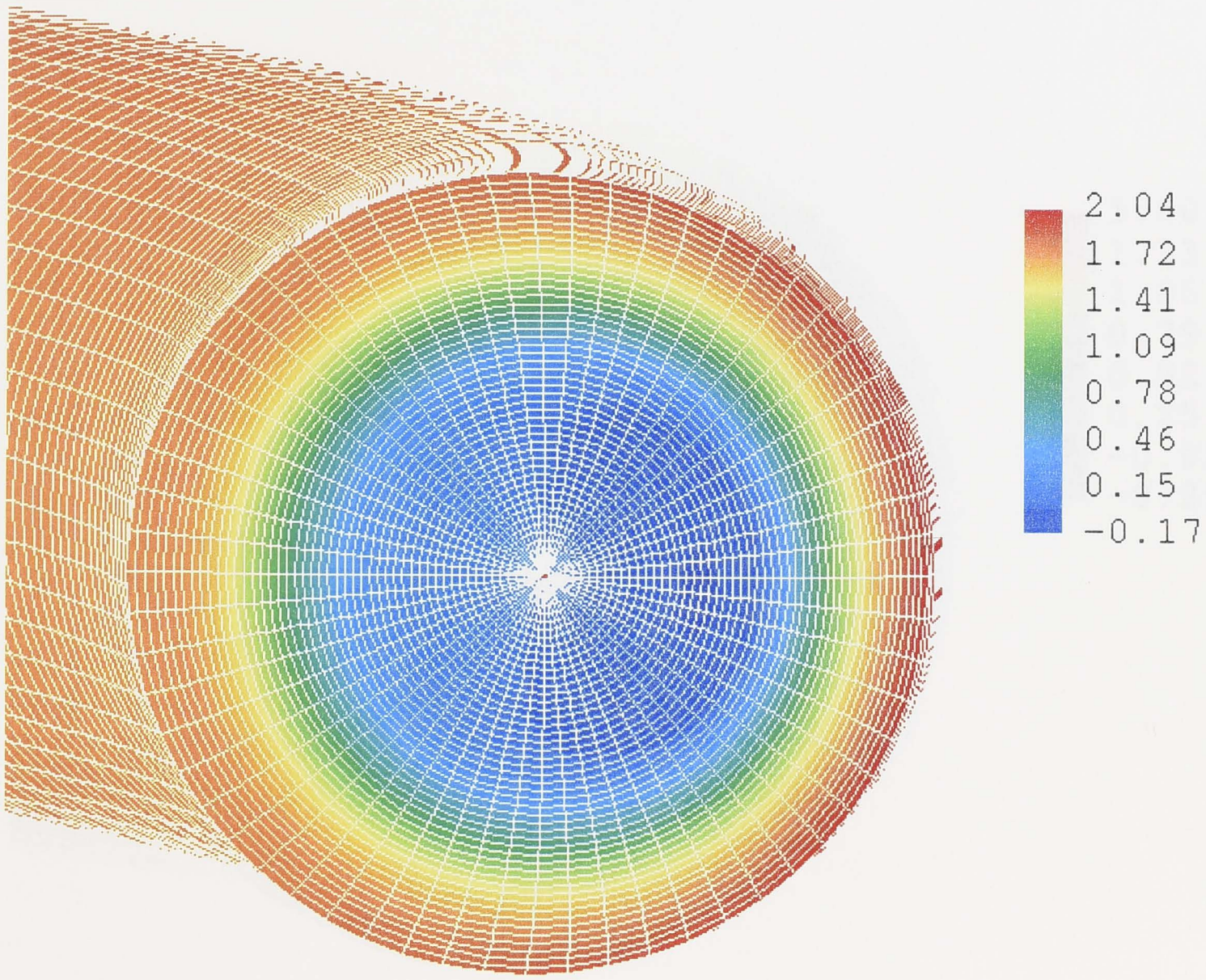

Figure 3.6: The local magnetic shear for a second-order equilibrium, with central $\beta = 0.5\%$, $q(0) = 1.1$, $q(a) = 2.4$, $\epsilon = 0.1$ and $\lambda = 4.0$. The region colored in dark blue corresponds to a negative LMS.

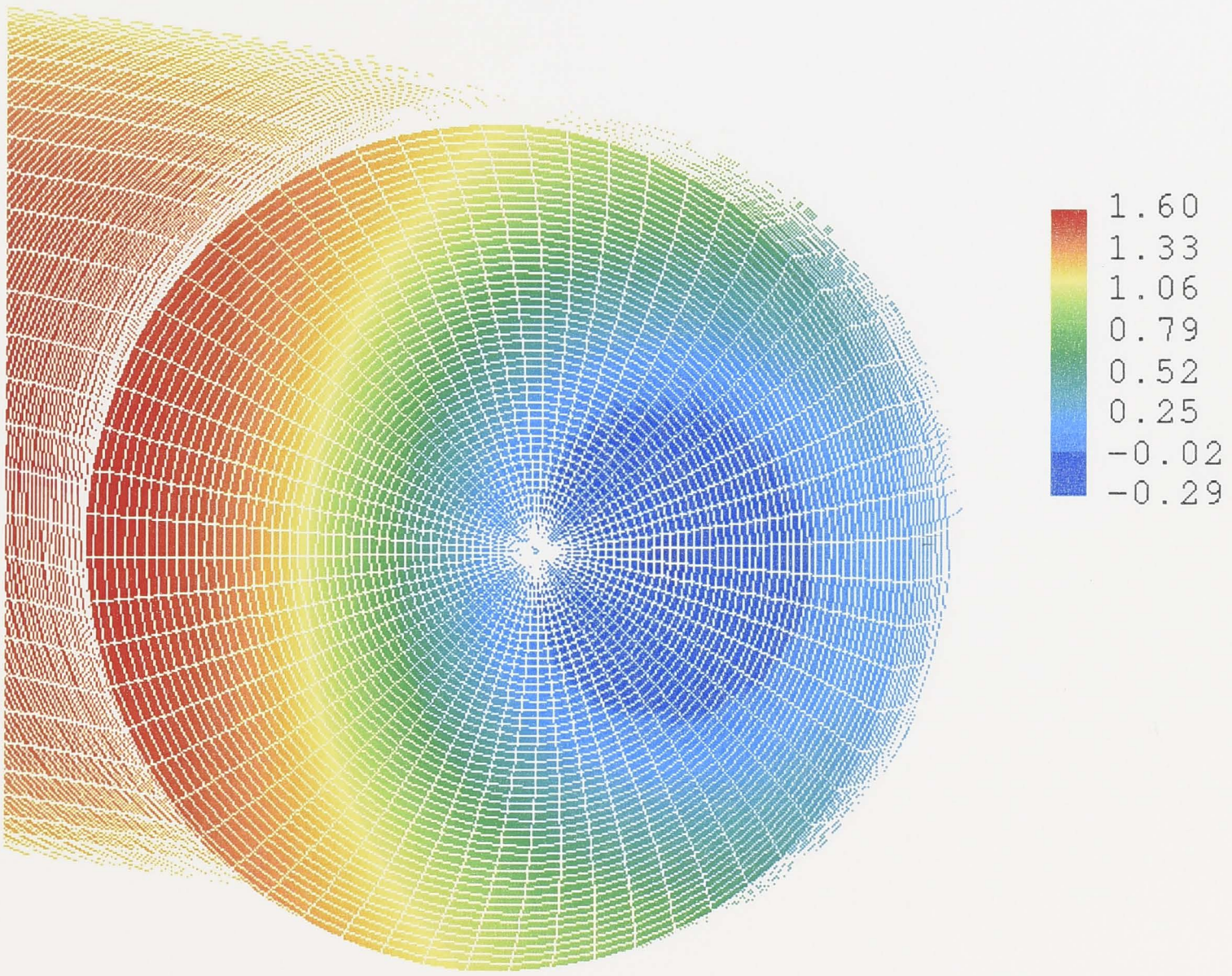

Figure 3.7: The local magnetic shear for a second-order equilibrium, with central $\beta = 2.0\%$, $q(0) = 1.1$, $q(a) = 2.4$, $\epsilon = 0.3$ and $\lambda = 1.2$. The region colored in dark blue corresponds to a negative LMS.

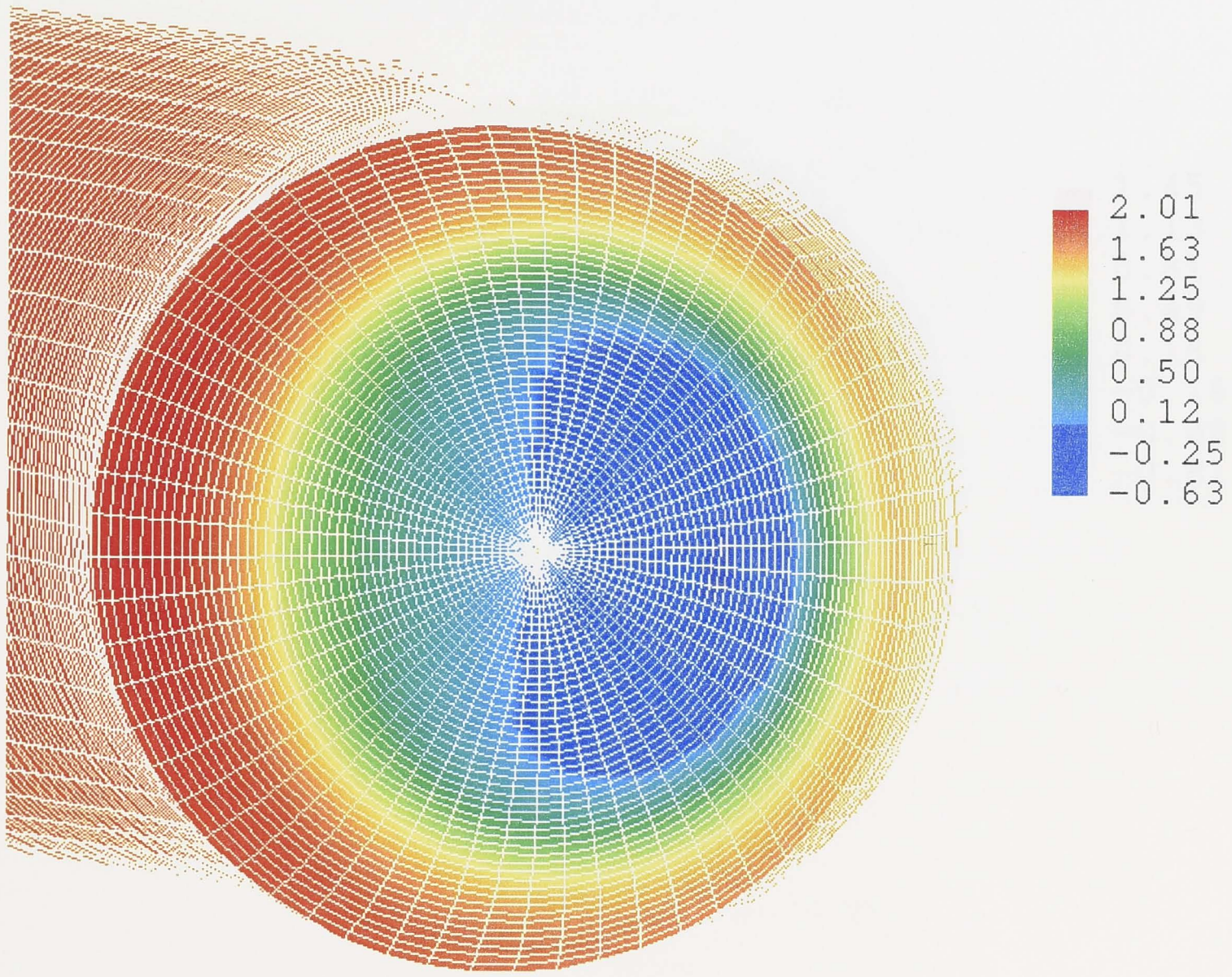

Figure 3.8: The local magnetic shear for a second-order equilibrium, with central $\beta = 2.0\%$, $q(0) = 1.1$, $q(a) = 2.4$, $\epsilon = 0.3$ and $\lambda = 4.0$. The region colored in dark blue corresponds to a negative LMS.

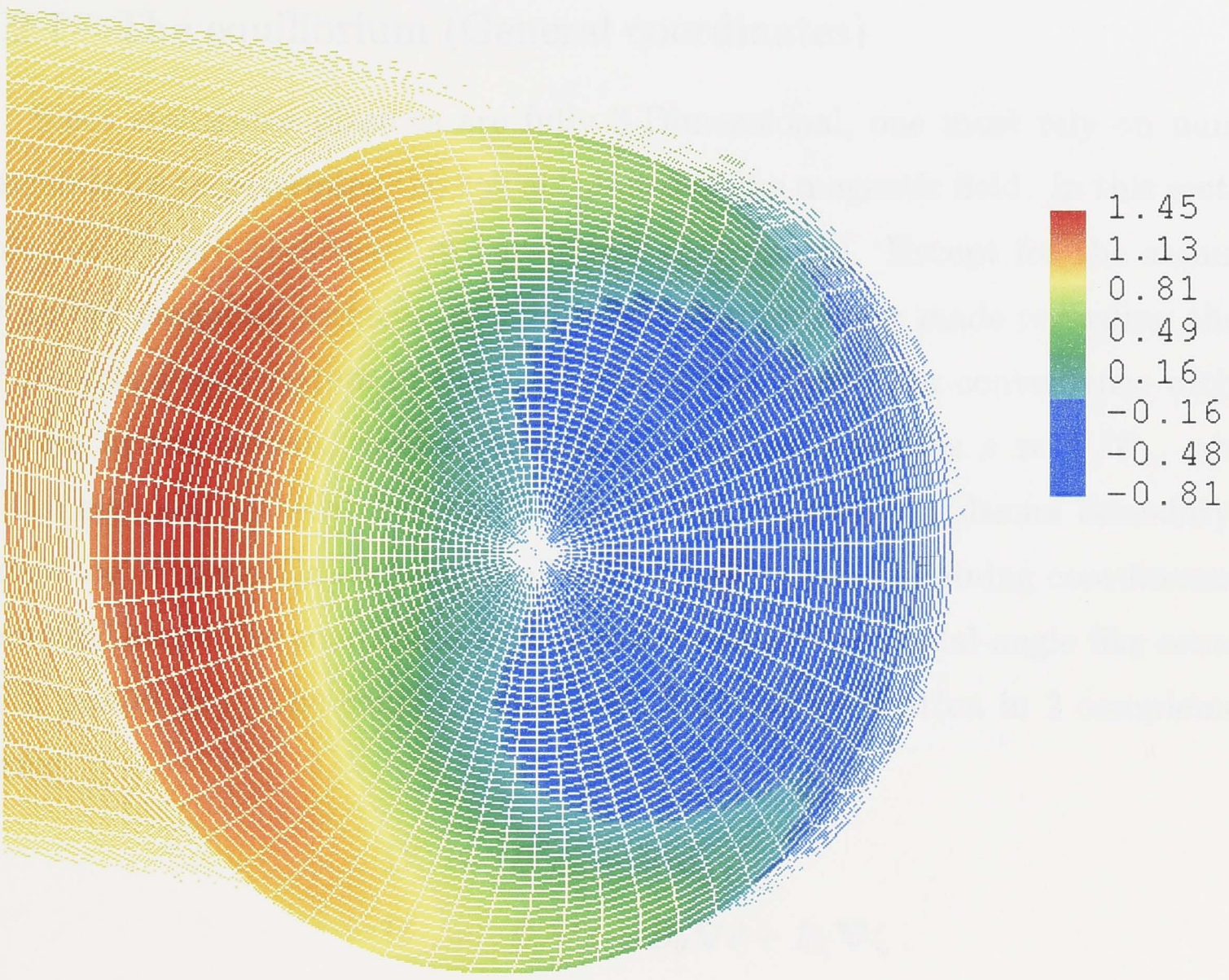

Figure 3.9: The local magnetic shear for a second-order equilibrium, with central $\beta = 2.0\%$, $q(0) = 1.1$, $q(a) = 2.4$, $\epsilon = 0.3$ and negative global shear for $r/a \leq 0.5$. The region colored in dark blue corresponds to a negative LMS.

3.2 The stellarator configuration

In this section, we calculate the key attributes of the magnetic field of four stellarators. We briefly discuss the code used to generate the equilibrium and we use our visualization techniques to display the quantities of interest.

3.2.1 The equilibrium (General coordinates)

Since stellarator plasmas are fully 3-Dimensional, one must rely on numerical calculations to determine the key attributes of the magnetic field. In this section all calculations are performed in curvilinear coordinates. Except for the assumption of nested magnetic surfaces, no additional assumption is made regarding the form of the coordinate system in the derivation given below. For convenience with what follows in the coming section, the radial label used here is $s \equiv \Psi/\Psi_{\rm b}$, where Ψ is the enclosed toroidal flux and $\Psi_{\rm b}$ is Ψ evaluated at the plasma boundary. The existence of magnetic surfaces implies $\mathbf{B}\cdot\boldsymbol{\nabla}s \equiv 0$. The remaining coordinates are θ (poloidal-angle like coordinate with period 2π) and ζ (toroidal-angle like coordinate with period 2π). The confining magnetic field can be written in 2 complementary forms

$$\begin{aligned} \mathbf{B} &= B^\theta \mathbf{e}_\theta + B^\zeta \mathbf{e}_\zeta \ , \\ \mathbf{B} &= B_{\rm s}\boldsymbol{\nabla}s + B_\theta \boldsymbol{\nabla}\theta + B_\zeta \boldsymbol{\nabla}\zeta \ . \end{aligned} \tag{3.34}$$

Here $B^\theta \equiv \mathbf{B}\cdot\boldsymbol{\nabla}\theta$, $B^\zeta \equiv \mathbf{B}\cdot\boldsymbol{\nabla}\zeta$, $B_\mu \equiv \mathbf{B}\cdot\mathbf{e}_\mu$, $\mathbf{e}_\mu \equiv \partial\mathbf{r}/\partial\mu$ ($\mathbf{r}$ is the position vector) for $\mu = \{s, \theta, \zeta\}$. In these coordinates, the gradient operator reads

$$\boldsymbol{\nabla} = \boldsymbol{\nabla}s\frac{\partial}{\partial s} + \boldsymbol{\nabla}\theta\frac{\partial}{\partial\theta} + \boldsymbol{\nabla}\zeta\frac{\partial}{\partial\zeta} \ . \tag{3.35}$$

Using equations (3.34,3.35), one can compute the magnetic curvature and the LMS. The details of the calculations are reported in appendix C. The normal component of the magnetic curvature is

$$\kappa_{\rm N} = \frac{1}{\sqrt{g^{ss}}}\left[2\, b^\theta\, b^\zeta\, \boldsymbol{\nabla}s\cdot\frac{\partial\mathbf{e}_\theta}{\partial\zeta} + \left(b^\theta\right)^2\, \boldsymbol{\nabla}s\cdot\frac{\partial\mathbf{e}_\theta}{\partial\theta} + \left(b^\zeta\right)^2\, \boldsymbol{\nabla}s\cdot\frac{\partial\mathbf{e}_\zeta}{\partial\zeta}\right] , \tag{3.36}$$

and the geodesic curvature reads

$$\kappa_{\rm G} = \frac{1}{\mathcal{J}\sqrt{g^{ss}}}\left[b_\zeta\, \kappa_\theta - b_\theta\, \kappa_\zeta\right] . \tag{3.37}$$

Here $b^\theta \equiv B^\theta/B$, $b^\zeta \equiv B^\zeta/B$, $b_\theta \equiv B_\theta/B$, $b_\zeta \equiv B_\zeta/B$ and $g^{ss} \equiv \nabla s \cdot \nabla s$ is a metric element. In the above equation, we have introduced

$$\begin{aligned}\kappa_\theta \;\equiv\; & \left(b^\theta \frac{\partial b^\theta}{\partial \theta} + b^\zeta \frac{\partial b^\theta}{\partial \zeta} \right) g_{\theta\theta} + \left(b^\theta \frac{\partial b^\zeta}{\partial \theta} + b^\zeta \frac{\partial b^\zeta}{\partial \zeta} \right) g_{\theta\zeta} \\ & + \; 2\, b^\theta\, b^\zeta\, \mathbf{e}_\theta \cdot \frac{\partial \mathbf{e}_\theta}{\partial \zeta} + \left(b^\theta\right)^2 \mathbf{e}_\theta \cdot \frac{\partial \mathbf{e}_\theta}{\partial \theta} + \left(b^\zeta\right)^2 \mathbf{e}_\theta \cdot \frac{\partial \mathbf{e}_\zeta}{\partial \zeta} \;, \end{aligned} \tag{3.38}$$

and

$$\begin{aligned}\kappa_\zeta \;\equiv\; & \left(b^\theta \frac{\partial b^\theta}{\partial \theta} + b^\zeta \frac{\partial b^\theta}{\partial \zeta} \right) g_{\theta\zeta} + \left(b^\theta \frac{\partial b^\zeta}{\partial \theta} + b^\zeta \frac{\partial b^\zeta}{\partial \zeta} \right) g_{\zeta\zeta} \\ & + \; 2\, b^\theta\, b^\zeta\, \mathbf{e}_\zeta \cdot \frac{\partial \mathbf{e}_\theta}{\partial \zeta} + \left(b^\theta\right)^2 \mathbf{e}_\zeta \cdot \frac{\partial \mathbf{e}_\theta}{\partial \theta} + \left(b^\zeta\right)^2 \mathbf{e}_\zeta \cdot \frac{\partial \mathbf{e}_\zeta}{\partial \zeta} \;. \end{aligned} \tag{3.39}$$

The LMS can also be derived in general curvilinear coordinates. The final expression is not illuminating but we give the general expression for sake of completeness

$$\begin{aligned}\mathcal{S} \;=\; & C \Bigg\{ (B_\zeta\, g_{s\theta} - B_\theta\, g_{s\zeta}) \Bigg[g_{\theta\theta} \frac{\partial B_\zeta}{\partial \zeta} - g_{\theta\zeta} \left(\frac{\partial B_\theta}{\partial \zeta} + \frac{\partial B_\zeta}{\partial \theta} \right) + g_{\zeta\zeta} \frac{\partial B_\theta}{\partial \theta} \\ & + \; B_\zeta \left(\frac{\partial g_{\theta\theta}}{\partial \zeta} - \frac{\partial g_{\theta\zeta}}{\partial \theta} \right) + B_\theta \left(\frac{\partial g_{\zeta\zeta}}{\partial \theta} - \frac{\partial g_{\theta\zeta}}{\partial \zeta} \right) \\ & + \; (B_\theta\, g_{\theta\zeta} - B_\zeta\, g_{\theta\theta}) \left(\frac{1}{\mathcal{J}} \frac{\partial \mathcal{J}}{\partial \zeta} + \frac{1}{\sqrt{g^{ss}}} \frac{\partial \sqrt{g^{ss}}}{\partial \zeta} + \frac{1}{B} \frac{\partial B}{\partial \zeta} \right) \\ & + \; (B_\zeta\, g_{\theta\zeta} - B_\theta\, g_{\zeta\zeta}) \left(\frac{1}{\mathcal{J}} \frac{\partial \mathcal{J}}{\partial \theta} + \frac{1}{\sqrt{g^{ss}}} \frac{\partial \sqrt{g^{ss}}}{\partial \theta} + \frac{1}{B} \frac{\partial B}{\partial \theta} \right) \Bigg] \\ & + \; (B_\zeta\, g_{\theta\theta} - B_\theta\, g_{\theta\zeta}) \Bigg[g_{\theta\zeta} \frac{\partial B_\zeta}{\partial s} - g_{\zeta\zeta} \frac{\partial B_\theta}{\partial s} - g_{s\theta} \frac{\partial B_\zeta}{\partial \zeta} + g_{s\zeta} \frac{\partial B_\theta}{\partial \zeta} \\ & + \; B_\zeta \left(\frac{\partial g_{\theta\zeta}}{\partial s} - \frac{\partial g_{s\theta}}{\partial \zeta} \right) + B_\theta \left(\frac{\partial g_{s\zeta}}{\partial \zeta} - \frac{\partial g_{\zeta\zeta}}{\partial s} \right) \\ & + \; (B_\theta\, g_{\zeta\zeta} - B_\zeta\, g_{\theta\zeta}) \left(\frac{1}{\mathcal{J}} \frac{\partial \mathcal{J}}{\partial s} + \frac{1}{\sqrt{g^{ss}}} \frac{\partial \sqrt{g^{ss}}}{\partial s} + \frac{1}{B} \frac{\partial B}{\partial s} \right) \\ & + \; (B_\zeta\, g_{s\theta} - B_\theta\, g_{s\zeta}) \left(\frac{1}{\mathcal{J}} \frac{\partial \mathcal{J}}{\partial \zeta} + \frac{1}{\sqrt{g^{ss}}} \frac{\partial \sqrt{g^{ss}}}{\partial \zeta} + \frac{1}{B} \frac{\partial B}{\partial \zeta} \right) \Bigg] \\ & + \; (B_\zeta\, g_{\theta\zeta} - B_\theta\, g_{\zeta\zeta}) \Bigg[g_{s\theta} \frac{\partial B_\zeta}{\partial \theta} - g_{s\zeta} \frac{\partial B_\theta}{\partial \theta} - g_{\theta\theta} \frac{\partial B_\zeta}{\partial s} + g_{\theta\zeta} \frac{\partial B_\theta}{\partial s} \\ & + \; B_\zeta \left(\frac{\partial g_{s\theta}}{\partial \theta} - \frac{\partial g_{\theta\theta}}{\partial s} \right) + B_\theta \left(\frac{\partial g_{\theta\zeta}}{\partial s} - \frac{\partial g_{s\zeta}}{\partial \theta} \right) \\ & + \; (B_\theta\, g_{s\zeta} - B_\zeta\, g_{s\theta}) \left(\frac{1}{\mathcal{J}} \frac{\partial \mathcal{J}}{\partial \theta} + \frac{1}{\sqrt{g^{ss}}} \frac{\partial \sqrt{g^{ss}}}{\partial \theta} + \frac{1}{B} \frac{\partial B}{\partial \theta} \right) \\ & + \; (B_\zeta\, g_{\theta\theta} - B_\theta\, g_{\theta\zeta}) \left(\frac{1}{\mathcal{J}} \frac{\partial \mathcal{J}}{\partial s} + \frac{1}{\sqrt{g^{ss}}} \frac{\partial \sqrt{g^{ss}}}{\partial s} + \frac{1}{B} \frac{\partial B}{\partial s} \right) \Bigg] \Bigg\} \;, \end{aligned} \tag{3.40}$$

where $g_{\lambda\mu} \equiv \mathbf{e}_\lambda \cdot \mathbf{e}_\mu$ and $\mathcal{J} \equiv [\boldsymbol{\nabla} s \cdot (\boldsymbol{\nabla}\theta \times \boldsymbol{\nabla}\zeta)]^{-1}$ is the Jacobian of the transformation.

3.2.2 The VMEC equilibrium

The 3-Dimensional equilibrium state has been computed using the VMEC code. A preconditioned steepest-descent method [58, 59] is used to find the equilibrium. The (magnetic) poloidal angle is chosen to optimize the convergence. The (magnetic) toroidal angle is chosen to be the cylindrical azimuthal angle ($\zeta = \phi$). In VMEC, two flux surface quantities are prescribed [60, 61]. One is the net toroidal plasma current enclosed within each flux tube and the second is the plasma pressure profile. For all VMEC equilibria used in this thesis, the net toroidal current on each magnetic surface is zero and the pressure profile is of the form

$$p(s) = p(0)\ (1 - s)^2\ , \tag{3.41}$$

where $p(0)$ is the plasma pressure at the magnetic axis. The VMEC equilibrium code outputs the curvilinear components of the magnetic field, the Jacobian of the transformation as well as the cylindrical components of a set of magnetic surfaces in terms of Fourier series. Specifically, the position vector $\mathbf{r}$, on a given magnetic surface $s = \text{const}$, is written in cylindrical coordinates as

$$\mathbf{r} = R\ \cos\phi\ \hat{\mathbf{x}} + R\ \sin\phi\ \hat{\mathbf{y}} + Z\ \hat{\mathbf{z}}\ , \tag{3.42}$$

where $(\hat{\mathbf{x}}, \hat{\mathbf{y}}, \hat{\mathbf{z}})$ are the Cartesian unit vectors and

$$\begin{aligned} R &= \sum_{m=0}^{M} \sum_{n=-N}^{n=+N} R_{mn}\ \cos(\mu_{mn})\ , \\ Z &= \sum_{m=0}^{M} \sum_{n=-N}^{n=+N} Z_{mn}\ \sin(\mu_{mn})\ , \\ \phi &= \phi\ , \end{aligned} \tag{3.43}$$

where $\mu_{mn} \equiv m\theta + N_p n\phi$ and N_p is the number of field periods. The volume-averaged $\bar{\beta}$, M and N are free parameters. Using equations (3.42,3.43), we can compute the covariant basis vectors $\mathbf{e}_\mu$. In particular, $\mathbf{e}_\theta$ and $\mathbf{e}_\zeta$ are given in terms of Fourier series while $\mathbf{e}_s$ is obtained by using finite differences between neighboring

magnetic surfaces. Then we determine the Jacobian of the transformation using $\mathcal{J} = \mathbf{e}_s \cdot (\mathbf{e}_\theta \times \mathbf{e}_\zeta)$ and also the contravariant basis vectors $\nabla\lambda = \mathcal{J}^{-1}\epsilon_{\mu\tau\lambda}(\mathbf{e}_\mu \times \mathbf{e}_\tau)$, where $\epsilon_{\mu\tau\lambda}$ is the Levi-Civita symbol for permutations [29].

3.2.3 Visualization

In this section, we present the numerically-computed key attributes of four stellarators; these are the toroidal heliacs H1-NF [21, 44] and TJ-II [45], the modular stellarator WII-AS [46] and the Large Helical Device (LHD) [41]. We use AVS numerical techniques to visualize the magnetic field strength, the normal curvature, the geodesic curvature and the local magnetic shear on a magnetic surface of the above-mentioned stellarators.

The toroidal heliac H1-NF [21, 44] is a three-field period machine with an average major radius $\bar{R} = 1$ m and an average minor radius $\bar{a} = 0.22$ m. The equilibrium is computed with the following parameters: $M = 14$, $N = 7$, volume-averaged $\bar{\beta} = 0.36\%$ and on-axis magnetic field strength $B_0 = 1$ T. For reference, all the plots presented below are for the same magnetic surface at the radial position $s = 0.97$. This magnetic surface is very close to the last closed magnetic surface.

The top-view of the magnetic surface of H1-NF is shown in Figure 3.10. The magnetic field strength is displayed. The region of high B is colored in red, while the blue/green region corresponds to a region of low B. The 3-fold symmetry of H1-NF is visible. The dark blue patches on the outside of the magnetic surface are due to the field coils.

Figure 3.11 shows the magnetic field strength on the same surface as in Figure 3.10, but for a different viewing angle. The field coil effects are clearly visible. The magnetic field strength is large near the central ring conductor (red region). We refer to the red region in Figure 3.11 as the inboard side of the plasma.

The geodesic curvature, on the same magnetic surface as before, is shown in Figure 3.12. We note the details of κ_G on that surface. The green region indicates where the geodesic curvature is small (positive or negative).

Figure 3.13 shows the normal curvature. As in the case for κ_G (Figure 3.12), we note the detailed structure of κ_N in the magnetic surface. The region of favorable

curvature is colored in yellow and red, while the region of unfavorable curvature is colored in blue and light green. We note the similarity between the normal curvature and the magnetic field strength (Figure 3.11).

The local magnetic shear is shown in Figure 3.14. The local magnetic shear is small over the entire magnetic surface. A large fraction of the surface has $\mathcal{S} \simeq 0$ (green region). A small ribbon (colored in red) indicates where the LMS is relatively stronger.

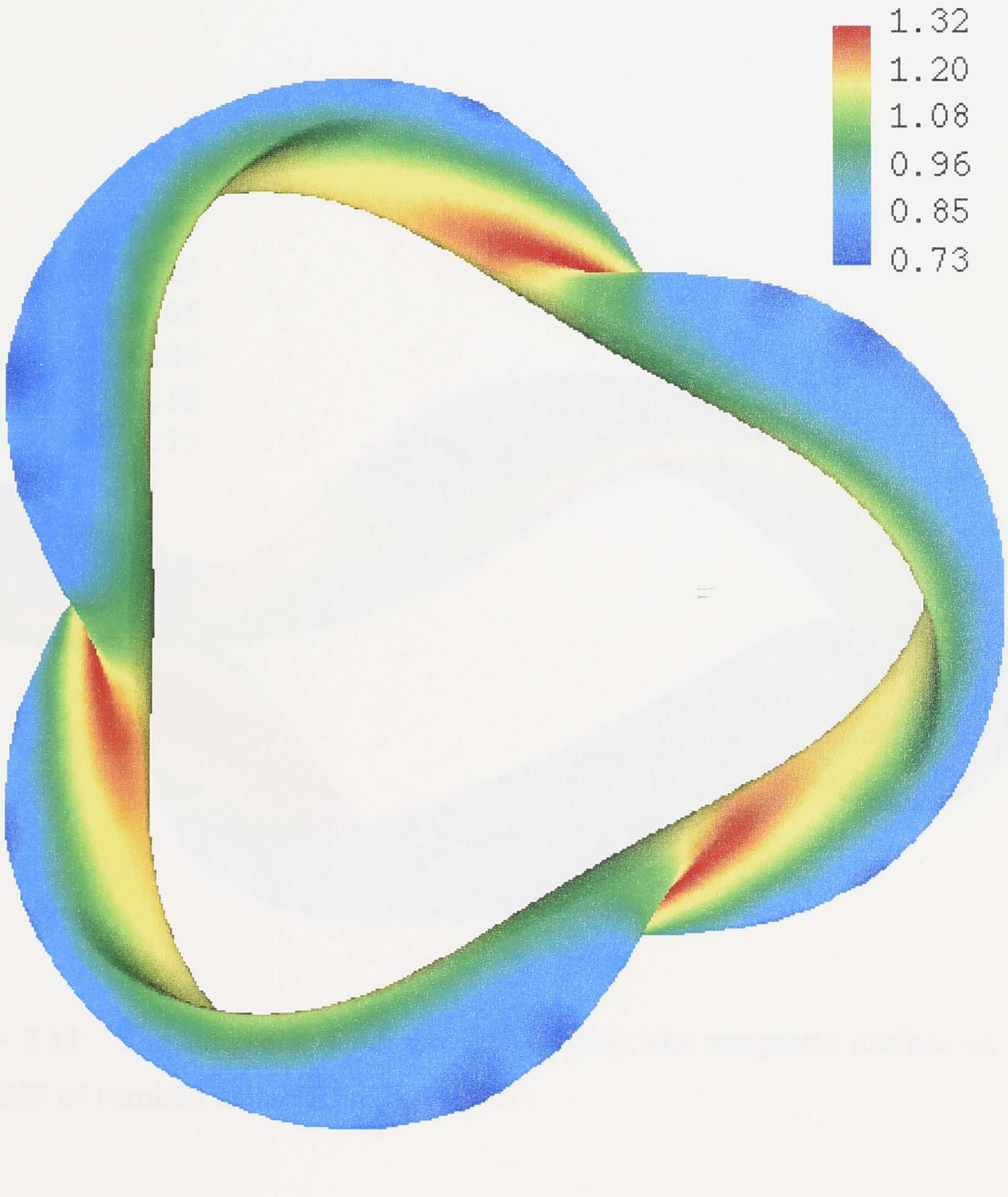

Figure 3.10: Top-view of the 3 field period, toroidal heliac H1-NF. The magnetic field strength (T) on the magnetic surface at $s = 0.965$ is shown.

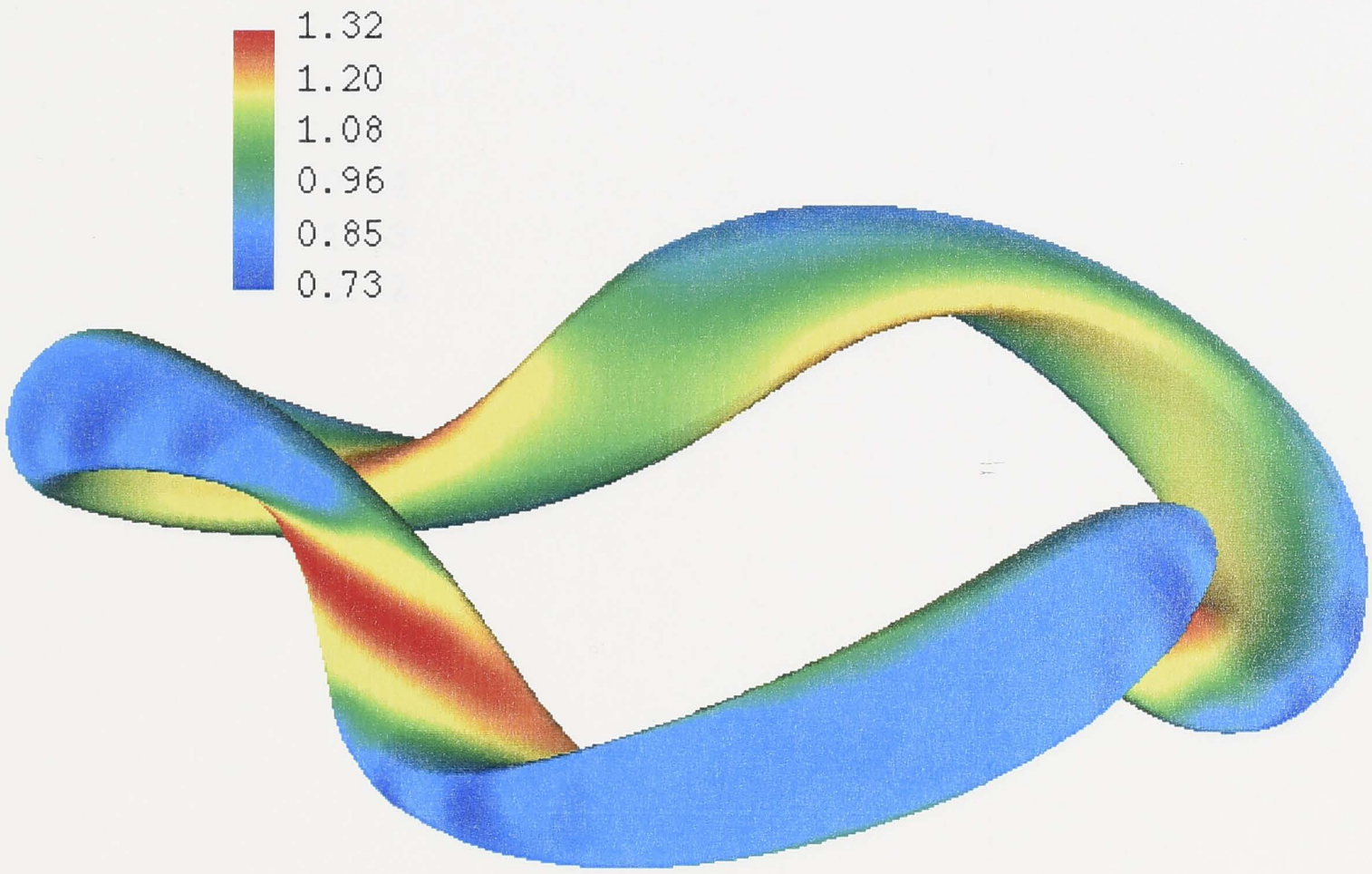

Figure 3.11: The magnetic field strength (T) on the magnetic surface at $s = 0.965$ of toroidal heliac H1-NF.

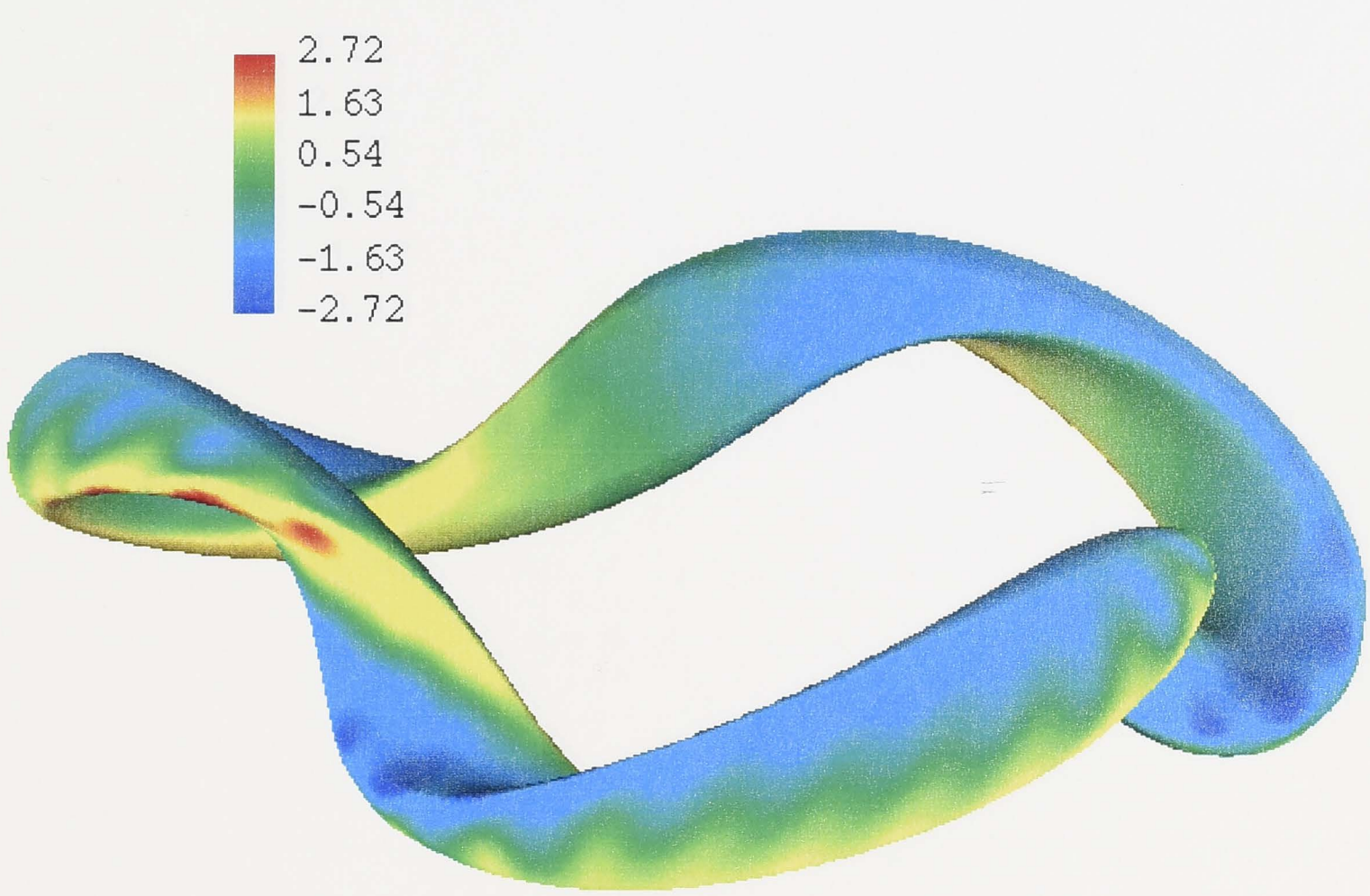

Figure 3.12: The geodesic curvature (m^{-1}) of the toroidal heliac H1-NF on the same magnetic surface as in Figure 3.11.

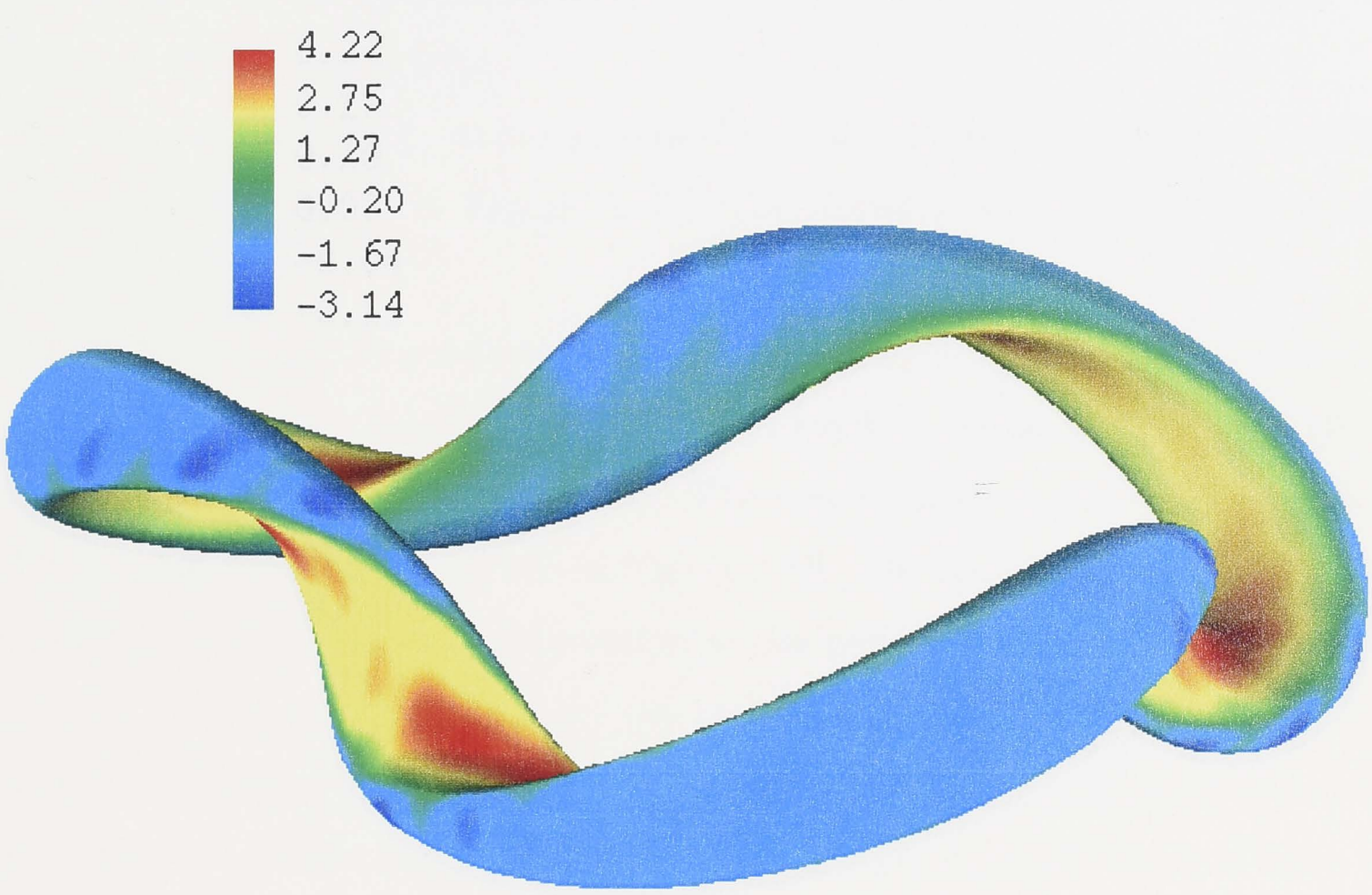

Figure 3.13: The normal curvature (m^{-1}) of the toroidal heliac H1-NF on the same magnetic surface as in Figure 3.11.

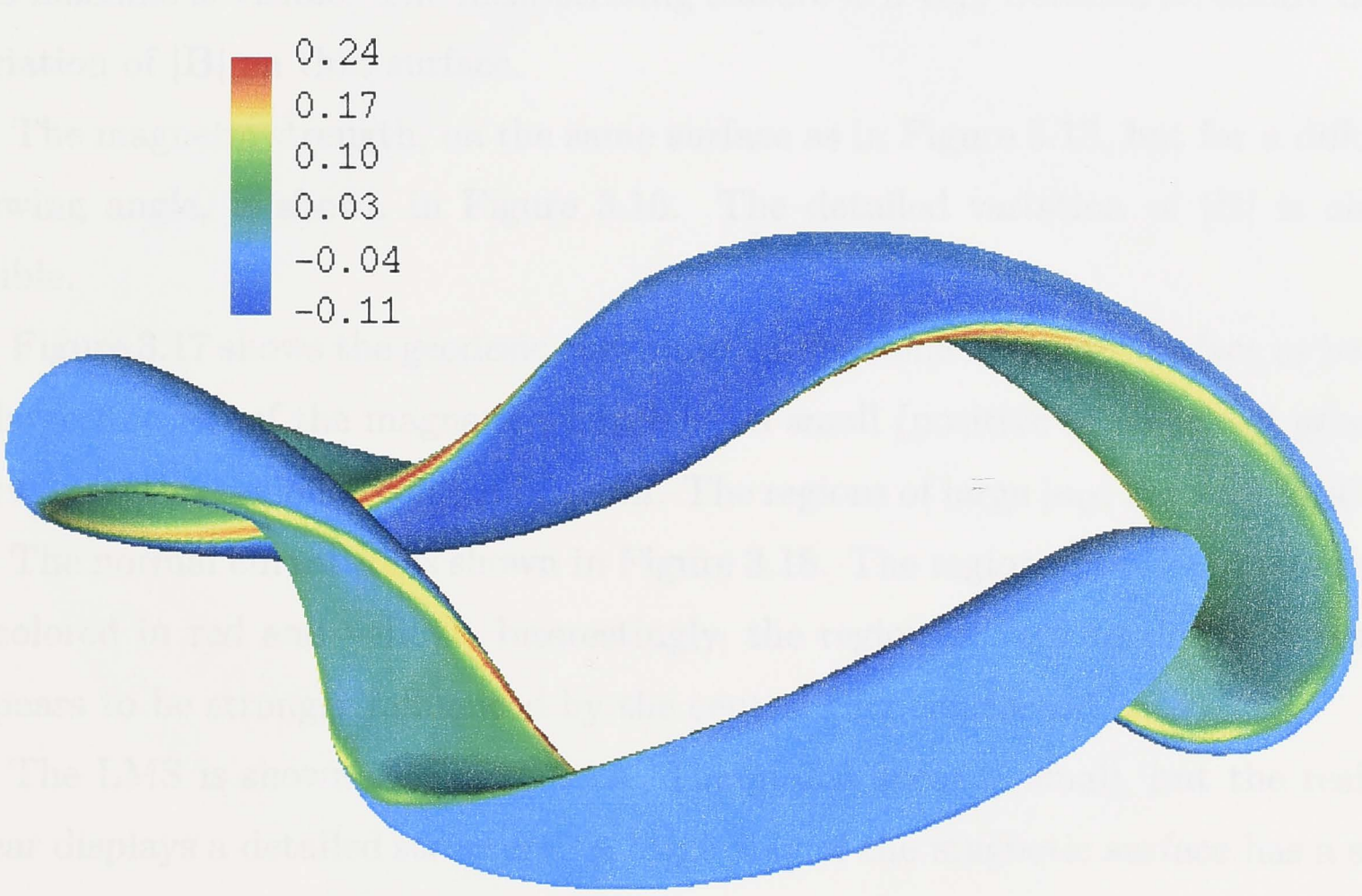

Figure 3.14: The local magnetic shear (m^{-3}) of the toroidal heliac H1-NF on the same magnetic surface as in Figure 3.11.

We now study another heliac, the 4-field period stellarator TJ-2 [45]. The main parameters of the machine are: average major radius $\bar{R} = 1$ m, average minor radius $\bar{a} = 0.25$ m and on-axis magnetic field strength $B_0 = 1$ T. These parameters are comparable to those of H1-NF. The equilibrium used here is computed with the following parameters: $M = 6$, $N = 12$ and volume-averaged $\bar{\beta} = 0.5\%$.

Figure 3.15 shows the top view of the magnetic surface $s = 0.97$ of the heliac TJ-2, where the coloring indicates the magnitude of $|\mathbf{B}|$. The 4-fold symmetry of this machine is visible. The most striking feature is a very detailed structure of the variation of $|\mathbf{B}|$ on that surface.

The magnetic strength, on the same surface as in Figure 3.15, but for a different viewing angle, is shown in Figure 3.16. The detailed variation of $|\mathbf{B}|$ is clearly visible.

Figure 3.17 shows the geodesic curvature for the same magnetic surface as before. A large fraction of the magnetic surface has a small (positive or negative) geodesic curvature; this region is colored in green. The regions of large $|\kappa_G|$ are very localized.

The normal curvature is shown in Figure 3.18. The region of favorable curvature is colored in red and yellow. Interestingly, the region of very favorable curvature appears to be strongly influenced by the central ring conductor.

The LMS is shown in Figure 3.19. The global shear is small, but the residual shear displays a detailed structure. A large area of the magnetic surface has a small positive LMS while the remaining area has a relatively strong negative shear.

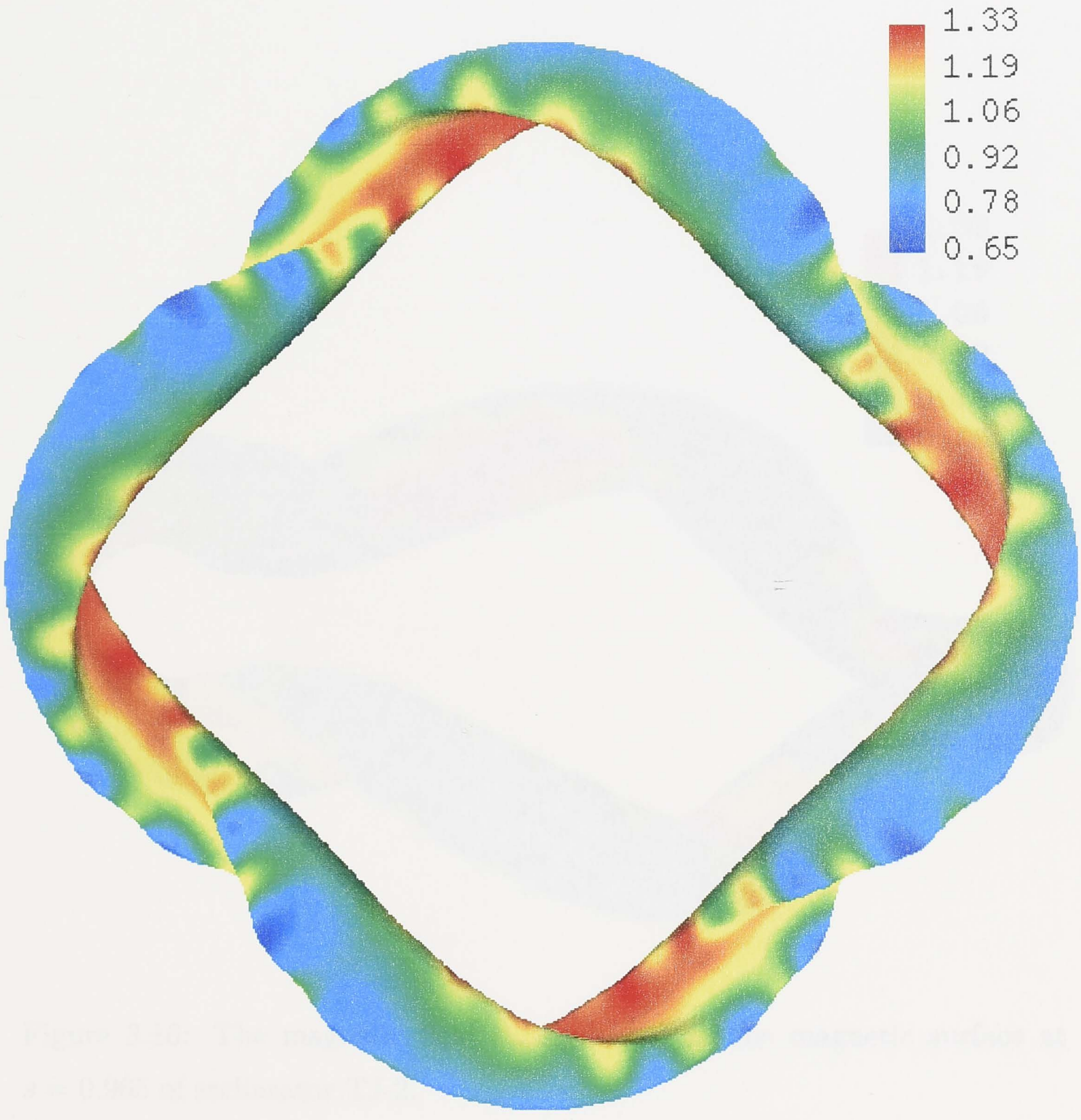

Figure 3.15: Top-view of the 4 field period stellarator TJ-2. The magnetic field strength (T) on the magnetic surface at $s = 0.965$ is shown.

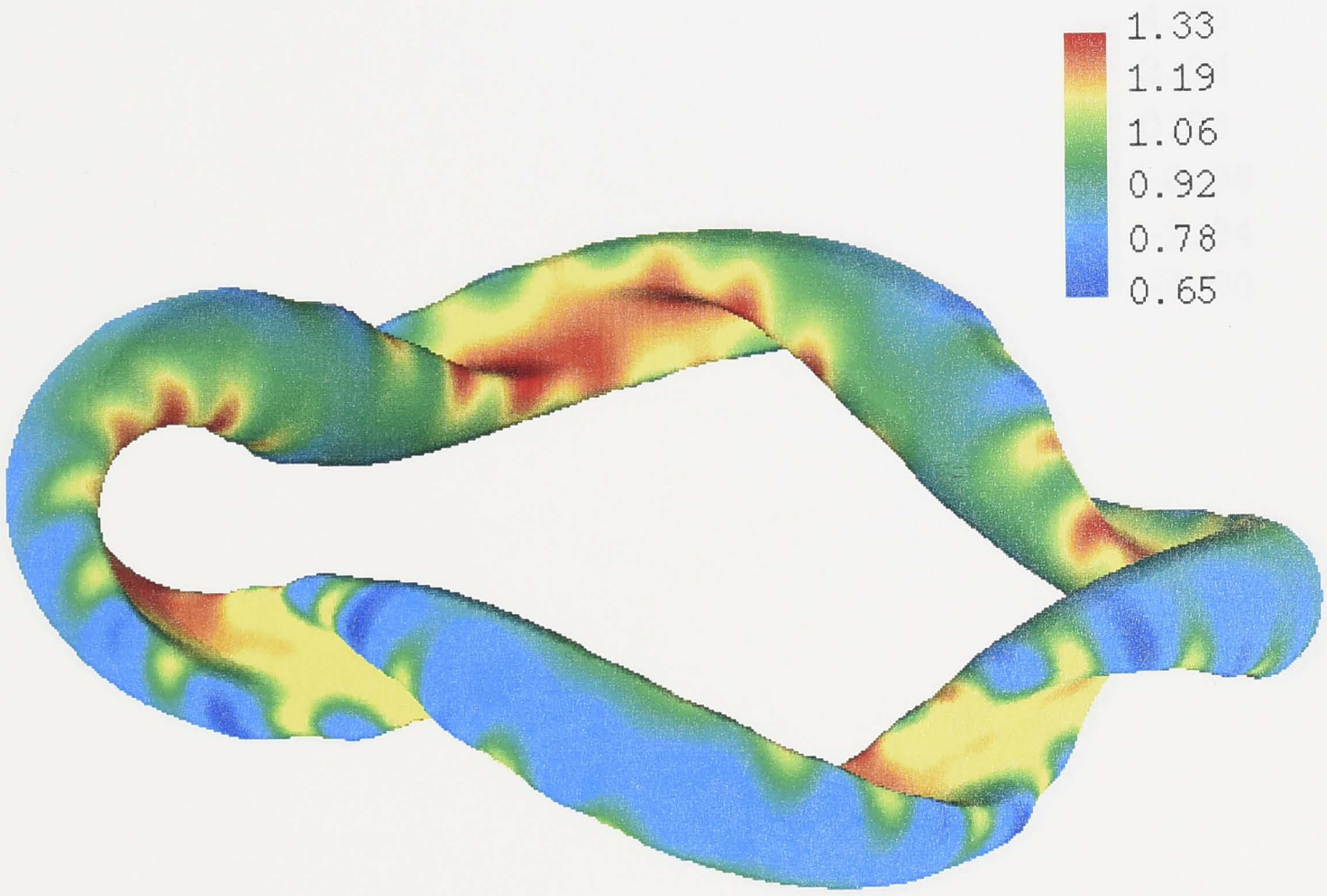

Figure 3.16: The magnetic field strength (T) on the magnetic surface at $s = 0.965$ of stellarator TJ-2.

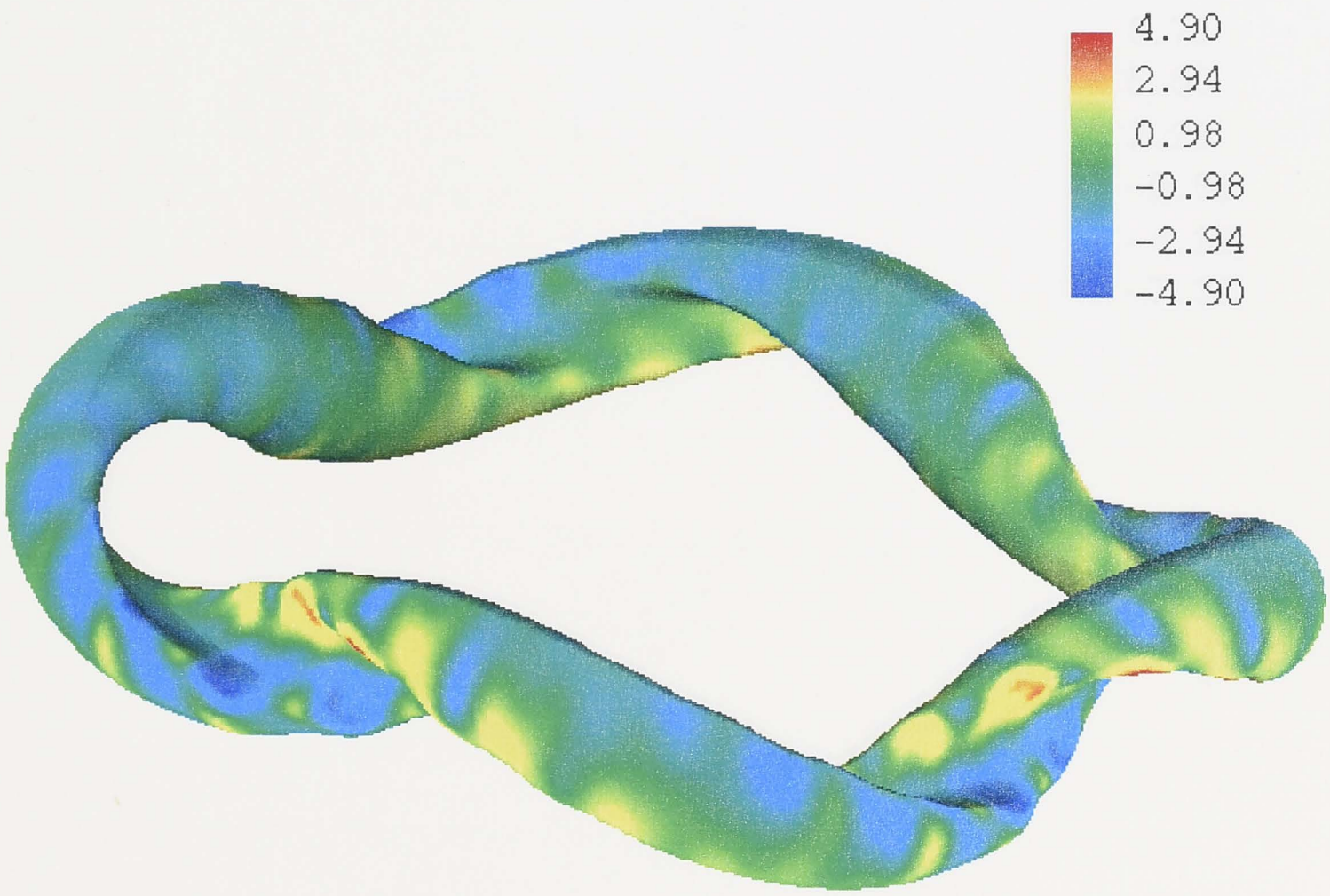

Figure 3.17: The geodesic curvature (m^{-1}) of the stellarator TJ-2 on the same magnetic surface as in Figure 3.16.

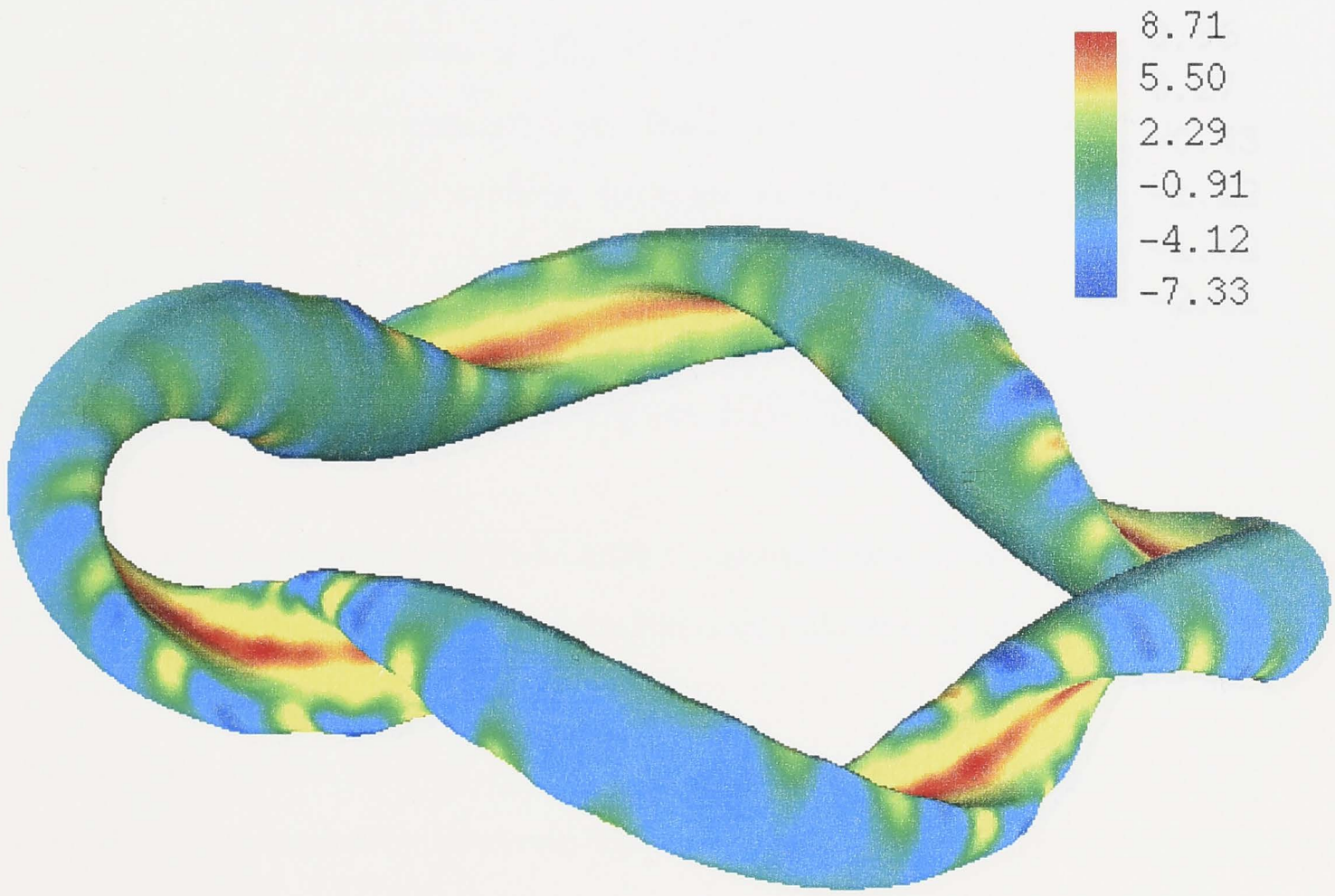

Figure 3.18: The normal curvature (m^{-1}) of stellarator TJ-2 on the same magnetic surface as in Figure 3.16.

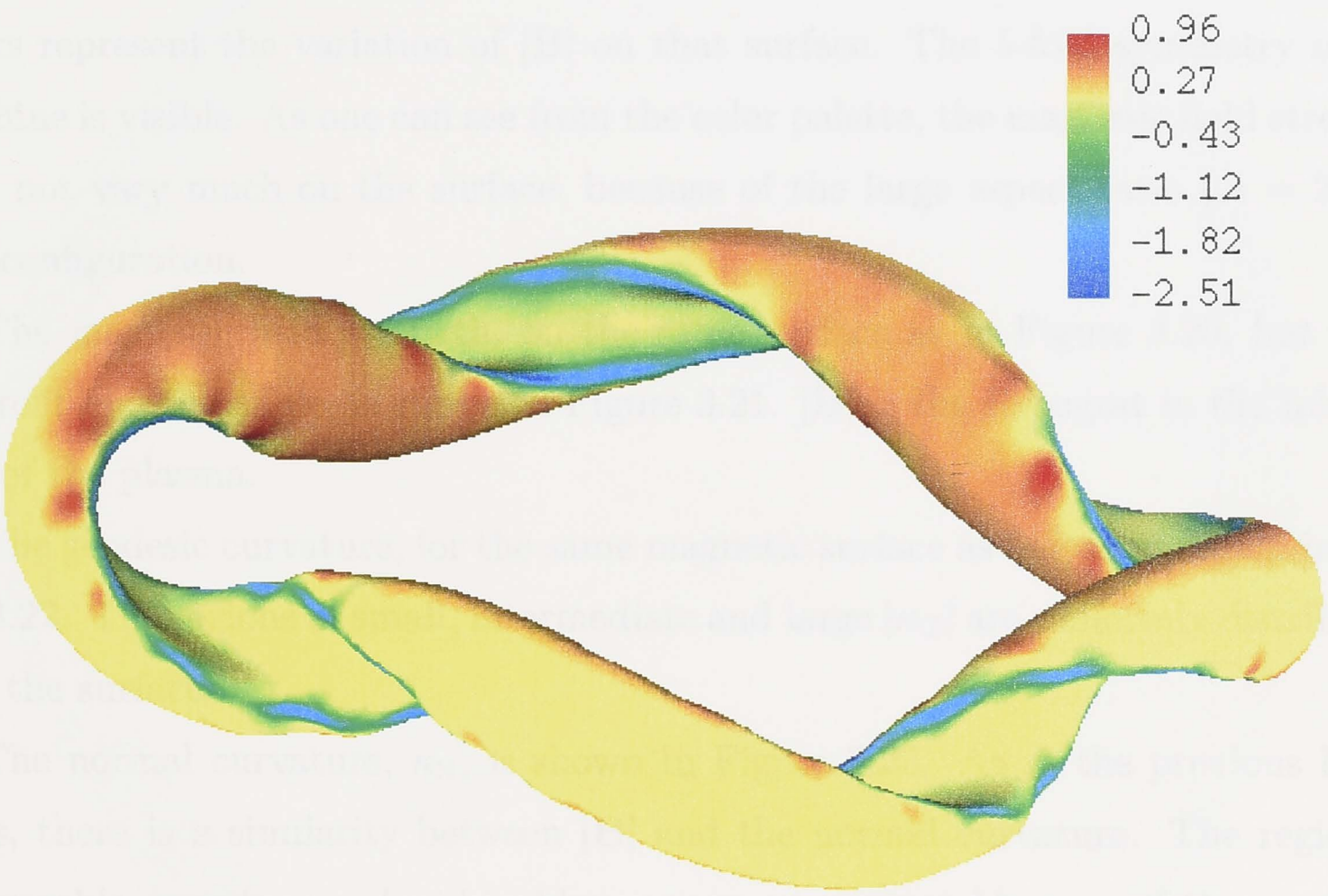

Figure 3.19: The local magnetic shear (m^{-3}) of the stellarator TJ-2 on the same magnetic surface as in Figure 3.16.

We now consider the modular stellarator Wendelstein 7-AS (W7-AS) [46]. This 5-field period stellarator has low shear, moderate rotational transform and a global magnetic well. The machine parameters are: average major radius $\bar{R} = 2.0$ m, average minor radius $\bar{a} = 0.2$ m and on-axis magnetic field strength $B_0 = 2.5$ T. The equilibrium is computed with the following parameters: $M = 3$, $N = 4$ and volume-averaged $\bar{\beta} = 0.65\%$.

The top-view of the magnetic surface of W7-AS is shown in Figure 3.20, where the colors represent the variation of $|\mathbf{B}|$ on that surface. The 5-fold symmetry of the machine is visible. As one can see from the color palette, the magnetic field strength does not vary much on the surface, because of the large aspect ratio ($A = 20$) of this configuration.

The magnetic field strength, on the same surface as in Figure 3.20, but for a different viewing angle, is shown in Figure 3.21. $|\mathbf{B}|$ is the strongest in the inboard side of the plasma.

The geodesic curvature, for the same magnetic surface as before, is shown in Figure 3.22. The regions of small, intermediate and large $|\kappa_G|$ are uniformly distributed over the surface.

The normal curvature, κ_N, is shown in Figure 3.23. As in the previous low-β cases, there is a similarity between $|\mathbf{B}|$ and the normal curvature. The region of unfavorable curvature, colored in blue, covers an appreciable area of the magnetic surface. However, the surface-averaged normal curvature is favorable.

The local magnetic shear is shown in Figure 3.24. A considerable area (yellow region) of the magnetic surface has negligible LMS. The strongest value of the LMS is located in the inboard side of the plasma.

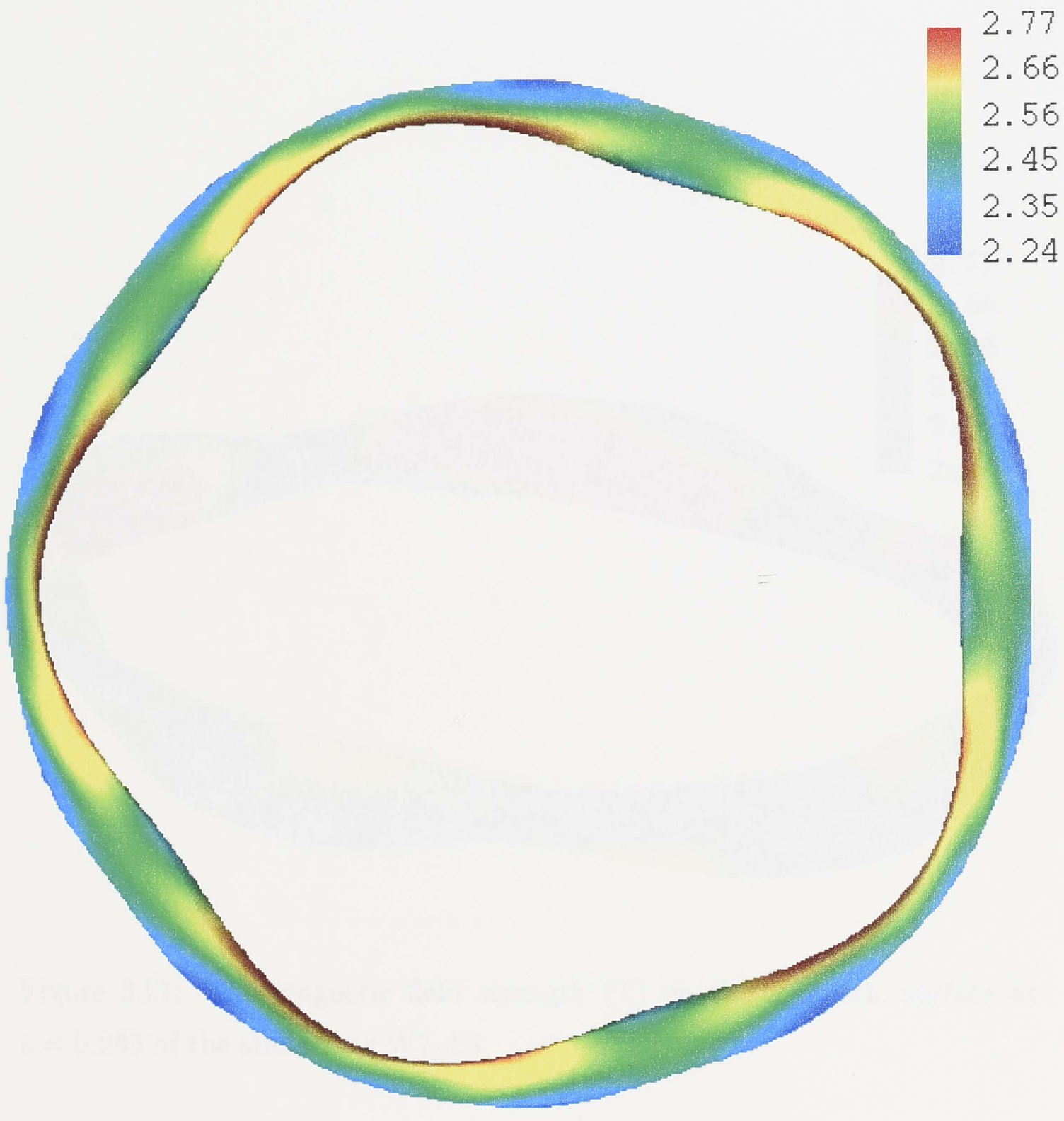

Figure 3.20: Top-view of the 5 field period stellarator W7-AS. The magnetic field strength (T) on the magnetic surface at $s = 0.965$ is shown.

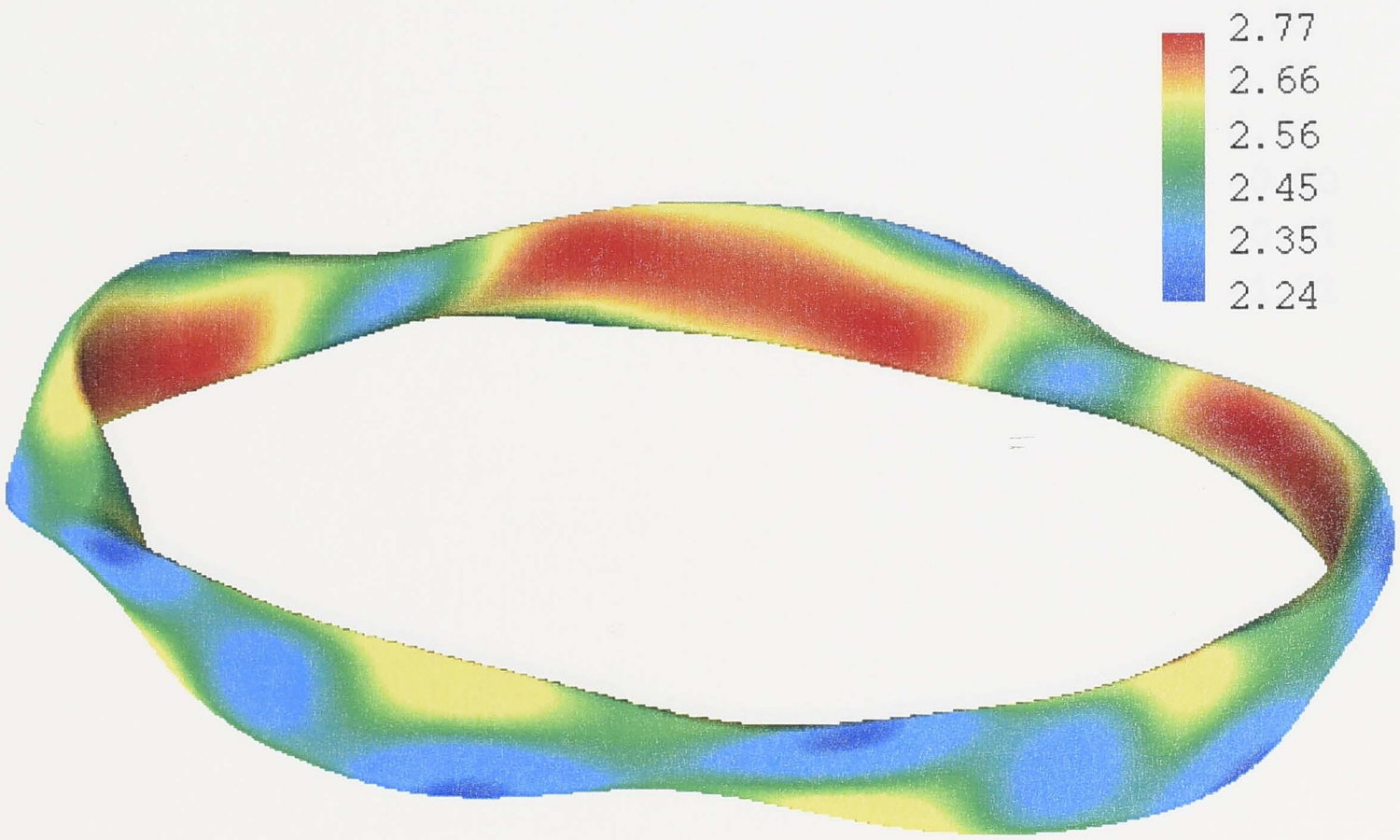

Figure 3.21: The magnetic field strength (T) on the magnetic surface at $s = 0.965$ of the stellarator W7-AS.

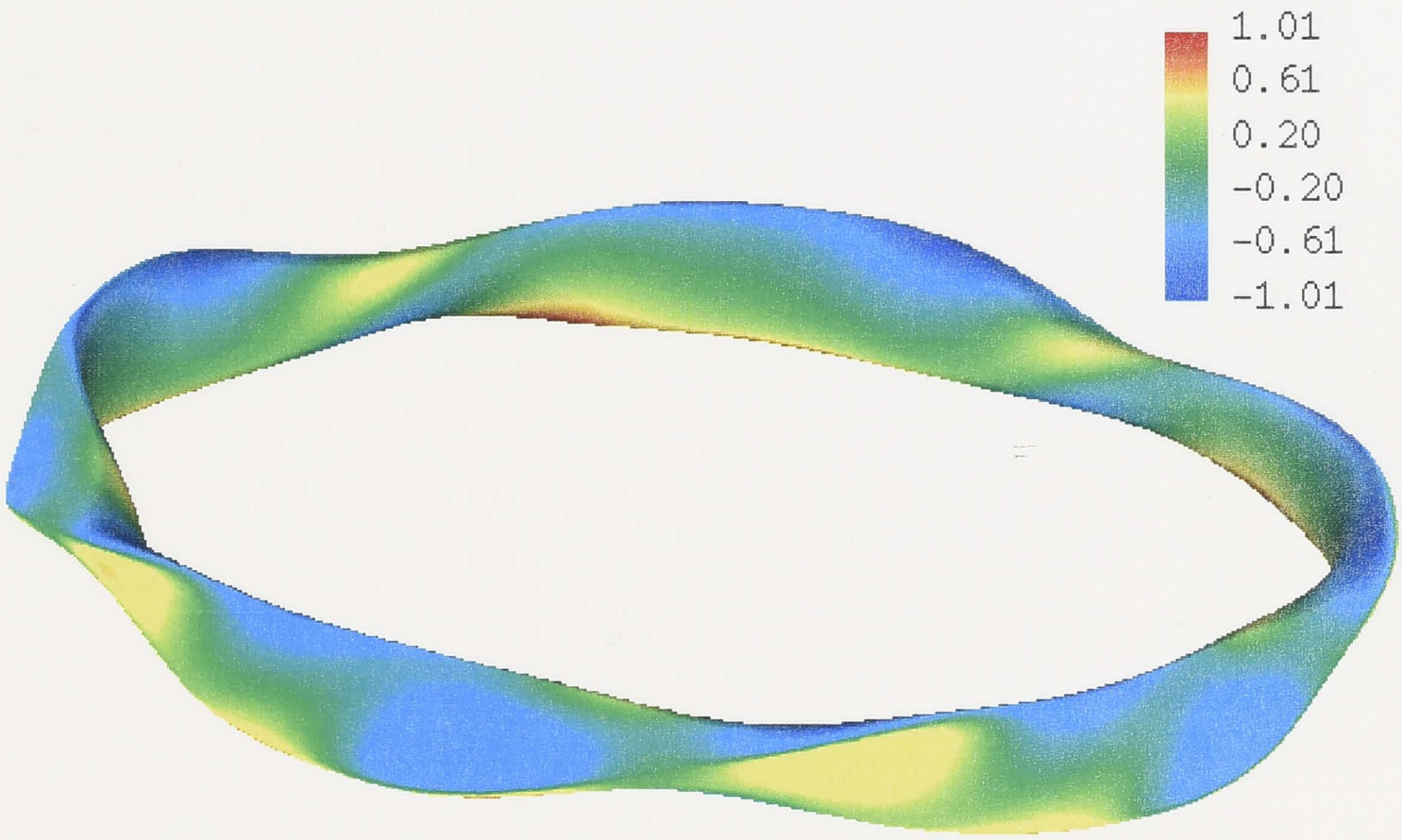

Figure 3.22: The geodesic curvature (m^{-1}) of the stellarator W7-AS on the same magnetic surface as in Figure 3.21.

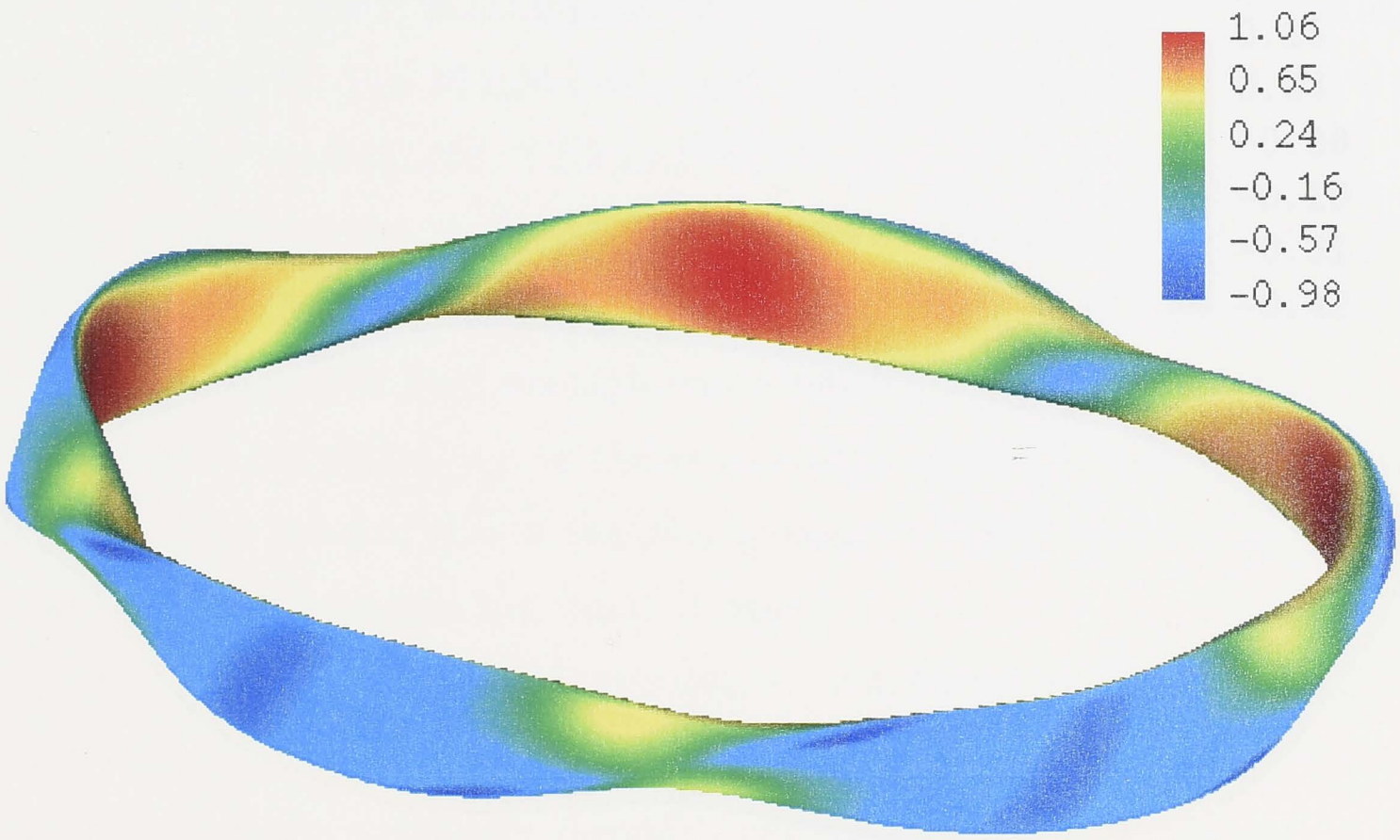

Figure 3.23: The normal curvature (m^{-1}) of stellarator W7-AS on the same magnetic surface as in Figure 3.21.

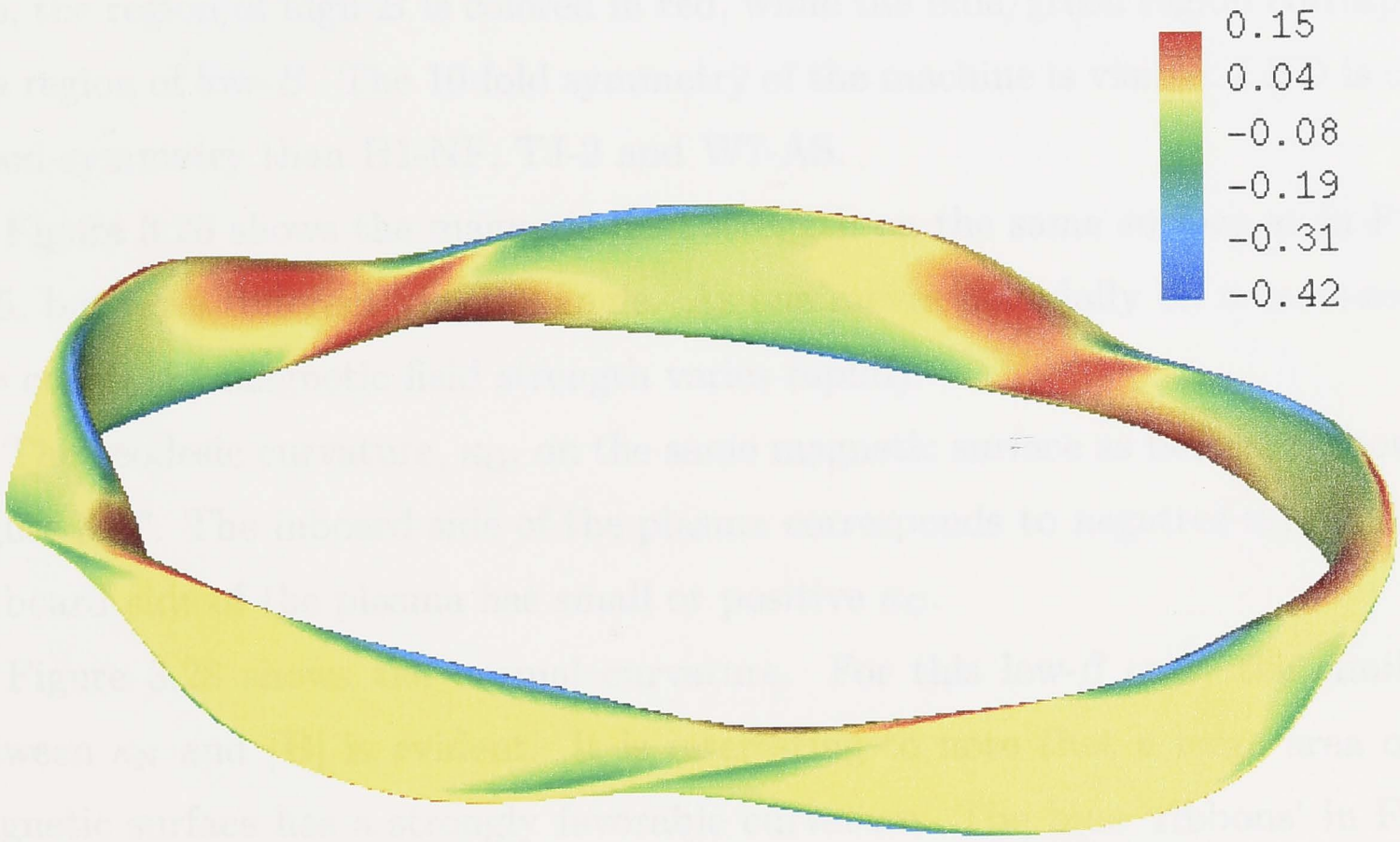

Figure 3.24: The local magnetic shear (m^{-3}) of the stellarator W7-AS on the same magnetic surface as in Figure 3.21.

We complete our study of the magnetic field structure of stellarator plasmas with the Large Helical Device (LHD) [41]. Unlike H1-NF, TJ-2 and W7-AS, LHD has a strong global shear. The Large Helical Device is a 10-field period torsatron with an average major radius $\bar{R} = 4$ m and an average minor radius $\bar{a} = 0.5$ m. The equilibrium is computed with the following parameters: $M = 5$ and $N = 6$, volume-averaged $\bar{\beta} = 0.23\%$ and on-axis magnetic field strength $B_0 = 4$ T.

The top-view of the magnetic surface of LHD is shown in Figure 3.25. As before, the region of high B is colored in red, while the blue/green region corresponds to a region of low-B. The 10-fold symmetry of the machine is visible. LHD is closer to axi-symmetry than H1-NF, TJ-2 and W7-AS.

Figure 3.26 shows the magnetic field strength on the same surface as in Figure 3.25, but for a different viewing angle. As one moves poloidally on a cross-section $\phi = \text{const}$, the magnetic field strength varies rapidly.

The geodesic curvature, κ_{G}, on the same magnetic surface as before, is shown in Figure 3.27. The inboard side of the plasma corresponds to negative κ_{G}, while the outboard side of the plasma has small or positive κ_{G}.

Figure 3.28 shows the normal curvature. For this low-β case, the similarity between κ_{N} and $|\mathbf{B}|$ is evident. It is interesting to note that a large area of the magnetic surface has a strongly favorable curvature. The blue 'ribbons' in Figure 3.28 show where the curvature is the most unfavorable.

Finally, the local magnetic shear is shown in Figure 3.29. Unlike the previous cases, most of the magnetic surface has a strong, negative LMS. The LMS is small over a small fraction of the magnetic surface, as indicated by the green 'ribbons' in Figure 3.29.

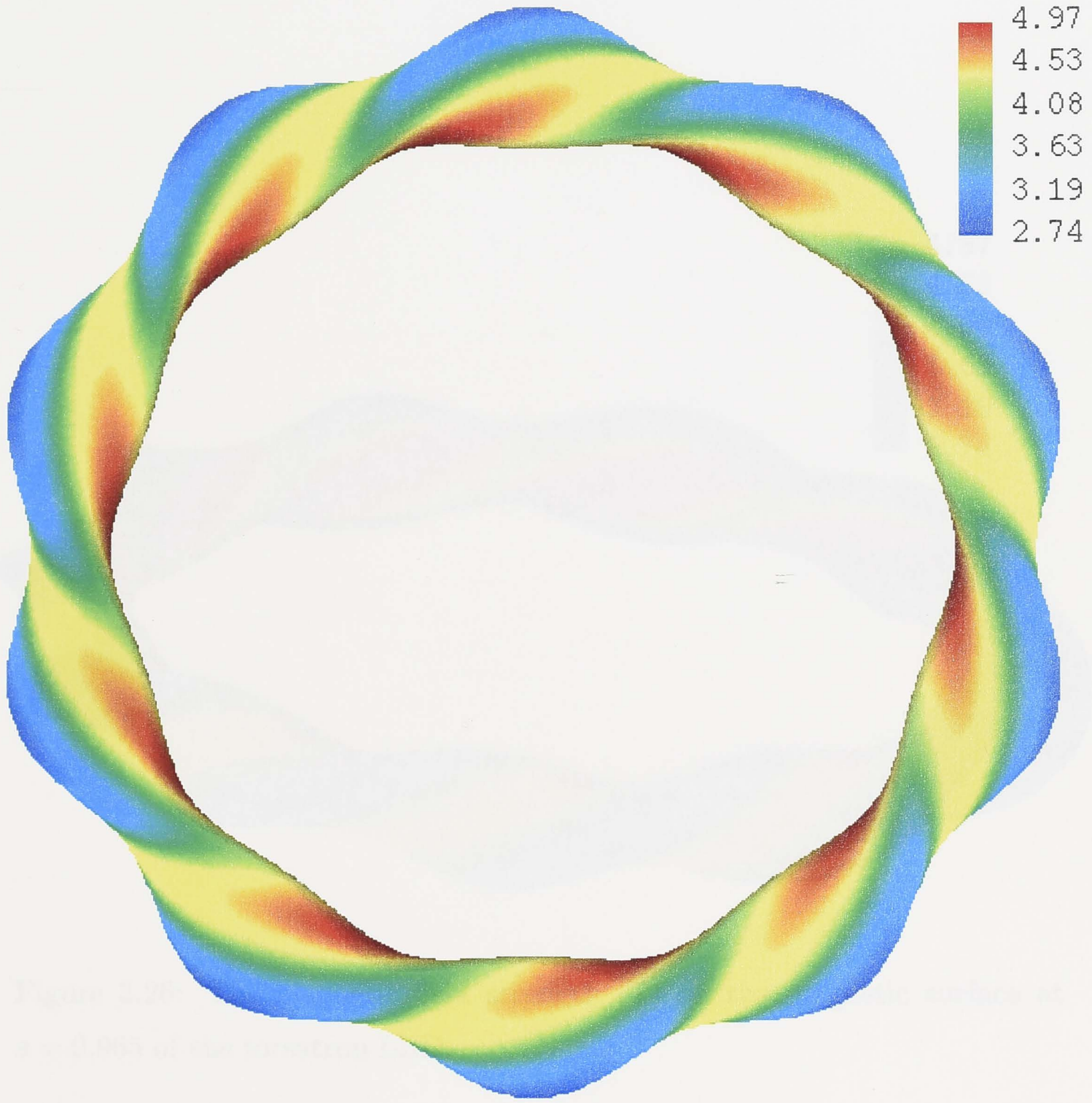

Figure 3.25: Top-view of the 10 field period torsatron LHD. The magnetic field strength (T) on the magnetic surface at $s = 0.965$ is shown.

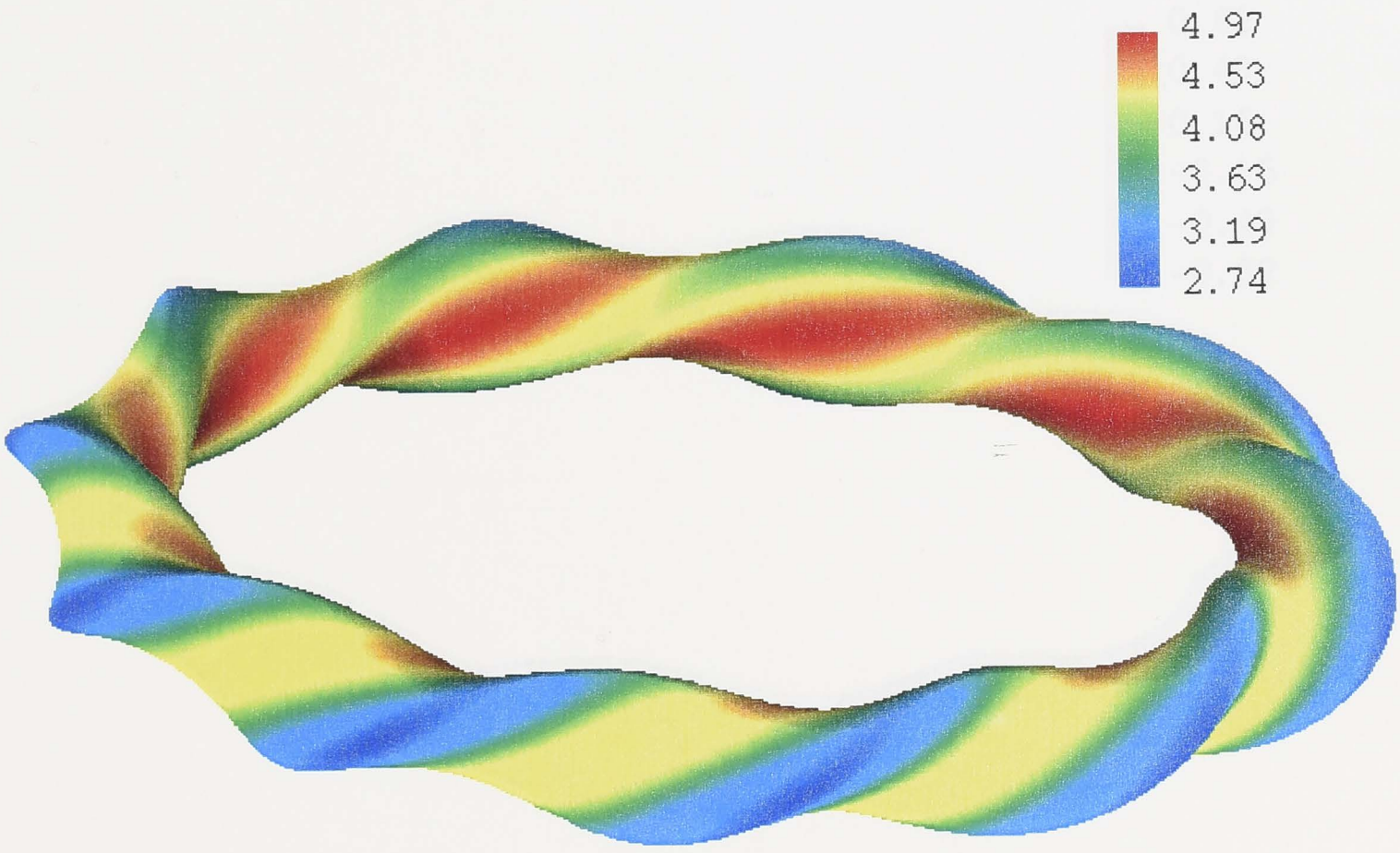

Figure 3.26: The magnetic field strength (T) on the magnetic surface at $s = 0.965$ of the torsatron LHD.

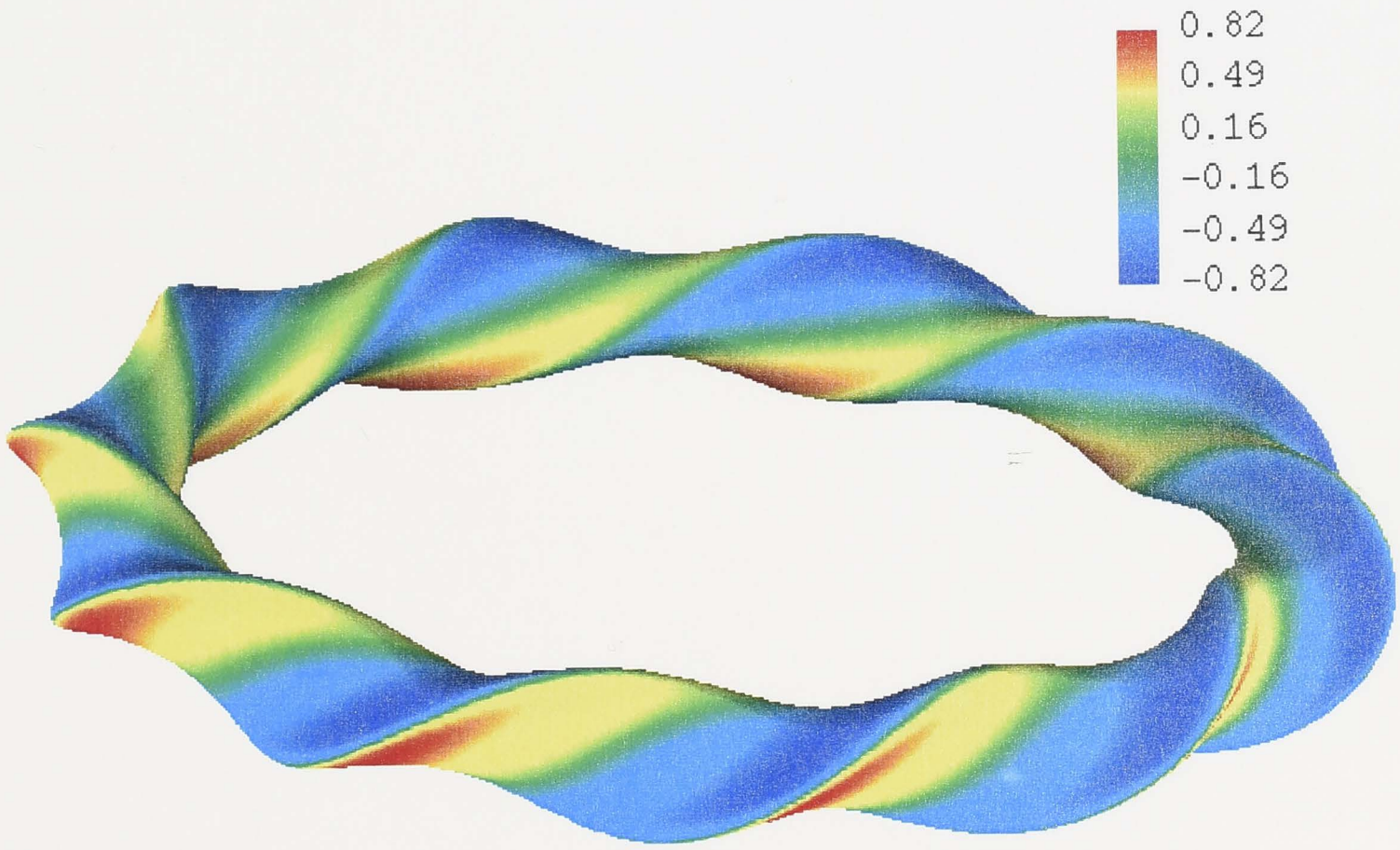

Figure 3.27: The geodesic curvature (m^{-1}) of the torsatron LHD on the same magnetic surface as in Figure 3.26.

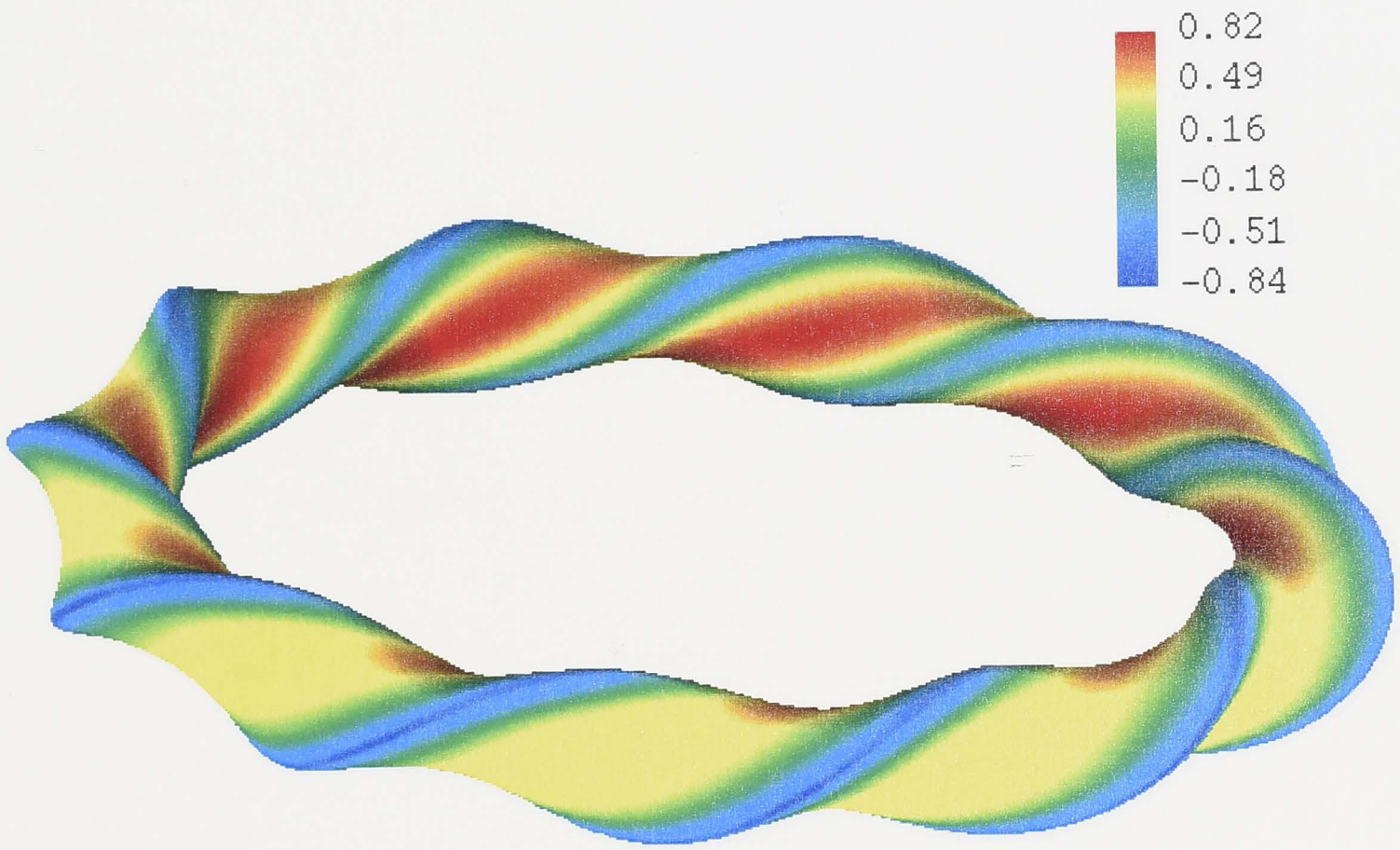

Figure 3.28: The normal curvature (m^{-1}) of the torsatron LHD on the same magnetic surface as in Figure 3.26.

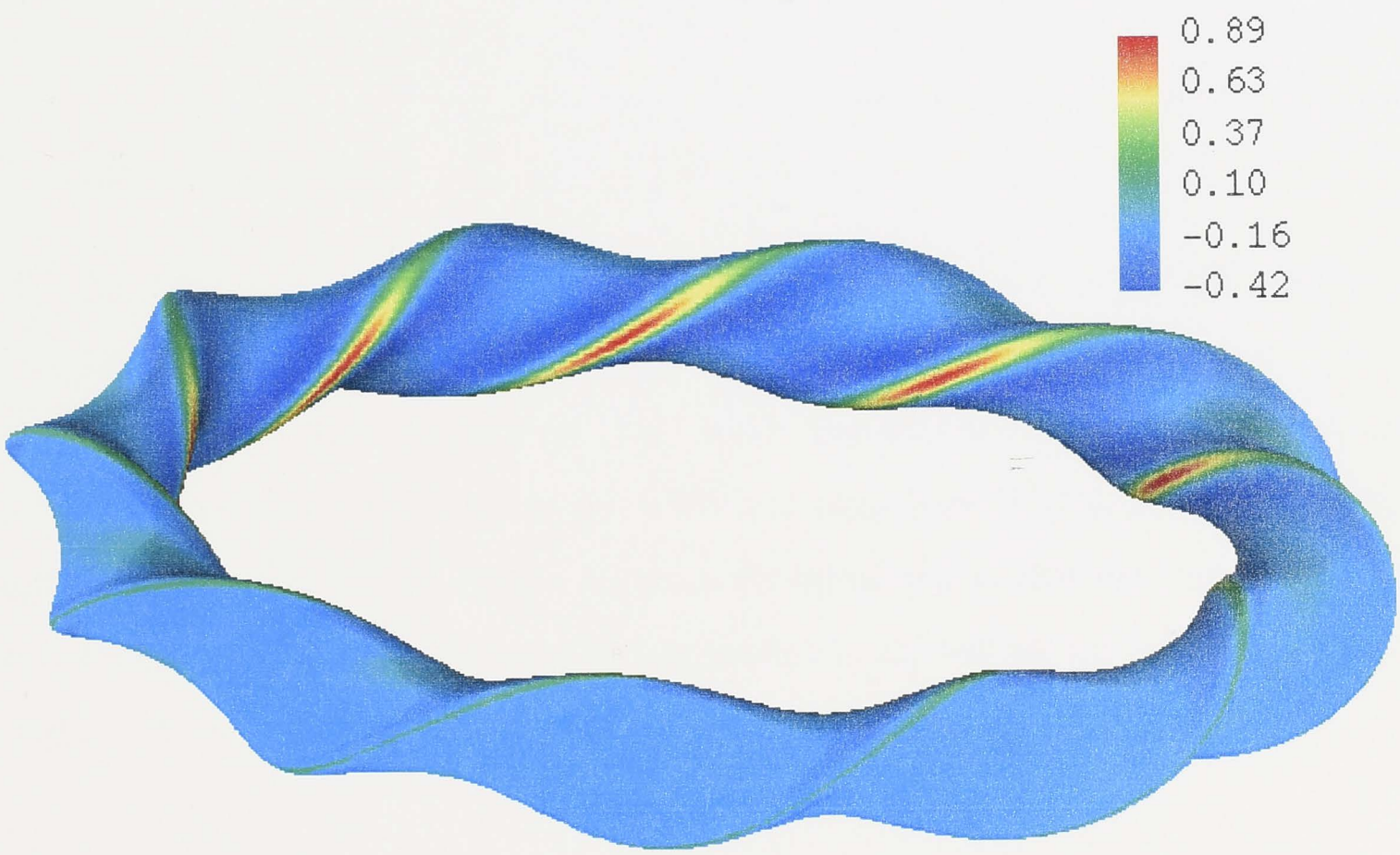

Figure 3.29: The local magnetic shear (m^{-3}) of the torsatron LHD on the same magnetic surface as in Figure 3.26.

In this chapter, we have studied the magnetic field key attributes of a low-β tokamak plasma and four stellarator plasmas. In the low-β tokamak configuration, it has been shown that the reversed-shear configuration leads to the formation of a large region of negative LMS where the normal curvature is unfavorable. This can yield an improvement in the tokamak performance. The magnetic field key attributes of four stellarators have been computed numerically. Numerical results were displayed in physical space and compared.

CHAPTER 4

Drift Wave Models

4.1 Introduction

In this chapter, we discuss possible fluid models to study drift waves in 3-Dimensional magnetic geometry. Only two fluid models are presented. One uses a set of simplified fluid equations [13], while the second one, the cold ion model, is obtained from the collisionless gyro-kinetic equation. Using the ballooning representation [57, 62, 63], a single eigenmode equation is derived for both models. The eigenmode equation of the cold ion model is solved for an helically-symmetric configuration and the drift wave spectrum is presented [3].

The plasma collisionality is a crucial factor that has to be taken into account when selecting a particular drift wave model. The relevant parameter is the collisional parameter $\nu_{\star j} \equiv \omega_{\mathrm{b}j}/\nu_j$, where $\omega_{\mathrm{b}j}$ is the bounce frequency, ν_{j} is the effective collision frequency and the subscript j labels the particle species. In a large fusion experiment, the plasma can be divided into 5 regions. The division below depends of course on the plasma parameters (density and temperature). The core plasma is in the collisionless regime, $\nu_{\star j} \gg 1$ (region I). Collisionless drift waves [64] can be destabilized here. The collisionless gyro-kinetic model can be used for this region. As one moves away from the magnetic axis, the ion population enters the banana regime $\nu_{\star \mathrm{i}} = \mathcal{O}(1)$ (region II). The trapped-ion instability [65, 66, 67] can be driven unstable in this region. Further away from the magnetic axis, the electron population enters the banana regime $\nu_{\star \mathrm{e}} = \mathcal{O}(1)$ (region III). The dissipative

trapped-electron mode [68, 69] and the trapped-electron mode [65, 70, 71] can be destabilized in this region. Closer to the vessel wall, the plasma is in the collisional regime $\nu_{\star i} \ll 1$ (region IV) and fluid equations can be used. The collision-driven drift wave [72, 73, 74, 75, 76, 77] can be excited in the plasma edge. Finally, very close to the vessel wall (region V), neutral particles, charge-exchange, ionization and other atomic effects can destabilize the drift wave. For instance, the radiative drift instability [78] can be excited in this region.

In this thesis, the emphasis is put on retaining the details of the confining magnetic field. Therefore, the first logical step consists in considering simple physics models while retaining the 3-dimensional details of the geometry. In this context, two simple fluid models are discussed in the present chapter.

The second logical step is to consider more refined and, therefore, more complex physics models while still retaining the 3-dimensionality of the problem. The gyro-kinetic model is more difficult than the previous two models since it takes into account particle trapping and collisional effects in a self-consistent way. The gyro-kinetic model is considered in chapters 5 and 6.

This chapter is organized as follows. In section 4.2, a fluid model to study drift waves in 3-dimensional plasmas is derived. The quantities related to the confining magnetic field are discussed. The cold ion model is presented in section 4.3. The differences between the fluid model of section 4.2 and the CIM are discussed. Numerical simulations of electron drift waves in the cold ion approximation for a helically-symmetric configuration are given in section 4.3.

4.2 The fluid approach

In this section, we derive a simple model to study drift waves in 3-dimensional plasmas. Braginskii fluid equations [13] are used and an eikonal representation for fluctuating quantities is assumed. An eigenmode equation, defined along the magnetic field, is derived. The curvature-driven contributions in the eigenmode equation are discussed.

4.2.1 Model equations

We consider a low-β, magnetized plasma with cold, singly-charged ions. Such a plasma is usually found near the edge of confinement devices. Ionization and charge-exchange can be effective in destabilizing the drift waves in edge plasmas [78], but ionization, charge-exchange, neutral drive and similar effects are neglected here.

The plasma is assumed to be in the collisional regime so that particle trapping and de-trapping effects are not important. We assume that the characteristic perpendicular wavelength of the drift wave is much larger than the ion thermal gyro-radius. Furthermore, the parallel wavelength of the mode is assumed to be much larger than the electron mean free path. When the above two requirements are fulfilled, the use of a fluid theory is valid [13]. The characteristic drift-wave wavelength is much larger than the Debye length so that, to a very good approximation, the plasma is quasineutral. For simplicity, we neglect collisional effects such as resistive and viscous effects. The heat transport, both for the ions and the electrons, is entirely neglected. We shall point out, however, that these *nonideal* effects are important for drift waves in a collisional plasma. For example, finite parallel resistivity and electron heat transport can drive the drift wave unstable [79]. Viscous effects, which arise from finite Larmor radius (FLR) effects, are usually stabilizing.

The magnetic field is written in straight-field-line coordinates [29]

$$\mathbf{B} = \dot{\psi} \boldsymbol{\nabla} \alpha \times \boldsymbol{\nabla} s \,, \tag{4.1}$$

where $\alpha \equiv \zeta - q\theta$ is the field line label and $2\pi\psi(s)$ is the poloidal magnetic flux enclosed within $s \equiv \Psi/\Psi_{\mathrm{b}}$. Here Ψ is the enclosed toroidal magnetic flux and Ψ_{b} is Ψ evaluated at the plasma boundary. By construction, the normalized radial label s ranges from 0 (at the magnetic axis) to 1 (at the plasma boundary). A dot denotes a derivative with respect to s.

Our basic model equations are the ion continuity equation

$$\frac{\partial n_{\mathrm{i}}}{\partial t} + \boldsymbol{\nabla} \left(n_{\mathrm{i}} \mathbf{v}_{\mathrm{i}} \right) = 0 \,, \tag{4.2}$$

and the ion momentum equation

$$m_{\rm i} n_{\rm i} \left(\frac{\partial}{\partial t} + \mathbf{v}_{\rm i} \cdot \boldsymbol{\nabla} \right) \mathbf{v}_{\rm i} = e n_{\rm i} \left(\mathbf{E} + \frac{\mathbf{v}_{\rm i} \times \mathbf{B}}{c} \right) . \tag{4.3}$$

In equations (4.2,4.3), $n_{\rm i}$ is the ion density, $\mathbf{v}_{\rm i}$ is the ion fluid velocity and $\mathbf{E}$ is the fluctuating electric field. Other symbols assume their usual meaning. For simplicity, equilibrium electric fields and plasma flows are neglected. On the right-hand side of the ion momentum equation (4.3), collisional and viscous effects have been neglected. For slow, drift-type modes the drift wave ordering

$$\frac{k_{||}}{k_{\perp}} \sim \frac{\omega}{\omega_{\rm ci}} \sim \frac{e\Phi}{T_{\rm e0}} \sim \epsilon \ll 1 . \tag{4.4}$$

is adopted. Here $k_{||}$ and $k_{\perp}$ are the characteristic parallel and perpendicular wavevectors, respectively. In a low-β plasma, the electric field can be written as $\mathbf{E} = -\boldsymbol{\nabla}\Phi$, where Φ is the electrostatic potential. The characteristic mode frequency ω is assumed to be much smaller than the ion cyclotron frequency $\omega_{\rm ci} \equiv eB/m_{\rm i}c$. Finally, $T_{\rm e0}$ is the equilibrium electron temperature. Taking the cross product of equation (4.3) with the unit parallel vector $\widehat{\mathbf{e}}_{||} \equiv \mathbf{B}/B$ and taking into account ordering (4.4), we get the ion cross-field drift velocity

$$\mathbf{v}_{\rm i\perp} = \mathbf{v}_{\rm E} + {\omega_{\rm ci}}^{-1} \widehat{\mathbf{e}}_{||} \times \frac{\partial \mathbf{v}_{\rm E}}{\partial t} , \tag{4.5}$$

where nonlinear terms and corrections of the order of $v_{\rm E}(\omega/\omega_{\rm ci})^2$ and higher have been neglected. The first term on the right-hand side of equation (4.5) is the lowest-order $\mathbf{E}\times\mathbf{B}$-drift velocity and it is the same for ions and electrons

$$\mathbf{v}_{\rm E} = \frac{c}{B^2} \, \mathbf{E}\times\mathbf{B} . \tag{4.6}$$

The second term on the right-hand side of equation (4.5) is the linear part of the ion polarization drift velocity. This term arises from the finite inertia of the ions. The parallel component of the ion fluid velocity is obtained by taking the scalar product of equation (4.3) with the unit vector $\widehat{\mathbf{e}}_{||}$ yielding

$$\frac{\partial v_{\rm i||}}{\partial t} = -\frac{e}{m_{\rm i}} \, \nabla_{||}\Phi . \tag{4.7}$$

Substituting (4.5) in the continuity equation (4.2) provides an equation for the plasma density, in the linear approximation

$$\begin{aligned} \frac{\partial n_{\rm i}}{\partial t} &= -n_0 \boldsymbol{\nabla}\cdot\mathbf{v}_{\rm E} - n_0 v_{\rm i||} \boldsymbol{\nabla}\cdot\widehat{\mathbf{e}}_{||} \\ &- \boldsymbol{\nabla} n_0 \cdot \mathbf{v}_{\rm E} - n_0 \nabla_{||} v_{\rm i||} - \frac{n_0 c}{B\omega_{\rm ci}} \, \frac{\partial}{\partial t} \, \boldsymbol{\nabla}\cdot\mathbf{E}_{\perp} , \end{aligned} \tag{4.8}$$

where n_0 is the equilibrium plasma density. The first two terms on the right-hand side of the above equation vanish in an homogeneous magnetic field. In the low-β approximation, the curvature-driven terms in the ion continuity equation are

$$\begin{aligned} \boldsymbol{\nabla}\cdot\mathbf{v}_{\mathrm{E}} &= -2\,\frac{\boldsymbol{\nabla}B}{B}\cdot\mathbf{v}_{\mathrm{E}}\,, \\ \boldsymbol{\nabla}\cdot\hat{\mathbf{e}}_{||} &= -\frac{\mathbf{B}\cdot\boldsymbol{\nabla}B}{B^2}\,. \end{aligned} \tag{4.9}$$

For modes with $k_{||}/k_{\perp} \ll 1$, a WKB representation can be used for fluctuating quantities [80]

$$\widetilde{n_{\mathrm{i}}} \equiv \frac{\delta n_{\mathrm{i}}}{n_0} = \widehat{n_{\mathrm{i}}}\exp\left(in\alpha - i\delta\right)\,\exp\left(-i\omega t\right)\,, \tag{4.10}$$

$$\widetilde{\Phi} \equiv \frac{e\Phi}{T_{\mathrm{e}0}} = \widehat{\Phi}\exp\left(in\alpha\right)\,\exp\left(-i\omega t\right)\,, \tag{4.11}$$

where $n \gg 1$ is the toroidal mode number, δn_{i} is the perturbed ion density and ω is the mode frequency. To lowest order in $1/n$, the perpendicular wavevector is $\mathbf{k}_{\perp} = n\boldsymbol{\nabla}\alpha$. $\widehat{n_{\mathrm{i}}}$ and $\widehat{\Phi}$ are the amplitudes of the (normalized) fluctuating ion density and electrostatic potential and vary slowly along the field line. Specifically we assume that the ordering $\bar{R}|\boldsymbol{\nabla}\widehat{\Phi}| \sim \bar{R}\,|\boldsymbol{\nabla}\widehat{n_{\mathrm{i}}}| = \mathcal{O}\left(1\right)$ is satisfied. $\bar{R}$ is the average radius of the magnetic axis. In equation (4.10), we have introduced a phase shift $|\delta| \ll 1$ in the representation for the fluctuating plasma density. In order to decouple the fluctuating and equilibrium parts in the ion continuity equation, we adopt the transport ordering for the equilibrium plasma density [81]

$$\frac{1}{n_0\omega_{\mathrm{ci}}}\frac{\partial n_0}{\partial t} = \mathcal{O}\left(\epsilon^3\right)\,. \tag{4.12}$$

The system of equations (4.7,4.8) relates the fluctuating parallel ion velocity, density and electrostatic potential. We have 2 equations [ie equations (4.7,4.8)] for 3 unknowns $(v_{\mathrm{i}||}, \Phi, n_{\mathrm{i}})$ so we need a closure relation in order to solve the problem. The closure relation is obtained by expanding the (small) phase shift in the representation for the fluctuating plasma density (4.8). Substituting equation (4.10) in equations (4.7,4.8) and taking into account the ordering (4.12), we obtain a single eigenmode equation for the amplitude $\widehat{\Phi}$

$$\frac{c_s^2}{\omega^2}\,\nabla_{||}^2\widehat{\Phi} = S_B^{||}\bar{R}\,\nabla_{||}\widehat{\Phi} - \frac{\omega_{\star\mathrm{e}0}}{\omega}\,\left(S_B^{\perp} + S_{\star}\right)\widehat{\Phi} - \left(1 + b\mathcal{L}_p - i\delta\right)\widehat{\Phi}\,. \tag{4.13}$$

Here $c_s \equiv \sqrt{T_{\rm e0}/m_{\rm i}}$ is the ion thermal velocity evaluated at the electron temperature, $b \equiv (k_\theta \rho_{s0})^2$ is a parameter of the order of unity, $k_\theta \equiv nq/\bar{a}$ is the characteristic perpendicular wavevector ($\bar{a}$ is the average radius of the last closed magnetic surface); $\rho_{s0} \equiv c_s/\omega_{\rm ci0}$; $\omega_{\rm ci0}$ is the ion cyclotron frequency evaluated at the magnetic axis; $\omega_{\star {\rm e}0} \equiv (cT_{\rm e0}k_\theta)/(eB_0 L_{\rm n})$ is the electron diamagnetic drift frequency where B_0 is the magnetic field strength at the magnetic axis and $L_{\rm n} \equiv -\bar{a}n_0/\dot{n}_0$ is the plasma density radial scalelength; finally $\nabla_{||}$ is the parallel gradient operator keeping the field line label constant. We have also introduced a set of non-dimensional quantities defined along the magnetic field line. These are:

$$S_B^{||} \equiv \bar{R}\,\frac{\mathbf{B}\cdot\boldsymbol{\nabla}B}{B^2} \quad , \tag{4.14}$$

which is related to the variation of B along the magnetic field line

$$S_B^{\perp} \equiv 2\,L_{\rm n}\frac{\boldsymbol{\nabla}B_\star}{B_\star^2}\cdot\left(\hat{\mathbf{e}}_{||}\times\hat{\mathbf{e}}_{\perp}\right) \quad , \tag{4.15}$$

which arises from the curvature of the magnetic field lines,

$$S_\star \equiv \bar{a}|\boldsymbol{\nabla}s|\,\frac{\hat{\mathbf{n}}\cdot\left(\hat{\mathbf{e}}_{||}\times\hat{\mathbf{e}}_{\perp}\right)}{B_\star} \quad , \tag{4.16}$$

which arises from the diamagnetic drift. Finally

$$\mathcal{L}_p \equiv \frac{\hat{\mathbf{e}}_{\perp}\cdot\hat{\mathbf{e}}_{\perp}}{B_\star^2} \quad , \tag{4.17}$$

comes from the divergence of the ion polarization drift velocity. In the above equations, $B_\star \equiv B/B_0 \sim 1$ is the normalized magnetic field strength, $\hat{\mathbf{e}}_{\perp} \equiv \mathbf{k}_{\perp}/k_\theta$ is the normalized perpendicular wavector and $\hat{\mathbf{n}} \equiv \boldsymbol{\nabla}s/|\boldsymbol{\nabla}s|$ is a unit vector normal to the magnetic surface. The functions $S_B^{||}$ and $S_B^{\perp}$ vanish in an homogeneous magnetic field. $S_{\rm B}^{||}$ is an oscillatory function but $S_B^{\perp}$ displays a secular behavior, in a configuration with non-zero global shear. It can be shown that $S_\star$ is constant along the magnetic field line (appendix D).

As we shall see in the next section, the eigenmode equation (4.13) is identical to the one obtained in the cold ion approximation, *except for the term involving the variation of B along the field line.* One can estimate the real and imaginary parts of the mode frequency. We can obtain an estimate of the real part of the mode

frequency, denoted ω_r, by balancing the left-hand side of equation (4.13) with the first term on the right-hand side. This yields $\omega_r \sim \omega_{||}$, where $\omega_{||} \equiv c_s/\bar{R}$ is the characteristic frequency associated with the parallel free streaming of the ions. The imaginary part of the mode, denoted γ, is approximately

$$\gamma \sim \delta \, \frac{\omega_{||}^2}{\omega_{\star \mathrm{e}}} \quad . \tag{4.18}$$

Clearly the mode will be driven unstable if the phase shift δ is positive. The eigenmode equation (4.13) can be solved using a shooting code, as discussed in section 4.4. The inhomogeneity of the magnetic field enters the eigenmode equation through $S_B^{||}$ and $S_B^{\perp}$. In a tokamak with circular magnetic surfaces, $S_B^{||}$ varies slowly along the field line. In a stellarator plasma, helical field coils induce a rapid variation of B along the field line. The curvature term $S_B^{\perp}$ can substantially modified the linear growth rate. After straightforward algebra, the curvature term can be written in a meaningful form

$$S_B^{\perp} = 2 \, \frac{\bar{a} B_0 L_{\mathrm{n}}}{q |\boldsymbol{\nabla} \psi|} \left[\kappa_{\mathrm{N}} - \frac{|\boldsymbol{\nabla} \psi|^2}{B} \, \kappa_{\mathrm{G}} \left(\bar{\mathcal{R}} + \frac{dq}{d\psi} \, \theta \right) \right] \, , \tag{4.19}$$

where we have made use of the low-β approximation, $\boldsymbol{\kappa} \simeq \boldsymbol{\nabla}_{\perp} B/B$. Here κ_{N} and κ_{G} are the normal and geodesic components of the magnetic curvature, respectively, and $\bar{\mathcal{R}}$ is the integrated residual shear [19]. The secular part in $S_B^{\perp}$ appears in the last term in the square bracket. If we choose ζ, the extended toroidal angle, as the position label along the magnetic field line, one can study the various contribution in the square brackets of equation (4.19) as one moves along the field line. For simplicity, we consider the specific case of the H1-NF [21] configuration at the symmetry plane $\phi = 0$. The point of reference at which the along-the-field-line integration is started is chosen to be $\theta_0 = \zeta_0 = 0$. The toroidal angle at which the secular behavior of $S_B^{\perp}$ becomes important can be estimated by considering the WKB perpendicular wavevector

$$\begin{aligned} \mathbf{k}_{\perp} &= n \boldsymbol{\nabla} \alpha \\ &= n \left(\boldsymbol{\nabla} \zeta - q \boldsymbol{\nabla} \theta - \dot{q} \theta \boldsymbol{\nabla} s \right) \, . \end{aligned} \tag{4.20}$$

Clearly for $\zeta \geq q/\dot{q}$ the *secular* part of $\mathbf{k}_{\perp}$ dominates over the remaining *periodic* contributions. For H1-NF, typical values are $|\dot{q}| \approx 0.1$ and $q \approx 1$ so that $\zeta_{\mathrm{c}} \approx 10$.

Therefore the secular behavior of $\mathbf{k}_\perp$ becomes important approximately after one transit around the machine.

For $\zeta \simeq 0$, the geodesic curvature is negligible while the normal curvature is destabilizing. As ζ increases, κ_N becomes less unfavorable and the interaction between the integrated local shear and the geodesic curvature becomes important. For $\zeta \gg \zeta_c$, the term involving the global shear and the geodesic curvature dominates.

The stabilizing effect of the global magnetic shear can be understood as follows. If the global shear is small, $|\dot{q}| \ll 1$, then the normal curvature will drive the mode, since the last term in the square brackets of equation (4.19) does not play a decisive role. In the strong global shear case, $|\dot{q}| \gg 1$, the coupling between the geodesic curvature and the global shear will be very effective in balancing the destabilizing influence of the normal curvature.

It is worth noting that the combination between the normal curvature, the geodesic curvature, the global shear and the integrated residual shear, as given in the square brackets of equation (4.19), enters the high-n ballooning equation [17], the curvature drift term in the cold ion approximation (section 4.3) and in the gyrokinetic model (chapter 6). This is not surprising: all the above-mentioned models make use of the eikonal representation (4.10) and, therefore, the curvature drive enters in a very similar way in each model. In the next section we study the gyrokinetic equation in the cold ion approximation. As it turns out, the final eigenmode equation is very similar to the one obtained in the present section.

Using fluid equations, we have derived a simple model for studying drift waves in arbitrary plasma geometry. Here, for simplicity, we have neglected resistive and viscous effects in the fluid equations. However, one can retain such effects in the model without difficulty (An example is given in section 6.3). The advantage of using fluid equations for studying drift waves is more apparent when one is interested in the nonlinear regime [75, 76, 77]. For instance, if we neglect the curvature terms ($S_B^{||} = S_B^{\perp} = 0$) and the parallel component of the ion velocity, but retain the *nonlinear* part of the ion polarization drift velocity (4.5), then we recover the well-known Hasegawa-Mima equation [82].

4.3 The cold ion model

Most of the published work dealing with drift waves in stellarator and helically-symmetric geometries has been done using the so-called cold ion model (CIM) [48, 18, 3]. The CIM retains key features of electron drift waves such as the polarization drift, the curvature drive and the coupling to the sound wave. The departure from a purely Boltzmann-like electron response is modeled with an *ad hoc* '$i\delta$' correction. We will briefly discussed the assumption made in the model and its limitations. A complete derivation of the CIM is given in appendix D. In this thesis, the nonadiabatic electron response $i\delta$ is treated as an *ad hoc* parameter, but this quantity can be calculated perturbatively, such as in the work of Horton [9].

The electron population is modeled with the drift-kinetic equation. A correct solution of the electron drift-kinetic equation would require a careful treatment of trapping and collisional mechanisms. For simplicity, the perturbed electron distribution is taken to be a Maxwellian with a small correction giving rise to $i\delta$. Therefore, the parameter δ models all mechanisms which prevent the electron distribution to reach a Maxwellian form.

The ion population is described by the gyro-kinetic equation in which collisional and trapping effects are entirely neglected. The collisionless gyro-kinetic is solved perturbatively in ascending powers of $v_{\mathrm{thi}}/V_{\mathrm{ph}} \ll 1$, where v_{thi} is the ion thermal velocity and $V_{\mathrm{ph}} \equiv (k_{||}/\omega)^{-1}$ is the parallel phase velocity. To bypass the difficulties associated with the curvature-driven resonances (a kinetic effect), the mode frequency is assumed to be much larger that the ion curvature drift frequency. The expanded form of the perturbed ion distribution is then substituted in the quasineutrality condition. The quasineutrality condition requires a velocity over the velocity space. This integration usually has to be carried out numerically; for simplicity, however, the equilibrium distribution function for the ions is assumed to be strongly peaked around the ion thermal velocity

$$F_{\mathrm{i0}} = n_0 \delta \left(\mathbf{v} - \mathbf{v}_{\mathrm{thi}} \right) \ . \tag{4.21}$$

Here $\delta\left(\mathbf{X}\right)$ is the 3-dimensional equivalent of the usual (1-dimensional) Delta function. With a Delta distribution function, the ions are cold. In the long-wavelength

limit, $k_\perp \rho_{\rm thi} \ll 1$, the final eigenmode equation is

$$\frac{c_{\rm s}^2}{\omega^2}\,\nabla_{||}^2\widehat{\Phi} = -\left(1 - i\delta + k_\perp^2\rho_{\rm s}^2 + \frac{\omega_{\star{\rm e}} + \omega_{\rm de}}{\omega}\right)\widehat{\Phi}\,, \tag{4.22}$$

where

$$\omega_{\star{\rm e}} \equiv \frac{cT_{\rm e}}{eB}\left(\frac{\boldsymbol{\nabla} n_0}{n_0} \times \widehat{\mathbf{e}}_{||}\right)\cdot\mathbf{k}_\perp\,, \tag{4.23}$$

is the electron diamagnetic drift frequency and

$$\omega_{\rm de} = 2\,\frac{cT_{\rm e}}{eB}\left(\widehat{\mathbf{e}}_{||}\times\frac{\boldsymbol{\nabla} B}{B}\right)\cdot\mathbf{k}_\perp\,, \tag{4.24}$$

is the electron curvature drift frequency. Using equations (4.15,4.16), it is easy to show that $\omega_{\star{\rm e}} = -\omega_{\star{\rm e}0}\,S_\star$ and $\omega_{\rm de} = -\omega_{\star{\rm e}0}\,S_{\rm B}^{\perp}$. Comparing the eigenmode equation obtained from the fluid equations (4.13) with the eigenmode equation obtained from the velocity-averaged gyro-kinetic equation (4.22), these equations only differ from the $S_{\rm B}^{||}$ term. In turn, this term arises from the compression of the unit parallel vector in the fluid approach. In the kinetic approach, this contribution is not present because it is assumed that the parallel phase velocity of the wave, $(k_{||}/\omega)^{-1}$, is much larger than the ion thermal velocity, $v_{\rm thi}$ (appendix D).

As far as the geometrical details of $\mathbf{B}$ are concerned, the eigenmode equation (4.22) is quite general. Because of its simplicity, the cold ion model is a good starting point for the calculations of drift waves in stellarator geometry. The eigenmode equation (4.22) was studied in a helically-symmetric configuration by Bhattacharjee *et al* [48] and later by Dominguez *et al* [83], Waltz and Boozer [18] and Persson *et al* [3]. Bhattacharjee *et al* [48] solved the eigenmode equation (4.22) and showed that extended and highly localized eigenmodes can be found.

In this section, we describe an extension of the work of Bhattacharjee *et al* [48] by considering the spectrum of the model and look for stable and unstable solutions of the eigenvalue problem (4.22) satisfying the appropriate boundary conditions. We present the dependence on the mode number and other parameters [3].

It is convenient to work with appropriate dimensionless units. The length scale is normalized to the average major radius $\bar{R}$, whereas the frequency scale is normalized to $\omega_{||} = c_s/\bar{R}$. There is some freedom in defining the density scalelength.

The equilibrium density is assumed to be a flux surface quantity, $n_0 = n_0(\Psi)$. The helical magnetic flux, Ψ, is however a function of all 3 cylindrical coordinates. We choose to define the density scalelength as

$$L_n \equiv -\left(\hat{\mathbf{n}}\cdot\frac{\boldsymbol{\nabla} n_0}{n_0}\right)^{-1}, \tag{4.25}$$

where $\hat{\mathbf{n}} = \boldsymbol{\nabla}\Psi/|\boldsymbol{\nabla}\Psi|$ is a unit vector normal to the magnetic surface. The density scalelength (4.25) is not a flux surface quantity and varies along the magnetic field line.

4.3.1 Numerical method

The eigenmode equation (4.22) can be written in the following form

$$\frac{d^2\widehat{\Phi}}{ds_{||}^2} = -Q\left(s_{||},\omega\right)\widehat{\Phi}\,, \tag{4.26}$$

where Q is the 'effective' potential and $s_{||}$ denotes the length along the field line. All the quantities entering the effective potential Q are given in appendix A. Equation (4.26) is solved by a shooting algorithm using a sixth-order Numerov scheme [84]. The boundary conditions for large $|s_{||}|$ are assumed to be of the WKB form. For positive $s_{||}$, the boundary condition

$$\frac{d\widehat{\Phi}}{ds_{||}} = \left(\sqrt{Q} - \frac{1}{4Q}\,\frac{dQ}{ds_{||}}\right)\widehat{\Phi}\,, \tag{4.27}$$

is used. The solution at the predetermined matching points has to be continuous and finding the eigenvalues in the complex frequency plane is achieved by finding the zeroes of the logarithmic derivatives of $\widehat{\Psi}$ at the matching point. The zeros are found using the Müller algorithm [50]. In order to determine the number of eigenvalues in a certain area of the complex frequency plane, the root-finding algorithm can be preceeded by a Cauchy integration. However, due to the degenerate spectrum with a large number of eigenvalues (see next section) we have found this to be excessively expensive. Instead the complex plane is divided into a number of areas each of which is then independently searched for a predetermined number of eigenvalues. The various components of Q are pre-calculated leaving only the complex frequency to be determined. While this necessitates a fixed integration step length, it is still a more efficient method than to re-calculate Q for each frequency.

4.3.2 Numerical results

The results of the numerical solution of the eigenmode equation (4.22) are now presented. The influence of the *ad hoc* drive δ is reported for 3 different cases: $\delta = 0$ (adiabatic case), $\delta = \text{const}$ (constant drive), $\delta k_{||}^2 = \text{const}$ (collisional drive). The influence of other parameters on the spectrum are also given. All the numerical calculations are carried out for only on magnetic surface. The magnetic surface used here in shown in Figure 2.1. The region of high magnetic field strength is colored in red, while regions of low $|\mathbf{B}|$ are shown in light and dark blue.

Adiabatic case

First we consider modes localized around the symmetry point $z = \phi = 0$. The electron response is assumed to be adiabatic, $\delta = 0$. The free parameter $\Lambda_0 \equiv \Lambda(s_{||} = 0)$ is set to 0. As noted by Bhattacharjee *et al* [48], this is well justified at the symmetry points. We choose the matching point to be the symmetry point. The second free parameter in the model is the value of $k_\perp \rho_s$ at the point at which the field line integration is started. We have chosen $\chi \equiv n\rho_s \boldsymbol{\nabla}\alpha|_{s_{||}=0} = 0.8$. The spectrum for these parameters is shown in Figure 4.1. The spectrum consists of a few modes close to marginal stability, indicated by crosses, and a large number of modes, apparently belong to a continuum, that diverge with an increasing parallel mode number along the field lines. These latter modes are not square integrable and while they fulfill the outgoing wave boundary condition are not physically acceptable solutions of equation (4.22). The modes which are not square integrable are indicated by squares in Figure 4.1. The low-frequency part of the spectrum is also shown. The spectrum is quite degenerate and we do not claim to have fully resolved it.

Constant drive

For a finite but small δ, modes close to marginal stability are driven unstable while the continuum remains stable, at least for reasonable frequencies. Figure 4.2 shows the spectrum for the same case as in Figure 4.1 but with a constant drive $\delta = 10^{-3}$. Eigenfunctions in the different parts of the spectrum are insets. We note the presence of helically-localized modes, more extended modes, as well as the non-

square integrable modes of the continuum. The non-square integrable modes are indicated by squares while the helically-localized and extended modes are indicated by crosses.

For larger driving, the continuum is driven unstable resulting in a system of apparent limitless growth. Figure 4.3 shows the obtained spectrum, for the same case as in Figure 4.1, but with $\delta = 10^{-2}$. The continuum of physically unacceptable modes driven unstable by this larger value of δ reflects on the limitations of the somewhat oversimplified model. In contrast to the spectrum of magnetohydrodynamics where finite resistivity breaks up the continuum, here the modes appear not to be square integrable. In this strongly driven case, the spectrum appears to be even more degenerate with a mixture of diverging and acceptable modes. No attempt has been made to separate the two types of modes in this limit.

Variable drive

One important limitation of the present model is the use of a constant δ. For instance, in some limits, a simple model of drift waves driven by collisions [85] can give a δ inversely proportional to $k_{||}^2$. This is because for smaller wavelengths the electrons can move swiftly along the field lines short circuiting any perturbed potentials. Figure 4.3 shows the results of such calculations where the local $k_{||}$ was determined dynamically along the field line with a finite $\delta_0 = 10^{-2}$. This was followed by a calculation with $\delta = \delta_0(k_{||0}/k_{||})^2$. In these latter calculations, the root finding routine was set to look for modes with frequencies close to the modes with constant driving. In the calculation presented here we used $k_{||0} = \sqrt{10}$. This was chosen in order to not alter the driving of the low-frequency modes considerably. The stabilizing effect of the high frequency part of the spectrum is due to an increasing $k_{||}$ in this part of the spectrum. Hence, in addition to being non square integrable these modes also violate the basic assumption of the ballooning mode formalism; the assumption that $k_{||}$ is small.

The use of $\Lambda_0 = 0$ is justified at symmetry points. However, for general matching points, this is not correct. $\Lambda(s_{||} = 0)$ is directly related to the component of

the perpendicular wave vector pointing out of the magnetic surfaces [see equation (2.44)] . This is a free parameter which the growth rate should be maximized with respect to. Figure 4.4 shows the result of such a scan using the same equilibria as above. The squares are for the field line going through $Z = \phi = 0$ and using this point as the matching point. The maximum growth rate is sensitive to $\Lambda(s_{||} = 0)$ and in accordance with the symmetry argument the most unstable mode has $\Lambda(s_{||} = 0) = 0$.

The growth of the modes should also be optimized with respect to the other mode number parameter χ. Figure 4.5 shows the result of such a scan using the same case as in Figure 4.4 with $\Lambda(s_{||} = 0) = 0$. Again we use the field line going through $Z = \phi = 0$ and also use this point as the matching point. Only the most unstable modes are plotted. The stabilizing effect for large mode numbers is due to the polarization drift which is quadratic in χ. The scaling with χ as well as that with $\Lambda(s_{||} = 0)$ is similar to what is observed in tokamak geometry.

In this chapter, two simple fluid models to study drift waves in three-dimensional plasmas have been discussed. One model is derived from simplified fluid equations while the other, the cold ion model, is derived from the velocity-averaged, collisionless gyro-kinetic equation. The two models yield similar, but not identical, eigenmode equations. A numerical study of the cold ion model for a helically-symmetric configuration has been presented. In particular, the drift wave spectrum for this configuration has been obtained and discussed [3].

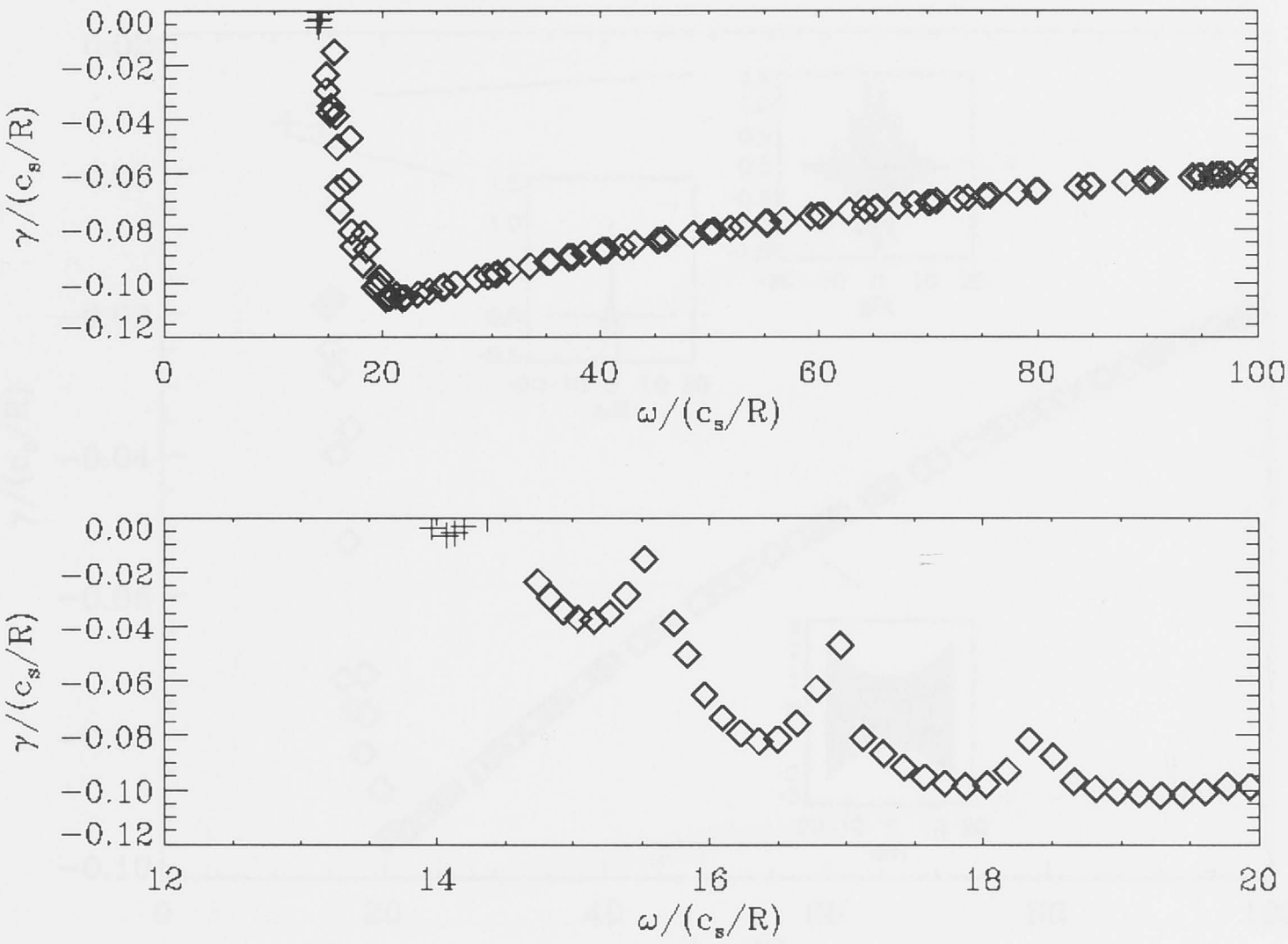

Figure 4.1: The spectrum of equation (4.22) with $\Lambda_0 = 0$, $\chi = 0$ and $\delta = 0$ obtained by matching around the symmetry point $z = \phi = 0$. Eigenvalues in the growth rate frequency plane close to marginal stability are indicated by crosses and a larger number of more stable modes with larger parallel mode number are indicated with squares.

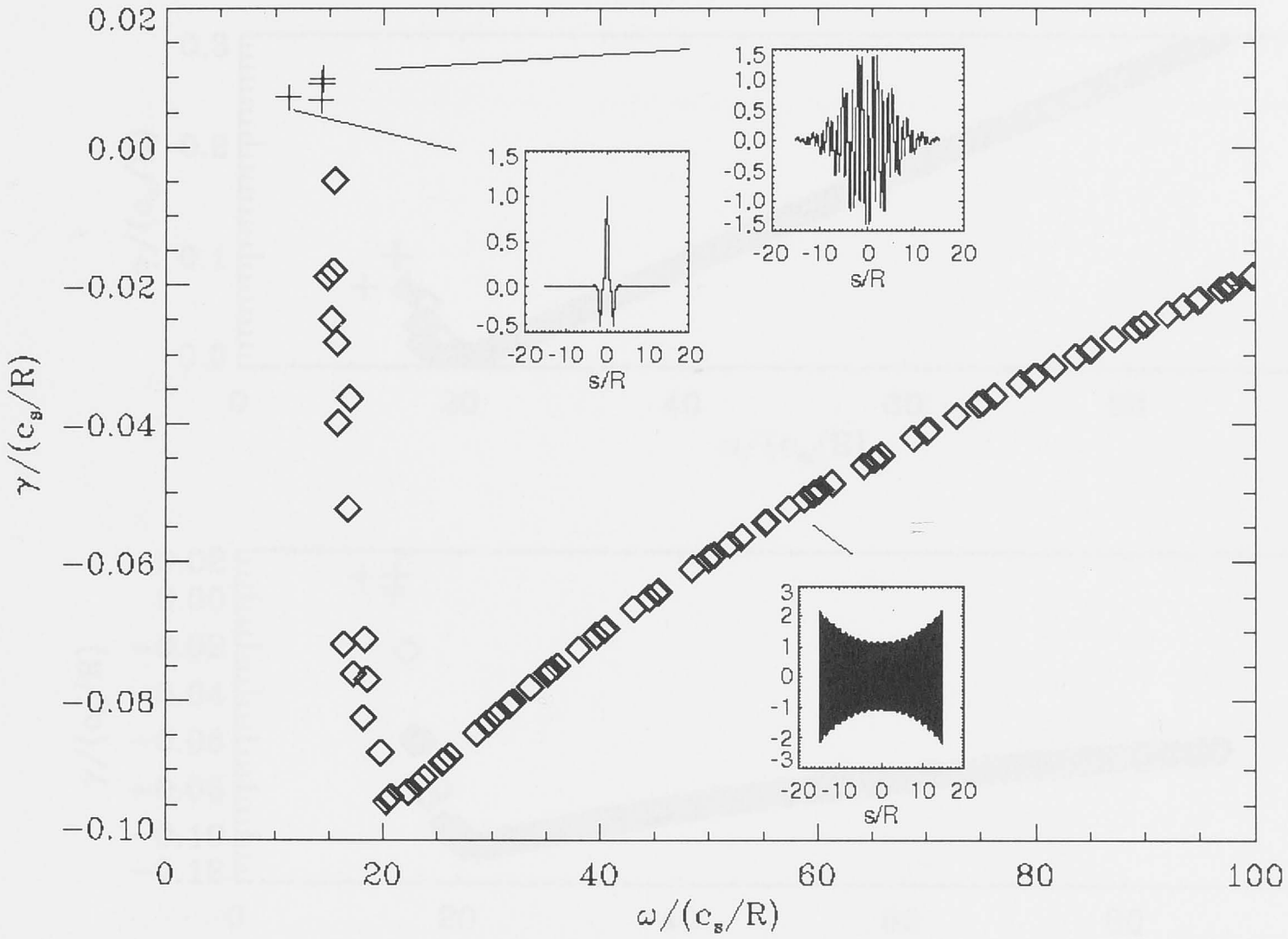

Figure 4.2: Same as figure 4.2 but with $\delta = 0.001$. Examples of helically localized eigenmodes, more extended modes, as well as the non-square integrable modes are insets. The first two types of modes have been indicated with crosses while the latter type has been indicated with squares.

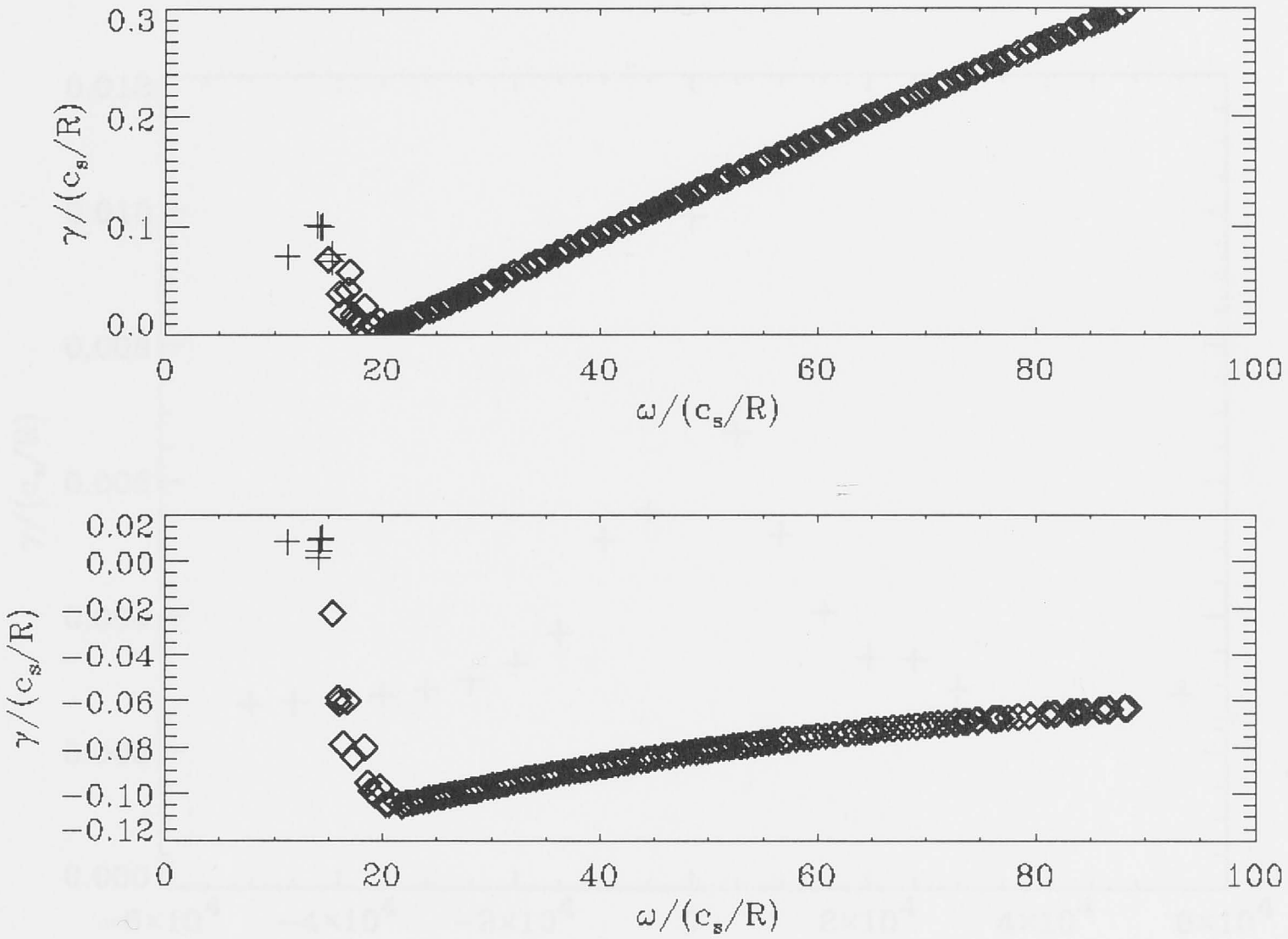

Figure 4.3: Same as figure 4.2 but with $\delta = 0.01$ (top) with δ scaling inversely with $k_{||}^2$ (bottom). The localized eigenmodes and more extended modes have been indicated with crosses while the diverging modes have been indicated with squares.

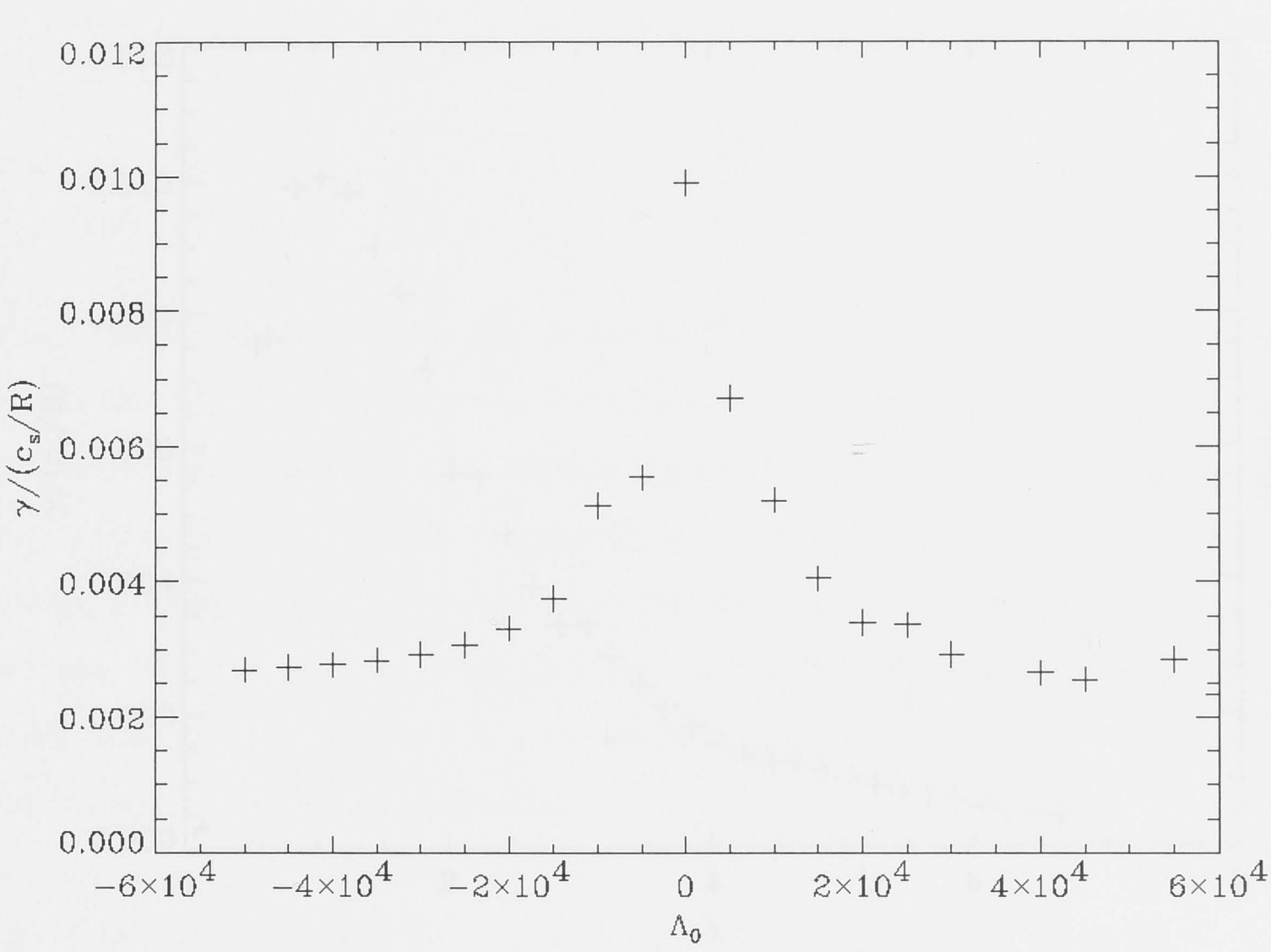

Figure 4.4: A scan in Λ_0 for the case in figure 4.3 indicating the most unstable modes using $Z = \phi = 0$ as the matching points.

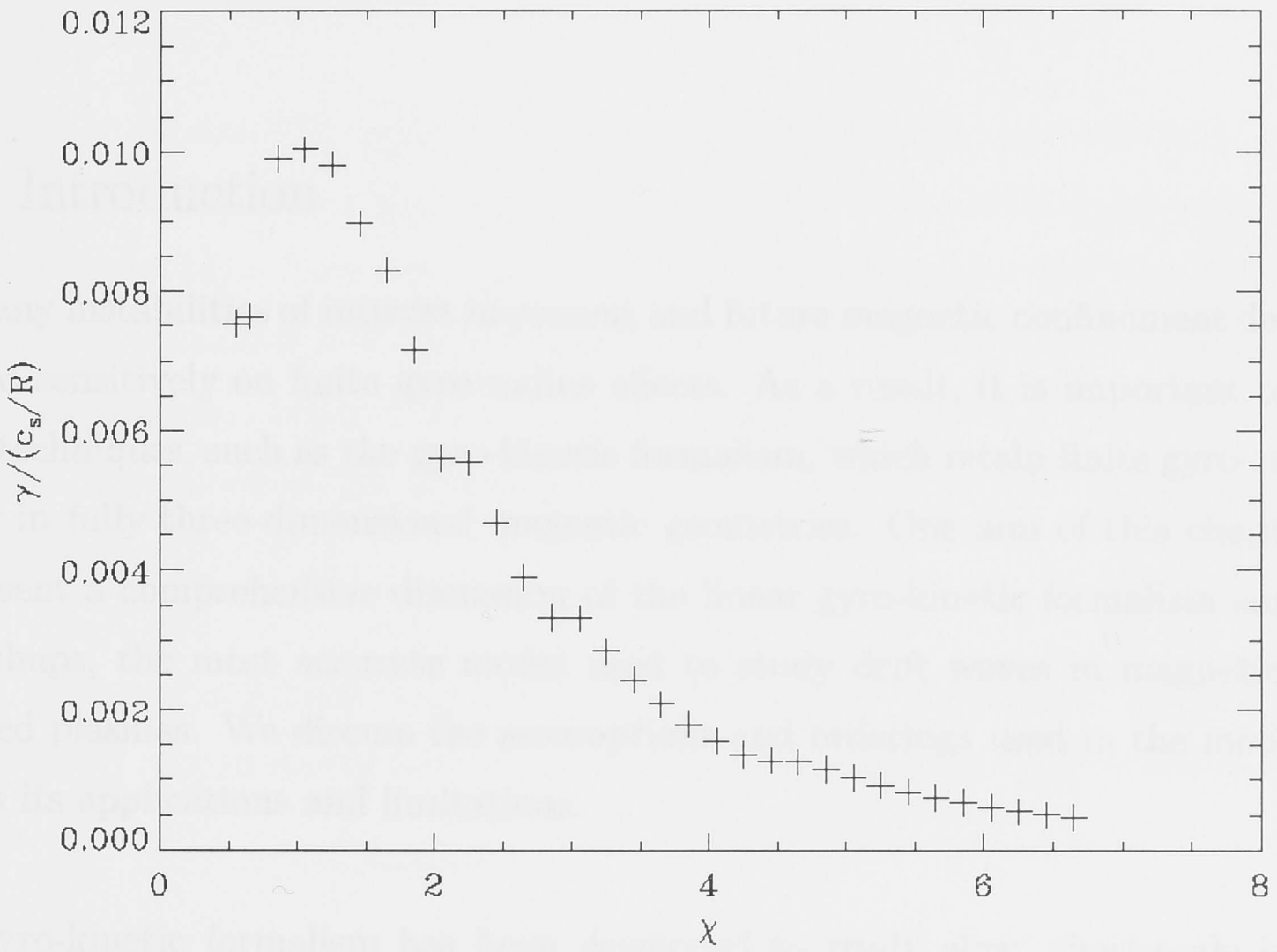

Figure 4.5: A scan in χ for the case in Figure 4.3 indicating the most unstable modes using $z = \phi = 0$ as the matching points.

CHAPTER 5

Linear Gyro-Kinetics

5.1 Introduction

Many instabilities of interest in present and future magnetic confinement devices depend sensitively on finite gyro-radius effects. As a result, it is important to develop techniques, such as the gyro-kinetic formalism, which retain finite gyro-radius effects in fully three-dimensional magnetic geometries. One aim of this chapter is to present a comprehensive discussion of the linear gyro-kinetic formalism since it is, perhaps, the most accurate model used to study drift waves in magnetically-confined plasmas. We discuss the assumptions and orderings used in the model as well as its applications and limitations.

The gyro-kinetic formalism has been developed to study slow, short-scale instabilities (microinstabilities). Microinstabilities are characterized by a time variation much smaller than the gyro-frequency ($\partial/\partial t \sim \omega \ll \omega_{cj}$, where $\omega_{cj} \equiv q_j B/m_j c$ is the gyro-frequency for particle species j with mass m_j and charge q_j). Approximate solutions of the general kinetic equation can be found when the characteristic equilibrium scalelength, L, is much larger than the thermal gyro-radius, $\rho_{thj} \equiv v_{thj}/\omega_{cj}$, where v_{thj} is the thermal velocity of particle species j.

The gyro-kinetic techniques may be employed to retain gyro-effects for arbitrary values of the gyro-radius over perpendicular wavelengths. Unlike drift-kinetic descriptions, gyro-kinetic models retain finite gyro-radius effects to lowest order in the equation for the perturbed distribution function.

Since the original work of Rutherford and Frieman [86] and Taylor and Hastie [87] various gyro-kinetic techniques have been developed. Between 1968 and 1978, various forms of the linear gyro-kinetic equation were reported [87, 88, 89, 90, 91, 86] in the literature. In 1978, Catto [92] presented a method which simplifies the form of the linear gyro-kinetic equation when arbitrary magnetic field configurations have to be treated. In Catto's method, the average over the fast gyro-motion is done *before* simplifying (if required) the form of the confining magnetic field [92].

Antonsen and Lane [63] included arbitrary electromagnetic perturbations which allowed studies of plasmas with arbitrary β (the ratio of the kinetic pressure to the magnetic pressure). They considered axi-symmetric equilibria but also discussed briefly the generalization of the gyro-kinetic equation to fully 3-Dimensional magnetic configurations. Frieman and Chen [81] extended previous works and retained nonlinear corrections in the gyro-kinetic equation, as well as fully electromagnetic perturbations.

The gyro-kinetic approach can have different degrees of complexity, depending on the plasma β, the magnetic field geometry and the amplitude of fluctuating quantities.

When the plasma pressure is very small, $\beta \sim (\bar{a}/\bar{R})^3$ (where $\bar{a}$ and $\bar{R}$ are the average minor and major radii of the machine, respectively), magnetic field perturbations can be neglected. Fluctuations in such a plasma are said to be electrostatic. In this case, a simplified system of 3 coupled equations has to be solved. These are the ion and electron gyro-kinetic equations and the quasineutrality equation. The quasineutrality equation provides a closure relation via the electrostatic potential. For plasmas with $\beta \sim (\bar{a}/\bar{R})^2$, the compressional component of the perturbed magnetic field has to be retained [63]. The previous system of equations is now augmented with the parallel component of Ampere's law. Finally, for high-β plasmas ($\beta \geq \bar{a}/\bar{R}$), parallel as well as perpendicular components of the perturbed magnetic field enter the gyro-kinetic formalism. The general solution involves the simulta-

neous solution of 6 coupled equations. These are the ion and electron gyro-kinetic equations, the quasineutrality condition and the parallel and 2 perpendicular components of Ampere's law.

A second factor of complexity is the magnetic geometry. For ideal, 2-dimensional tokamak plasmas, the solution of the ion and electron gyro-kinetic equations can be found by means of Fourier transforms in (r, θ) space [93]. Here r is the local minor radius and θ is the local minor radius. Furthermore, tokamak plasmas with $\beta \sim (\bar{a}/\bar{R})^2$ have circular magnetic surfaces (chapter 3). However, even for $\beta \sim (\bar{a}/\bar{R})^2$, one must formally include geometrical effects using curvilinear coordinates. However, when the plasma pressure gradient is large, the analytical formulation of the equilibrium can be further simplified. An example of such simplified equilibrium is the widely used $\hat{s}-\alpha$ model [57], where $\hat{s}$ is the shear parameter and α is the ballooning parameter (proportional to the pressure gradient). However, some tokamak plasmas (such as in JET [36] and DIII-D [37]) have magnetic surfaces which strongly depart from perfect circularity. This is of course true for the fully 3-dimensional plasmas of stellarators. In a such plasmas, the use of curvilinear (or magnetic) coordinates is necessary. One aim of chapter 6 is to write the gyro-kinetic equation in straight-field-line-coordinates so that any plasma of arbitrary shape can be treated, provided the numerically-computed equilibrium is known.

The third factor that contributes to the complexity of the gyro-kinetic formalism is the amplitude of the fluctuations. It is well known that the fluctuation level in stellarators and tokamak edge plasmas is usually large. In the plasma edge, one must use a nonlinear gyro-kinetic formalism. However, as pointed out in chapter 4, the high-density, low-temperature edge plasmas are usually in the collisional regime. Therefore, it might be advantageous to use fluid equations, such as Braginskii's equations [13] or the reduced fluid equations of Drake and Antonsen [94], to study nonlinear effects in the collisional edge plasma.

Linear and nonlinear gyro-kinetic formalisms have found many applications. Reweldt *et al* [93] have given a detailed mode structure for axi-symmetric tokamak

plasmas. Perturbed quantities, such as the electrostatic potential and compressional component of the magnetic field, are expanded in Hermite polynomials. The problem then reduces to a matrix form. Eigenfunctions and eigenvalues can then be calculated using the Ritz method [93].

Collisional effects in the linear gyro-kinetic formalism were studied by various authors [95, 96, 97, 98, 99, 100, 101, 102]. The specific form of the collision operator can be important in some cases. For example, the linear growth rate of trapped-particle instabilities can be altered depending on the (approximate) collision operator used. Rewoldt *et al* [95] investigated the accuracy of different models for electron collision operators in slab geometry; they determined which properties of a collision operator are important for linear gyro-kinetic modes. Guided by their results, these authors investigated the mode structure of low-frequency electromagnetic modes in unsheared slab geometry and in axi-symmetric, toroidal geometry ($\hat{s}-\alpha$ model) [96]. For weakly-collisional, large-aspect-ratio tokamak plasmas, approximate solutions of the linear gyro-kinetic equation have been found using techniques such as the variational approach [103, 97, 98], approximate collision operators [104, 99] and expansion in eigenfunctions [100, 101, 102].

The gyro-kinetic formalism is also used for particle simulations. In the original work of Lee [105], an electrostatic particle simulation scheme in slab geometry was developed; the gyro-averaged ion motion (retaining arbitrary finite ion Larmor radius) calculated from the linear gyro-kinetic equation was coupled to a particle pushing scheme for the electrons. Dubin *et al* [106] derived an appropriate energy-conserving form of the gyro-kinetic equations system using perturbative Hamiltonian methods. Extension of this formalism was subsequently carried out by Hahm [107]. Electromagnetic effects in sheared slab geometry were introduced by Hahm *et al* [108], and the extension of this analysis to general geometry was addressed by Brizard [109]. These improvements in gyro-kinetic particle simulation were followed by the discovery of a low-noise particle simulation scheme known as the δf method [110]. This scheme evolves the perturbed part of the distribution function along a set of characteristics that solves the fully nonlinear gyro-kinetic equations

[111, 112, 113, 114, 115, 116, 110, 117].

In practice, solving the full linear (or nonlinear) gyro-kinetic equations system is a rather a difficult task, even in the simplest geometry. Inclusion of kinetic effects in fluid equations was done in the work of Hammett and Perkins [118]. These authors took moments of the linear gyro-kinetic equation and showed that, with appropriate closure relations, the linear, fluid plasma response can appropriately reproduce some purely kinetic features (such as Landau damping). Their model is often referred to as the 'gyro-Landau fluid (GLF) model'.

Interestingly Hammett and Perkins's fluid closure is accurate for weakly and almost collisionless plasmas. The GLF model is therefore of interest for studying microinstabilities in the hot core plasmas. Waltz *et al* [119] and Dorland *et al* [120] generalized Hammett-Perkins results to include linear gyro-motion and curvature drift motion in axi-symmetric, toroidal plasmas. Recently, Brizard [121] presented a nonlinear version of the original GLF model valid in arbitrary magnetic geometry.

5.2 The kinetic equation

Microinstabilities are characterized by typical wave frequency much lower than the ion gyro-frequency, and by perpendicular wavelength comparable to the ion gyro-radius [122]. An accurate theoretical analysis of microinstabilities therefore requires a kinetic treatment. Standard fluid models, on the other hand, are *not* valid in the regime $k_\perp \rho_\mathrm{i} \geq 1$.

A statistical description of a plasma involves the distribution function $\mathcal{F}_j(\mathbf{r}, \mathbf{v}, t)$ which measures the probability density for particle species j in the six-dimensional phase space $(\mathbf{r}, \mathbf{v})$ at a given time t. The behavior of the distribution function is described by the kinetic equation [123]

$$\mathcal{L}\left[\mathcal{F}_j\right] \equiv \left[\frac{\partial}{\partial t} + \mathbf{v}\cdot\boldsymbol{\nabla} + \frac{q_j}{m_j}\left(\mathbf{E} + \frac{\mathbf{v}\times\mathbf{B}}{c}\right)\cdot\boldsymbol{\nabla}_\mathbf{v}\right]\mathcal{F}_j = \mathcal{C}\left(\mathcal{F}_j\right) \ . \tag{5.1}$$

Here, $\mathcal{C}$ is the collision operator. There is not exact version of the collision operator, but only a sequence of more accurate forms, one of which being the Fokker-Planck operator [124].

5.3 The gyro-kinetic ordering

If L is the equilibrium scalelength characterizing the plasma and $\rho_{\rm thi}$ is the ion thermal gyro-radius, a plasma is said to be *magnetized* if the parameter $\delta \equiv \rho_{\rm thi}/L$ is much smaller than unity. The electron thermal gyro-radius is roughly $\sqrt{m_{\rm e}/m_{\rm i}}$ times smaller than the ion thermal gyro-radius (for $T_{\rm e} \sim T_{\rm i}$). In a magnetized plasma, the term associated with Larmor gyration

$$\frac{q_j}{m_j c}\ (\mathbf{v}\times\mathbf{B})\cdot\boldsymbol{\nabla}_{\mathbf{v}}\mathcal{F}_j \ \sim\ \omega_{cj}\mathcal{F}_j\ , \tag{5.2}$$

is the dominant term in the kinetic equation, making an averaging over the fast gyro-motion relevant. The plasma is assumed to be in the low-collisionality regime. Writing $\mathcal{C}(\mathcal{F}_j) \sim \nu_j \mathcal{F}_j$, where ν_j is a typical collision frequency for particle species j, we assume

$$\frac{\nu_j}{\omega_{\rm ci}}\ \sim\ \delta \ll 1\ . \tag{5.3}$$

The collision frequency is much smaller that the ion gyro-frequency. The ordering (5.3) includes the case of almost collisionless plasmas, like those observed in todays large-scale experiments. If the collision frequency is large, $\nu_j \sim \omega_{\rm ci}$, the gyro-averaging technique is not meaningful.

The second term in the kinetic equation (5.1), called the convective term, requires a careful analysis. In a magnetized plasma, the strong confining magnetic field tends to isolate the plasma on adjacent field lines. The spatial anisotropy of the plasma implies that its behavior is expected to be very different *across* and *along* the magnetic field lines. For convenience, we split the distribution function $\mathcal{F}_j$ into an equilibrium part, F_j, and a perturbed (or fluctuating) part, f_j [63]

$$\mathcal{F}_j\ =\ F_j\ +\ \Delta\, f_j\ , \tag{5.4}$$

where Δ is a smallness parameter measuring the amplitude of the perturbation. In the context of the linear gyro-kinetic formalism, the amplitude of the fluctuations is assumed to be small, $\Delta \sim \delta$. When fluctuations are vanishingly small ($\Delta \mapsto 0$) and when the $\mathbf{E}\times\mathbf{B}$-drift motion is slow, an approximate solution of the kinetic equation can be found: the drift-kinetic equation. The drift-kinetic equation [91]

evolves the distribution function of particle guiding centers: the fast, short-scale motion dynamics due to particles gyration have been averaged out [63].

Since the plasma motion occurs on disparate lengthscales, the perpendicular and parallel gradients of the equilibrium and perturbed parts of the distribution function can be written as

$$\nabla_{||} F_j \sim \frac{F_j}{L_{||}} \ , \ \nabla_{\perp} F_j \sim \frac{F_j}{L_{\perp}} \ , \ \nabla_{||} f_j \sim \frac{f_j}{\lambda_{||}} \ , \ \nabla_{\perp} f_j \sim \frac{f_j}{\lambda_{\perp}} \ . \tag{5.5}$$

In the gyro-kinetic formalism, it is assumed that [86]

$$L_{||} \sim L_{\perp} \sim \lambda_{||} \gg \lambda_{\perp} \sim \rho_{\mathrm{thi}} \ . \tag{5.6}$$

The ordering (5.6) states that perturbations are characterized as having short wavelengths across the confining magnetic field and relatively long wavelengths along the magnetic field. The linear gyro-kinetic equation is determined using the lowest order in the expansion parameter δ (see below). To this order, subsidiary ordering, that distinguishes between $L_{\perp}$, $L_{||}$ and $\lambda_{||}$, does not enter the gyro-kinetic formalism [125].

The convective derivative, the second term in the kinetic equation (5.1), involves the particle velocity. Velocities along and across the magnetic field direction are different. The perpendicular fluctuating electric field, $\mathbf{E}_{\perp}$, generates a slow drift of the guiding centers across $\mathbf{B}$ with velocity

$$\mathbf{v}_E = c \frac{\mathbf{E} \times \mathbf{B}}{B^2} \ . \tag{5.7}$$

The drift ordering [125] is adopted

$$\frac{v_E}{v_{\mathrm{th}j}} = \mathcal{O}(\delta) \ . \tag{5.8}$$

To lowest order, the cross-field drift velocities for the ions and the electrons are the same and no instability arises. To next order, the ion drift velocity and the electron drift velocity are not equal and a fluctuating perpendicular current, $\tilde{\mathbf{J}}_{\perp}$, may arise. The force on the plasma due to $\tilde{\mathbf{J}}_{\perp}$ can enhance the fluctuating electrostatic potential and this leads to one of the principal mechanisms for anomalous transport [5, 126,

6, 127]. The drift ordering (5.8) is motivated by experiments [128, 129, 130], as well as theoretical studies [131, 7, 132, 133, 134]. In a low-β plasma, the electric field is irrotational, $\mathbf{E} \simeq -\boldsymbol{\nabla}\Phi$. From equation (5.8), it follows that the fluctuation level is small

$$\frac{e\Phi}{T_{\mathrm{e}}} \sim \delta \,. \tag{5.9}$$

However, experimental evidence [135, 136, 137, 138, 139, 140] suggests that the estimate (5.9) is *not* verified at the plasma edge.

For near-equilibrium plasmas, no large imbalanced parallel electric field can arise and it is assumed [81]

$$\frac{q_j E_{||}}{m_j v_{\mathrm{th}j} \omega_{cj}} \sim \delta \,. \tag{5.10}$$

It is worth noting that the parallel electric field and the collisional processes are the only two contributions that affect the acceleration in the direction of $\mathbf{B}$.

5.4 Perturbation analysis

The equilibrium distribution function is assumed to be slowly varying in time. Following Frieman and Chen [81], we adopt the so-called transport ordering for the equilibrium distribution function

$$\omega_{\mathrm{c}j}^{-1} \frac{1}{F_j} \frac{\partial F_j}{\partial t} = \mathcal{O}\left(\delta^3\right) \,. \tag{5.11}$$

This allows us to neglect the slow evolution of equilibrium quantities. Furthermore, if the equilibrium distribution function varies on the fast time-scale the plasma is far from equilibrium, a situation that we cannot accurately model. Substituting equation (5.4) in the kinetic equation (5.1) and linearizing yields

$$\mathcal{L}_0\left[f_j\right] = \mathcal{C}^{(L)}\left[\mathcal{F}_j\right] - \frac{q_j}{m_j}\left(\mathbf{E} + \frac{\mathbf{v}\times\widetilde{\mathbf{B}}}{c}\right)\cdot\boldsymbol{\nabla}_{\mathbf{v}} F_j \,, \tag{5.12}$$

where $\mathcal{C}^{(L)}$ is the linearized collision operator and

$$\mathcal{L}_0 \equiv \frac{\partial}{\partial t} + \mathbf{v}\cdot\boldsymbol{\nabla} + + \frac{q_j}{m_j}\left(\mathbf{E}_0 + \frac{\mathbf{v}\times\mathbf{B}}{c}\right)\cdot\boldsymbol{\nabla}_{\mathbf{v}} \,. \tag{5.13}$$

Here $\mathbf{E}_0$ is the equilibrium electric field. The right-hand side of equation (5.12) can be interpreted as a 'source term' for the evolution of the perturbed distribution function. For a low-β plasma, the case considered here, one can neglect the

perturbed magnetic field $\widetilde{\mathbf{B}} \simeq 0$. In the strongly-turbulent regime, nonlinear corrections have to be retained. Nonlinear gyro-kinetic equations have been derived by various authors [81, 141, 142]. In the present study we restrict our discussion to the linear case only.

5.5 The eikonal representation

The linearized kinetic equation (5.12) depends on the 7 variables $(\mathbf{r}, \mathbf{v}, t)$. A tractable solution can be obtained by exploiting the plasma anisotropy. The plasma anisotropy is reflected by the smallness parameter δ. For a magnetized plasma, $\delta \ll 1$, the confining magnetic field tends to isolate the plasma on adjacent field lines. Perturbations are allowed to have typical perpendicular wavelength comparable to the ion thermal gyro-radius. In the direction along $\mathbf{B}$, the plasma motion is solely influenced by the parallel electric field and the collisions. In turn, these two effects are assumed to be small (because of the large parallel transport and the near-equilibrium state). One therefore expect the variation along $\mathbf{B}$ to be slow, $k_{||}L \sim 1$. Variations along the field line are, usually, stabilizing. The most unstable situation will presumably be when $k_{||} \simeq 0$. However, $k_{||}$ cannot strictly vanish because of toroidicity effects. Thus, it is natural to adopt the one-dimensional WKB representation for perturbed quantities [57, 62, 63]

$$\Phi = \widehat{\Phi} \exp\left(in\alpha\right) \ , \tag{5.14}$$

where $n \gg 1$ is the toroidal mode number and α is the field line label in the Clebsch representation for the confining magnetic field [29]

$$\mathbf{B} = \boldsymbol{\nabla}\alpha \times \boldsymbol{\nabla}\psi \ . \tag{5.15}$$

The slow variation of Φ along the field line is retained in the amplitude $\widehat{\Phi}$. The lowest-order wavector is orthogonal to $\mathbf{B}$ and we write $\mathbf{k}_\perp \equiv n\boldsymbol{\nabla}\alpha$. Each perturbed quantity is assumed to have a form similar to equation (5.14). However, in a system with shear, the representation (5.14) violates the periodicity requirements in the poloidal and toroidal directions. In axi-symmetric configurations, the problem of reconciling long parallel wavelength, short perpendicular wavelength and periodicity have been resolved by the so-called ballooning transformation [62, 57].

The final step consists of writing the perturbed distribution function in ascending powers of δ

$$f_j = \left(\widehat{f}_j^{(0)} + \widehat{f}_j^{(1)} + \widehat{f}_j^{(2)} + ...\right) \exp\left(in\alpha\right) \tag{5.16}$$

where $\widehat{f}_j^{(k)} = \mathcal{O}(\delta^k)$, for k integer. The equilibrium distribution function is expanded in a similar way.

5.6 The space transformation

As previously pointed out, in a strongly magnetized plasma, the term in the kinetic equation associated with the Larmor gyration (5.2) dominates. Since we are interested in the behavior of the (total) distribution function, it is convenient to 'smooth out' the fast processes associated with Larmor gyration. In order to average over the fast gyro-motion, we transform the linearized kinetic equation from the particle phase space $\{\mathbf{r}, \mathbf{v}, t\}$ to the guiding center phase space $\{\mathbf{R}_j, \mu_j, E_j, \xi, t\}$. Here $\mathbf{R}_j$ is the guiding center position, $\mu_j \equiv m_j v_\perp^2/2B$ is the magnetic moment, $E_j \equiv m_j v^2/2 + q_j \Phi_0$ is the total particle energy and ξ is the gyro-angle. Then, the spatial and velocity gradients in the linearized kinetic equation can be written in guiding center coordinates [63, 81].

5.7 The equilibrium distribution function

Substituting expansion (5.16) in the linearized, guiding-center kinetic equation, it can be shown that the lowest-order equilibrium distribution function satisfies

$$\frac{\partial F_j^{(0)}}{\partial \xi} = 0 \,, \tag{5.17}$$

and

$$\mathbf{B}\cdot\boldsymbol{\nabla} F_j^{(0)} = 0 \,. \tag{5.18}$$

The lowest-order equilibrium distribution function is independent of the gyro-angle and is constant along the magnetic field line. Requirements (5.17,5.18) are fulfilled for a Maxwellian distribution $F_{\mathrm{M}j}$ provided the parallel gradient of plasma density and temperature vanish. In the following we use $F_j^{(0)} = F_{\mathrm{M}j}$.

5.8 The perturbed distribution function

Order-by-order solution for the perturbed distribution function can also be obtained. To lowest order in δ, this yields

$$\widehat{f}_j^{(0)} = -\frac{q_j \widehat{\Phi}}{T_j} F_j^{(0)} + \widehat{h}_j \exp\left(i\mathbf{k}_\perp \cdot \boldsymbol{\rho}_j\right) , \tag{5.19}$$

where $\boldsymbol{\rho}_j$ is the local gyro-radius vector for particle species j. The first term on the right-hand side of equation (5.19) is the adiabatic response. The second term is associated with nonadiabatic phenomena, such as particle trapping and de-trapping, collisions, Landau damping, etc., and it has yet to be determined with the next order solution to the kinetic equation. The left-hand side represents the perturbed distribution of *guiding centers*. In other words, if one averages $\widehat{f}_j^{(0)}$ over the velocity space, one gets the density of *guiding centers* ($\widetilde{n}_{\mathrm{gc}j}$), not the actual plasma density ($\widetilde{n}_j$). The difference between these two densities is usually negligible for the electron population, but it can be substantial in the ion case. Hereafter, except when explicitly stated, all perturbed quantities are given in guiding center phase space.

Substituting equation (5.19) in the next order linearized kinetic equation and demanding $\widehat{f}_j^{(0)}$ to be periodic in the gyro-angle ξ, the linear gyro-kinetic equation is obtained

$$\mathcal{L}_{\mathrm{gc}j}\left[\widehat{h}_j\right] = \left\langle \mathcal{C}\left[\widehat{f}_j^{(0)}\right] \exp\left(-ik_\perp \rho_j\right)\right\rangle_\xi + J_0\left(k_\perp \rho_j\right) F_{\mathrm{M}j} \left(\frac{\partial}{\partial t} + i\omega_{\star j}^T\right) \widehat{\sigma}_j , \tag{5.20}$$

where $\widehat{\sigma}_j$ depends on the perturbed electrostatic potential $\widehat{\Phi}$ and the parallel vector potential $\widehat{A}_{||}$

$$\widehat{\sigma}_j \equiv \frac{q_j \widehat{\Phi}}{T_j} - \frac{v_{||}\widehat{A}_{||}}{cT_j} . \tag{5.21}$$

On the left-hand side of equation (5.20)

$$\mathcal{L}_{\mathrm{gc}j} \equiv \frac{\partial}{\partial t} + i\,\omega_{\mathrm{d}j} + v_{||}\nabla_{||} , \tag{5.22}$$

is an operator similar to the one given in equation (5.1) but written in guiding center coordinates. In equation (5.20), J_0 is the Bessel function of order zero which arises because of the averaging over the gyro-angle. The gyro-average of a physical

quantity G is defined as

$$\langle G \rangle_\xi \equiv \frac{1}{2\pi} \int_{-\pi}^{+\pi} G(\xi') d\xi' \ . \tag{5.23}$$

The gyro-averaged, linearized collision operator on the right-hand side of equation (5.20) requires the *total* perturbed distribution function, as given by equation (5.19). In turn, the non-adiabatic part of $\widehat{f}_j^{(0)}$ must satisfy the linear gyro-kinetic equation (5.20). Therefore, one can approximate the collision operator or proceed by successive iterations between equation (5.19) and equation (5.20).

In equation (5.20), we have introduced the diamagnetic drift frequency

$$\omega_{\star j}^T \equiv -\frac{cT_j}{q_j B^2} \ (\mathbf{B} \times \mathbf{k}_\perp) \cdot \frac{\boldsymbol{\nabla} F_{\mathrm{M}j}}{F_{\mathrm{M}j}} \ , \tag{5.24}$$

and the curvature drift frequency

$$\omega_{\mathrm{d}j} \equiv \omega_{\mathrm{c}j}^{-1} \left[\frac{\mathbf{B}}{B} \times \left(v_\parallel^2 \boldsymbol{\kappa} + \frac{v_\perp^2}{2} \frac{\boldsymbol{\nabla} B}{B} + \frac{q_j}{m_j} \boldsymbol{\nabla} \Phi_0 \right) \right] \cdot \mathbf{k}_\perp \ , \tag{5.25}$$

where $\boldsymbol{\kappa}$ is the magnetic curvature and Φ_0 is the equilibrium electrostatic potential. It is worth noting that all the equilibrium quantities in the gyro-kinetic equation (5.20) are evaluated along the magnetic field line.

The gyro-kinetic equation (5.20) is valid for a low-β plasma and for arbitrary magnetic geometry. The details of the confining magnetic field enter in scalar quantities and in one operator.

The operator is simply the parallel gradient, keeping the field line label constant

$$\begin{aligned} \nabla_\parallel &= \left(\frac{\mathbf{B} \cdot \boldsymbol{\nabla}}{B} \right)_\alpha \ , \\ &= H(L) \frac{\partial}{\partial L} \ , \end{aligned} \tag{5.26}$$

where L is the length along the field line. In the above equation, $H(L)$ is a non-dimensional quantity which, in general, depends on the position along the magnetic field line.

The 3 scalar quantities that depend on the magnetic field structure are the magnetic field strength, the lowest-order perpendicular wavevector and the curvature drift frequency. The magnetic field strength enters the gyro-kinetic equation

through the ion cyclotron frequency, in the argument of the Bessel function and in the curvature drift frequency. The details of $\mathbf{B}$ also enter the lowest-order perpendicular wavevector, $\mathbf{k}_\perp = n\nabla\alpha$. The lowest-order perpendicular wavevector enters the gyro-kinetic equation (5.20) in scalar form in the argument of the Bessel function and in vector form in the curvature drift frequency. Finally, it can be shown that the diamagnetic drift frequency, as defined by equation (5.24), is constant along the magnetic field line (appendix D). In fully 3-dimensional geometry, the above quantities can be written in straight-field-line coordinates (chapter 6).

In this chapter, a comprehensive presentation of the linear gyro-kinetic theory has been given. The assumptions, ordering and limitations of the model were discussed. We have identified the quantities that depend on the details of the confining magnetic field. In the next chapter, the numerical solution of the collisionless ion gyro-kinetic in stellarator geometry is presented.

CHAPTER 6

Collisionless Gyro-Kinetic Calculations in Stellarator Geometry

In this chapter, we present calculations of the ion collisionless gyro-kinetic equation in the linear regime for a low-β stellarator plasma. For simplicity, we neglect the effects of trapped particles. Braginskii's fluid equations [13] are used to determine the electron dynamics. The perturbed ion density is obtained by a direct integration over velocity space of the ion distribution function, while the perturbed electron density is determined from the electron continuity equation. The closure relation for the perturbed electrostatic potential is the quasineutrality condition. We use the ballooning representation [57, 62, 63] for fluctuating quantities and the equations are written in straight-field-line coordinates [29]. Our initial-value code is convenient for studying the Ion-Temperature-Gradient driven (ITG) mode [143] in general 3-dimensional plasmas. Numerical results for the toroidal heliac H1-NF [21] are presented.

This chapter is organized as follows. In section 6.1, we briefly review the progress in the ITG mode theory. We pay special attention to the toroidal branch (essentially tokamak geometry) of this mode. In section 6.2, we discuss the assumptions made to obtain our model; the collisionless ion gyro-kinetic equation is written in a form convenient for numerical work; finally, the quasineutrality condition is derived. In section 6.3, a fluid model for the electron dynamics is presented, the numerical method is discussed in section 6.4 and numerical results for the toroidal heliac H1-NF are presented in section 6.5. We conclude with some remarks and

possible extension of our work in section 6.6.

6.1 Toroidal ITG mode

The Ion-Temperature-Gradient-Driven (ITG) mode is a drift-type instability which arises from the free energy stored in the ion pressure gradient. In slab geometry and for a flat density profile, the mode is attributed to the coupling between the electron drift wave and the ion acoustic waves. The ITG mode was discovered by Rudakov and Sagdeev [143]. These authors considered a simple model in slab geometry and for a flat density profile, neglecting kinetic effects. The inclusion of magnetic shear and kinetic effects were investigated by Pogutse [144]. Using a fluid model and assuming an adiabatic response for the electrons, a systematic study of the mode structure of the ITG mode, in sheared slab geometry, was carried out by Coppi and co-workers [145] and others [146, 147].

As shown by Coppi *et al* [17] and by Horton *et al* [148], the ITG mode in toroidal geometry is mainly driven by unfavorable magnetic curvature rather than the coupling of the electron drift wave to the ion acoustic waves [148]. It is worth noting that other pressure-gradient-driven modes, such as the collisionless trapped-particle mode [149], the trapped-electron mode [150] and the residual trapped-ion mode [151], can be driven unstable in the presence of unfavorable magnetic curvature.

Since the ion pressure is a source of free energy that can drive the mode, the linear growth rate depends on the radial density scalelength, L_n, and the radial ion temperature scalelength, $L_{T\mathrm{i}}$. In toroidal geometry, the growth rate also depends on the toroidicity parameter, $\epsilon_n \equiv L_n/\bar{R}$, the safety factor, q, and the global magnetic shear, $\hat{s} \equiv r dq/dr/q$. For a peaked density profile, the η_i mode can be driven unstable when $\eta_\mathrm{i} \equiv L_n/L_{T\mathrm{i}}$ exceeds a threshold value $\eta_{\mathrm{i}c}$. The threshold value $\eta_{\mathrm{i}c}$ is typically of the order of one. In the weak density limit ($1/L_n = 0$), the relevant parameter governing this mode is $L_{T\mathrm{i}}/R$ [152].

Many authors have considered a fluid approach in order to determine of the threshold η_{ic} [153, 154, 155, 156]. However fluid models have the fundamental problem that, for $\eta_i \sim \eta_{ic}$, the fluid approximation is not valid since the mode is affected both by magnetic drift and Landau resonances. These fluid models usually assume that the effect of the parallel dynamics is to localize the eigenfunction in the bad curvature region, while the effect on the threshold is small. A more accurate treatment requires a kinetic theory. However, some fluid models [154] can provide a fairly accurate picture of the ITG and η_i modes in some specific regimes. Furthermore, fluid models are mathematically more tractable than kinetic models. In particular, the *nonlinear* dynamics can be studied with fluid models [157, 158, 159, 160, 161, 162, 163, 164, 165]. New fluid equations which retain kinetic effects, the gyro-Landau fluid equations, have been recently developed [118, 119, 166]. These models are in good agreement with fully kinetic models [167, 120].

Most of the papers dealing with the kinetic η_i and ITG modes use a simple geometry of a tokamak with circular, concentric magnetic surfaces. The work of Rewoldt and Tang [168] is the notable exception. Using an integral kinetic equation, Dong and co-workers [169] present a systematic study of the effects of toroidicity, safety factor, global magnetic shear and ion-to-electron temperature ratio, $\tau \equiv T_i/T_e$. The authors show that, for moderate shear and $\epsilon_n = 0.2$, the maximum growth rate peaks around $k_\theta \rho_s \simeq 0.5$, where $k_\theta = nq/r$ and ρ_s is the ion thermal gyro-radius evaluated at the electron temperature. The growth rate is maximized for $\epsilon_n \simeq 0.2$, while other parameters are kept fixed. Numerical calculations show that the maximum growth rate is obtained for moderate global magnetic shear, $\hat{s} \simeq 0.5$. The mode rotates in the ion direction with a real frequency which becomes more negative as $k_\theta \rho_s$ increases.

The electron dynamics also modifies the ITG and η_i modes. In the flat density limit, the effect of trapped electron dynamics on these modes is small [170]. As the parameter η_i increases, it has been shown by Rewoldt and Tang [168] that the dominant electrostatic instability evolves from the trapped electron mode to the ITG

mode. At low electron collisionality, the mode rotates in the electron direction; as the electron collision frequency increases, the real part of the frequency decreases, vanishes and ultimately becomes negative (ion direction) [168]. Fluid models, such as the one of Nilsson and Weiland [171], can also be used to retain the effects of trapped electrons. The trapped ions can also alter the mode [172, 169, 173, 174]. In particular, a detailed study of the η_i mode in tokamak geometry, including an accurate Fokker-Planck collision operator for ion-ion collisions, has been carried out by Xu and Rosenbluth [173]. These authors show that one important consequence of the effects of ion-ion collisions is the stabilization of the long-wavelength part of the spectrum. This is an important result because long-wavelength instabilities can produce large cross-field transport.

As discussed in the beginning of this section, it is important to treat finite Larmor radius (FLR) effects and kinetic effects, such as Landau damping, accurately. We therefore use the ion gyro-kinetic equation to study the η_i mode in stellarator geometry. As a first approximation, we neglect the ion trapping and ion-ion collisions. As we shall see below, the neglect of these effects drastically simplifies the solution of the gyro-kinetic equation. Collisional and trapping effects can be retained in the model; the code developed by M. Kotschenreuther [111, 175] for tokamak geometry takes into account such effects.

6.2 Ion dynamics

This section is divided in 3 parts; in subsection 6.2.1, we specify the equilibrium; the representation of the perturbed quantities is presented in subsection 6.2.2. The ion collisionless gyro-kinetic equation is written in a form convenient for numerical work in subsection 6.2.3, where the quasineutrality condition is also given.

6.2.1 Equilibrium

One aim of this chapter is to study the ion gyro-kinetic equation in fully 3-dimensional geometry. It is therefore convenient to write the confining magnetic

field in straight-field-line coordinates [29]

$$\mathbf{B} = \boldsymbol{\nabla}\alpha \times \boldsymbol{\nabla}\psi \,, \tag{6.1}$$

where $\alpha \equiv \zeta - q\theta$ is the field line label and $2\pi\psi$ is the enclosed poloidal flux. θ and ζ are the poloidal and toroidal angle-like coordinates (with period 2π), respectively. As before, s is the normalized radial label. The effective radius of the magnetic surfaces is $r_{\text{eff}} \equiv \bar{a}\sqrt{s}$, where $\bar{a}$ is the average minor radius of the last closed magnetic surface. We recall that, in the coordinate system (s, θ, ζ), the Jacobian of the transformation, $\mathcal{J} \equiv [\boldsymbol{\nabla} s \cdot (\boldsymbol{\nabla}\theta \times \boldsymbol{\nabla}\zeta)]^{-1}$, has the dimensionality of a volume.

6.2.2 Perturbation representation

As discussed in chapter 4, the most unstable modes are characterized by $k_{||}/k_{\perp} \ll 1$, where, as before, $k_{||}$ and $k_{\perp}$ are the magnitude of the parallel and perpendicular components of the wavevector $\mathbf{k}$, respectively. The theory presented here is valid in the linear regime and the amplitude of the fluctuations are assumed to be small. For instance, a physical quantity F is written as $F = F_0 + \delta F$, where F_0 and δF are the equilibrium and perturbed parts of F, respectively and $\delta F/F_0 \ll 1$ is assumed. We exploit the smallness of $\delta F/F_0$ and $k_{||}/k_{\perp}$ by using the ballooning representation [57, 62, 63]

$$\tilde{F} \equiv \frac{\delta F}{F_0} = \widehat{F} \exp\left(i\frac{S}{\epsilon}\right) \,, \tag{6.2}$$

where S is the eikonal and $\epsilon \ll 1$ is a smallness parameter (expansion parameter). The eikonal and the amplitude F are assumed to vary on the equilibrium scalelength so that the ordering $|\bar{R}\boldsymbol{\nabla}\widehat{F}| \sim |\bar{R}\boldsymbol{\nabla}S| = \mathcal{O}(1)$ is assumed. Formally the amplitude $\widehat{F}$ must be expanded in ascending powers of ϵ. Following Dewar *et al* [80] we demand that the eikonal satisfies $\mathbf{B}\cdot\boldsymbol{\nabla}S = 0$ to all orders in ϵ. The spatial variation of $\widehat{F}$ represents the deviation from flute-like modes.

In stellarator geometry, one can use the extended toroidal angle ζ (instead of θ as in the tokamak case) as a label along the field line and the amplitude in equation (6.2) is written as $\widehat{F} = \widehat{F}(\zeta, t)$. To recover the standard form of the normal mode analysis, we make the transformation $\widehat{F}(\zeta, t) \mapsto \widehat{F}(\zeta)\exp(-i\omega t)$, where ω is

the normal mode frequency. The requirement $\mathbf{B}\cdot\boldsymbol{\nabla}S = 0$ implies that $S = S(\alpha, q)$ where here q is used as a radial instead of s or ψ. It is natural to introduce the lowest-order perpendicular wavevector as [80]

$$\begin{aligned} \mathbf{k}_\perp &\equiv \epsilon^{-1}\boldsymbol{\nabla}S\,, \\ &= \epsilon^{-1}\frac{\partial S}{\partial \alpha}\,(\boldsymbol{\nabla}\alpha + \theta_k\boldsymbol{\nabla}q)\,, \\ &= n\frac{\partial S}{\partial \alpha}\,(\boldsymbol{\nabla}\alpha + \theta_k\dot{q}\boldsymbol{\nabla}s)\,, \end{aligned} \tag{6.3}$$

where $\theta_k \equiv (\partial S/\partial s)/(\partial S/\partial q)$ and $n \equiv 1/\epsilon \gg 1$. A dot denotes a derivative with respect to the normalized radial label s. For simplicity, we consider an eikonal of the form $S = \alpha + \bar{S}(q)$, and θ_k can now be seen as a free parameter (or 'radial mode number'). With this simplification, the lowest-order perpendicular wavevector reads

$$\mathbf{k}_\perp = n\left[\boldsymbol{\nabla}\zeta - q\boldsymbol{\nabla}\theta - \dot{q}\,(\theta - \theta_k)\,\boldsymbol{\nabla}s\right]\,, \tag{6.4}$$

and n can be interpreted as the toroidal mode number. The left-hand side of equation (6.2) must satisfy the periodicity requirements in the poloidal and toroidal directions. The phase factor on the right-hand side of equation (6.2), however, is clearly not a periodic function of θ and ζ when the global shear is nonzero, $\dot{q} \neq 0$. Therefore one has to consider the amplitude $\widehat{F}$ to be defined on the covering space, $\zeta = [-\infty, +\infty]$. The problem of periodicity requirements in toroidal systems has been discussed by Dewar *et al* [80] and others [63, 57].

6.2.3 Ion gyro-kinetic equation

In this section, we describe the assumptions used in our model. We write the collisionless ion gyro-kinetic equation in a form convenient for numerical work and identify the quantities which depend on the structure of $\mathbf{B}$.

We consider a low-β plasma with singly-charged ions and the magnetic perturbations are neglected. In such a plasma the (fluctuating) electric field is derivable from a potential, $\mathbf{E} = -\boldsymbol{\nabla}\Phi$, where Φ is the fluctuating electrostatic potential. We also assume that collisional and trapping effects on the ion dynamics can be neglected. This neglect cannot always be justified, especially in the highly inhomogeneous magnetic field of a stellarator plasma.

For sake of simplicity, we use the linear, collisionless gyro-kinetic equation for the ions. On the other hand, the electron population is assumed to be in the collisional regime (low T_e) and, again, particle trapping is neglected. Fluid equations [13] are used to describe the electron dynamics. Therefore the dissipative trapped electron mode (DTEM), and many other trapped particle modes, cannot be study with our model. Trapped particles and collisional effects can be treated accurately with the code developed by Kotschenreuther [111, 175] for tokamak geometry using the $\hat{s} - \alpha$ model [57].

The method used in the present model is the following. The perturbed ion density is obtained by solving the ion gyro-kinetic equation while the perturbed electron density is calculated from fluid equations. These quantities depend on the electrostatic potential and we use the quasineutrality condition

$$n_i(\Phi) = n_e(\Phi) \ , \tag{6.5}$$

as a closure relation. The perturbed ion density is determined below and the perturbed electron density is given in section (6.4).

Making use of the ballooning representation (6.2), the fluctuating electrostatic potential can be written in normalized form as

$$\tilde{\Phi} \equiv \frac{e\Phi}{T_{e0}} = \hat{\Phi} \exp\left(i\frac{S}{\epsilon}\right) \ , \tag{6.6}$$

where T_{e0} is the equilibrium electron temperature. As discussed in chapter 5, the equilibrium distribution for the ions must be independent of the gyro-angle and constant along the magnetic field line [63, 81, 87, 86]. These requirements are fulfilled for a Maxwellian distribution provided the equilibrium plasma density and ion temperature satisfy $\nabla_{||} n_0 = \nabla_{||} T_{i0} = 0$ which is automatically satisfied since n_0 and T_{i0} are flux surface quantities. Since we are interested in small departure from thermodynamic equilibrium, it is a good approximation to set the parallel gradients of the equilibrium ion temperature and plasma density to zero. We assume that the equilibrium ion distribution function is indeed a Maxwellian

$$F_{Mi} = \frac{n_0}{\pi^{3/2} {v_{thi}}^3} \exp\left(-\frac{v^2}{{v_{thi}}^2}\right) \ , \tag{6.7}$$

where $v_{\rm thi} \equiv \sqrt{2T_{\rm i0}/m_{\rm i}}$ is the ion thermal velocity.

Following Xu and Rosenbluth [173], the amplitude of the perturbed ion distribution function can be written as

$$\widehat{f}_{\rm i} = -\frac{\widehat{\Phi}}{\tau}\, F_{\rm Mi} + \left(\widehat{h}_{\rm i} + \frac{\widehat{\Phi}}{\tau}\, J_0 F_{\rm Mi}\right) J_0 \ , \tag{6.8}$$

where the nonadiabatic part $\widehat{h}_{\rm i}$ satisfies the linear, collisionless gyro-kinetic equation

$$\frac{\partial \widehat{h}_{\rm i}}{\partial t} = -v_{||}\nabla_{||}\left(\widehat{h}_{\rm i} + \frac{\widehat{\Phi}}{\tau}\, F_{Mi} J_0\right) - i\,\omega_{di}\,\widehat{h}_{\rm i} + i\left(\omega_{\star {\rm i}}^{T} - \omega_{di}\right)\frac{\widehat{\Phi}}{\tau}\, F_{Mi} J_0 \ . \tag{6.9}$$

In equations (6.8,6.9), $\tau \equiv T_{\rm i0}/T_{\rm e0}$, J_0 is the zeroth-order Bessel function (arising from the averaging over the fast gyro-motion) with argument $\xi_\perp \equiv k_\perp v_\perp/\omega_{\rm ci}$, $k_\perp = \sqrt{\mathbf{k}_\perp \cdot \mathbf{k}_\perp}$ is the magnitude of the lowest-order perpendicular wavevector and $\omega_{\rm ci} \equiv eB/(m_{\rm i}c)$ is the ion cyclotron frequency. Note that $\xi_\perp$ depends on the perpendicular velocity as well as the position along the field line through the dependence of B and $k_\perp$. The effect of the global magnetic shear manifests itself in the secular behavior of $k_\perp$.

The first term on the right-hand side of equation (6.8) is the adiabatic part of the perturbed ion distribution function, while the last term represents the contribution from the polarization. The polarization term arises because the guiding center density and the particle density do not coincide when the ion Larmor radius is finite. For instance, in an infinitely magnetized plasma, $B \mapsto \infty$, then $\xi_\perp \mapsto 0$ and $J_0 \mapsto 1$; in this case $\widehat{f}_{\rm i} \mapsto \widehat{h}_{\rm i}$, that is to say the guiding center density and the particle density are equal, as they should be.

In equation (6.9)

$$\omega_{\star {\rm i}}^{T} \equiv \frac{cT_{\rm i}}{eBF_{\rm Mi}}\left(\widehat{\mathbf{e}}_{||} \times \mathbf{k}_\perp\right) \cdot \boldsymbol{\nabla} F_{\rm Mi} \ , \tag{6.10}$$

is the velocity-dependent ion diamagnetic drift frequency and

$$\omega_{\rm di} \equiv {\omega_{\rm ci}}^{-1}\left[\widehat{\mathbf{e}}_{||} \times \left({v_{||}}^2 \boldsymbol{\kappa} + \frac{{v_\perp}^2}{2}\,\frac{\boldsymbol{\nabla} B}{B} + \frac{e}{m_{\rm i}}\,\boldsymbol{\nabla}\Phi_0\right)\right] \cdot \mathbf{k}_\perp \ , \tag{6.11}$$

is the velocity-dependent ion curvature drift frequency. In equations (6.10,6.11), $\widehat{\mathbf{e}}_{||} \equiv \mathbf{B}/B$ is the unit vector along $\mathbf{B}$, $\boldsymbol{\kappa}$ is the magnetic curvature, Φ_0 is the equilibrium electrostatic potential and $\nabla_{||}$ is the parallel gradient operator keeping the

field line label constant. For simplicity, we neglect the equilibrium electric field $\mathbf{E}_0 = -\boldsymbol{\nabla}\Phi_0 = 0$. A nonvanishing $\mathbf{E}_0$ implies the presence of equilibrium plasma flows, which are neglected in the gyro-kinetic equation (6.9). Furthermore, in the presence of plasma flows, the ballooning representation (6.2) must also be modified [176, 177, 178].

The perturbed ion density is obtained by direct integration of equation (6.8). Introducing the amplitude of the normalized perturbed ion density $\widehat{n}_\mathrm{i} \equiv \widehat{\delta n_\mathrm{i}}/n_0$ we obtain

$$\widehat{n}_\mathrm{i} = -\frac{\widehat{\Phi}}{\tau}\int d^3\,v\frac{F_{M\mathrm{i}}}{n_0} + \frac{1}{n_0}\int d^3v\; J_0\, F_{M\mathrm{i}}\,\widehat{g} + \frac{\widehat{\Phi}}{\tau}\int d^3v\; {J_0}^2\,\frac{F_{M\mathrm{i}}}{n_0}\;, \tag{6.12}$$

where $\widehat{g} \equiv \widehat{h}_\mathrm{i}/F_{M\mathrm{i}}$. The second integral on the right-hand side of equation (6.12) is computed numerically once $\widehat{g}$ is known (Section 6.4). After an appropriate change of variable, the last integral can be written [51]

$$\begin{aligned}\frac{1}{n_0}\int d^3v\; {J_0}^2\, F_{M\mathrm{i}} &= \frac{1}{b_\mathrm{i}}\int_0^{+\infty} dy\; y\; {J_0}^2\,(y)\exp\left(-\frac{y^2}{2b_\mathrm{i}}\right)\;,\\ &= I_0\,(b_\mathrm{i})\exp\,(-b_\mathrm{i})\;,\end{aligned} \tag{6.13}$$

where I_0 is the modified Bessel function of zeroth order with argument $b_\mathrm{i} \equiv (k_\perp \rho_{\mathrm{thi}})^2/2$ and ρ_{thi} is the ion thermal gyro-radius. Substituting equation (6.13) in equation (6.12), the quasineutrality condition (6.5) yields an equation for the perturbed electrostatic potential

$$\widehat{\Phi} = \frac{\tau}{G\,(b_\mathrm{i})}\left[\widehat{n_\mathrm{e}} - \frac{2}{\sqrt{\pi}}\int_0^{\infty} dx_\perp \int_{-\infty}^{+\infty} dx_{||} x_\perp J_0\,(\xi_\perp)\,\widehat{g}\exp\left(-{x_{||}}^2 - {x_\perp}^2\right)\right]\;, \tag{6.14}$$

where $x_{||} \equiv v_{||}/v_{\mathrm{thi}}$, $x_\perp \equiv v_\perp/v_{\mathrm{thi}}$ and $\xi_\perp = \sqrt{2b_\mathrm{i}}x_\perp$. Here $\widehat{n_\mathrm{e}}$ represents the amplitude of the normalized electron density perturbation and is yet undetermined. We have also introduced $G\,(b_\mathrm{i}) \equiv I_0\,(b_\mathrm{i})\exp\,(-b_\mathrm{i}) - 1$ which scales linearly with its argument in the long-wavelength limit.

Returning to the ion gyro-kinetic equation, one can show that

$$\omega_{d\mathrm{i}} = 2\,\tau\,\omega_{\star\mathrm{e}}\,\epsilon_n \xi_d\,(\zeta)\left({x_{||}}^2 + \frac{{x_\perp}^2}{2}\right)\;, \tag{6.15}$$

and

$$\omega_{\star \mathrm{i}}^{T} = -\tau\, \omega_{\star \mathrm{e}}\, \xi_{\star}\left(\zeta\right) \left[1 + \eta_{\mathrm{i}} \left({x_{||}}^{2} + {x_{\perp}}^{2} - \frac{3}{2} \right)\right] . \tag{6.16}$$

Here, $\omega_{\star \mathrm{e}} \equiv \left(cT_{\mathrm{e}0} k_{\theta}\right) / \left(eB_0 L_n\right)$ is the electron diamagnetic drift frequency; $k_{\theta} \equiv nq/\bar{a}$ is the characteristic magnitude of the perpendicular wavevector; $\eta_{\mathrm{i}} \equiv L_n / L_{T\mathrm{i}}$; B_0 is the magnetic field strength at the magnetic axis; $\epsilon_n \equiv L_n / \bar{R}$ is the toroidicity parameter;

$$\xi_{\star}\left(\zeta\right) \equiv \frac{B_0}{B}\, \bar{a} \boldsymbol{\nabla} s \cdot \left(\widehat{\mathbf{e}}_{||} \times \widehat{\mathbf{e}}_{\perp} \right) , \tag{6.17}$$

where $\widehat{\mathbf{e}}_{\perp} \equiv \mathbf{k}_{\perp} / k_{\theta}$ is the normalized perpendicular wavevector; finally

$$\xi_{d}\left(\zeta\right) \equiv \frac{B_0}{B}\, \widehat{\mathbf{e}}_{\perp} \cdot \left(\widehat{\mathbf{e}}_{||} \times \frac{\boldsymbol{\nabla} B}{B} \right) . \tag{6.18}$$

All the terms on the right-hand sides of equations (6.17,6.18) are evaluated along the magnetic field line. After straightforward algebra, the normalized gyro-kinetic equation reads

$$\frac{\partial \widehat{g}}{\partial t''} = -\Omega_{b\mathrm{i}}\, \epsilon_n x_{||}\, \xi_{||}\, \left(\zeta\right) \frac{\partial}{\partial \zeta} \left(\widehat{g} + \frac{\widehat{\Phi}}{\tau}\, J_0 \right) - i\, \Omega_{d\mathrm{i}}\, \widehat{g} + i \left(\Omega_{\star \mathrm{i}}^{T} - \Omega_{d\mathrm{i}} \right) \frac{\widehat{\Phi}}{\tau} , \tag{6.19}$$

where $\Omega_{b\mathrm{i}} \equiv v_{\mathrm{thi}} / \left(\omega_{\star \mathrm{e}} L_n\right) = \sqrt{2\tau / b}$, $\Omega_{d\mathrm{i}} \equiv \omega_{d\mathrm{i}} / \omega_{\star \mathrm{e}}$ and $\Omega_{\star \mathrm{i}}^{T} = \omega_{\star \mathrm{i}}^{T} / \omega_{\star \mathrm{e}}$. We have introduced the normalized time $t'' \equiv \omega_{\star \mathrm{e}} t$ and the parameter $b \equiv \left(k_{\theta} \rho_{s0}\right)^2$, where ρ_{s0} is ρ_s evaluated at the magnetic axis. The nondimensional quantities $\xi_{||}\left(\zeta\right)$, $\xi_{d}\left(\zeta\right)$ and $\xi_{\star}\left(\zeta\right)$ are given in appendix D. The remaining quantities that depend on the details of the magnetic field are b_{i}, which enters the quasineutrality condition, and $\xi_{\perp}$, which is the argument of the Bessel function in the gyro-kinetic equation. It can be shown that these quantities can be written as $\xi_{\perp} = \sqrt{2\tau b}\; x_{\perp}\; P\left(\zeta\right)$ and $b_{\mathrm{i}} = \tau b P^2\left(\zeta\right)$ where

$$P\left(\zeta\right) \equiv B_0 \frac{\sqrt{\widehat{\mathbf{e}}_{\perp} \cdot \widehat{\mathbf{e}}_{\perp}}}{B} . \tag{6.20}$$

6.3 Electron dynamics

The perturbed electron density, which is yet unspecified, is required in the quasineutrality condition (6.14). One possible model is to simply assume that

the transport along the field line is large enough to short-circuit charge separation. In this model, the electron response is adiabatic so that $\widehat{n_e} \simeq \hat{\Phi}$. However, if the temperature of the electrons is not too large, then ion-electron collisions can prevent the electron density perturbation from reaching a Boltzmann distribution. We can use a fluid model to obtain the perturbed electron density $\widehat{n_e}$ provided the parallel wavelength of the mode is much larger than the electron mean free path. The electron mean free path, denoted λ_e, scales like ${T_e}^2/n$, and it is therefore strongly dependent on the electron temperature. With $k_{||}$ denoting the magnitude of the parallel wavevector, we assume that $k_{||}\lambda_e \sim \epsilon$, where ϵ is a smallness parameter. The second requirement for a fluid theory to be applicable is that the characteristic perpendicular wavelength of the mode must be larger than the electron thermal gyro-radius. For our modes of interest, this condition is largely satisfied. For instance, for an isothermal discharge ($T_e \simeq T_i$), we have $k_\perp \rho_{the} \sim (m_e/m_i)^{1/2} k_\perp \rho_{thi} \sim (m_e/m_i)^{1/2} \ll 1$, assuming $k_\perp \rho_{thi} \sim 1$. The most stringent condition is thus $k_{||}\lambda_e = \mathcal{O}(\epsilon)$.

Another possible approach is to use the drift-kinetic equation for the electrons. However the solution of the electron drift kinetic equation requires a careful treatment of regions of trapping and circulating electrons [83]. For simplicity we neglect trapped electrons, even though the fraction of trapped electrons can be substantial in stellarator plasmas.

Our aim is to derive an equation which relates the perturbed electron density to the perturbation in the electrostatic potential. In general, the electron temperature fluctuations must be retained in the model. The treatment of temperature fluctuation requires an additional equation, the energy equation. For simplicity, we also neglect temperature fluctuations. Hence our model equations are the electron continuity equation [13]

$$\frac{\partial n_e}{\partial t} + \boldsymbol{\nabla}\cdot(n_e \mathbf{V}_e) = 0 \,, \tag{6.21}$$

and the electron momentum equation

$$e n_e \left(\mathbf{E} + \frac{\mathbf{V}_e \times \mathbf{B}}{c} \right) + \boldsymbol{\nabla} p_e = \mathbf{R}_{ei} \,. \tag{6.22}$$

In equations (6.21,6.22), $\mathbf{V}_\mathrm{e}$ is the electron *fluid* velocity and $p_\mathrm{e} = n_\mathrm{e} T_\mathrm{e}$ is the electron pressure. In equation (6.22), we have neglected the electron inertia and the electron stress tensor. The term on the right-hand side of the electron momentum equation is the friction force arising from electron-ion collisions which, for a plasma with singly-charged ions, is [13]

$$\mathbf{R}_\mathrm{ei} = \eta_{||} \mathbf{J}_{||} + \eta_\perp \mathbf{J}_\perp - 0.71\, n_\mathrm{e} \boldsymbol{\nabla}_{||} T_\mathrm{e} - \frac{3\, n_\mathrm{e}}{2\, \omega_{ce} T_\mathrm{e}}\, \widehat{\mathbf{e}}_{||} \times \boldsymbol{\nabla} T_\mathrm{e} \,. \tag{6.23}$$

Here $\eta_{||}$ and $\eta_\perp$ are the parallel and perpendicular classical resistivities, respectively; the parallel and perpendicular current densities are denoted $\mathbf{J}_{||}$ and $\mathbf{J}_\perp$, respectively; $\omega_{ce} \equiv (eB)\,/\,(m_\mathrm{e} c)$ is the electron cyclotron frequency; finally, τ_e is the electron basic collisional time. In the low-frequency regime, $\omega/\omega_{ci} \sim \epsilon \ll 1$, we can solve equation (6.22) perturbatively for $\mathbf{V}_{\mathrm{e}\perp}$ yielding

$$\mathbf{V}_{\mathrm{e}\perp} = \mathbf{V}_E + \mathbf{V}_{de} + \mathbf{V}_c \,, \tag{6.24}$$

where

$$\begin{aligned} \mathbf{V}_E &\equiv \frac{c}{B}\, \mathbf{E} \times \widehat{\mathbf{e}}_{||} \,, \\ \mathbf{V}_{de} &\equiv \frac{c}{e n_\mathrm{e} B}\, \boldsymbol{\nabla} p_\mathrm{e} \times \widehat{\mathbf{e}}_{||} \,, \\ \mathbf{V}_c &\equiv \frac{c}{e n_\mathrm{e} B}\, \widehat{\mathbf{e}}_{||} \times \mathbf{R}_\mathrm{ei} \,, \end{aligned} \tag{6.25}$$

are the lowest-order $\mathbf{E}\times\mathbf{B}$ drift velocity, the electron diamagnetic drift velocity and the ion-electron-collision-driven drift velocity, respectively. The last contribution in equation (6.24) is $(\omega_{ce}\tau_\mathrm{e})^{-1}$ times smaller than $\mathbf{V}_E$ or $\mathbf{V}_{de}$. For a low-T_e, high-density edge plasma, one gets $\omega_{ce}\tau_\mathrm{e} \approx 10^5$. To a good approximation the perpendicular electron flux can be written as $\boldsymbol{\Gamma}_{\mathrm{e}\perp} \simeq n_\mathrm{e}\,(\mathbf{V}_E + \mathbf{V}_{de})$. Taking the scalar product of equation (6.22) with $\mathbf{B}$ and neglecting the electron temperature fluctuation yields

$$\eta_{||} J_{||} = p_{\mathrm{e}0} \nabla_{||} \widehat{h} \,, \tag{6.26}$$

where $\widehat{h} \equiv \widehat{n_\mathrm{e}} - \widehat{\Phi}$ is the nonadiabatic response of the electrons. We have neglected the equilibrium parallel current density when deriving equation (6.26); this is a low-β approximation and is well justified in small and medium size stellarator plasmas. If $J_{||0}$ is retained in the model, one can study the current-driven instability [179].

Using equation (6.26), the divergence of the parallel electron flux is given by

$$\boldsymbol{\nabla}\cdot\boldsymbol{\Gamma}_{\mathrm{e}||} = \boldsymbol{\nabla}\cdot\boldsymbol{\Gamma}_{\mathrm{i}||} - \frac{1}{e}\,\boldsymbol{\nabla}\cdot\mathbf{J}_{||}\ . \tag{6.27}$$

We pay special attention to the geometrical details. In particular we note that, in the low-β approximation,

$$\begin{aligned}
\boldsymbol{\nabla}\cdot\mathbf{V}_E &= -2\,\frac{\boldsymbol{\nabla}B}{B}\cdot\mathbf{V}_E\ , \\
\boldsymbol{\nabla}\cdot\left(n_{\mathrm{e}}\mathbf{V}_{de}\right) &= -2\,n_{\mathrm{e}}\,\frac{\boldsymbol{\nabla}B}{B}\cdot\mathbf{V}_{de}\ , \\
\boldsymbol{\nabla}\cdot\widehat{\mathbf{e}}_{||} &= -\widehat{\mathbf{e}}_{||}\cdot\frac{\boldsymbol{\nabla}B}{B}\ .
\end{aligned} \tag{6.28}$$

All these terms are curvature effects that vanish in slab geometry. The divergence of the perpendicular electron flux reads

$$\boldsymbol{\nabla}\cdot\boldsymbol{\Gamma}_{\mathrm{e}\perp} = \boldsymbol{\Gamma}_E\cdot\left(\frac{\boldsymbol{\nabla}n_{\mathrm{e}}}{n_{\mathrm{e}}} - 2\frac{\boldsymbol{\nabla}B}{B}\right) - 2\boldsymbol{\Gamma}_{de}\cdot\frac{\boldsymbol{\nabla}B}{B}\ . \tag{6.29}$$

where we have introduced $\boldsymbol{\Gamma}_E \equiv n_{\mathrm{e}}\mathbf{V}_E$ and $\boldsymbol{\Gamma}_{de} \equiv n_{\mathrm{e}}\mathbf{V}_{de}$. After straightforward algebra, using the ballooning representation, one gets

$$\boldsymbol{\nabla}\cdot\boldsymbol{\Gamma}_{\mathrm{e}\perp} = i\,n_0\,\omega_{\mathrm{e}\star}\left[S_\perp\widehat{n_{\mathrm{e}}} - \left(R_\perp + S_\perp\right)\widehat{\Phi}\right]\ , \tag{6.30}$$

where we have introduced two non-dimensional functions defined along the magnetic field line

$$\begin{aligned}
R_\perp &\equiv \bar{a}\boldsymbol{\nabla}s\cdot\frac{\left(\widehat{\mathbf{e}}_{||}\times\widehat{\mathbf{e}}_\perp\right)}{B_\star}\ , \\
S_\perp &\equiv 2\mathbf{Q}\cdot\frac{\left(\widehat{\mathbf{e}}_{||}\times\widehat{\mathbf{e}}_\perp\right)}{B_\star}\ .
\end{aligned} \tag{6.31}$$

We have defined $\mathbf{Q} \equiv L_n\boldsymbol{\nabla}B/B \sim \epsilon_n \equiv L_n/\bar{R}$ and we note that $\boldsymbol{\nabla}\cdot\widehat{\mathbf{e}}_{||} = -Q_{||}/L_n$. Substituting equation (6.26) in equation (6.27) and using equation (6.30) in the electron continuity equation (6.21) yields

$$\begin{aligned}
\frac{\partial\widehat{n_{\mathrm{e}}}}{\partial t''} &= 2\,\xi_c\left(L_n{}^2\nabla_{||}{}^2\widehat{h} - Q_{||}L_n\nabla_{||}\widehat{h}\right) - \frac{\boldsymbol{\nabla}\cdot\boldsymbol{\Gamma}_{\mathrm{i}||}}{n_0\omega_{\star\mathrm{e}}} \\
&+ i\left[\left(\xi_\star - 2\,\epsilon_n\,\xi_d\right)\,\widehat{\Phi} + 2\,\epsilon_n\,\xi_d\,\widehat{n}\right]\ ,
\end{aligned} \tag{6.32}$$

where we have made use of the relations $R_\perp = \xi_\star$ and $S_\perp = -2\epsilon_n\xi_d$ and where we have introduced the 'collisional parameter' $\xi_c \equiv \left(\omega_{ce0}\tau_{\mathrm{e}}\right)/\left(k_\theta L_n\right)$. Here ω_{ce0} is

the electron cyclotron frequency evaluated at the magnetic axis. For modes with $k_\theta \rho_s \sim 1$, it can be shown that the collisional parameter is much larger than unity.

The divergence of the parallel ion flux in equation (6.32) is determined directly from the perturbed ion distribution function (6.8). Letting $\widehat{H} \equiv J_0 \widehat{g} + \tau^{-1} \widehat{\Phi} \left({J_0}^2 - 1 \right)$ we have $\widehat{f}_{\rm i} = F_{M{\rm i}} \widehat{H}$. The divergence of the parallel ion flux is then

$$\boldsymbol{\nabla} \cdot \boldsymbol{\Gamma}_{{\rm i}||} = \sqrt{2\tau/b}\, n_0\, \omega_{\star {\rm e}} \left(L_n \nabla_{||} \widehat{\mathcal{L}} - Q_{||} \widehat{\mathcal{L}} \right) \ , \tag{6.33}$$

where

$$\widehat{\mathcal{L}} \equiv \frac{2}{\sqrt{\pi}} \int_0^\infty dx_\perp \int_{-\infty}^{+\infty} dx_{||}\, x_\perp\, x_{||}\, \exp\left(-{x_\perp}^2 - {x_{||}}^2 \right) \widehat{H} \ . \tag{6.34}$$

Then the perturbed electron density is governed by the following time-dependent, linear equation

$$\begin{aligned} \frac{\partial \widehat{n_{\rm e}}}{\partial t''} &= 2\, \xi_c \left({L_n}^2 \nabla_{||}{}^2 \widehat{h} - Q_{||} L_n \nabla_{||} \widehat{h} \right) \\ &+ \sqrt{2\tau/b} \left(Q_{||} \widehat{\mathcal{L}} - L_n \nabla_{||} \widehat{\mathcal{L}} \right) \\ &+ i \left(\xi_\star \widehat{\Phi} + 2\, i\, \epsilon_n\, \xi_d\, \widehat{h} \right) \ . \end{aligned} \tag{6.35}$$

The first term on the right-hand side of equation (6.35) describes the transport of current density along the magnetic field line; the second term represents the parallel ion *fluid* motion; and finally the third term is the transport of current density across the magnetic field.

6.4 Numerical method

In this section, we discuss the numerical solution of the time-dependent equations (6.19) and (6.35). These equations depend on the electrostatic potential. The quasineutrality condition (6.14) provides a closure relation for $\widehat{\Phi}$. The numerical solution of equations (6.19,6.35) involves two kinds of difficulties. The first is associated with the secular terms, $\Omega_{d{\rm i}}$, in the ion collisionless gyro-kinetic equation (6.19), and ξ_d, in the electron density equation (6.35). In the limit of large toroidal angle, it can be shown that these quantities scale linearly with ζ. Therefore, if the modes have a broad extent along the magnetic field line, the secular terms will be become important and the numerical integration then requires a small time step. It

is worth noting that both Ω_{di} and ξ_d, as well as $Q_{||}$, vanish in slab geometry.

Returning to the ion gyro-kinetic equation (6.19), we note that this equation is of the form

$$\frac{\partial \widehat{g}}{\partial t''} = -i\,\Omega_{\rm di}\,\widehat{g} + \ldots\,. \tag{6.36}$$

where the periodic terms and the contribution arising from the free streaming along **B** have been temporarily neglected. Clearly, at large values of the extended toroidal angle, Ω_{di} is large and equation (6.36) can be numerically unstable, depending on the numerical method used. The equation for the perturbed electron density also contains a secular term similar to equation (6.36).

The second difficulty is associated with the different characteristic time scales of the ion and electron dynamics. In particular, the characteristic time scale of equation (6.35) is much smaller than the ion time scale. The electron characteristic time scale is small because the transport along the field line is large [terms mutiplied by the collisional parameter ξ_c in equation (6.35)].

The perturbed ion distribution is stored in a three-dimensional array $\widehat{g}\left(\zeta, x_{||}, x_{\perp}\right)$ at each time step. The perturbed electron density $\widehat{n_{\rm e}}$ and the perturbed electrostatic potential $\widehat{\Phi}$ are stored in one-dimensional arrays. The infinite velocity domains of $x_{||}$ and $x_{\perp}$ are approximated by large finite domains. Specifically, a uniform grid for the (normalized) parallel velocity is setup as follows

$$x_{||_p} = -x_{||\rm max} + (p - 1/2)\,\Delta x_{||}\,, \tag{6.37}$$

where $\Delta x_{||} = 2x_{||\rm max}/N_{||}$, $x_{||\rm max}$ is the (positive-definite) maximum parallel velocity used in the integration, $N_{||}$ is the number of grid points and p is an integer running from 1 to $N_{||}$. Similarly, a uniform grid for the normalized perpendicular velocity is setup

$$x_{\perp r} = -x_{\perp\rm max} + (r - 1/2)\,\Delta x_{\perp}\,, \tag{6.38}$$

where $\Delta x_{\perp} = x_{\perp\rm max}/N_{\perp}$, $x_{\perp\rm max}$ is the maximum perpendicular in the integration and $N_{\perp}$ is the number of grid points. Here r is an integer which runs from 1 to $N_{\perp}$. The parameters $x_{||\rm max}, x_{\perp\rm max}, N_{||}$ and $N_{\perp}$ must be varied to ensure the reliability of

the results. Finally, a discrete grid along the toroidal angle is setup as follows

$$\zeta_j = -\zeta_{\max} + (j - 1/2)\,\Delta\zeta \tag{6.39}$$

where $\Delta\zeta = 2\ \zeta_{\max}/N_\zeta$ is the mesh size, $2\ \zeta_{\max}$ is the length of the domain of integration and the integer N_ζ is the number of grid points. The perturbed distribution function for the ions is advanced in time using the Lax method [50]. The Lax method is appropriate when the parameter ϵ_n is not too large. It should be noted that the secular term ω_d is multiplied by the parameter ϵ_n. Introducing $\mathcal{D} \equiv \widehat{g} + \phi$ and $\phi \equiv J_0\widehat{\Phi}/\tau$, the nonadiabatic part of the perturbed ion distribution is updated in time according to (dropping the hats for clarity)

$$\begin{aligned} g^{(n+1)}_{jpr} &= \frac{1}{2}\left[g^{(n)}_{j+1pr} + g^{(n)}_{j-1pr}\right] - C_{||jp}\frac{\Delta t}{2\Delta\zeta}\left[\mathcal{D}^{(n)}_{j+1pr} - \mathcal{D}^{(n)}_{j-1pr}\right] \\ &- i\omega_{djpr}\,\Delta t\,\mathcal{D}^{(n)}_{jpr} + i\omega_{\star jpr}\,\Delta t\,\phi^{(n)}_{jr}\ , \end{aligned} \tag{6.40}$$

where Δt is the time step of integration. Setting $\widehat{n}_e \mapsto N$ and dropping the hat notation, the electron continuity equation can be written as

$$\frac{\partial N}{\partial t} = D_{||}\frac{\partial^2 h}{\partial\zeta^2} - \beta_{||}\frac{\partial h}{\partial\zeta} - R_{||}\frac{\partial\mathcal{L}}{\partial\zeta} + W_{||}\mathcal{L} + 2i\left(\Phi + \epsilon_n\xi_d h\right)\ , \tag{6.41}$$

where

$$\begin{aligned} D_{||} &\equiv 2\,\xi_c\,\xi_{||}^2\,\epsilon_n^2\ , \\ \beta_{||} &\equiv \xi_c\,\xi_{||}\,\epsilon_n\left(2\,Q_{||} + \frac{\xi_{||}\epsilon_n}{\mathcal{J}}\,\frac{\partial\mathcal{J}}{\partial\zeta}\right)\ , \\ R_{||} &\equiv \sqrt{2\tau/b}\,\xi_{||}\,\epsilon_n\ , \\ W_{||} &\equiv \sqrt{2\tau/b}\,Q_{||}\ . \end{aligned} \tag{6.42}$$

The critical time step for the electrons is obtained by balancing the left-hand side of equation (6.41) with the diffusive term on the right-hand side. If one uses an explicit method to advance the electron continuity equation, then the time step must be chosen so that

$$\Delta t \ll \Delta t_e = \frac{(\Delta\zeta)^2}{\xi_c\epsilon_n^2}\ . \tag{6.43}$$

We note the strongly unfavorable scaling with the mesh size $\Delta\zeta$. As we shall see below, the magnetic field structure varies rapidly along ζ so that a small mesh size must be used. To bypass the stringent condition (6.43), it is advantageous to

advance equation (6.41) using an implicit method. The first and second terms and also the term with the secular contribution ξ_{d} are treated fully implicitly, while the remaining terms are treated with explicit finite differences. The resulting equation reads

$$a_j N_{j-1}^{(n+1)} + b_j N_j^{(n+1)} + c_j N_{j-1}^{(n+1)} = S_j^{(n)} \ , \tag{6.44}$$

where

$$\begin{aligned} a_j &= \frac{\Delta t}{\Delta\zeta}\left(\frac{\alpha_{||j}}{\Delta\zeta} + \frac{\beta_{||j}}{2}\right) , \\ b_j &= -\left[1 + 2\,\frac{\alpha_{||j}\Delta t}{(\Delta\zeta)^2}\right] , \\ c_j &= \frac{\Delta t}{\Delta\zeta}\left(\frac{\alpha_{||j}}{\Delta\zeta} - \frac{\beta_{||j}}{2}\right) , \end{aligned} \tag{6.45}$$

and the 'source term' on the right-hand side of equation (6.44) is

$$\begin{aligned} S_j^{(n)} &= \frac{\alpha_{||j}\Delta t}{(\Delta\zeta)^2}\left[\Phi_{j+1}^{(n)} - 2\Phi_j^{(n)} + \Phi_{j-1}^{(n)}\right] - \frac{\beta_{||j}\Delta t}{2\Delta\zeta}\left[\Phi_{j+1}^{(n)} - \Phi_{j-1}^{(n)}\right] \\ &+ 2\,i\Delta t\,(\epsilon_n - 1)\,\Phi_j^{(n)} + \frac{R_{||j}\Delta t}{2\Delta\zeta}\left[\mathcal{L}_{j+1}^{(n)} - \mathcal{L}_{j-1}^{(n)}\right] - N_j^{(n)} \ . \end{aligned} \tag{6.46}$$

The system of equations (6.44) can be written as a tridiagonal matrix, which is solved using the LU decomposition method [50]. Note that the solution of equation (6.44) does not require pivoting, a feature which considerably improves the vectorization of the numerical code. For all the runs presented in this chapter, a vectorization of ≥ 92 % was achieved.

6.5 Numerical results

In this section, the model equations described in the previous sections are solved numerically for the toroidal heliac H1-NF [21]. The dependences of the linear growth rate and the real part of the mode frequency on the toroidal mode number and the η_{i} parameter are presented. Most of the calculations are performed for only one field line. However, we also present some results for a set of different field lines.

The 3-dimensional equilibrium state is computed using the VMEC equilibrium [60,

61], with zero net toroidal current within each flux tube. The plasma pressure profile is of the form

$$p(s) = p(0)\ (1-s)^2\ . \tag{6.47}$$

The full equilibrium is computed for a set of 100 magnetic surfaces and for a volume-averaged $\bar{\beta}$ of 0.36 %. A mapping code is used to specify the equilibrium in straight-field-line coordinates. The magnetic surfaces are specified in a series of Fourier harmonics. For instance, the position vector $\mathbf{r}$ is written as

$$\mathbf{r} = R\cos\phi\ \widehat{\mathbf{x}} + R\sin\phi\ \widehat{\mathbf{y}} + Z\ \widehat{\mathbf{z}} \tag{6.48}$$

where

$$\begin{aligned} R &= \sum_{m=0}^{M}\sum_{n=-N}^{n=+N} R_{mn}\ \cos(\mu_{mn})\ , \\ Z &= \sum_{m=0}^{M}\sum_{n=-N}^{n=+N} Z_{mn}\ \sin(\mu_{mn})\ , \\ \phi &= \zeta - \frac{2\pi}{N_p}\sum_{m=0}^{M}\sum_{n=-N}^{n=+N} \widetilde{\phi}_{mn}\sin(\mu_{mn})\ . \end{aligned} \tag{6.49}$$

Here $\mu_{mn} \equiv m\theta + N_p n\zeta$ and $N_p = 3$ is the number of field periods of H1-NF. In equation (6.49), the input parameters are chosen as $N = 27$ and $M = 13$. Using equations (6.48,6.49), we can determine the covariant and contravariant basis vectors and any combinations of these quantities required in the calculations of equilibrium quantities such as $B(\zeta)$, $\xi_d(\zeta)$, $k_\perp(\zeta)$ and $\xi_{||}(\zeta)$.

All our calculations are performed on the magnetic surface $s_0 = 0.97$, which is shown in figures 3.10 and 3.11. The safety factor profile as a function of the normalized radial label s is shown in figure 6.1. The global shear is slightly negative for the magnetic surface used in our calculations.

The linear growth rate, normalized to the electron diamagnetic drift frequency $\omega_{\star e}$, is computed as follows

$$\gamma(t'') = \frac{1}{|\left\langle\widehat{\Phi}\right\rangle_\zeta|}\ \frac{\partial|\left\langle\widehat{\Phi}\right\rangle_\zeta|}{\partial t''}\ . \tag{6.50}$$

where $|G|$ denotes the norm of G and $\left\langle \widehat{\Phi} \right\rangle_\zeta$ denotes an average along the magnetic field line

$$\left\langle \widehat{\Phi} \right\rangle_\zeta \equiv \frac{1}{2\zeta_\mathrm{m}} \int_{\zeta_0-\zeta_\mathrm{m}}^{\zeta_0+\zeta_\mathrm{m}} \widehat{\Phi}\left(\zeta'\right) d\zeta' \ . \tag{6.51}$$

Here ζ_0 represents a toroidal angle of reference. Unlike the axi-symmetric tokamak configuration, the poloidal angle, θ_0, *and* the toroidal angle, ζ_0, must be given to specify the field line of reference (on a given magnetic surface with radial position s_0). The real part of the mode frequency, normalized to $\omega_{\star\mathrm{e}}$, is denoted ω_r. It is computed as follows

$$\omega_\mathrm{r}(t'') = \Re\left(\frac{1}{\left\langle \widehat{\Phi} \right\rangle_\zeta} \frac{\partial \left\langle \widehat{\Phi} \right\rangle_\zeta}{\partial t''} \right) \ , \tag{6.52}$$

where $\Re(\eta)$ denotes the real part of η. The parameter ζ_m must be chosen sufficiently large so that the growth rate (6.50) and the real part of the mode frequency (6.52) become independent of ζ_m itself. The physically meaningful growth rate and real frequency are obtained for large t'', when $\partial\gamma/\partial t'' \simeq 0$ and $\partial\omega_\mathrm{r}/\partial t'' \simeq 0$.

For our calculations, we have chosen the following parameters: $x_{||\mathrm{max}} = v_{||\mathrm{max}}/v_\mathrm{thi} = 8$, $x_{\perp\mathrm{max}} = v_{\perp\mathrm{max}}/v_\mathrm{thi} = 4$, $N_{||} = 140$, $N_\perp = 70$, a mesh size $\Delta\zeta = \pi/100$ and a time step $\Delta t'' = 5 \times 10^{-3}$. These parameters have been varied to test their sensitivities. As it turns out, the growth rate at the end of the calculations is independent of $N_{||}$ and $N_\perp$ when $N_{||} \geq 40$ and $N_\perp \geq 20$. For simplicity, we used $\theta_k = 0$ in all our calculations. At the beginning of the calculations, the perturbed ion distribution is assumed to be small Maxwellian located around ζ_0 and the electron response is assumed to be adiabatic, $\widehat{n_\mathrm{e}} = \widehat{\Phi}$.Then, the electrostatic potential is computed using equation (6.14) followed by the perturbed ion distribution function (6.19) and the perturbed electron density (6.35). The 'new' electrostatic potential can be computed from equation (6.14) and the process is repeated until convergence is obtained.

The magnetic field strength, normalized to the magnetic field strength at the magnetic axis, as a function of the extended toroidal angle is shown in figure 6.2a. The field line of reference is labeled $\theta_0 = \zeta_0 = 0$, which corresponds to $\zeta = 0$ in figure 6.2a. The point $\theta_0 = \zeta_0 = 0$ is a symmetry point so that $B(+\zeta) = B(-\zeta)$. We have chosen the point of reference $\theta_0 = \zeta_0 = 0$ because the destabilizing influence of the

normal curvature is the strongest at that point.

Figure 6.2b shows the curvature drift term ξ_d, defined by equation (6.18), for the same field line as in figure 6.2a. The secular behavior becomes important for $|\zeta| \geq 10$.

The time evolution of the growth rate and the real part of the mode frequency is shown in figure 6.3. The parameters are $\tau = 3$, $T_e = 15$ eV, $n_0 = 5 \times 10^{12}$ cm^{-3}, $L_n = 10$ cm, $k_\theta \rho_{s0} = 1.0$ and $\eta_i = 2.3$. These parameters are representative of H1-NF experimental conditions. The large electron transport along the field line is responsible for the rapid variation of γ and ω_r for $t'' \leq 0.01$. An equilibrium state is reached for $t'' \geq 0.05$.

The eigenfunction of the electrostatic potential at the end of the calculations is shown in figure 6.4a. The mode has a ballooning character. The real part of $\widehat{\Phi}$ displays a rapid, coil-induced variation along ζ, superimposed to a slow, curvature-driven variation. The eigenfunction of the perturbed ion density at the end of the calculations is shown in figure 6.4b. The imaginary part of n_i is not in phase with the imaginary part of $\widehat{\Phi}$.

We now study the dependence on the toroidal mode number. Figure 6.5 shows the real and imaginary parts of the mode frequency as a function of $k_\theta \rho_s$, for the field line of reference $\theta_0 = \zeta_0 = 0$. Other parameters are the same as in Figure 6.3. The growth rate (Figure 6.5a) peaks around $k_\theta \rho_s \simeq 0.6$. For the parameters used in the calculations, the electron population is deeply in the collisional regime. The mode rotates in the ion direction, and ω_r becomes more negative as the toroidal mode number increases. However, for $k_\theta \rho_s \geq 0.8$, the dependence of ω_r on the toroidal mode number is weak.

We have also investigated the influence of the ion temperature gradient on the linear growth rate, while the density scalelength is fixed. The dependence of γ as a function of the parameter η_i is shown in figure 6.6a. Other parameters are the same as in figure 6.3. At a small value of η_i the mode is stable, while for large ion temperature gradient (large η_i), the mode is unstable. The threshold is $\eta_{ic} \simeq 1.1$.

Finally, we have studied a set of different field lines, each of them having the same toroidal angle of reference $\zeta_0 = 0$. The poloidal angle of reference, θ_0, has been increased from 0 to 2π. In real space, this corresponds to moving from the

outboard side of the plasma ($\theta_0 = 0$) to the inboard side of the plasma ($\theta_0 = \pi$) and back again to the outboard side. The linear growth rate as a function of θ_0 is shown in figure 6.6b. Interestingly, the maximum growth rate is at $\theta \simeq 2.7$, which corresponds to a point in the *inboard side* of the plasma where the normal curvature is *stabilizing*. This result is surprising since one would expect the maximum growth rate to be found where the destabilizing influence of the normal curvature is the strongest, that is at $\theta_0 = 0$. However, as shown in chapter 4 [Equation (4.19)], the curvature term ξ_{d} depends on a combination of the normal curvature, the geodesic curvature, the integrated residual shear and the global shear. Therefore, it is not sufficient to consider the point where the normal curvature is the most destabilizing to determine the poloidal angle at which the growth rate is the largest.

6.6 Concluding remarks

We have presented a hybrid fluid/gyro-kinetic model for studying drift waves in stellarator geometry. Assuming that the electron temperature is not too large, we have used fluid equations to determine the perturbed density of the electrons. The perturbed ion density has been obtained by solving the collisionless ion gyro-kinetic equation, followed by an integration over velocity space. The quasineutrality condition provides a closure relation for the problem. Using the ballooning representation for fluctuating quantities, a set of two along-the-field-line equations was solved numerically. We have presented numerical results for the geometry of the toroidal heliac H1-NF.

A limitation of our model is the neglect of trapped particles (ions and electrons). As we can see in Figure 6.2a, the magnetic field strength varies rapidly along the field line, and we can expect the particle trapping to be important. The importance of the trapped particles on the mode frequency depends on the plasma collisionality. We have calculated the η_{i} threshold for instability to be $\eta_{\mathrm{ic}} \simeq 1.1$, for the field line starting at $\theta_0 = \zeta_0 = 0$. In general, the threshold will be different for different field lines, that is $\eta_{\mathrm{ic}} = \eta_{\mathrm{ic}}(\theta_0, \zeta_0)$. As a consequence, for a not too large η_{i}, it might be possible that to find a region of the magnetic surface such that $\eta_{\mathrm{i}} \geq \eta_{\mathrm{ic}}(\theta_0, \zeta_0)$ and

the mode can be destabilized there. The rest of the surface has $\eta_i \leq \eta_{ic}(\theta_0, \zeta_0)$ and the mode is linearly stable.

We have also studied the drift wave spectrum for one field line. For the field line $\theta_0 = \zeta_0 = 0$, we have shown that the largest linear growth rate occurs at $k_\theta \rho_s \simeq 0.6$. This result can be understood by inspection of the electron equation (6.35). The parallel ion motion in equation (6.35) is given by the second term on the right-hand side. This term varies as $b^{-1/2} = 1/(k_\theta \rho_s)$ and we can expect a qualitative change around $k_\theta \rho_s \sim 1$.

When ion collision and trapping effects are retained, one must solved the gyro-kinetic equation in guiding center coordinates (chapter 5). This complicates the numerical solution of the gyro-kinetic equation. The gyro-kinetic code developed by Kotschenreuther [111, 175] takes into account collisional and trapping effects, for a tokamak plasma using the $\hat{s} - \alpha$ model. It is hoped to generalize Kotschenreuther's code to fully three-dimensional plasmas using straight-field-line coordinates. All the geometrical factors that depend on the structure of $\mathbf{B}$, which enter the three-dimensional version of Kotschenreuther's code, have been calculated in the present chapter (and also in appendices D and E).

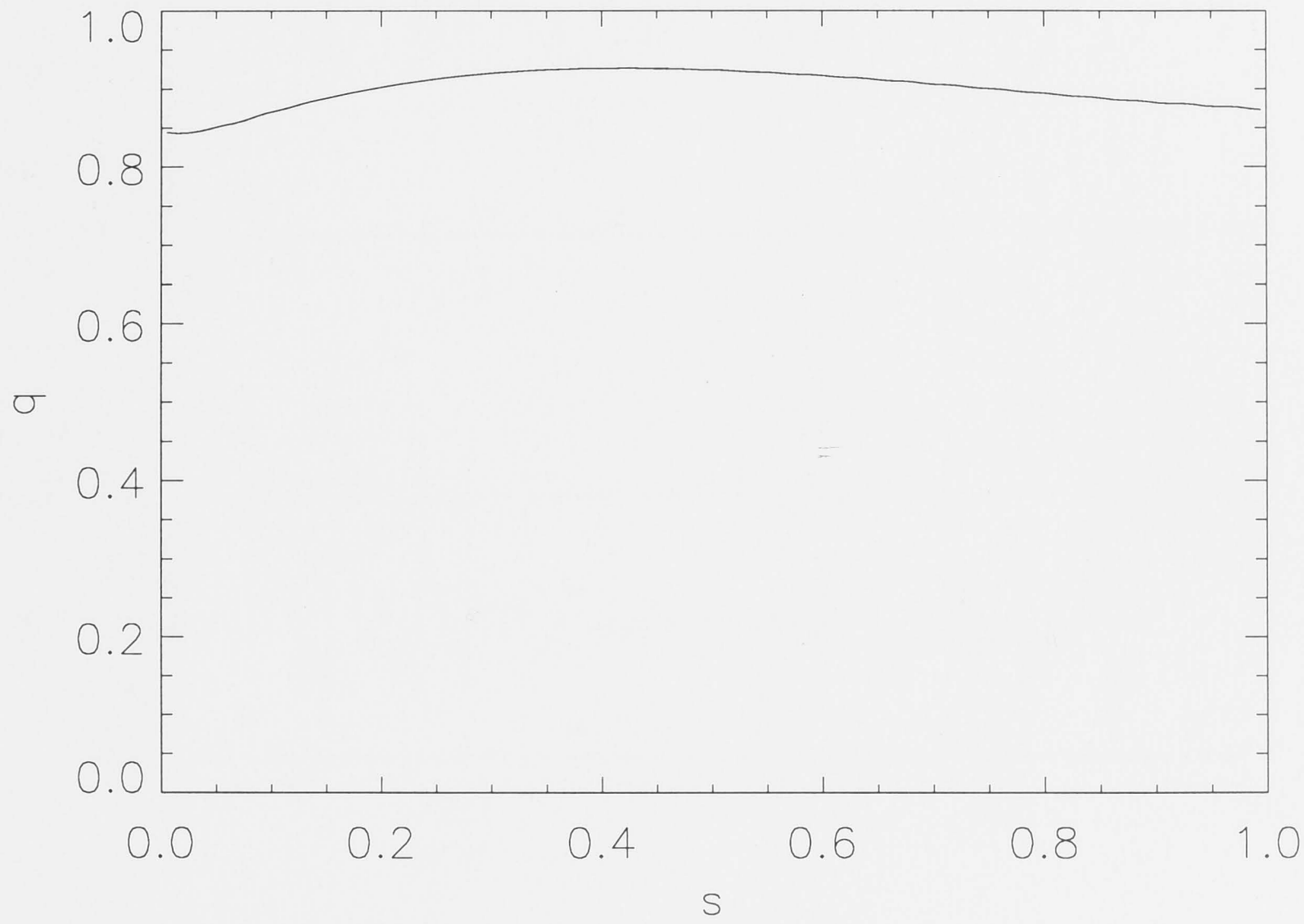

Figure 6.1: Safety factor as a function of the normalized radial s for the toroidal heliac H1-NF

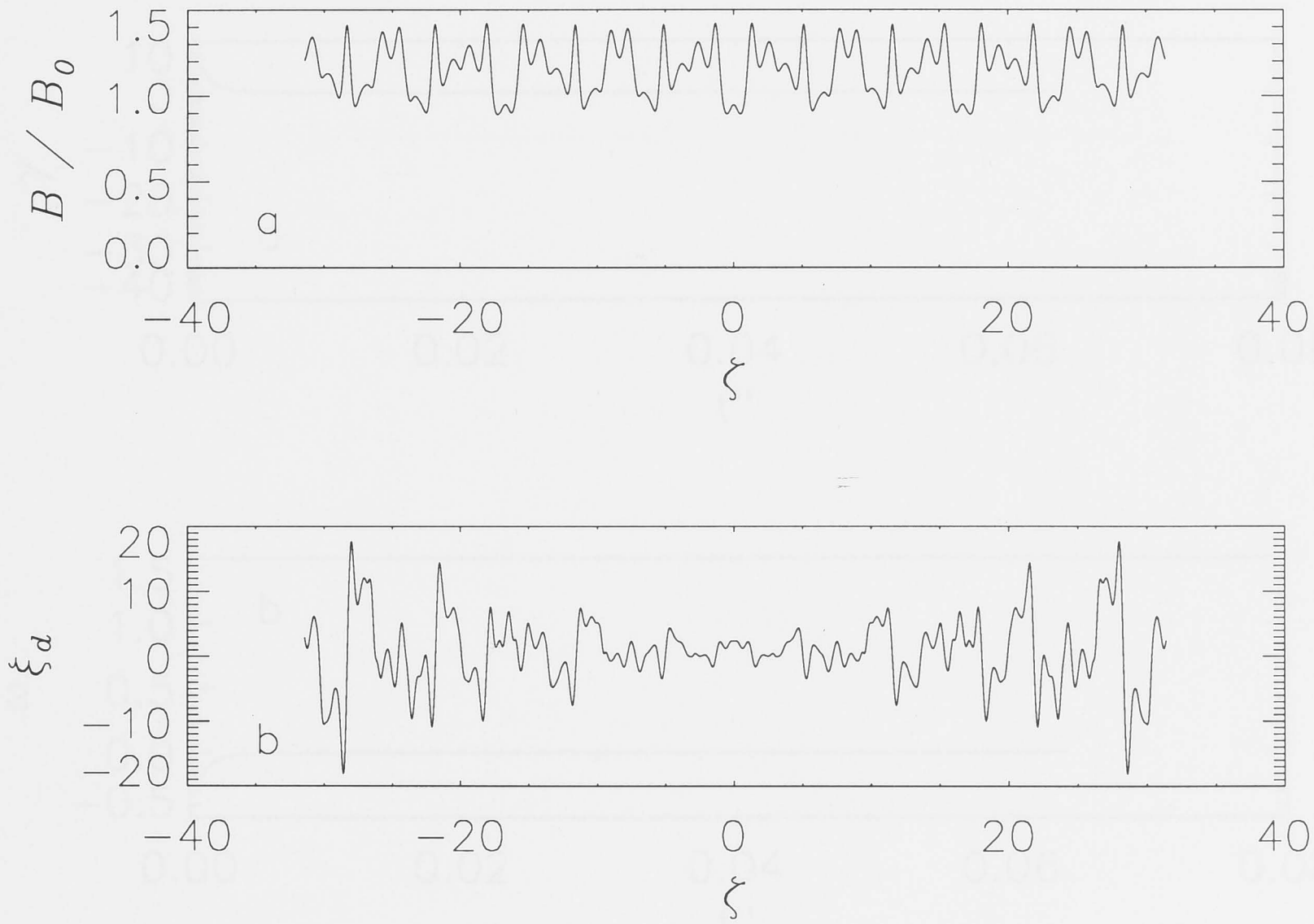

Figure 6.2: The magnetic field strength (a) and the normalized curvature drift frequency (b) as a function of the extended toroidal angle. The field line of reference is $\theta_0 = \zeta_0 = 0$.

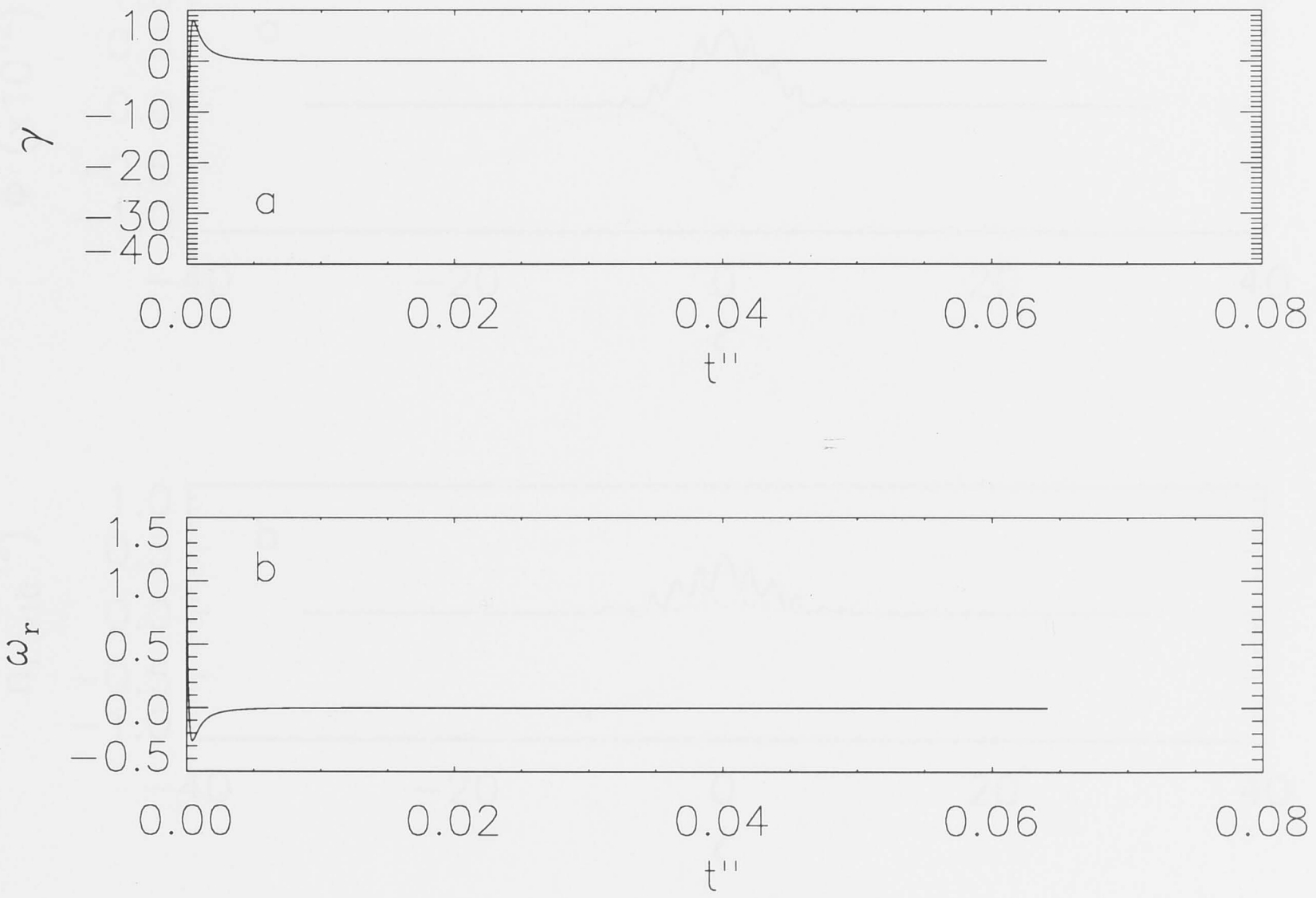

Figure 6.3: The normalized growth rate (a) and the real frequency (b) as a function of the normalized time $t'' = \omega_{\star e} t$.

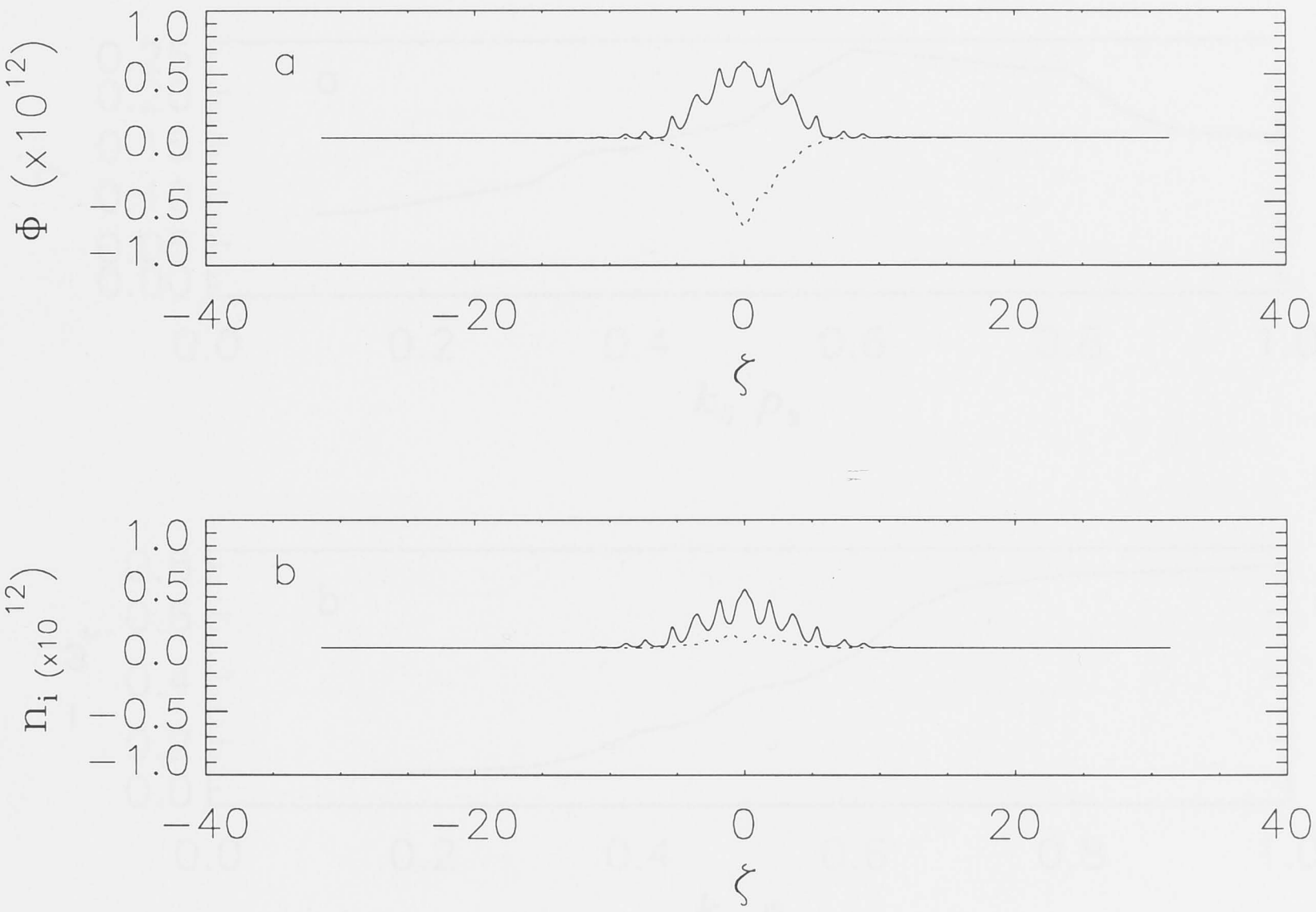

Figure 6.4: Real (plain line) and imaginary (dotted line) parts of the eigenfunctions of the electrostatic potential (a) and ion density (b) at the end of the calculations.

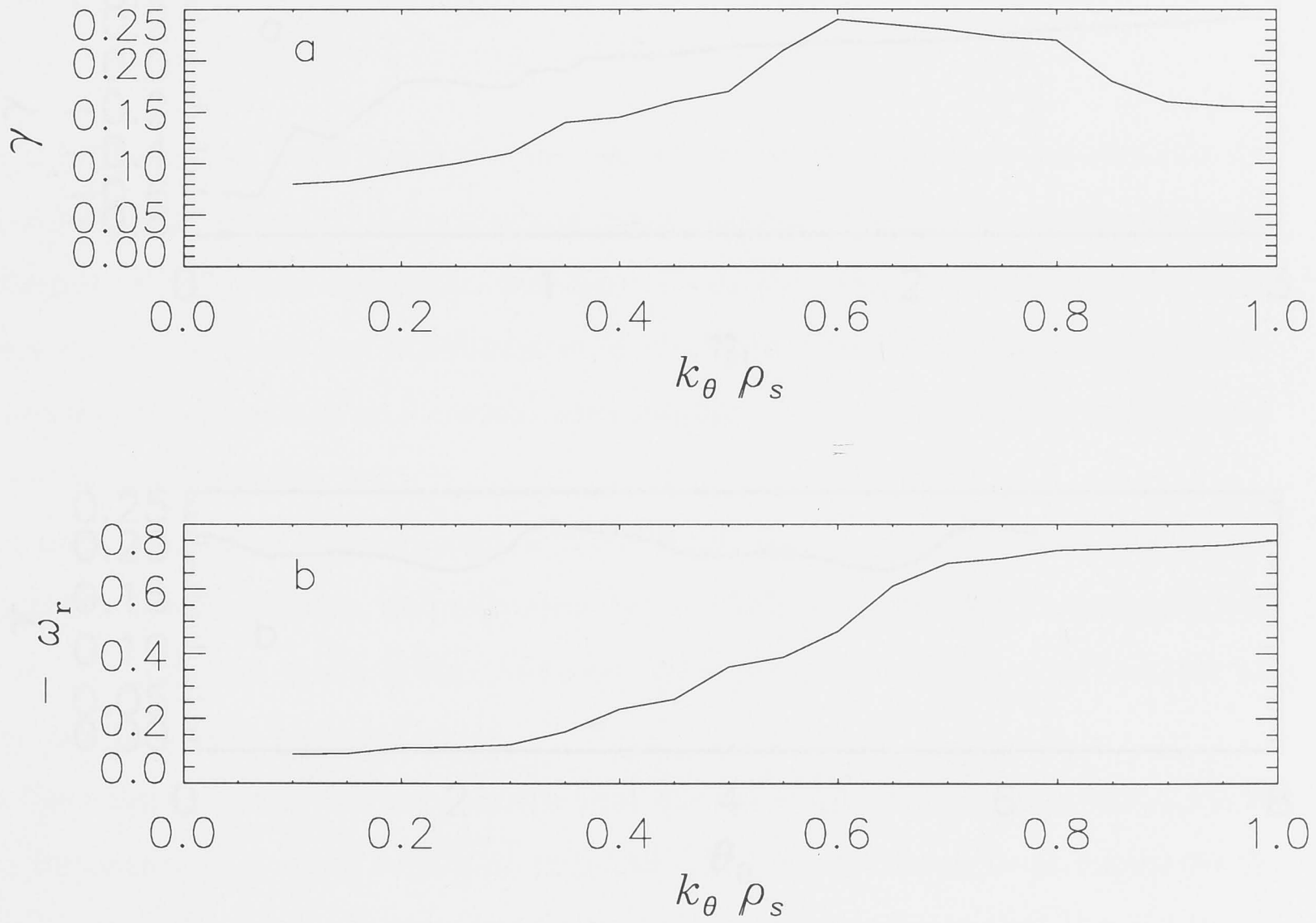

Figure 6.5: The normalized growth rate (a) and the real frequency (b) as a function of $k_\theta \rho_s$ for the field of reference $\theta_0 = \zeta_0 = 0$.

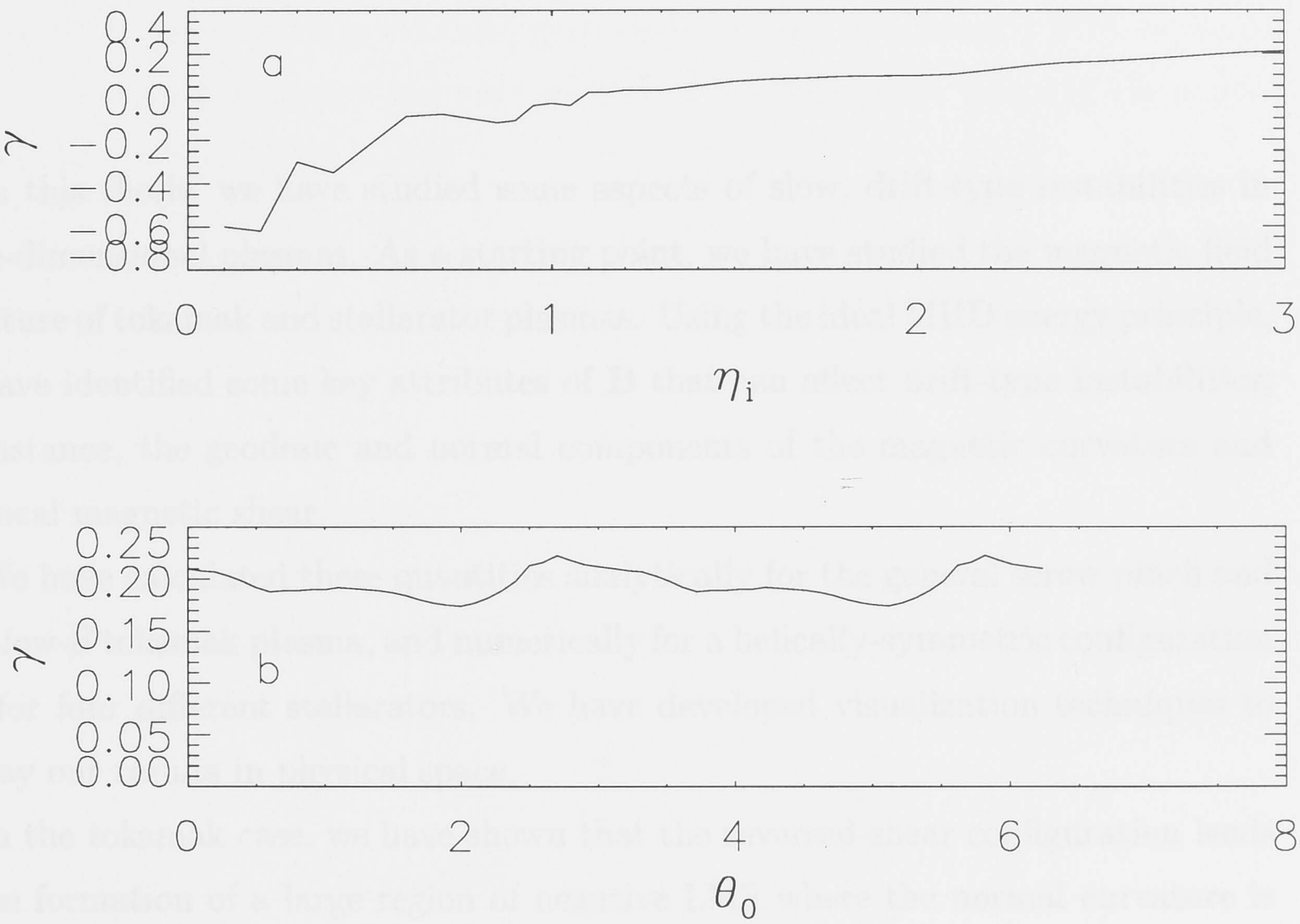

Figure 6.6: The normalized growth rate (a) as a function of the ion temperature gradient parameter η_i for the same field line as in Figure 6.5; and (b) for different field lines starting in poloidal cross-section $\phi = 0$.

CHAPTER 7

Conclusion

In this thesis, we have studied some aspects of slow, drift-type instabilities in three-dimensional plasmas. As a starting point, we have studied the magnetic field structure of tokamak and stellarator plasmas. Using the ideal MHD energy principle, we have identified some key attributes of $\mathbf{B}$ that can affect drift-type instabilities; for instance, the geodesic and normal components of the magnetic curvature and the local magnetic shear.

We have calculated these quantities analytically for the general screw pinch and for a low-β tokamak plasma, and numerically for a helically-symmetric configuration and for four different stellarators. We have developed visualization techniques to display our results in physical space.

In the tokamak case, we have shown that the reversed-shear configuration leads to the formation of a large region of negative LMS where the normal curvature is destabilizing. This result is consistent with experimental evidence that the reversed-shear configuration yields improved global and local confinement properties.

We have studied the magnetic field key attributes of four different stellarators; three of the studied stellarators (H1-NF, TJ-II and W7-AS) have small global magnetic shear over the entire plasma volume, while the remaining machine, LHD, has a strong global magnetic shear. Although the stellarators H1-NF, TJ-II and W7-AS have comparable global shear, numerical calculations and visualization examples show that the variation of the key attributes *in* the magnetic surface are quite different.

In the second part of this thesis, we have considered models for studying drift waves in three-dimensional plasmas. We first discussed two simple fluid models,

while retaining the details of **B** with some accuracy. The eigenmode equation of one of these fluid models, the cold ion model, has been solved numerically for a helically-symmetric configuration. In particular, we have calculated the drift wave spectrum for such a configuration.

The gyro-kinetic model has been discussed in chapters 5 and 6. The gyro-kinetic model has the advantage of retaining finite Larmor radius effects accurately. These effects can be important for present and future magnetic confinement devices. In chapter 6, we presented a novel fluid/gyro-kinetic model for studying drift waves in three-dimensional geometry and gave numerical results of drift waves in the geometry of the toroidal heliac H1-NF.

APPENDIX A

Straight stellarator geometry

A.1 The equilibrium

The magnetic field is written in Clebsch form

$$\mathbf{B} = \boldsymbol{\nabla}\alpha \times \boldsymbol{\nabla}\Psi \,, \tag{A.1}$$

where α is the field line label and

$$\Psi = \frac{MB_0R^2}{2N}\left(\rho^2 - 2\frac{b}{B_0}\,\rho I'_M \cos\lambda\right) \,, \tag{A.2}$$

is the helical flux. Here $\lambda \equiv M\phi - Nz/R$, I_M is the modified Bessel function of order M with argument $\xi \equiv M\rho$, $\rho \equiv Qr$ and $Q \equiv N/(MR)$ is the local pitch. A prime denotes a derivative with respect to ξ. It is convenient to work in normalized units

$$\begin{aligned} \Psi &\mapsto \frac{\Psi}{B_0R^2} \,, \\ \mathbf{B} &\mapsto \frac{B}{B_0} \,, \\ z &\mapsto \frac{z}{R} \,, \\ r &\mapsto \frac{r}{R} \,, \end{aligned} \tag{A.3}$$

where $2\pi R$ is the periodicity length of the cylinder and B_0 is the magnetic field strength at the axis ($r = 0$). In these units, the cylindrical components of the magnetic field are

$$B_r = AMI'_M \sin\lambda \,,$$

$$B_\phi = A\frac{M^2}{\xi}\, I_M \cos\lambda\,, \qquad (A.4)$$
$$B_z = 1 - AMI_M \cos\lambda\,,$$

where $A \equiv b/B_0$ is a parameter less than unity. The vector $\boldsymbol{\nabla}\alpha$ is a multiple-valued function. From (A.1), we have

$$\boldsymbol{\nabla}\alpha = \Lambda\boldsymbol{\nabla}\Psi + \mathbf{s}\,, \qquad (A.5)$$

where $\Lambda \equiv \boldsymbol{\nabla}\alpha\cdot\boldsymbol{\nabla}\Psi/\boldsymbol{\nabla}\Psi\cdot\boldsymbol{\nabla}\Psi$ is proportional to the part of $\boldsymbol{\nabla}\alpha$ normal to the surface and $\mathbf{s} \equiv \boldsymbol{\nabla}\Psi\times\mathbf{B}/\boldsymbol{\nabla}\Psi\cdot\boldsymbol{\nabla}\Psi$ is a vector anti-parallel to the unit binormal vector $\widehat{\mathbf{b}}$. Operating on equation (A.5) with $\widehat{\mathbf{b}}\cdot\boldsymbol{\nabla}\times$ we get

$$\widehat{\mathbf{b}}\cdot(\boldsymbol{\nabla}\times\boldsymbol{\nabla}\alpha) = \boldsymbol{\nabla}\Lambda\cdot\left(\boldsymbol{\nabla}\Psi\times\widehat{\mathbf{b}}\right) + \widehat{\mathbf{b}}\cdot(\boldsymbol{\nabla}\times\mathbf{s})\,, \qquad (A.6)$$

or, since $\boldsymbol{\nabla}\times\boldsymbol{\nabla}A \equiv 0$ for any scalar A,

$$\widehat{\mathbf{e}}_{||}\cdot\boldsymbol{\nabla}\Lambda = -\sqrt{\boldsymbol{\nabla}\Psi\cdot\boldsymbol{\nabla}\Psi}\;\widehat{\mathbf{b}}\cdot(\boldsymbol{\nabla}\times\mathbf{s})\,,$$
$$= -\frac{\mathcal{S}}{B}\,, \qquad (A.7)$$

where we have used the definition of the local magnetic shear $\mathcal{S} \equiv -\mathbf{s}\cdot\boldsymbol{\nabla}\times\mathbf{s}$ to simplify the last equation. The local magnetic shear is derived in the next section.

A.2 The local magnetic shear

The unit normal vector

$$\widehat{\mathbf{n}} \equiv \frac{\boldsymbol{\nabla}\Psi}{\sqrt{\boldsymbol{\nabla}\Psi\cdot\boldsymbol{\nabla}\Psi}}\,, \qquad (A.8)$$

can be written in cylindrical coordinates as

$$\widehat{\mathbf{n}} = \left[\frac{\xi}{Mg} - \frac{A}{g}\cos\lambda\,(I'_M + \xi I''_M)\right]\widehat{\mathbf{r}} + AM\frac{I'_M}{g}\sin\lambda\,\widehat{\boldsymbol{\phi}} - A\frac{\xi I'_M}{g}\sin\lambda\,\widehat{\mathbf{z}}\,, \qquad (A.9)$$

where

$$g(r,\phi,z) \equiv \left\{\frac{1}{M^2}\left[\xi - AM\cos\lambda\,(I'_M + \xi I''_M)\right] + \left(AI'_M\sin\lambda\right)^2\left(M^2+\xi^2\right)\right\}^{1/2}\,, \qquad (A.10)$$

is a non-dimensional quantity related to the gradient of the helical flux. The unit binormal vector $\widehat{\mathbf{b}} = \widehat{\mathbf{e}}_{||}\times\widehat{\mathbf{n}}$ can also be written in cylindrical coordinates

$$\widehat{\mathbf{b}} = b_r\,\widehat{\mathbf{r}} + b_\phi\,\widehat{\boldsymbol{\phi}} + b_z\,\widehat{\mathbf{z}}\,, \qquad (A.11)$$

where

$$
\begin{aligned}
b_\phi &= -A\,\frac{I'_M}{gh}\,\left\{\xi\sin\lambda\,(1-AMI_M\cos\lambda)+\cos\lambda\,[\xi-AM\cos\lambda\,(I'_M+\xi I''_M)]\right\}\ ,\\
b_r &= AM\,\frac{I'_M}{gh}\,\sin\lambda\,\left[AMI_M\,(\sin\lambda-\cos\lambda)-1\right]\ , \qquad \text{(A.12)}\\
b_z &= \frac{AM}{gh}\,\left\{AM\,(I'_M\sin\lambda)^2-\frac{I_M}{\xi}\,\cos\lambda\,[\xi-AM\cos\lambda\,(I'_M+\xi I''_M)]\right\}\ ,
\end{aligned}
$$

where

$$
h(r,\phi,z)\equiv\left\{A^2M^2\left[(I'_M\sin\lambda)^2+M^2\frac{I_M^2}{\xi^2}\,\cos^2\lambda\right]+(1-AM\cos\lambda)^2\right\}^{1/2}\ . \qquad \text{(A.13)}
$$

The normalized gradient operator in cylindrical coordinates

$$
\boldsymbol{\nabla}=\hat{\mathbf{r}}\,N\,\frac{\partial}{\partial\xi}\,+\hat{\boldsymbol{\phi}}\,\frac{N}{\xi}\,\,\frac{\partial}{\partial\phi}\,+\hat{\mathbf{z}}\,\frac{\partial}{\partial z}\ , \qquad \text{(A.14)}
$$

is used to compute the local magnetic shear

$$
\mathcal{S}=-\frac{h^2}{g^2}\,\hat{\mathbf{b}}\cdot\boldsymbol{\nabla}\times\hat{\mathbf{b}}\ . \qquad \text{(A.15)}
$$

After some algebra we get (in normalized units)

$$
\mathcal{S}=\frac{h}{g^3}\,\left(\mu_r b_r+\mu_\phi b_\phi+\mu_z b_z\right)\ , \qquad \text{(A.16)}
$$

where

$$
\begin{aligned}
\mu_r &\equiv AN\sin\lambda\left[(I'_M+\xi I''_M)\,(2AMI_M\cos\lambda-1)-\xi I_M-2AM\,(I'_M)^2\right]\\
&- ANM^2\frac{\sin\lambda}{\xi}\,\left\{I_M+2AM\cos\lambda\left[(I'_M)^2-\frac{I_M}{\xi}\,\,(I'_M+\xi I''_M)\right]\right\}\ , \qquad \text{(A.17)}
\end{aligned}
$$

$$
\begin{aligned}
\mu_\phi &\equiv AMNI'_M\left(2AM\sin^2\lambda I''_M-\cos\lambda\right)\\
&- AMN\frac{\cos\lambda}{\xi}\,\left\{\left(I'_M-\frac{I_M}{\xi}\right)[\xi-AM\cos\lambda\,(I'_M+\xi I''_M)]\right.\\
&+ \left. I_M\,[1-AM\cos\lambda\,(2I''_M+\xi I'''_M)]\right\}\ , \qquad \text{(A.18)}
\end{aligned}
$$

$$
\begin{aligned}
\mu_z &\equiv ANI'_M\cos\lambda\left(1-\frac{M}{\xi}\right)-\frac{N}{\xi}\,\left\{A^2M\xi\,(I'_M)^2\sin^2\lambda\right.\\
&+ \left.\frac{N}{M}\,\,(1-AMI_M\cos\lambda)\,[\xi AM\cos\lambda\,(I'_M+\xi I''_M)]\right\}\\
&- A^2MNI'_M\left[I''_M\sin^2\lambda+M\,(I'_M+\xi I''_M)\right]\\
&- \frac{N}{M}\,\,(1-AMI_M\cos\lambda)\,[1-AM\cos\lambda\,(2I''_M+\xi I'''_M)]\ . \qquad \text{(A.19)}
\end{aligned}
$$

To get the LMS in unnormalized units, the right-hand side of equation (A.16) must be multiplied by R^{-3}.

A.3 The magnetic curvature

The magnetic curvature can be written

$$\boldsymbol{\kappa} = \left(\widehat{\mathbf{e}}_{||}\cdot\boldsymbol{\nabla}\right)\widehat{\mathbf{e}}_{||}\ , \tag{A.20}$$

where, as before, $\widehat{\mathbf{e}}_{||} \equiv \mathbf{B}/B$ is the unit parallel vector which can be written in cylindrical coordinates as

$$\widehat{\mathbf{e}}_{||} = \lambda_r\widehat{\mathbf{r}} + \lambda_\phi\widehat{\boldsymbol{\phi}} + \lambda_z\widehat{\mathbf{z}}\ , \tag{A.21}$$

where $\lambda_r \equiv B_r/B \sim A$, $\lambda_\phi \equiv B_\phi/B \sim A$, $\lambda_z \equiv B_z/B \sim 1-A$ and $B = \sqrt{B_r^2+B_\phi^2+B_z^2}$ is the magnitude of $\mathbf{B}$. Noting that the unit vectors $\widehat{\mathbf{r}}$ and $\widehat{\boldsymbol{\phi}}$ satisfy $\partial\widehat{\mathbf{r}}/\partial\phi = +\widehat{\boldsymbol{\phi}}$ and $\partial\widehat{\boldsymbol{\phi}}/\partial\phi = -\widehat{\mathbf{r}}$, we write the magnetic curvature in cylindrical coordinates as

$$\boldsymbol{\kappa} = \kappa_r\ \widehat{\mathbf{r}} + \kappa_\phi\ \widehat{\boldsymbol{\phi}} + \kappa_z\ \widehat{\mathbf{z}}\ , \tag{A.22}$$

where

$$\begin{aligned}
\kappa_r &= N\lambda_r\frac{\partial\lambda_r}{\partial\xi} + N\frac{\lambda_\phi}{\xi}\left(\frac{\partial\lambda_r}{\partial\phi} - \lambda_\phi\right) + \lambda_z\frac{\partial\lambda_r}{\partial z}\ , \\
\kappa_\phi &= N\lambda_r\frac{\partial\lambda_\phi}{\partial\xi} + N\frac{\lambda_\phi}{\xi}\left(\lambda_r + \frac{\partial\lambda_\phi}{\partial\phi}\right) + \lambda_z\frac{\partial\lambda_\phi}{\partial z}\ , \qquad \text{(A.23)} \\
\kappa_z &= N\lambda_r\frac{\partial\lambda_z}{\partial z} + N\frac{\lambda_\phi}{\xi}\frac{\partial\lambda_z}{\partial\phi} + \lambda_z\frac{\partial\lambda_z}{\partial z}\ . \qquad \text{(A.24)}
\end{aligned}$$

The partial derivatives in the above equation are given according to the rule

$$\frac{\partial\lambda_i}{\partial j} = \frac{1}{B}\left(\frac{\partial B_i}{\partial j} - \lambda_i\sum_{k=r,\phi,z}\frac{\partial B_k}{\partial j}\right) \tag{A.25}$$

for $(i,j) = \{r,\phi,z\}$. The 9 elements $\partial B_i/\partial j$ are

$$\begin{aligned}
\frac{\partial B_r}{\partial\xi} &= AMI''_M\sin\lambda\ , \\
\frac{\partial B_\phi}{\partial\xi} &= \frac{AM^2}{\xi}\left(I'_M - \frac{I_M}{\xi}\right)\cos\lambda\ ,
\end{aligned}$$

$$
\begin{aligned}
\frac{\partial B_z}{\partial \xi} &= -AMI'_M \cos\lambda \,, \\
\frac{\partial B_r}{\partial \phi} &= AM^2 I'_M \cos\lambda \,, \\
\frac{\partial B_\phi}{\partial \phi} &= -AM^3 \frac{I_M}{\xi} \sin\lambda \,, \\
\frac{\partial B_z}{\partial \phi} &= AM^2 I_M \sin\lambda \,, \\
\frac{\partial B_r}{\partial z} &= -AMNI'_M \cos\lambda \,, \\
\frac{\partial B_\phi}{\partial z} &= AM^2 N \frac{I_M}{\xi} \sin\lambda \,, \\
\frac{\partial B_z}{\partial z} &= -AMNI_M \sin\lambda \,.
\end{aligned}
\tag{A.26}
$$

The geodesic component of the magnetic curvature is obtained by dotting (A.22) with the unit binormal vector (A.11)

$$\kappa_{\mathrm{G}} = \kappa_r b_r + \kappa_\phi b_\phi + \kappa_z b_z \tag{A.27}$$

whereas the normal component of $\boldsymbol{\kappa}$ is obtained by dotting (A.22) with the unit normal vector (A.8)

$$\kappa_{\mathrm{N}} = \kappa_r \left(\hat{\mathbf{r}}\cdot\hat{\mathbf{n}}\right) + \kappa_\phi \left(\hat{\boldsymbol{\phi}}\cdot\hat{\mathbf{n}}\right) + \kappa_z \left(\hat{\mathbf{z}}\cdot\hat{\mathbf{n}}\right) . \tag{A.28}$$

APPENDIX B

Magnetic curvature and local magnetic shear for a low-β tokamak plasma

In this appendix, we present the derivation of the local magnetic shear (LMS) and the normal and geodesic curvatures for a low-β tokamak plasma with shifted, circular magnetic surfaces. The surface average of the LMS and the of normal curvature are also given.

B.1 The local magnetic shear

Calculations are carried out in cylindrical coordinates (R, Z, ϕ), right-handed in that order. A set of local coordinates, closely related to Shafranov coordinates, is introduced. The coordinates R and Z, the Shafranov shift and the local minor radius measured from the magnetic axis, are normalized to the magnetic axis radius (R_0). The magnetic field is normalized to its magnitude evaluated at the magnetic axis (B_0). The normalized cylindrical coordinates are

$$\begin{aligned} R &\mapsto \frac{R}{R_0} = 1 + r\cos\theta - \Delta\,, \\ Z &\mapsto \frac{Z}{R_0} = r\sin\theta\,, \\ \phi &\mapsto \phi\,. \end{aligned} \tag{B.1}$$

The transformation $r \mapsto r/R_0$ and $\Delta \mapsto \Delta/R_0$ is implied in equation (B.1). In normalized units, we note the following ordering

$$\ddot{\Delta} = \mathcal{O}(1)\,,$$

$$\dot{\Delta} \sim r = \mathcal{O}(\epsilon) \ , \tag{B.2}$$
$$\Delta \sim r^2 = \mathcal{O}\left(\epsilon^2\right) \ ,$$

where a dot denotes a derivative with respect to r. The position vector $\mathbf{r}$ can be written as

$$\mathbf{r} = R\cos\phi\ \widehat{\mathbf{x}} - R\sin\phi\ \widehat{\mathbf{y}} + Z\ \widehat{\mathbf{z}} \ , \tag{B.3}$$

where $(\widehat{\mathbf{x}}, \widehat{\mathbf{y}}, \widehat{\mathbf{z}})$ are the unit Cartesian vectors. Using (B.3,B.1) we compute the covariant basis vectors $\mathbf{e}_r \equiv \partial\mathbf{r}/\partial r$, $\mathbf{e}_\theta \equiv \partial\mathbf{r}/\partial\theta$ and $\mathbf{e}_\phi \equiv \partial\mathbf{r}/\partial\phi$ followed by the Jacobian of the transformation $\mathcal{J}_\star \equiv [\boldsymbol{\nabla} r\cdot(\boldsymbol{\nabla}\theta\times\boldsymbol{\nabla}\phi)]^{-1} = R\ r\ \bar{\eta}$ from the local coordinates (r, θ, ϕ) to Cartesian coordinates. Here $\bar{\eta} \equiv 1 - \dot{\Delta}\cos\theta$. The contravariant basis vectors are then derived

$$\begin{aligned}
\boldsymbol{\nabla} r &= \frac{\cos\theta}{\bar{\eta}}\ \widehat{\mathbf{R}} + \frac{\sin\theta}{\bar{\eta}}\ \widehat{\mathbf{Z}} \ , \\
\boldsymbol{\nabla}\theta &= -\frac{\sin\theta}{r\bar{\eta}}\ \widehat{\mathbf{R}} + \frac{\cos\theta - \dot{\Delta}}{r\bar{\eta}}\ \widehat{\mathbf{Z}} \ , \\
\boldsymbol{\nabla}\phi &= \frac{\widehat{\boldsymbol{\phi}}}{R} \ ,
\end{aligned} \tag{B.4}$$

where $\widehat{\mathbf{R}}$, $\widehat{\mathbf{Z}}$ and $\widehat{\boldsymbol{\phi}}$ are the unit cylindrical vectors. For a vanishing Shafranov shift, the vectors (B.4) are orthogonal. For a flat current profile, the Clebsch representation for the magnetic field is

$$\mathbf{B} = \dot{\psi}\left(\boldsymbol{\nabla}\phi\times\boldsymbol{\nabla} r + Q\boldsymbol{\nabla} r\times\boldsymbol{\nabla}\theta\right) \ , \tag{B.5}$$

where ψ is the enclosed poloidal flux and $Q \equiv q\bar{\eta}/R$ is the local pitch of the magnetic field lines. Using (B.4) the magnetic field can also be written as

$$\mathbf{B} = B_\theta\ \widehat{\boldsymbol{\theta}} + B_\phi\ \widehat{\boldsymbol{\phi}} \ , \tag{B.6}$$

where $B_\theta = r/(qR\bar{\eta})$ and $B_\phi = 1/R$ are, respectively, the poloidal and toroidal components of the magnetic field. We have introduced the unit poloidal vector $\widehat{\boldsymbol{\theta}} \equiv \cos\theta\ \widehat{\mathbf{Z}} - \sin\theta\ \widehat{\mathbf{R}}$. For circular magnetic surfaces, the enclosed poloidal flux depends on r only. Therefore the unit vector normal to the magnetic surface is

$$\begin{aligned}
\widehat{\mathbf{n}} &\equiv \frac{\boldsymbol{\nabla}\psi}{\left(\boldsymbol{\nabla}\psi\cdot\boldsymbol{\nabla}\psi\right)^{1/2}} \ , \\
&= \frac{\boldsymbol{\nabla} r}{\left(\boldsymbol{\nabla} r\cdot\boldsymbol{\nabla} r\right)^{1/2}} \ , \\
&= \cos\theta\ \widehat{\mathbf{R}} + \sin\theta\ \widehat{\mathbf{Z}} \ ,
\end{aligned} \tag{B.7}$$

and the unit binormal vector $\widehat{\mathbf{b}} \equiv \widehat{\mathbf{e}}_{||} \times \widehat{\mathbf{n}}$, where $\widehat{\mathbf{e}}_{||} \equiv \mathbf{B}/B$, then becomes

$$\widehat{\mathbf{b}} = \lambda_\phi \, \widehat{\boldsymbol{\theta}} - \lambda_\theta \, \widehat{\boldsymbol{\phi}} \, . \tag{B.8}$$

Here $\lambda_\theta \equiv B_\theta/B = \mathcal{O}(\epsilon)$ and $\lambda_\phi \equiv B_\phi/B = \mathcal{O}(1)$. The local magnetic shear can be written as

$$\mathcal{S} = -H^2 \widehat{\mathbf{b}} \cdot \boldsymbol{\nabla} \times \widehat{\mathbf{b}} \, , \tag{B.9}$$

where $H \equiv B/\sqrt{\boldsymbol{\nabla}\psi \cdot \boldsymbol{\nabla}\psi}$ is a positive-definite quantity. Writing $\widehat{\mathbf{b}} = b_r \boldsymbol{\nabla} r + b_\theta \boldsymbol{\nabla}\theta + b_\phi \boldsymbol{\nabla}\phi$ where

$$\begin{aligned} b_r &\equiv \widehat{\mathbf{b}} \cdot \mathbf{e}_r = \dot{\Delta} \lambda_\phi \sin\theta = \mathcal{O}(\epsilon) \, , \\ b_\theta &\equiv \widehat{\mathbf{b}} \cdot \mathbf{e}_\theta = r \lambda_\phi = \mathcal{O}(\epsilon) \, , \\ b_\phi &\equiv \widehat{\mathbf{b}} \cdot \mathbf{e}_\phi = -R \lambda_\theta = \mathcal{O}(\epsilon) \, , \end{aligned} \tag{B.10}$$

the local magnetic shear can be cast in the following form

$$\mathcal{S} = \mathcal{S}_1 + \mathcal{S}_2 \, , \tag{B.11}$$

where

$$\mathcal{S}_1 = \frac{H^2}{\mathcal{J}_\star} \left(b_\theta \frac{\partial b_\phi}{\partial r} - b_\phi \frac{\partial b_\theta}{\partial r} \right) , \tag{B.12}$$

$$\mathcal{S}_2 = \frac{H^2}{\mathcal{J}_\star} \left(b_\phi \frac{\partial b_r}{\partial \theta} - b_r \frac{\partial b_\phi}{\partial \theta} \right) . \tag{B.13}$$

The axi-symmetry property is evident in the above equations because all terms of the form $\partial G/\partial\phi = 0$, for any *scalar* quantity G, vanish. $\mathcal{S}_1$ contains the global magnetic shear and $\mathcal{S}_2$ will be shown to vanish when the Shafranov shift is zero. After straightforward algebra, we derive the following useful relations

$$\begin{aligned} \frac{\partial \lambda_\theta}{\partial r} &= \frac{F}{r} \lambda_\theta \left(1 - {\lambda_\theta}^2\right) + \lambda_\theta {\lambda_\phi}^2 \frac{\cos\theta - \dot{\Delta}}{R} \, , \\ \frac{\partial \lambda_\phi}{\partial r} &= \frac{\dot{\Delta} - \cos\theta}{R} \lambda_\phi \left(1 - {\lambda_\phi}^2\right) - \frac{F}{r} {\lambda_\theta}^2 \lambda_\phi \, , \\ \frac{\partial \lambda_\theta}{\partial \theta} &= \sin\theta \left[\left(\frac{r}{R} - \frac{\dot{\Delta}}{\bar{\eta}} \right) \lambda_\theta \left(1 - {\lambda_\theta}^2\right) - \frac{r}{R} \lambda_\theta {\lambda_\phi}^2 \right] \, , \\ \frac{\partial \lambda_\phi}{\partial \theta} &= \sin\theta \left[\frac{r}{R} \lambda_\phi \left(1 - {\lambda_\phi}^2\right) - \left(\frac{r}{R} - \frac{\dot{\Delta}}{\bar{\eta}} \right) \lambda_\phi {\lambda_\theta}^2 \right] \, , \end{aligned} \tag{B.14}$$

where we have defined

$$F \equiv 1 - \hat{s} + r\left(\frac{\ddot{\Delta}}{\bar{\eta}} - \frac{1}{R}\right)\cos\theta + \frac{r\dot{\Delta}}{R} \ . \tag{B.15}$$

The function F involves the global magnetic shear parameter $\hat{s} \equiv r\dot{q}/q$. Substituting (B.10) in (B.9) and using (B.14) we get

$$\mathcal{S}_1 = \frac{H^2\lambda_\theta\lambda_\phi}{\mathcal{J}_\star}\left[R\,(1-F) - 2r\left(\cos\theta - \dot{\Delta}\right)\right] \ , \tag{B.16}$$

and

$$\mathcal{S}_2 = -\frac{H^2\dot{\Delta}\lambda_\theta\lambda_\phi}{\mathcal{J}_\star}\left[R\cos\theta + \sin^2\theta\left(r + \frac{R\dot{\Delta}}{\bar{\eta}}\right)\right] \ . \tag{B.17}$$

$\mathcal{S}_1$ contains the lowest-order global shear since $1 - F = \hat{s} + \mathcal{O}(\epsilon)$, whereas the contribution $\mathcal{S}_2$ vanishes when the Shafranov shift also vanishes [as can be seen from (B.17) by setting $\dot{\Delta} = 0$]. Equations (B.16,B.17) are expanded in ascending powers of ϵ. The multiplying factor $H^2\lambda_\theta\lambda_\phi/\mathcal{J}_\star$ in (B.16,B.17) is *not* a flux surface quantity and must be multiplied with the terms in square brackets *before* the expansion is carried out.

After some algebra, we get the LMS (in normalized units)

$$\begin{aligned}
\mathcal{S} &= \hat{s} - r\cos\theta\left[1 + \ddot{\Delta} + y\,(1 - 2\hat{s})\right] \\
&- r^2\left\{\cos^2\theta\left[2y - 1 + \ddot{\Delta}\,(3y-1) + \hat{s}y^2\right]\right. \\
&+ \left. y^2\left[1 + \cos^2\theta\,(1 - 1/y)\right]\right\} + \mathcal{O}(\epsilon^3) \ ,
\end{aligned} \tag{B.18}$$

where $y \equiv \dot{\Delta}/r = \mathcal{O}\,(1)$. In normalized units, we make the transformation inverse to (B.1)

$$\begin{aligned}
\Delta &\mapsto R_0\Delta \ , \\
\dot{\Delta} &\mapsto \dot{\Delta} \ , \\
r &\mapsto R_0 r \ , \\
\ddot{\Delta} &\mapsto \frac{\ddot{\Delta}}{R_0} \ ,
\end{aligned} \tag{B.19}$$

leading to

$$\mathcal{S} = \mathcal{S}^{(0)} + \mathcal{S}^{(1)} + \mathcal{S}^{(2)} \ , \tag{B.20}$$

where $\mathcal{S}^{(k)} = \mathcal{O}(\epsilon^k)$ and k is an integer,

$$\mathcal{S}^{(0)} = \frac{\hat{s}}{{R_0}^3} \ , \tag{B.21}$$

$$\mathcal{S}^{(1)} = -\frac{r}{{R_0}^4} \cos\theta \left[1 + R_0\ddot{\Delta} + \frac{R_0\dot{\Delta}}{r} \ (1 - 2\hat{s})\right] \ , \tag{B.22}$$

and

$$\begin{aligned} \mathcal{S}^{(2)} &= -\frac{r}{{R_0}^4} \cos^2\theta \left[2\dot{\Delta} - \frac{r}{R_0} + R_0\ddot{\Delta}\left(3\dot{\Delta} - \frac{r}{R_0}\right) + R_0\hat{s}\frac{\dot{\Delta}^2}{r}\right] \\ &- \dot{\Delta}^2\left[1 + \cos^2\theta\left(1 - \frac{r}{R_0\dot{\Delta}}\right)\right] \ . \end{aligned} \tag{B.23}$$

B.2 The magnetic curvature

Using equation (B.6) for $\mathbf{B}$, the magnetic curvature is

$$\boldsymbol{\kappa} = \left(\lambda_\theta\widehat{\boldsymbol{\theta}}\cdot\boldsymbol{\nabla} + \lambda_\phi\widehat{\boldsymbol{\phi}}\cdot\boldsymbol{\nabla}\right)\left(\lambda_\theta\widehat{\boldsymbol{\theta}} + \lambda_\phi\widehat{\boldsymbol{\phi}}\right) \ . \tag{B.24}$$

Using (B.4), we note that

$$\begin{aligned} \widehat{\boldsymbol{\theta}}\cdot\boldsymbol{\nabla}\theta &= \frac{1}{r} \ , \\ \widehat{\boldsymbol{\phi}}\cdot\boldsymbol{\nabla}\theta &= 0 \ , \\ \widehat{\boldsymbol{\theta}}\cdot\boldsymbol{\nabla}\phi &= 0 \ , \\ \widehat{\boldsymbol{\phi}}\cdot\boldsymbol{\nabla}\phi &= \frac{1}{R} \ , \end{aligned} \tag{B.25}$$

and the curvature vector can be written in cylindrical coordinates as

$$\boldsymbol{\kappa} = \kappa_R\,\widehat{\mathbf{R}} + \kappa_Z\,\widehat{\mathbf{Z}} + \kappa_\phi\,\widehat{\boldsymbol{\phi}} \ , \tag{B.26}$$

where

$$\begin{aligned} \kappa_R &= -\frac{\lambda_\theta}{r}\left(\sin\theta\,\frac{\partial\lambda_\theta}{\partial\theta} + \lambda_\theta\,\cos\theta\right) - \frac{{\lambda_\phi}^2}{R} \ , \\ \kappa_Z &= \frac{\lambda_\theta}{r}\left(\cos\theta\,\frac{\partial\lambda_\phi}{\partial\theta} - \lambda_\theta\,\sin\theta\right) \ , \\ \kappa_\phi &= \frac{\lambda_\theta}{r}\,\frac{\partial\lambda_\phi}{\partial\theta} - \frac{\lambda_\theta\lambda_\phi}{R}\,\sin\theta \ . \end{aligned} \tag{B.27}$$

Taking the scalar product of (B.26) with the unit normal vector (B.7) and using (B.4,B.27), we get the normal component of the magnetic curvature

$$\kappa_{\rm N} = -\frac{{\lambda_\phi}^2}{R}\,\cos\theta - \frac{{\lambda_\theta}^2}{r}\quad , \tag{B.28}$$

where all orders in ϵ have been retained. Noting $R = 1 + \mathcal{O}(\epsilon)$ and $\lambda_\phi = 1 + \mathcal{O}(\epsilon)$, the lowest-order normal curvature varies as $-\cos\theta$. The geodesic component of the magnetic curvature is obtained by taking the scalar product of (B.26) with $\widehat{\mathbf{b}}$, given by (B.8),

$$\kappa_{\rm G} = \sin\theta\left(\frac{\lambda_\phi}{R}\;-\lambda_\phi{\lambda_\theta}^2\frac{\dot\Delta}{r\bar\eta}\right)\quad , \tag{B.29}$$

where we have used (B.14). Noting that $\bar\eta = 1 + \mathcal{O}(\epsilon)$ and $\dot\Delta \sim r \sim \lambda_\theta = \mathcal{O}(\epsilon)$, the lowest order geodesic curvature varies as $\sin\theta$. Expanding (B.28,B.29) in ascending powers of ϵ yield

$$\begin{aligned}\kappa_{\rm N} &= -\cos\theta + r\left(\cos^2\theta - \frac{1}{q^2}\right)\\ &- r^2\cos\theta\left[\cos^2\theta + \frac{1}{q^2}\left(2\,\frac{\dot\Delta}{r}\;-1\right) + \frac{\Delta}{r^2}\right] + \mathcal{O}\left(\epsilon^3\right)\quad ,\end{aligned} \tag{B.30}$$

for the normal curvature and

$$\begin{aligned}\kappa_{\rm G} &= \sin\theta - r\;\sin\theta\;\cos\theta\\ &+ r^2\sin\theta\left[\cos^2\theta - \frac{1}{2q^2}\left(1 + 2\,\frac{\dot\Delta}{r}\right) + \frac{\Delta}{r^2}\right] + \mathcal{O}\left(\epsilon^3\right)\quad ,\end{aligned} \tag{B.31}$$

for the geodesic curvature. In unnormalized units the normal curvature becomes, neglecting corrections of order ϵ^3 and higher

$$\kappa_{\rm N} = \kappa_{\rm N}^{(0)} + \kappa_{\rm N}^{(1)} + \kappa_{\rm N}^{(2)}\quad , \tag{B.32}$$

where

$$\kappa_{\rm N}^{(0)} = -\frac{\cos\theta}{R_0}\quad , \tag{B.33}$$

$$\kappa_{\rm N}^{(1)} = \frac{r}{{R_0}^2}\left(\cos\theta - \frac{1}{q^2}\right)\quad , \tag{B.34}$$

$$\kappa_{\rm N}^{(2)} = -\frac{r^2}{{R_0}^3}\;\cos\theta\left[\cos^2\theta + \frac{1}{q^2}\left(2\frac{R_0\dot\Delta}{r}\;-1\right) + \frac{R_0\Delta}{r^2}\right]\quad . \tag{B.35}$$

Similarly the geodesic curvature in unnormalized units is

$$\kappa_{\mathrm{G}} = \kappa_{\mathrm{G}}^{(0)} + \kappa_{\mathrm{G}}^{(1)} + \kappa_{\mathrm{G}}^{(2)} \ , \tag{B.36}$$

where

$$\kappa_{\mathrm{G}}^{(0)} = \frac{\sin\theta}{R_0} \ , \tag{B.37}$$

$$\kappa_{\mathrm{G}}^{(1)} = -\frac{r}{R_0} \ \sin\theta\cos\theta \ , \tag{B.38}$$

$$\kappa_{\mathrm{G}}^{(2)} = \frac{r^2}{R_0^3} \ \sin\theta \left[\cos^2\theta + \frac{R_0\Delta}{r^2} \ - \frac{1}{2q^2} \ \left(1 + 2\frac{R_0\dot{\Delta}}{r}\right)\right] \ . \tag{B.39}$$

B.3 Surface averaging

For an axi-symmetric tokamak configuration, the surface average of F is

$$\langle F \rangle (r) \equiv \frac{1}{A} \ \int_0^{2\pi} \mathcal{J}_\star (r,\theta') \, F(r,\theta') \ d\theta' \ , \tag{B.40}$$

where $A(r)$ is the area of the magnetic surface

$$\begin{aligned} A(r) &\equiv \int_0^{2\pi} \mathcal{J}_\star (r,\theta') \ d\theta' \\ &= 2\pi \left(r - \Delta - \frac{r\dot{\Delta}}{2}\right) \ . \end{aligned} \tag{B.41}$$

The Jacobian of the transformation is expanded in ascending powers of ϵ in the form $\mathcal{J}_\star = \mathcal{J}_\star^{(1)} + \mathcal{J}_\star^{(2)} + \mathcal{O}(\epsilon^3)$ where

$$\begin{aligned} \mathcal{J}_\star^{(1)} &= r \ , \\ \mathcal{J}_\star^{(2)} &= r^2 \cos\theta \left(1 - \frac{\dot{\Delta}}{r}\right) \ . \end{aligned} \tag{B.42}$$

It is worth noting that $\mathcal{J}_\star^{(1)}$ corresponds to the cylindrical contribution to $\mathcal{J}_\star$, whereas $\mathcal{J}_\star^{(2)}$ arises because of toroidicity effects. Substituting $F \mapsto \mathcal{S}$ in (B.40) and using (B.18,B.41,B.42) yields the global magnetic shear $\langle \mathcal{S} \rangle = \hat{s}$ or, in unnormalized units,

$$\langle \mathcal{S} \rangle = \frac{\hat{s}}{R_0^3} \ . \tag{B.43}$$

Similarly, substituting $F \mapsto \kappa_{\mathrm{N}}$ in (B.40) and using (B.30,B.41,B.42) yields the average normal curvature $\langle \kappa_{\mathrm{N}} \rangle = -r/q^2$ or, in unnormalized units,

$$\langle \kappa_{\mathrm{N}} \rangle = -\frac{r}{R_0^2 q^2} \ . \tag{B.44}$$

APPENDIX C

Field line curvature and local magnetic shear in general curvilinear coordinates

In this appendix, we derive the expressions for the magnetic field-line curvature and for the local magnetic shear (LMS) in general curvilinear coordinates. The curvilinear coordinates used here are (s, θ, ζ). The non-dimensional coordinate s labels the magnetic surfaces and $\mathbf{B}\cdot\boldsymbol{\nabla} s \equiv 0$ is assumed. The radial label s runs from 0 at the magnetic axis to 1 at the last closed magnetic surface. θ and ζ are the poloidal and toroidal angle-like coordinates, respectively. For convenience, we assume that θ and ζ are cyclic coordinates with period 2π. In the coordinate system (s, θ, ζ), the Jacobian of the transformation $\mathcal{J} \equiv [\boldsymbol{\nabla} s\cdot(\boldsymbol{\nabla}\theta\times\boldsymbol{\nabla}\zeta)]^{-1}$ scales like a volume because s, θ and ζ are dimensionless.

C.1 The magnetic curvature

The field line curvature is defined as

$$\boldsymbol{\kappa} \equiv \left(\widehat{\mathbf{e}}_{||}\cdot\boldsymbol{\nabla}\right)\widehat{\mathbf{e}}_{||}\ , \tag{C.1}$$

where $\widehat{\mathbf{e}}_{||} \equiv \mathbf{B}/B$ is a unit vector along the direction of the confining magnetic field. The magnetic field can be written as

$$\mathbf{B} = B^{\theta}\,\mathbf{e}_{\theta} + B^{\zeta}\,\mathbf{e}_{\zeta}\ . \tag{C.2}$$

Here $\mathbf{e}_{\theta} \equiv \partial\mathbf{r}/\partial\theta$, $\mathbf{e}_{\zeta} \equiv \partial\mathbf{r}/\partial\zeta$, where $\mathbf{r}$ is the position vector, and $B^{\theta} \equiv \mathbf{B}\cdot\boldsymbol{\nabla}\theta$ and $B^{\zeta} \equiv \mathbf{B}\cdot\boldsymbol{\nabla}\zeta$. The assumption of nested magnetic surfaces, $B^{s} = 0$, has been used

in the above equation. $\mathbf{B}$ can also be written in an alternative form

$$\mathbf{B} = B_s \boldsymbol{\nabla} s + B_\theta \boldsymbol{\nabla}\theta + B_\zeta \boldsymbol{\nabla}\zeta \ , \tag{C.3}$$

where $B_s \equiv \mathbf{B}\cdot\mathbf{e}_s$, $B_\theta \equiv \mathbf{B}\cdot\mathbf{e}_\theta$ and $B_\zeta \equiv \mathbf{B}\cdot\mathbf{e}_\zeta$. We now assume that the components B_s, B_θ, B_ζ and the position vector $\mathbf{r}$ are known everywhere in the plasma. Taking the scalar product of the gradient operator

$$\boldsymbol{\nabla} = \boldsymbol{\nabla} s \frac{\partial}{\partial s} \ + \boldsymbol{\nabla}\theta \frac{\partial}{\partial \theta} \ + \boldsymbol{\nabla}\zeta \frac{\partial}{\partial \zeta} \ , \tag{C.4}$$

with equation (C.2) and dividing by the magnetic field strength $B = \sqrt{B_\theta B^\theta + B_\zeta B^\zeta}$ yields

$$\nabla_{||} \equiv \hat{\mathbf{e}}_{||}\cdot\boldsymbol{\nabla} = b^\theta \ \frac{\partial}{\partial \theta} \ + b^\zeta \ \frac{\partial}{\partial \zeta} \ , \tag{C.5}$$

where $b^\theta \equiv B^\theta/B$ and $b^\zeta \equiv B^\zeta/B$. By operating with $\nabla_{||}$ on $\hat{\mathbf{e}}_{||} = b^\theta \mathbf{e}_\theta + b^\zeta \mathbf{e}_\zeta$, we get the field line curvature

$$\begin{aligned} \boldsymbol{\kappa} \ &= \ \left(b^\theta \frac{\partial b^\theta}{\partial \theta} \ + b^\zeta \frac{\partial b^\theta}{\partial \zeta} \right) \mathbf{e}_\theta + \left(b^\theta \frac{\partial b^\zeta}{\partial \theta} \ + b^\zeta \frac{\partial b^\zeta}{\partial \zeta} \right) \mathbf{e}_\zeta \\ &+ \ 2\, b^\theta\, b^\zeta \, \frac{\partial \mathbf{e}_\theta}{\partial \zeta} \ + \left(b^\theta\right)^2 \ \frac{\partial \mathbf{e}_\theta}{\partial \theta} \ + \left(b^\zeta\right)^2 \ \frac{\partial \mathbf{e}_\zeta}{\partial \zeta} \ . \end{aligned} \tag{C.6}$$

The right-hand side of equation (C.6) involves the first-order derivatives of the position vector (first 2 terms) as well as its second-order derivatives (last 3 terms). Taking the scalar product of the magnetic curvature vector (C.6) with the unit normal vector

$$\mathbf{n} \equiv \frac{\boldsymbol{\nabla} s}{\sqrt{g^{ss}}} \ , \tag{C.7}$$

where $g^{ss} \equiv \boldsymbol{\nabla} s \cdot \boldsymbol{\nabla} s$ is a metric element, yields the normal magnetic curvature

$$\kappa_{\mathrm{N}} = \frac{1}{\sqrt{g^{ss}}} \left[2\, b^\theta\, b^\zeta \ \boldsymbol{\nabla} s \cdot \frac{\partial \mathbf{e}_\theta}{\partial \zeta} \ + \left(b^\theta\right)^2 \ \boldsymbol{\nabla} s \cdot \frac{\partial \mathbf{e}_\theta}{\partial \theta} \ + \left(b^\zeta\right)^2 \ \boldsymbol{\nabla} s \cdot \frac{\partial \mathbf{e}_\zeta}{\partial \zeta} \right] . \tag{C.8}$$

Finally, the geodesic magnetic curvature is obtained by taking the scalar product of equation (C.6) with the unit binormal vector

$$\hat{\mathrm{b}} \equiv \frac{\mathbf{B}\times\boldsymbol{\nabla} s}{B\sqrt{g^{ss}}} \ , \tag{C.9}$$

yielding

$$\kappa_{\mathrm{G}} = \frac{1}{\mathcal{J}\sqrt{g}^{ss}} \ \left[b_\zeta \ \kappa_\theta - b_\theta \ \kappa_\zeta \right] \ , \tag{C.10}$$

where we have introduced

$$\begin{aligned}\kappa_\theta &\equiv \left(b^\theta\frac{\partial b^\theta}{\partial\theta}+b^\zeta\frac{\partial b^\theta}{\partial\zeta}\right)g_{\theta\theta}+\left(b^\theta\frac{\partial b^\zeta}{\partial\theta}+b^\zeta\frac{\partial b^\zeta}{\partial\zeta}\right)g_{\theta\zeta}\\ &+ 2\,b^\theta\,b^\zeta\,\mathbf{e}_\theta\cdot\frac{\partial\mathbf{e}_\theta}{\partial\zeta}+\left(b^\theta\right)^2\mathbf{e}_\theta\cdot\frac{\partial\mathbf{e}_\theta}{\partial\theta}+\left(b^\zeta\right)^2\mathbf{e}_\theta\cdot\frac{\partial\mathbf{e}_\zeta}{\partial\zeta}\ ,\end{aligned}\tag{C.11}$$

and

$$\begin{aligned}\kappa_\zeta &\equiv \left(b^\theta\frac{\partial b^\theta}{\partial\theta}+b^\zeta\frac{\partial b^\theta}{\partial\zeta}\right)g_{\theta\zeta}+\left(b^\theta\frac{\partial b^\zeta}{\partial\theta}+b^\zeta\frac{\partial b^\zeta}{\partial\zeta}\right)g_{\zeta\zeta}\\ &+ 2\,b^\theta\,b^\zeta\,\mathbf{e}_\zeta\cdot\frac{\partial\mathbf{e}_\theta}{\partial\zeta}+\left(b^\theta\right)^2\mathbf{e}_\zeta\cdot\frac{\partial\mathbf{e}_\theta}{\partial\theta}+\left(b^\zeta\right)^2\mathbf{e}_\zeta\cdot\frac{\partial\mathbf{e}_\zeta}{\partial\zeta}\ ,\end{aligned}\tag{C.12}$$

where $g_{\theta\theta}\equiv\mathbf{e}_\theta\cdot\mathbf{e}_\theta$, $g_{\theta\zeta}\equiv\mathbf{e}_\theta\cdot\mathbf{e}_\zeta$ and $g_{\zeta\zeta}\equiv\mathbf{e}_\zeta\cdot\mathbf{e}_\zeta$.

C.2 The local magnetic shear

Following Dewar *et al* [19], the local magnetic shear is defined as follows:

$$\mathcal{S}\equiv-\mathbf{s}\cdot\left(\boldsymbol{\nabla}\times\mathbf{s}\right)\ ,\tag{C.13}$$

where $\mathbf{s}\equiv\left(\boldsymbol{\nabla}\psi\times\mathbf{B}\right)/\left(\boldsymbol{\nabla}\psi\cdot\boldsymbol{\nabla}\psi\right)$ and $2\pi\psi$ is the enclosed poloidal flux. The poloidal flux is a flux surface quantity so that the vector $\mathbf{s}$ can also be written as

$$\mathbf{s}=-\frac{B}{\dot{\psi}\sqrt{g^{ss}}}\,\hat{\mathbf{b}}\ ,\tag{C.14}$$

where $\dot{\psi}\equiv d\psi/ds$. The above equation shows that $\mathbf{s}$ is a vector lying in the magnetic surface and anti-parallel to the binormal vector. Substituting equation (C.14) in equation (C.13) gives

$$\mathcal{S}=-H\,\mathbf{b}\cdot\left(\boldsymbol{\nabla}\times\mathbf{b}\right)\ ,\tag{C.15}$$

where $H\equiv\left(B/\dot{\psi}\sqrt{g^{ss}}\right)^2$. The LMS is then proportional to the projection of the rotational of the unit binormal vector onto itself. Taking the curl of $\mathbf{b}=b_s\boldsymbol{\nabla}s+b_\theta\boldsymbol{\nabla}\theta+b_\zeta\boldsymbol{\nabla}\zeta$ where

$$\begin{aligned}b_s &= \mathbf{b}\cdot\mathbf{e}_s=\mathcal{J}\,\frac{B^\theta g^{s\zeta}-B^\zeta g^{s\theta}}{B\sqrt{g^{ss}}}\ ,\\ b_\theta &= \mathbf{b}\cdot\mathbf{e}_\theta=\mathcal{J}\sqrt{g^{ss}}\,\frac{B^\zeta}{B}\ ,\\ b_\zeta &= \mathbf{b}\cdot\mathbf{e}_\zeta=-\mathcal{J}\sqrt{g^{ss}}\,\frac{B^\theta}{B}\ ,\end{aligned}\tag{C.16}$$

yields

$$\boldsymbol{\nabla}\times\mathbf{b} = \boldsymbol{\nabla}b_s\times\mathbf{e}^s + \boldsymbol{\nabla}b_\theta\times\mathbf{e}^\theta + \boldsymbol{\nabla}b_\zeta\times\mathbf{e}^\zeta \ , \tag{C.17}$$

since, for any scalar μ, we have $\boldsymbol{\nabla}\times\boldsymbol{\nabla}\mu = 0$. Taking the scalar product of (C.17) with $\widehat{\mathbf{b}}$, we get the LMS in curvilinear coordinates

$$\mathcal{S} = H\ \left[b_s\left(\frac{\partial b_\theta}{\partial\zeta} - \frac{\partial b_\zeta}{\partial\theta}\right) + b_\theta\left(\frac{\partial b_\zeta}{\partial s} - \frac{\partial b_s}{\partial\zeta}\right) + b_\zeta\left(\frac{\partial b_s}{\partial\theta} - \frac{\partial b_\theta}{\partial s}\right)\right] \ . \tag{C.18}$$

The explicit expression for the LMS is

$$\begin{aligned}
\mathcal{S} \ = \ & C\Bigg\{(B_\zeta\, g_{s\theta} - B_\theta\, g_{s\zeta})\left[g_{\theta\theta}\,\frac{\partial B_\zeta}{\partial\zeta} - g_{\theta\zeta}\left(\frac{\partial B_\theta}{\partial\zeta} + \frac{\partial B_\zeta}{\partial\theta}\right) + g_{\zeta\zeta}\,\frac{\partial B_\theta}{\partial\theta}\right.\\
& + \ B_\zeta\left(\frac{\partial g_{\theta\theta}}{\partial\zeta} - \frac{\partial g_{\theta\zeta}}{\partial\theta}\right) + B_\theta\left(\frac{\partial g_{\zeta\zeta}}{\partial\theta} - \frac{\partial g_{\theta\zeta}}{\partial\zeta}\right)\\
& + \ (B_\theta\, g_{\theta\zeta} - B_\zeta\, g_{\theta\theta})\left(\frac{1}{\mathcal{J}}\,\frac{\partial\mathcal{J}}{\partial\zeta} + \frac{1}{\sqrt{g^{ss}}}\,\frac{\partial\sqrt{g^{ss}}}{\partial\zeta} + \frac{1}{B}\,\frac{\partial B}{\partial\zeta}\right)\\
& + \ \left.(B_\zeta\, g_{\theta\zeta} - B_\theta\, g_{\zeta\zeta})\left(\frac{1}{\mathcal{J}}\,\frac{\partial\mathcal{J}}{\partial\theta} + \frac{1}{\sqrt{g^{ss}}}\,\frac{\partial\sqrt{g^{ss}}}{\partial\theta} + \frac{1}{B}\,\frac{\partial B}{\partial\theta}\right)\right]\\
& + \ (B_\zeta\, g_{\theta\theta} - B_\theta\, g_{\theta\zeta})\left[g_{\theta\zeta}\,\frac{\partial B_\zeta}{\partial s} - g_{\zeta\zeta}\,\frac{\partial B_\theta}{\partial s} - g_{s\theta}\frac{\partial B_\zeta}{\partial\zeta} + g_{s\zeta}\,\frac{\partial B_\theta}{\partial\zeta}\right.\\
& + \ B_\zeta\left(\frac{\partial g_{\theta\zeta}}{\partial s} - \frac{\partial g_{s\theta}}{\partial\zeta}\right) + B_\theta\left(\frac{\partial g_{s\zeta}}{\partial\zeta} - \frac{\partial g_{\zeta\zeta}}{\partial s}\right)\\
& + \ (B_\theta\, g_{\zeta\zeta} - B_\zeta\, g_{\theta\zeta})\left(\frac{1}{\mathcal{J}}\,\frac{\partial\mathcal{J}}{\partial s} + \frac{1}{\sqrt{g^{ss}}}\,\frac{\partial\sqrt{g^{ss}}}{\partial s} + \frac{1}{B}\,\frac{\partial B}{\partial s}\right)\\
& + \ \left.(B_\zeta\, g_{s\theta} - B_\theta\, g_{s\zeta})\left(\frac{1}{\mathcal{J}}\,\frac{\partial\mathcal{J}}{\partial\zeta} + \frac{1}{\sqrt{g^{ss}}}\,\frac{\partial\sqrt{g^{ss}}}{\partial\zeta} + \frac{1}{B}\,\frac{\partial B}{\partial\zeta}\right)\right]\\
& + \ (B_\zeta\, g_{\theta\zeta} - B_\theta\, g_{\zeta\zeta})\left[g_{s\theta}\,\frac{\partial B_\zeta}{\partial\theta} - g_{s\zeta}\,\frac{\partial B_\theta}{\partial\theta} - g_{\theta\theta}\,\frac{\partial B_\zeta}{\partial s} + g_{\theta\zeta}\,\frac{\partial B_\theta}{\partial s}\right.\\
& + \ B_\zeta\left(\frac{\partial g_{s\theta}}{\partial\theta} - \frac{\partial g_{\theta\theta}}{\partial s}\right) + B_\theta\left(\frac{\partial g_{\theta\zeta}}{\partial s} - \frac{\partial g_{s\zeta}}{\partial\theta}\right)\\
& + \ (B_\theta\, g_{s\zeta} - B_\zeta\, g_{s\theta})\left(\frac{1}{\mathcal{J}}\,\frac{\partial\mathcal{J}}{\partial\theta} + \frac{1}{\sqrt{g^{ss}}}\,\frac{\partial\sqrt{g^{ss}}}{\partial\theta} + \frac{1}{B}\,\frac{\partial B}{\partial\theta}\right)\\
& + \ \left.\left.(B_\zeta\, g_{\theta\theta} - B_\theta\, g_{\theta\zeta})\left(\frac{1}{\mathcal{J}}\,\frac{\partial\mathcal{J}}{\partial s} + \frac{1}{\sqrt{g^{ss}}}\,\frac{\partial\sqrt{g^{ss}}}{\partial s} + \frac{1}{B}\,\frac{\partial B}{\partial s}\right)\right]\right\} \ ,
\end{aligned} \tag{C.19}$$

where

$$C \equiv \left(\frac{1}{\dot{\psi}g^{ss}\mathcal{J}^{3/2}}\right)^2 \ . \tag{C.20}$$

In equation (C.19), we note the following

$$\begin{aligned}
\frac{\partial\sqrt{g^{ss}}}{\partial\lambda} \ = \ & -\frac{\sqrt{g^{ss}}}{\mathcal{J}}\,\frac{\partial\mathcal{J}}{\partial\lambda} + \frac{1}{g^{ss}\mathcal{J}^2}\ [g_{\zeta\zeta}\mathbf{e}_\theta\cdot\mathbf{G}_{\theta\lambda} + g_{\theta\theta}\mathbf{e}_\zeta\cdot\mathbf{G}_{\zeta\lambda}\\
& - \ g_{\theta\zeta}\left(\mathbf{e}_\zeta\cdot\mathbf{G}_{\theta\lambda} + \mathbf{e}_\theta\cdot\mathbf{G}_{\zeta\lambda}\right)\ ] \ ,
\end{aligned} \tag{C.21}$$

$$\frac{\partial \mathcal{J}}{\partial \lambda} = \mathbf{G}_{s\lambda} \cdot (\mathbf{e}_\theta \times \mathbf{e}_\zeta) + \mathbf{e}_s \cdot (\mathbf{G}_{\theta\lambda} \times \mathbf{e}_\zeta - \mathbf{G}_{\zeta\lambda} \times \mathbf{e}_\theta) \ , \tag{C.22}$$

$$\frac{\partial g_{\alpha\beta}}{\partial \lambda} = \mathbf{e}_\alpha \cdot \mathbf{G}_{\beta\lambda} + \mathbf{e}_\beta \cdot \mathbf{G}_{\alpha\lambda} \ , \tag{C.23}$$

and

$$\frac{\partial B}{\partial \lambda} = \frac{1}{2\sqrt{B_\theta B^\theta + B_\zeta B^\zeta}} \left(B_\theta \frac{\partial B^\theta}{\partial \lambda} + B^\theta \frac{\partial B_\theta}{\partial \lambda} + B_\zeta \frac{\partial B^\zeta}{\partial \lambda} + B^\zeta \frac{\partial B_\zeta}{\partial \lambda} \right) . \tag{C.24}$$

In equations (C.21-C.23), α, β or λ stands for s, θ or ζ. Equations (C.21-C.23) depend on the curvature of the position vector

$$\mathbf{G}_{\alpha\beta} \equiv \frac{\partial^2 \mathbf{r}}{\partial \alpha \partial \beta} \ , \tag{C.25}$$

for $(\alpha, \beta) = \{s, \theta, \zeta\}$.

APPENDIX D

Drift waves in the cold ion approximation

D.1 The model equation

We consider modes satisfying

$$\frac{k_{||}}{k_\perp} \sim \frac{\omega}{\omega_{cj}} \sim \frac{\rho_{thj}}{L} \sim \frac{e\Phi}{T_e} \sim \epsilon \ll 1 \,, \tag{D.1}$$

where $k_{||}$ and $k_\perp$ are the characteristic magnitude of the parallel and perpendicular wavevectors; ω is the characteristic mode frequency; $\omega_{cj} \equiv eB/(m_j c)$ is the cyclotron frequency for particle species j; $\rho_{thj} \equiv v_{thj}/\omega_{cj}$ is the thermal gyro-radius for particle species j and $v_{thj} \equiv \sqrt{2T_j/m_j}$ is the thermal velocity; Φ is the fluctuating electrostatic potential and L is a characteristic equilibrium scalelength. Furthermore, we consider modes with perpendicular wavelength comparable to the thermal gyro-radius,

$$k_\perp \rho_{thj} = \mathcal{O}(1) \,. \tag{D.2}$$

The perturbed distribution for particle species j is written as

$$\widetilde{F}_j = \widehat{F}_j \, \exp(in\alpha) \, \exp(-i\omega t) \,, \tag{D.3}$$

where $\widehat{F}_j$ is the slowly-varying amplitude, n is the (large) toroidal mode number and α is the field line label. It is convenient to write the amplitude in (D.3) as

$$\widehat{F}_j = -\frac{q_j \widehat{\Phi}}{T_j} \, F_{0j} + \widehat{h}_j \exp\left(i\varphi_j\right) \,, \tag{D.4}$$

where the first term on the right-hand side represents the adiabatic response (F_{0j} is the equilibrium distribution function), q_j is the charge for particle species j and

$\varphi_j \equiv \omega_{cj}^{-1}(\mathbf{v}\times\widehat{\mathbf{e}}_{||})\cdot\mathbf{k}_\perp$ is a phase. $\widehat{h}_j$ is the nonadiabatic response and satisfies the linear gyro-kinetic equation:

$$-i\left(\omega-\omega_{dj}+iv_{||}\nabla_{||}\right)\widehat{h}_j = \left\{C_L\left(\widehat{F}_j\right)\right\}_\xi - i\omega\left[\frac{F_{0j}}{T_j}+\frac{\left(\widehat{\mathbf{e}}_{||}\times\mathbf{k}_\perp\right)\cdot\boldsymbol{\nabla}F_{0j}}{m_j\omega\omega_{cj}}\right] \times J_0\left(q_j\widehat{\Phi}-\frac{q_jv_{||}}{c}\,\widehat{A}_{||}\right)\,, \tag{D.5}$$

where

$$\left\{C_L\left(\widehat{F}_j\right)\right\}_\xi \equiv \frac{1}{2\pi}\int_{-\pi}^{+\pi}d\xi\exp\left(-i\varphi_j\right)C_L\left(\widehat{F}_j\right)\,, \tag{D.6}$$

is the linearized collision operator averaged over the gyro-angle ξ. J_0 is the Bessel function with argument $k_\perp\rho_j$ and $\rho_j = k_\perp v_\perp/\omega_{cj}$. F_{0j} is the equilibrium distribution function. Letting

$$\widehat{g}_j \equiv \frac{\widehat{h}_j}{F_{0j}}\,, \tag{D.7}$$

the linear gyro-kinetic equation can be written in the following form

$$-i\left(\omega-\omega_{dj}+iv_{||}\nabla_{||}\right)\widehat{g}_j = -i\left(\omega+\omega_{\star j}\right)J_0\left(\frac{q_j\widehat{\Phi}}{T_j}-\frac{q_jv_{||}}{cT_j}\,\widehat{A}_{||}\right)\,, \tag{D.8}$$

where

$$\omega_{dj}\left(v\right) \equiv \frac{\mathbf{k}_\perp}{\omega_{cj}}\cdot\left[\widehat{\mathbf{e}}_{||}\times\left(v_{||}^2\boldsymbol{\kappa}+\frac{v_\perp^2}{2}\,\frac{\boldsymbol{\nabla}B}{B}\right)\right]\,, \tag{D.9}$$

is the *velocity-dependent* curvature drift frequency ($\boldsymbol{\kappa}$ is the magnetic curvature) and

$$\omega_{\star j}\left(v\right) \equiv \frac{cT_j}{eB}\,\left(\widehat{\mathbf{e}}_{||}\times\mathbf{k}_\perp\right)\cdot\frac{\boldsymbol{\nabla}F_{0j}}{F_{0j}} \tag{D.10}$$

is the *velocity-dependent* diamagnetic drift frequency. In the electrostatic limit ($\widehat{A}_{||}=0$), the gyro-kinetic equation for the electrons and the ions are only coupled through the quasineutrality condition

$$\int d^3v\left(\widetilde{F}_{\rm e}-\widetilde{F}_{\rm i}\right)=0\,. \tag{D.11}$$

We solve the gyro-kinetic equation (D.8) in the limit of fluid ions and adiabatic electrons

$$v_{\rm thi}\ll\frac{\omega}{k_{||}}\ll v_{\rm the}\,. \tag{D.12}$$

The nonadiabatic response for the electrons is expanded in powers of $\delta_{\rm e}\equiv|\omega/k_{||}v_{\rm the}|\ll 1$, while the nonadiabatic response for the ions is expanded in powers of $\delta_{\rm i}\equiv|k_{||}v_{\rm thi}/\omega|\ll 1$.

D.2 The electron response

The lowest-order nonadiabatic electron response for circulating electrons is

$$\mathbf{B}\cdot\boldsymbol{\nabla}\widehat{h}_{\mathrm{e}} = 0 \; . \tag{D.13}$$

Since $\widehat{h}_{\mathrm{e}}$ must vanish at infinity, then $\widehat{h}_{\mathrm{e}} = 0$. For trapped electrons, the solution for $\widehat{h}_{\mathrm{e}}$ requires an average between the turning points $v_{||} = 0$ (bounce averaging). In the general case, there is an infinite number of trapping regions and numerical methods must be used. For simplicity, we assume an *ad hoc* nonadiabatic electron response and the perturbed distribution function for the electrons reduces to

$$\widetilde{f}_{\mathrm{e}} = \frac{e\Phi}{T_{\mathrm{e}}} \, F_{0\mathrm{e}} \, (1 - i\delta) \; , \tag{D.14}$$

where δ is a parameter which models all kinetic effects preventing the perturbed electron distribution to reach a Boltzmann form.

D.3 The ion response

For simplicity we neglect collisions. The nonadiabatic ion response is written as

$$\widehat{g}_{\mathrm{i}} = \widehat{g}_{\mathrm{i}}^{(0)} + \widehat{g}_{\mathrm{i}}^{(1)} + \widehat{g}_{\mathrm{i}}^{(2)} \; , \tag{D.15}$$

where the superscripts indicate the corresponding order in δ_{i}. In general, the volume element in velocity space d^3v must be written in terms of μ_{i} (ion magnetic moment), $E_{\mathrm{i}} = m_{\mathrm{i}}v^2/2$ (ion kinetic energy) and ξ (gyro-angle). However, the neglect of collisions allows us to write $d^3v = 2\pi v_{\perp} dv_{\perp} dv_{||}$, since the parallel and perpendicular components of the velocity now enter as dummy coordinates (in phase space). Substituting equations (D.15,D.14) in the quasineutrality condition (D.11) yields

$$\begin{aligned} \frac{e\widehat{\Phi}}{T_{\mathrm{e}}} \, (1 - i\delta) \; - \; \int d^3v \frac{F_{0\mathrm{i}}}{n_0} \, \Bigg[& \frac{\omega + \omega_{\star\mathrm{i}}}{\omega - \omega_{\mathrm{di}}} \, J_0^2 \frac{e\widehat{\Phi}}{T_{\mathrm{i}}} \\ & - \frac{v_{||} J_0}{\omega} \, \nabla_{||} \frac{v_{||}}{\omega - \omega_{\mathrm{di}}} \, \nabla_{||} \frac{\omega J_0}{\omega - \omega_{\mathrm{di}}} \, \frac{e\widehat{\Phi}}{T_{\mathrm{i}}} \, \Bigg] + \frac{e\widehat{\Phi}}{T_{\mathrm{i}}} \; = 0 \; . \end{aligned} \tag{D.16}$$

In the above equation, $F_{0\mathrm{i}}$, $\omega_{\star\mathrm{i}}$, ω_{di} and J_0 are all velocity-dependent quantities. In the general case, the velocity integration must be performed numerically. We assume the equilibrium ion distribution is strongly peaked around the thermal velocity

$$F_{0\mathrm{i}} = n_0 \, \delta^{\star} \left(\mathbf{v} - \mathbf{v}_{\mathrm{thi}} \right) \; , \tag{D.17}$$

where

$$\int_{-\infty}^{+\infty} d^3X G(\mathbf{X})\delta^\star(\mathbf{X}-\mathbf{X}_0) = G(\mathbf{X}_0)\ , \tag{D.18}$$

for any $G(\mathbf{X})$. Furthermore, we relax the condition $k_\perp \rho_{\mathrm{thi}} = \mathcal{O}(1)$ and instead consider the long-wavelength (fluid) limit $k_\perp \rho_{\mathrm{thi}} = \mathcal{O}(\epsilon)$, where ϵ is the ordering parameter as given in (D.1). In the long-wavelength limit, we note that $J_0(k_\perp \rho_{\mathrm{i}}) = 1 - (k_\perp \rho_{\mathrm{i}})^2/4 + \mathcal{O}(\epsilon^4)$. However the difficulty associated with the curvature-driven resonances (terms of the form $(\omega - \omega_{\mathrm{di}})^{-1}$) remains. For simplicity, we assume that the condition

$$\frac{\omega_{\mathrm{di}}}{\omega} \ll 1\ , \tag{D.19}$$

is satisfied. Then substituting (D.17) into the quasineutrality condition (D.11), performing the integration over the velocity space and taking into account (D.19) we get

$$\frac{e\widehat{\Phi}}{T_{\mathrm{e}}}\ (1 - i\delta) + \left(1 - J_0^2\right)\frac{e\widehat{\Phi}}{T_{\mathrm{i}}} = \left(\frac{\langle\omega_{\star \mathrm{i}}\rangle}{\omega} + \frac{\langle\omega_{\mathrm{di}}\rangle}{\omega}\right)\frac{e\widehat{\Phi}}{T_{\mathrm{i}}} + \frac{v_{\mathrm{thi}}^2}{\omega^2}\ \nabla_{||}^2 \frac{e\widehat{\Phi}}{T_{\mathrm{i}}} \tag{D.20}$$

where $\langle ... \rangle$ denotes a velocity average. Corrections of order $(\omega_{\mathrm{di}}/\omega)^2$ and higher have been neglected. The first term on the left-hand side of equation (D.20) is the total electron response. The second term on the left-hand side is the ion polarization drift. This term is *a priori* small, $1 - J_0^2 = \mathcal{O}(\epsilon^2)$. However, in a system with nonvanishing global magnetic shear, the lowest-order perpendicular wavevector $k_\perp$ displays a secular behavior along the field line and the polarization contribution can become important.

D.4 The eigenmode equation

We note that each term arising from the ion response in equation (D.20) contains a linear contribution in T_{i} in the denominator and in the numerator. Therefore, we can use the electron temperature to normalize the equation, since the use of an 'ion temperature' for a distribution function of the form (D.17) is not meaningful. Expanding the $1 - J_0^2$ term, the final eigenmode equation reads

$$\frac{c_s^2}{\omega^2}\ \nabla_{||}^2 \frac{e\widehat{\Phi}}{T_{\mathrm{e}}} = -\left(1 - i\delta + k_\perp^2 \rho_s^2 + \frac{\omega_{\star \mathrm{e}}}{\omega} + \frac{\omega_{\mathrm{de}}}{\omega}\right)\frac{e\widehat{\Phi}}{T_{\mathrm{e}}}\ , \tag{D.21}$$

where $c_s \equiv \sqrt{T_\mathrm{e}/m_\mathrm{i}}$ and $\rho_s \equiv c_s/\omega_\mathrm{ci}$. We have also introduced the electron diamagnetic drift frequency

$$\omega_{\star\mathrm{e}} \equiv \frac{cT_\mathrm{e}}{eB}\left(\widehat{\mathbf{e}}_{||}\times\mathbf{k}_\perp\right)\cdot\frac{\boldsymbol{\nabla} n_0}{n_0} \ , \tag{D.22}$$

and the electron curvature drift frequency

$$\omega_\mathrm{de} \equiv 2\,\frac{cT_\mathrm{e}}{eB}\,\mathbf{k}_\perp\cdot\left(\widehat{\mathbf{e}}_{||}\times\frac{\boldsymbol{\nabla} B}{B}\right) \ . \tag{D.23}$$

D.5 Stellarator geometry

In this section, the eigenmode equation (D.21) is written in straight-field-line coordinates. As it turns out, the quantities which depend on the details of $|\mathbf{B}|$ also enter the gyro-kinetic equation (chapter 6). The final eigenmode equation is put in a wave-like form convenient for numerical work. It is convenient to work in normalized units. Let $\Omega \equiv \omega/\omega_{||}$, $\Omega_{\star\mathrm{e}} \equiv \omega_{\star\mathrm{e}}/\omega_{||}$ and $\Omega_\mathrm{de} \equiv \omega_\mathrm{de}/\omega_{||}$ where $\omega_{||} \equiv c_s/\bar{R}$. We also introduce a set of non-dimensional quantities defined along the magnetic field line. These are

$$\xi_\star \equiv L_n\frac{B_0}{B}\left(\widehat{\mathbf{e}}_{||}\times\frac{\mathbf{k}_\perp}{k_\theta}\right)\cdot\frac{\boldsymbol{\nabla} n_0}{n_0} \ , \tag{D.24}$$

$$\xi_d \equiv 2B_0\bar{R}\,\frac{\mathbf{k}_\perp}{k_\theta}\cdot\left(\widehat{\mathbf{e}}_{||}\times\frac{\boldsymbol{\nabla} B}{B}\right) \ , \tag{D.25}$$

$$\mathcal{L}_p = \left(\frac{\bar{a}B_0}{qB}\right)^2\boldsymbol{\nabla}\alpha\cdot\boldsymbol{\nabla}\alpha \ . \tag{D.26}$$

$\xi_\star$, ξ_d and $\mathcal{L}_p$ are related to the electron diamagnetic drift frequency, the electron curvature drift frequency and the ion polarization drift velocity, respectively. We also have to determine the appropriate form of the parallel gradient operator. Letting $\bar{\eta} \equiv \theta B_\theta(s) + \zeta B_\zeta(s)$, one writes the magnetic field in the form

$$\mathbf{B} = \boldsymbol{\nabla}\bar{\eta} + B_s^\star\boldsymbol{\nabla} s \ , \tag{D.27}$$

where $B_s^\star \equiv B_s - \theta\dot{B}_\theta - \zeta\dot{B}_\zeta$ and, as before, a dot denotes a derivative with respect to s. Then the parallel gradient operator, keeping the radial label and the field line label constants, can be written as

$$\nabla_{||} \equiv \left.\frac{\mathbf{B}\cdot\boldsymbol{\nabla}}{B}\right|_{s,\alpha} \ ,$$

$$
\begin{aligned}
&= \frac{\mathbf{B}\cdot\boldsymbol{\nabla}\bar{\eta}}{B}\,\Big|_{s,\alpha}\frac{\partial}{\partial\bar{\eta}}\ , \\
&= B\,\Big|_{s,\alpha}\frac{\partial}{\partial\bar{\eta}}\ , \\
&= \frac{\xi_{||}}{\bar{R}}\,\frac{\partial}{\partial\zeta}\ ,
\end{aligned}
\tag{D.28}
$$

where $\xi_{||}(\zeta) \equiv \bar{R}q\dot{\psi}/(\mathcal{J}B)$ is a non-dimensional function, defined along the extended toroidal angle, of the order of unity. Here $\mathcal{J} \equiv [\boldsymbol{\nabla}s\cdot(\boldsymbol{\nabla}\theta\times\boldsymbol{\nabla}\zeta)]^{-1}$ is the Jacobian of the transformation. Writing

$$
\widehat{\Psi} \equiv \sqrt{B}\,\widehat{\Phi}\ , \tag{D.29}
$$

then the eigenmode equation (D.21) can be cast in a wave-like form

$$
\frac{d^2\widehat{\Psi}}{d\zeta^2} = Q(\zeta;\Omega)\,\widehat{\Psi} \tag{D.30}
$$

where Q is the effective potential

$$
Q(\zeta,\Omega) \equiv C(\zeta) - \frac{\Omega\sqrt{b}}{\xi_{||}^2}\left(\frac{\xi_\star}{\epsilon_n} + \xi_d\right) - \frac{\Omega^2}{\xi_{||}^2}\left(1 - i\delta + b\mathcal{L}_p\right)\ . \tag{D.31}
$$

Here $b \equiv (k_\theta\rho_{s0})^2$ is a parameter of the order of unity, $\rho_{s0} = c_s/\omega_{ci0}$ and ω_{ci0} is the ion cyclotron frequency evaluated at the magnetic axis. In equation (D.31), we have introduced the following non-dimensional quantity

$$
C(\zeta) \equiv \frac{1}{2B}\,\frac{\partial^2 B}{\partial\zeta^2} - \frac{1}{4B^2}\left(\frac{\partial B}{\partial\zeta}\right)^2\ . \tag{D.32}
$$

We now determine the explicit form for $\xi_\star$, ξ_d and $\mathcal{L}_p$. The gradient of the equilibrium plasma density is

$$
\boldsymbol{\nabla}n_0 = -\frac{n_0}{L_n}\,\bar{a}\boldsymbol{\nabla}s\ , \tag{D.33}
$$

where $L_n \equiv -(\dot{n_0}/\bar{a}n_0)^{-1}$ is the radial density scalelength. Then

$$
\begin{aligned}
\xi_\star &= \frac{B_0\bar{a}^2}{Bq(s)}\,\boldsymbol{\nabla}s\cdot\left(\boldsymbol{\nabla}\alpha\times\frac{\mathbf{B}}{B}\right)\ , \\
&= -\frac{B_0\bar{a}^2}{q(s)\,\dot{\psi}}\ ,
\end{aligned}
\tag{D.34}
$$

where we have made use of the relation $B^2 = \dot{\psi}^2\left[\boldsymbol{\nabla}\alpha\cdot\boldsymbol{\nabla}\alpha\ \boldsymbol{\nabla}s\cdot\boldsymbol{\nabla}s - (\boldsymbol{\nabla}s\cdot\boldsymbol{\nabla}\alpha)^2\right]$. Equation (D.34) shows that $\xi_\star$ is a flux surface quantity. After straightforward

algebra, the normalized drift frequency can be written

$$\begin{aligned}\xi_d &= \frac{\bar{a}\bar{R}B_0}{q(s)B}\left[\left(\frac{\dot{F}}{F}-\frac{1}{\mathcal{J}}\frac{\partial\mathcal{J}}{\partial s}\right)\boldsymbol{\nabla}\alpha\cdot\left(\hat{\mathbf{e}}_{||}\times\boldsymbol{\nabla}s\right)-\frac{1}{\mathcal{J}}\frac{\partial\mathcal{J}}{\partial\theta}\boldsymbol{\nabla}\alpha\cdot\left(\hat{\mathbf{e}}_{||}\times\boldsymbol{\nabla}\theta\right)\right.\\ &- \left.\frac{1}{\mathcal{J}}\frac{\partial\mathcal{J}}{\partial\zeta}\boldsymbol{\nabla}\alpha\cdot\left(\hat{\mathbf{e}}_{||}\times\boldsymbol{\nabla}\zeta\right)\right] \qquad \text{(D.35)}\end{aligned}$$

where, in Boozer coordinates, $F(s)\equiv\mathcal{J}B^2$ is a flux surface quantity. For numerical calculations, it is convenient to write the above equation in term of metric elements. After some algebra, one can show that

$$\begin{aligned}\xi_d &= \frac{\bar{a}\bar{R}B_0}{q\dot{\psi}}\left[\frac{1}{\mathcal{J}}\frac{\partial\mathcal{J}}{\partial s}-\frac{\dot{F}}{F}\right.\\ &+ \frac{\dot{\psi}^2}{F}\frac{\partial\mathcal{J}}{\partial\theta}\left(\boldsymbol{\nabla}\alpha\cdot\boldsymbol{\nabla}\alpha\;\boldsymbol{\nabla}s\cdot\boldsymbol{\nabla}\theta-\boldsymbol{\nabla}\theta\cdot\boldsymbol{\nabla}\alpha\;\boldsymbol{\nabla}s\cdot\boldsymbol{\nabla}\alpha\right)\\ &+ \left.\frac{\dot{\psi}^2}{F}\frac{\partial\mathcal{J}}{\partial\zeta}\left(\boldsymbol{\nabla}\alpha\cdot\boldsymbol{\nabla}\alpha\;\boldsymbol{\nabla}s\cdot\boldsymbol{\nabla}\zeta-\boldsymbol{\nabla}\zeta\cdot\boldsymbol{\nabla}\alpha\;\boldsymbol{\nabla}s\cdot\boldsymbol{\nabla}\alpha\right)\right]. \qquad \text{(D.36)}\end{aligned}$$

Using

$$\boldsymbol{\nabla}\alpha=\boldsymbol{\nabla}\zeta-q\boldsymbol{\nabla}\theta-\dot{q}\theta\boldsymbol{\nabla}s\,, \qquad \text{(D.37)}$$

one gets the polarization drift term

$$\begin{aligned}\mathcal{L}_p &= \left(\frac{\bar{a}B_0}{qB}\right)^2\left[\boldsymbol{\nabla}\zeta\cdot\boldsymbol{\nabla}\zeta-2q\boldsymbol{\nabla}\theta\cdot\boldsymbol{\nabla}\zeta+q^2\boldsymbol{\nabla}\theta\cdot\boldsymbol{\nabla}\theta\right.\\ &+ \left.\dot{q}\theta\left(q\boldsymbol{\nabla}s\cdot\boldsymbol{\nabla}\theta-2\boldsymbol{\nabla}s\cdot\boldsymbol{\nabla}\zeta+\dot{q}\boldsymbol{\nabla}s\cdot\boldsymbol{\nabla}s\right)\right]. \qquad \text{(D.38)}\end{aligned}$$

APPENDIX E

Gyro-kinetic coefficients in Boozer coordinates

In this appendix, the WKB perpendicular wavevector, the diamagnetic drift frequency and the curvature drift frequency, all of which the gyro-kinetic equation, are derived in straight-field-line coordinates.

E.1 The perpendicular wavevector

The magnetic field is written in straight-field-line coordinates

$$\mathbf{B} = \dot{\psi}\boldsymbol{\nabla}\alpha\times\boldsymbol{\nabla}s\ , \tag{E.1}$$

where s is the normalized radial label, $\alpha \equiv \zeta - q(s)\theta$ is the field line label, $2\pi\psi$ is the poloidal flux enclosed within s. A dot denotes a derivative with respect to s. In the coordinate system $\{s,\theta,\zeta\}$, the Jacobian of the transformation is $\mathcal{J} \equiv [\boldsymbol{\nabla}s\cdot(\boldsymbol{\nabla}\theta\times\boldsymbol{\nabla}\zeta)]^{-1}$. In the WKB representation, the lowest-order perpendicular wavevector is

$$\begin{aligned}\mathbf{k}_\perp &= n\boldsymbol{\nabla}\alpha\ , \\ &= n\left(\boldsymbol{\nabla}\zeta - q\boldsymbol{\nabla}\theta - \dot{q}\theta\boldsymbol{\nabla}s\right)\ ,\end{aligned} \tag{E.2}$$

where $n \gg 1$ is the toroidal mode number. In the gyro-kinetic equation, the argument of the Bessel function is $k_\perp v_\perp/\omega_{cj}$, where ω_{cj} is the cyclotron frequency for particle species j. This term can be written as

$$\frac{k_\perp v_\perp}{\omega_{cj}} = C_\perp \frac{\bar{a}B_0}{q(s)B}\,|\boldsymbol{\nabla}\alpha|\ , \tag{E.3}$$

where $C_\perp \equiv k_\theta v_\perp/\omega_{cj0}$, $k_\theta \equiv mq(s)/\bar{a}$ is the characteristic perpendicular wavevector, ω_{cj0} is the cyclotron frequency for particle species j evaluated at the magnetic axis and $|\boldsymbol{\nabla}\alpha|$ is the magnitude of the multiple-valued function $\boldsymbol{\nabla}\alpha$

$$\begin{aligned} |\boldsymbol{\nabla}\alpha| &= \{\, \boldsymbol{\nabla}\zeta\cdot\boldsymbol{\nabla}\zeta - 2q(s)\boldsymbol{\nabla}\theta\cdot\boldsymbol{\nabla}\zeta + q^2(s)\boldsymbol{\nabla}\theta\cdot\boldsymbol{\nabla}\theta \\ &+ \dot{q}(s)\theta\,[q(s)\boldsymbol{\nabla}s\cdot\boldsymbol{\nabla}\theta - 2\boldsymbol{\nabla}s\cdot\boldsymbol{\nabla}\zeta + \dot{q}(s)\boldsymbol{\nabla}s\cdot\boldsymbol{\nabla}s]\,\}^{1/2} \,. \end{aligned} \tag{E.4}$$

The first 3 terms on the right-hand side of equation (E.4) are periodic functions of the extended toroidal angle ζ while the last 3 terms are responsible for the secular behavior of $|\boldsymbol{\nabla}\alpha|$.

E.2 The diamagnetic drift frequency

The diamagnetic drift frequency, for particle species j, is defined as

$$\omega^T_{\star j} \equiv -\frac{cT_j}{q_j B}\,\left(\widehat{\mathbf{e}}_{||}\times\mathbf{k}_\perp\right)\cdot\frac{\boldsymbol{\nabla}F_{Mj}}{F_{Mj}} \,, \tag{E.5}$$

where q_j is the charge, T_j is the equilibrium temperature and

$$F_{Mj} = \frac{n_0}{\pi^{3/2}v^3_{thj}}\,\exp\left(-\frac{v^2}{v^2_{thj}}\right) \,, \tag{E.6}$$

is the Maxwellian distribution function for particle species j, n_0 is the equilibrium plasma density and $v_{thj} \equiv \sqrt{2T_j/m_j}$ is the thermal velocity. One can show that

$$\frac{\boldsymbol{\nabla}F_{Mj}}{F_{Mj}} = -\frac{\bar{a}\boldsymbol{\nabla}s}{L_n}\,\left[1+\eta_j\left(\frac{E_j}{T_j} - \frac{3}{2}\right)\right] \,. \tag{E.7}$$

Here L_n is the radial density scalelength, $\eta_j \equiv n_0\dot{T}_j/T_j\dot{n}_0$ and $E_j \equiv m_j v^2/2$ is the particle kinetic energy. Letting $\omega_{\star j} \equiv (cT_j k_\theta)/(q_j B_0 L_n)$ then

$$\omega^T_{\star j} = -\omega_{\star j}\,\xi_\star\left[1+\eta_j\left(\frac{E_j}{T_j} - \frac{3}{2}\right)\right] \,, \tag{E.8}$$

where the non-dimensional quantity $\xi_\star$ has been derived in appendix D.

E.3 The curvature drift frequency

The curvature drift frequency, for particle species j, is defined as

$$\omega_{dj} \equiv \frac{1}{\omega_{cj}}\,\mathbf{k}_\perp\cdot\widehat{\mathbf{e}}_{||}\times\left(v^2_{||}\boldsymbol{\kappa} + \frac{v^2_\perp}{2}\,\frac{\boldsymbol{\nabla}B}{B} + \frac{q_j}{m_j}\,\boldsymbol{\nabla}\Phi_0\right) \,, \tag{E.9}$$

where Φ_0 is the equilibrium electrostatic potential and $\boldsymbol{\kappa}$ is the magnetic curvature. For simplicity we set $\boldsymbol{\nabla}\Phi_0$ to zero and make use of the low-β approximation $\boldsymbol{\kappa} \simeq \boldsymbol{\nabla}_\perp B/B$ to write

$$\omega_{dj} = \omega_{\star j} \frac{B_0 L_n m_j}{B T_j} \left(v_{||}^2 + \frac{v_\perp^2}{2} \right) \frac{\mathbf{k}_\perp}{k_\theta} \cdot \left(\widehat{\mathbf{e}}_{||} \times \frac{\boldsymbol{\nabla}_\perp B}{B} \right) \tag{E.10}$$

The one can show that

$$\omega_{dj} = \omega_{\star j} \frac{\xi_d}{\epsilon_n} \left[\left(\frac{v_{||}}{v} \right)^2 + \frac{1}{2} \left(\frac{v_\perp}{v} \right)^2 \right], \tag{E.11}$$

where the non-dimensional quantity ξ_d has been derived in appendix D.

Bibliography

[1] LEWANDOWSKI, J. L. V. and PERSSON, M., Plasma Physics and Controlled Fusion **37** (1995) 1199.

[2] LEWANDOWSKI, J. L. V. and PERSSON, M., Australian Journal of Physics **49** (1996) 1121.

[3] PERSSON, M., LEWANDOWSKI, J. L. V., and NORDMAN, H., Physics of Plasmas **2** (1996) 3440.

[4] CHAND, B., National seminar on electrical energy and environment, Number I-1, p. 204, New Delhi (India), 1989, Indian National Academy of Engineering.

[5] TANG, W. M., Nuclear Fusion **18** (1978) 1089.

[6] LIEWER, P. C., Nuclear Fusion **25** (1985) 543.

[7] WOOTON, A. J., CARRERAS, B. A., MATSUMOTO, H., et al., Physics of Fluids **B2** (1990) 2879.

[8] WAGNER, F. and STROTH, U., Plasma Physics and Controlled Fusion **35** (1993) 1321.

[9] HORTON, W., *Handbook of Plasma Physics*, volume 2, Elsevier Science, Amsterdam, The Netherlands, 1984.

[10] PERKINS, F. W., BARNES, C. W., JOHNSON, D. W., et al., Physics of Fluids **B5** (1993) 477.

[11] PETTY, C. C., LUCE, T. C., BURRELL, K. H., et al., Physical Review Letters **74** (1995) 1763.

[12] STROTH, U., MAASSBERG, H., and RINGLER, H., Physical Review Letters **70** (1993) 936.

[13] BRAGINSKII, S., *Review of Plasma Physics*, volume 1, Consultants Bureau, New York, 1965.

[14] GREENE, J. M. and JOHNSON, J. L., Plasma Physics **10** (1968) 729.

[15] FURTH, H. P., KILLEEN, J., ROSENBLUTH, M. N., and COPPI, B., in *Plasma Physics and Controlled Fusion Research*, volume 1, p. 617, Vienna (Austria), 1966, International Atomic Energy Agency.

[16] BATEMAN, G., *MHD. Instabilities*, MIT Press, Cambridge, 1978.

[17] COPPI, B., Physical Review Letters **39** (1977) 939.

[18] WALTZ, R. E. and BOOZER, A. H., Physics of Fluids **B5** (1993) 2201.

[19] DEWAR, R. L., MONTICELLO, D. A., and SY, W. N.-C., Physics of Fluids **27** (1984) 1723.

[20] GREENE, J. M. and CHANCE, M. S., Nuclear Fusion **21** (1981) 453.

[21] HAMBERGER, S. M., BLACKWELL, B. D., SHARP, L. E., and SHENTON, D. B., Fusion Technology **17** (1990) 123.

[22] COOPER, W. A. and GARDNER, H. J., Nuclear Fusion **34** (1994) 729.

[23] GREENE, J. M. and JOHNSON, J. L., Physics of Fluids **5** (1962) 510.

[24] GREENE, J. M., JOHNSON, J. L., KRUSKAL, M. D., and WILETS, L., Physics of Fluids **5** (1962) 1063.

[25] NEWCOMB, W. A., Annals of Physics **3** (1958) 347.

[26] BERNSTEIN, I. B., FRIEMAN, E. A., KRUSKAL, M. D., and KULSRUD, R. M., Proceedings of the Royal Society London **A 244** (1958) 17.

[27] SCHNEIDER, W. and BATEMAN, G., in *Plasma Physics and Controlled Fusion Research*, volume 1, p. 429, Vienna (Austria), 1974, International Atomic Energy Agency.

[28] TODD, A. M., CHANCE, M. S., GREENE, J. M., et al., Physical Review Letters **38** (1977) 826.

[29] D'HAESELEER, W. D., HITCHON, W. N. G., CALLEN, J., and SHOHET, J. L., *Flux Coordinates and Magnetic Field Structure*, Springer, Berlin, 1991.

[30] GREENE, J. M. and JOHNSON, J. L., *Advances in Theoretical Physics*, 1965.

[31] WARE, A. A., Technical Report CLM-M53 (unpublished), Culham Laboratory, 1965.

[32] WHITE, R. B., *Theory of Tokamak Plasmas*, Frontiers in Physics, North-Holland Physics, Amsterdam, Holland, 1989.

[33] BATHA, S. H., LEVINTON, F. M., SCOTT, S. D., et al., Physics of Plasmas **3** (1996) 1348.

[34] PHILLIPS, M. W., ZARNSTORFF, M. C., MANICKAM, J., LEVINTON, F. M., and HUGHES, M. H., Physics of Plasmas **3** (1996) 1673.

[35] RICE, B. W., BURRELL, K. H., LAO, L. L., et al., Physics of Plasmas **3** (1996) 1983.

[36] HUGON, M., MILLIGEN, B. P. V., SMEULDERS, P., et al., Nuclear Fusion **32** (1992) 33.

[37] STRAIT, E. J., Physics of Plasmas **1** (1994) 1415.

[38] LAZARUS, E. A., CHU, M. S., FERRON, J. R., et al., Physics of Fluids **B3** (1991) 2220.

[39] BOOZER, A. H., Physics of Fluids **23** (1980) 904.

[40] BOOZER, A. H., Physics of Fluids **24** (1981) 1999.

[41] IIYOSHI, A., FUJIWARA, M., MOTOJIMA, O., OHYABU, N., and YAMAZAKI, K., Nuclear Fusion **17** (1990) 169.

[42] KESSEL, C., MANICKAM, J., REWOLDT, G., and TANG, W., Physical Review Letters **72** (1994) 1212.

[43] ANTONSEN, T. M., DRAKE, J. J., GUZDAR, P. N., et al., Physics of Plasmas **3** (1996) 2221.

[44] GARDNER, H. J. and BLACKWELL, B. D., Nuclear Fusion **32** (1992) 2009.

[45] ALEJALDRE, C., GONZALO, J. J. A., PEREZ, J. B., et al., Fusion Technology **17** (1990) 131.

[46] GRIEGER, G., RENNER, H., and WOBIG, H., Nuclear Fusion **25** (1985) 1231.

[47] FREIDBERG, J. P., *Ideal Magnetohydrodynamics*, Modern Perspectives in Energy, Plenum Press, New York, 1987.

[48] BHATTACHARJEE, A., SEDLAK, J. E., SIMILON, P. L., ROSENBLUTH, M. N., and ROSS, D. W., Physics of Fluids **26** (1983) 880.

[49] MOROZOV, A. I. and SOLOVEV, L. S., *Reviews of Plasma Physics*, volume 2, Consultants Bureau, New York, 1966.

[50] PRESS, W. H., FLANNERY, B. P., TEUKOLSKY, S., and VETTERLING, W. T., *Numerical Recipes in Fortran*, Cambridge University Press, Cambridge, U.K., 1983.

[51] ABRAMOWITZ, M. and STEGUN, I., *Handbook of Mathematical Functions*, Dover Publications, Inc., New York, 1983.

[52] Advanced Visual Sytems Inc., Waltham, MA 02154, U.S.A., *AVS User's guide*, 1992.

[53] SHAFRANOV, V. D., Journal of Nuclear Energy **C 5** (1963) 251.

[54] GRAD, H. and RUBIN, H., Proceedings of the 2nd United Nations International Conference on the Peaceful Uses of Atomic Energy **31** (1959) 190.

[55] GREENE, J. M., JOHNSON, J. L., and WEIMER, K. E., Physics of Fluids **14** (1971) 671.

[56] GREENE, J. M., Communications in Pure and Applied Mathematics **36** (1983) 537.

[57] CONNOR, J. W., HASTIE, R. J., and TAYLOR, J. B., Physical Review Letters **40** (1978) 396.

[58] HIRSHMAN, S. P. and WHITSON, J. C., Physics of Fluids **26** (1983) 3553.

[59] HIRSHMAN, S. P. and MEIER, H. K., Physics of Fluids **28** (1985) 1387.

[60] HIRSHMAN, S. P. and LEE, D. K., Computer Physics Communications **38** (1986) 161.

[61] HIRSHMAN, S. P. and BETANCOURT, O., Journal of Computational Physics **86** (1991) 99.

[62] CONNOR, J. W., HASTIE, R. J., and TAYLOR, J. B., Proceedings of the Royal Society London **A 365** (1979) 1.

[63] ANTONSEN, T. M. and LANE, J. B., Physics of Fluids **23** (1980) 1205.

[64] CHENG, C. Z. and CHEN, L., Physics of Fluids **23** (1980) 1770.

[65] KADOMSTEV, B. B. and POGUTSE, O. P., Nuclear Fusion **11** (1971) 67.

[66] GLADD, N. T. and ROSS, D. W., Physics of Fluids **16** (1973) 1706.

[67] TANG, W. M., Physics of Fluids **17** (1974) 1249.

[68] LIEWER, P. C., MANHEIMER, W. M., and TANG, W. M., Physics of Fluids **19** (1976) 276.

[69] REWOLDT, G., TANG, W. M., and FRIEMAN, E. A., Physics of Fluids **20** (1977) 402.

[70] ROSS, D. W., TANG, W. M., and ADAM, J. C., Physics of Fluids **20** (1977) 613.

[71] TSANG, K. T., CALLEN, J. D., and CATTO, P. J., Physics of Fluids **20** (1977) 2113.

[72] HORTON, C. W. and VARMA, R. K., Physics of Fluids **15** (1972) 620.

[73] WAKATANI, M. and HASEGAWA, A., Physics of Fluids **27** (1984) 611.

[74] DRAKE, J. F. and HASSAM, A. B., Physics of Fluids **24** (1981) 1262.

[75] SCOTT, B. D., BIGLARI, H., TERRY, P. W., and DIAMOND, P. H., Physics of Fluids **B3** (1991) 51.

[76] SCOTT, B. D., Physics of Fluids **B4** (1992) 2468.

[77] SCOTT, B., Plasma Physics and Controlled Fusion **39** (1997) 471.

[78] WARE, A. S., DIAMOND, P. H., BIGLARI, H., et al., Physics of Fluids **B4** (1992) 877.

[79] HINTON, F. L. and HORTON, C. W., Physics of Fluids **14** (1971) 116.

[80] DEWAR, R. L. and GLASSER, A. H., Physics of Fluids **26** (1983) 3038.

[81] FRIEMAN, E. A. and CHEN, L., Physics of Fluids **25** (1982) 502.

[82] HASEGAWA, A. and MIMA, K., Physical Review Letters **39** (1977) 205.

[83] DOMINGUEZ, N., CARRERAS, B. A., and LYNCH, V. E., Physics of Fluids **B4** (1992) 2894.

[84] GLADD, N. T. and HORTON, W., Physics of Fluids **16** (1973) 879.

[85] CHEN, L., GUZDAR, P. N., HSU, J. Y., and KAW, P. K., Nuclear Fusion **19** (1979) 373.

[86] RUTHERFORD, P. H. and FRIEMAN, E. A., Physics of Fluids **11** (1968) 569.

[87] TAYLOR, J. B. and HASTIE, R. J., Plasma Physics **10** (1968) 479.

[88] FRIEMAN, E. A., Physics of Fluids **13** (1970) 490.

[89] CONNOR, J. W. and HASTIE, R. J., Plasma Physics **17** (1975) 97.

[90] CATTO, P. J. and TSANG, K. T., Physics of Fluids **20** (1977) 396.

[91] HAZELTINE, R. D., Plasma Physics **15** (1973) 77.

[92] CATTO, P. J., Plasma Physics **20** (1978) 719.

[93] REWOLDT, G., TANG, W. M., and CHANCE, M. S., Physics of Fluids **25** (1982) 480.

[94] DRAKE, J. F. and ANTONSEN, T. M., Physics of Fluids **27** (1984) 898.

[95] REWOLDT, G., TANG, W. M., and HASTIE, R. J., Physics of Fluids **29** (1986) 2893.

[96] REWOLDT, G., TANG, W. M., and HASTIE, R. J., Physics of Fluids **30** (1987) 807.

[97] TESSAROTTO, M., Nuovo Cimento B **75** (1983) 19.

[98] GRAD, H., in *Workshop on Mathematical Aspects of Fluid and Plasma Dynamics*, volume 1, p. 253, Trieste (Spain), 1985.

[99] TAGUCHI, M., Plasma Physics and Controlled Fusion **30** (1988) 1987.

[100] CORDEY, J., Nuclear Fusion **16** (1976) 499.

[101] HSU, C. T., CATTO, P. J., and SIGMAR, D. J., Physics of Fluids **B2** (1990) 280.

[102] TESSAROTTO, M., GREGORATTO, D., and ZHENG, L. J., Physics of Plasmas **2** (1995) 3614.

[103] ROSENBLUTH, M. N., ROSS, D. W., and KOSTOMAROV, D. P., Nuclear Fusion **12** (1972) 3.

[104] HIRSHMAN, S. P. and SIGMAR, D. J., Physics of Fluids **19** (1976) 1532.

[105] LEE, W. W., Physics of Fluids **26** (1983) 556.

[106] DUBLIN, D. H. E., KROMMES, J. A., OBERMAN, C., and LEE, W. W., Physics of Fluids **26** (1983) 3524.

[107] HAHM, T. S., Physics of Fluids **31** (1988) 2670.

[108] HAHM, T. S., LEE, W. W., and BRIZARD, A., Physics of Fluids **31** (1988) 1940.

[109] BRIZARD, A., Journal of Plasma Physics **41** (1989) 541.

[110] DENTON, R. E. and KOTSCHENREUTHER, M., Journal of Computational Physics **119** (1995) 283.

[111] KOTSCHENREUTHER, M., Bulletin of the American Physical Society **34** (1988) 2107.

[112] LEE, W. W., Journal of Computational Physics **72** (1987) 612.

[113] LEE, W. W. and TANG, W. M., Physics of Fluids **31** (1988) 612.

[114] SYDORA, R. D., Physics of Fluids **B2** (1990) 1455.

[115] PARKER, S. E. and LEE, W. W., Physics of Fluids **B5** (1993) 77.

[116] MYNICK, H. E. and PARKER, S. E., Physics of Plasmas **2** (1995) 1217.

[117] COHEN, B. I., WILLIAMS, T. J., and BYERS, J. A., Physics of Fluids **B5** (1993) 2697.

[118] HAMMETT, G. W. and PERKINS, F. W., Physical Review Letters **64** (1990) 3019.

[119] WALTZ, R. E., DOMINGUEZ, R. R., and HAMMETT, G. W., Physics of Fluids **B4** (1992) 3138.

[120] DORLAND, W. and HAMMETT, G. W., Physics of Fluids **B5** (1993) 812.

[121] BRIZARD, A., Physics of Fluids **B4** (1992) 1213.

[122] MANHEIMER, W. D. and LASHMORE-DAVIES, C. N., *MHD and Microinstabilities in Confined Plasma*, Adam Hilger, IOP Publishing Ltd, Bristol, U.K., 1989.

[123] SPITZER, L., *The Physics of Fully Ionized Gases*, Interscience, New York, U.S.A., 1956.

[124] ROSENBLUTH, M. N., MACDONALD, W. M., and JUDD, D. C., Physical Review **107** (1957) 1.

[125] HAZELTINE, R. D. and MEISS, J. D., *Plasma Confinement*, Frontiers in Physics, Addison-Wesley Publishing Company, Redwood City, CA, U.S.A., 1992.

[126] MIKHAILOVSKII, A. B., *Theory of Plasma Instabilites*, volume 2, Consultants Bureau, New York, U.S.A., 1974.

[127] MIYAMOTO, K., *Plasma Physics for Nuclear Fusion*, MIT Press, Cambridge, MA, U.S.A., 1976.

[128] SURKO, C. M. and SLUSHER, R. E., Physical Review Letters **36** (1976) 1747.

[129] MAZZUCATO, E., Physical Review Letters **36** (1976) 792.

[130] BROWER, D. L., PEEBLES, W. A., and LUHMANN, N. C., Physical Review Letters **55** (1985) 2579.

[131] PEARLSTEIN, L. D. and BERK, H. L., Physical Review Letters **23** (1969) 220.

[132] CALLEN, J. D., Physical Review Letters **39** (1977) 1540.

[133] WALTZ, R. E., Physics of Fluids **28** (1985) 577.

[134] TERRY, P. W. and DIAMOND, P. H., Physics of Fluids **28** (1985) 1419.

[135] WATTERSON, R. L., Bulletin of The American Physical Society **27** (1982) 937.

[136] LEVINSON, S. J., BELL, J. M., POWERS, E. J., and BENGSTON, R. D., Nuclear Fusion **24** (1984) 527.

[137] RITZ, C. P., Physics of Fluids **27** (1984) 2956.

[138] OHTSUKA, H., Plasma Physics **20** (1978) 749.

[139] ZWEBEN, S. J. and TAYLOR, R. J., Nuclear Fusion **21** (1981) 193.

[140] ZWEBEN, S. J., LIEWER, P. C., and GOULD, R. W., Journal of Nuclear Materials **112** (1982) 39.

[141] ARTUN, M. and TANG, W. M., Physics of Plasmas **1** (1994) 2662.

[142] BRIZARD, A. J., Physics of Plasmas **2** (1995) 459.

[143] RUDAKOV, L. I. and SAGDEEV, R. Z., Soviet Physics-Doklady **6** (1961) 415.

[144] POGUTSE, O. P., Soviet Physics JETP **25** (1967) 498.

[145] COPPI, B., ROSENBLUTH, M. N., and SAGDEEV, R. Z., Physics of Fluids **10** (1967) 582.

[146] ANTONSEN, T., COPPI, B., and ENGLADE, R., Nuclear Fusion **19** (1979) 641.

[147] HASSAM, A. B., ANTONSEN, T. M., DRAKE, J. F., and GUDZAR, P. N., Physics of Fluids **B2** (1990) 1822.

[148] HORTON, W., CHOI, D., and TANG, W. M., Physics of Fluids **24** (1981) 1077.

[149] KADOMSTEV, B. B. and POGUTSE, O. P., Nuclear Fusion **11** (1971) 67.

[150] COPPI, B. and REWOLDT, G., Physical Review Letters **33** (1974) 1329.

[151] TANG, W. M., ADAM, J. C., and ROSS, D. W., Physics of Fluids **20** (1977) 430.

[152] TANG, W. M., REWOLDT, G., and CHEN, L., Physics of Fluids **29** (1986) 3715.

[153] GUZDAR, P. N., CHEN, L., TANG, W. M., and RUTHERFORD, P. H., Physics of Fluids **26** (1983) 673.

[154] JARMEN, A., ANDERSSON, P., and WEILAND, J., Nuclear Fusion **27** (1987) 941.

[155] DOMINGUEZ, R. R. and WALTZ, R. E., Physics of Fluids **31** (1988) 3147.

[156] SHUKLA, P. K., Physics of Fluids **B2** (1990) 848.

[157] NORDMAN, H., WEILAND, J., and JARMEN, A., Nuclear Fusion **30** (1990) 983.

[158] HORTON, W., ESTES, R. D., and BISKAMP, D., Plasma Physics **22** (1980) 663.

[159] WALTZ, R. E., Physics of Fluids **31** (1988) 1962.

[160] HONG, B. G. and HORTON, W., Physics of Fluids **B2** (1990) 978.

[161] GUZDAR, P. N., DRAKE, J. F., DIMITS, A. M., and HASSAM, A. B., Physics of Fluids **B3** (1991) 1381.

[162] DRAKE, J. F., GUZDAR, P. N., and DIMITS, A., Physics of Fluids **B3** (1991) 1937.

[163] HAMAGUCHI, S. and HORTON, W., Physics of Fluids **B2** (1990) 1833.

[164] KIM, Y. B., DIAMOND, P. H., BIGLARI, K., and CALLEN, J. D., Physics of Fluids **B3** (1991) 384.

[165] HAMAGUCHI, S. and HORTON, W., Physics of Fluids **B4** (1992) 319.

[166] HEDRICK, C. L. and LEBOEUF, J.-N., Physics of Fluids **B4** (1992) 3915.

[167] PARKER, S. E., DORLAND, W., SANTORO, R. A., et al., Physics of Plasmas **1** (1994) 1481.

[168] REWOLDT, G. and TANG, W. M., Physics of Fluids **B2** (1990) 318.

[169] DONG, J. Q., HORTON, W., and KIM, J. Y., Physics of Fluids **B4** (1992) 1867.

[170] ROMANELLI, F. and BRIGUGLIO, S., Physics of Fluids **B2** (1990) 754.

[171] NILSSON, J. and WEILAND, J., Nuclear Fusion **34** (1994) 803.

[172] BIGLARI, H., DIAMOND, P. H., and ROSENBLUTH, M. N., Physics of Fluids **B1** (1989) 109.

[173] XU, X. Q. and ROSENBLUTH, M. N., Physics of Fluids **B3** (1991) 627.

[174] XU, X. Q. and ROSENBLUTH, M. N., Physics of Fluids **B3** (1991) 1807.

[175] KOTSCHENREUTHER, M., BERK, H. L., LEBRUN, M., et al., Number IAEA-CN-56/D1-2, p. 11, Wurzburg (Germany), 1992, International Atomic Energy Agency.

[176] ARTUN, M. and TANG, W. M., Physics of Fluids **B4** (1992) 1102.

[177] WAELBROECK, F. L. and CHEN, L., Physics of Fluids **B3** (1991) 601.

[178] COOPER, W. A., Plasma Physics and Controlled Fusion **30** (1988) 1805.

[179] COPPI, B. and MAZZUCATO, E., Physics of Fluids **114** (1971) 134.